

**Geological Evolution of the Monte Rosa:  
Constraints from Geochronology and  
Geochemistry of a Talc-Kyanite-Chloritoid  
Shear Zone within the Monte Rosa Granite  
(Monte Rosa Nappe, Italian Western Alps)**

Dissertation zur Erlangung des Grades

“Doktor der Naturwissenschaft”

am Fachbereich Geowissenschaften  
der Johannes Gutenberg-Universität in Mainz

Sabine Pawlig,  
geboren am 01.06.1973  
in Osnabrück

Mainz, September 2001

## Erklärung

Hiermit versichere ich, die vorliegende Arbeit selbständig und nur unter Verwendung der angegebenen Quellen und Hilfsmittel verfaßt zu haben.

All views and results presented in this thesis are those of the author unless stated otherwise.

Mainz, September 2001

Tag der mündlichen Prüfung: 23. November 2001



# Table of Contents

**Acknowledgements**

**Zusammenfassung**

**Summary**

<b>Chapter 1 General introduction .....</b>	<b>1</b>
1.1 <i>Published parts</i> .....	4
<b>Chapter 2 Geological overview.....</b>	<b>6</b>
2.1 <i>The Monte Rosa nappe within the framework of the Western Alps</i> .....	6
2.1.1 <i>The European continental basement</i> .....	7
2.1.2 <i>The Valais basin</i> .....	8
2.1.3 <i>The Briançonnais continental lithosphere</i> .....	8
2.1.4 <i>The Tethyan oceanic unit</i> .....	9
2.1.5 <i>The Austroalpine and South Alpine continental lithosphere</i> .....	11
2.2 <i>Previous studies in the Monte Rosa area</i> .....	12
2.3 <i>Aims and problems</i> .....	17
2.4 <i>Figures</i> .....	18
<b>Chapter 3 New U-Pb data on the crystallization age of the Monte Rosa granite, Western Alps – a combined SHRIMP, TIMS and cathodoluminescence study... 22</b>	
3.1 <i>Abstract</i> .....	22
3.2 <i>Introduction</i> .....	23
3.3 <i>Geology and sample selection</i> .....	24
3.4 <i>Analytical techniques</i> .....	26
3.5 <i>Morphology and CL-investigations</i> .....	27
3.6 <i>Geochronological results</i> .....	28
3.6.1 <i>SHRIMP ion probe measurements</i> .....	28
3.6.2 <i>TIMS multigrain and single zircon dating</i> .....	29
3.7 <i>Discussion</i> .....	30
3.8 <i>Geodynamic implications</i> .....	31
3.9 <i>Acknowledgements</i> .....	33
3.10 <i>Tables</i> .....	34
3.11 <i>Figures</i> .....	38

**Chapter 4 Retention of pre-Alpine white mica ages through Alpine high-pressure metamorphism in a talc-kyanite-chloritoid shear zone in the Monte Rosa (Western Alps): insights *in-situ* <sup>40</sup>Ar/<sup>39</sup>Ar UV-laser ablation analyses combined with a Sr isotopic study..... 47**

4.1	<i>Abstract</i> .....	47
4.2	<i>Introduction</i> .....	48
4.3	<i>Geological background</i> .....	49
4.4	<i>Analytical procedures</i> .....	51
4.5	<i>Sample description</i> .....	52
4.6	<i>Results</i> .....	54
4.6.1	<i>In-situ <sup>40</sup>Ar/<sup>39</sup>Ar UV-laser ablation analyses of white micas</i> .....	54
4.6.2	<i>Rb-Sr geochemistry</i> .....	55
4.7	<i>Discussion</i> .....	56
4.8	<i>Conclusion</i> .....	59
4.9	<i>Acknowledgements</i> .....	60
4.10	<i>Tables</i> .....	61
4.11	<i>Figures</i> .....	67

**Chapter 5 Geochemistry of a talc-kyanite-chloritoid shear zone within the Monte Rosa granite, Val d' Ayas, Italy ..... 76**

5.1	<i>Abstract</i> .....	76
5.2	<i>Introduction</i> .....	77
5.3	<i>Geology and petrography of the talc-kyanite-chloritoid shear zone in the upper Val d' Ayas</i> .....	78
5.4	<i>Analytical methods</i> .....	81
5.5	<i>Mass balance calculations</i> .....	81
5.6	<i>Stable isotope geochemistry</i> .....	84
5.7	<i>Discussion</i> .....	84
5.8	<i>Acknowledgements</i> .....	88
5.9	<i>Tables</i> .....	89
5.10	<i>Figures</i> .....	95

**Chapter 6 Chemical dating of monazite and fission track dating of apatite – Preliminary data ..... 104**

6.1	<i>Chemical dating of monazite – an overview</i> .....	104
6.2	<i>Monazites of the Monte Rosa nappe – preliminary results</i> .....	106
6.3	<i>Fission track dating of apatite</i> .....	109
6.4	<i>Tables</i> .....	112
6.5	<i>Figures</i> .....	115

<b>References .....</b>	<b>118</b>
-------------------------	------------

<b>Appendix.....</b>	<b>129</b>
----------------------	------------

<i>A1 Sample lists and maps.....</i>	<i>130</i>
--------------------------------------	------------

<i>A2 Tectonic data.....</i>	<i>142</i>
------------------------------	------------

<i>B CD-Rom.....</i>	<i>149</i>
----------------------	------------

**Curriculum vitae**

***“Man hatte Müh’, in Gedanken seine Wurzeln wieder an der Erde  
zu befestigen”***

***Johann Wolfgang von Goethe***



## Zusammenfassung

Im Rahmen dieser Dissertation wurde eine detaillierte geochemische und geochronologische Studie an Gesteinen der Monte Rosa Decke durchgeführt, welche zu den Penninischen Einheiten der Westalpen gehört. Die Monte Rosa Decke stellt ein strukturelles Äquivalent zum Gran Paradiso und dem Dora Maira Massiv dar. Sie besteht aus einem hochgradig metamorphen, metapelitischen Basement, welches vom Monte Rosa Granit intrudiert wurde. Teilweise ist die post-variszische Sedimenthülle erhalten. Die Monte Rosa Decke wurde während der alpinen Orogenese zunächst hochdruckmetamorph (eklogitfaziell) und nachfolgend grünschieferfaziell überprägt.

Die paläogeographische Rekonstruktion der prä-alpinen Grundgebirgs-einheiten in den Alpen konnte bisher noch nicht eindeutig gelöst werden, da prä-alpine Strukturen durch die komplexe alpine Evolutionsgeschichte meist fast komplett ausgelöscht wurden. Um die Monte Rosa Decke paläogeographisch in diesen großräumigen Gesamtkontext einordnen zu können, wurde eine detaillierte U-Pb geochronologische Studie an Proben des Monte Rosa Granits mit Hilfe von hochauflösenden Datierungsmethoden (SHRIMP und konventionelle Isotopenverdünnung) an Zirkonen und Monaziten durchgeführt. Sie ergab ein Permische Intrusionsalter für den Monte Rosa Granit von  $270 \pm 4$  Ma. Die Interpretation der gewonnenen geochronologischen Daten wurde durch Untersuchung der Zonierungsstrukturen der datierten Körner mit Hilfe von Kathodolumineszenz unterstützt. Somit gehört der Monte Rosa Granit zu den post-variszischen magmatischen Einheiten, welche hauptsächlich in den internen Bereichen des Alpenbogens vorkommen. Sie deuten die Instabilität der variszischen kontinentalen Kruste durch beginnende kontinentale Extension an. Diese Instabilität führt letztendlich zum Aufbrechen des Super-Kontinents Pangäa im Mesozoikum und weiterführend zur Öffnung der Tethys. Die Ergebnisse dieser Studie zeigen außerdem, daß für die Monte Rosa Decke eine paläogeographische Position entweder am Südrand der dem europäischen Kontinent vorgelagerten "Briançonnais-Schwelle" bzw. südlich davon als separater Mikrokontinent angenommen werden kann. Weiterhin finden sich Anzeichen einer Störung des U-Pb Systems besonders in uranreichen Zirkonen des Monte Rosa Granits, welche durch eine partielle Öffnung des U-Pb Systems und damit verbundenem Pb-Verlust während der alpinen Evolution der Monte Rosa Decke charakterisiert wird.

Innerhalb des Monte Rosa Granits treten unter anderem entlang von Scherzonen Talk-Kyanit-Chloritoid-Gesteine, sogenannte "Weißschiefer", auf. Diese stellen neben gelegentlich auftretenden Eklogit-Boudins wesentliche Indikatoren für eine alpine Hochdruckmetamorphose in der Monte Rosa Decke dar. Eine solche Scherzone wurde detailliert geochemisch und geochronologisch untersucht. Innerhalb dieser Scherzone kann klar der lithologische Übergang von undefor miertem Monte Rosa Granit über granitischen Gneis bis hin zu Weißschiefer verfolgt werden. Im Zentrum der Scherzone findet man eine Zone, welche sulfidreiche Karbonate enthält. Massenbilanzberechnungen wurden durchgeführt, um die Art und den Anteil des Massentransfers zu quantifizieren, welcher für die Bildung eines Weißschiefers aus einem granitischen Protolith notwendig ist. Dieser führt zu einer deutlichen Anreicherung von Mg, H<sub>2</sub>O und zum Teil Si, Fe und K, wohingegen Na, Ca, Sr, Ba, Pb und zum Teil U verarmt wurden. Die stabile Isotopie von Kohlenstoff und Sauerstoff des Karbonats besitzt magmatische Signatur und deutet an, daß es sich bei der Karbonatzone um eine spätmagmatische, hydrothermale Gangfüllung im Granit handelt. Ein solches spätmagmatisches Fluid alteriert den Granit entlang dieser Gangfüllung zu einer chlorit- und serizitreichen Paragenese, die während der alpinen, eklogitfaziellen Metamorphose in die kritische Paragenese Talk-Kyanit-Chloritoid umgewandelt wird.

## Zusammenfassung

An zwei Proben aus der Scherzone wurde eine *in-situ*  $^{40}\text{Ar}/^{39}\text{Ar}$  UV-Laser-Ablationsstudie an Hellglimmern durchgeführt. Es ergab sich eine heterogene Altersverteilung in beiden Proben. Basierend auf mikrostrukturellen sowie chemischen Untersuchungen gehören die datierten Phengite in beiden Proben zur alpinen Mineralparagenese. Die Ergebnisse zeigen allerdings nur  $^{40}\text{Ar}/^{39}\text{Ar}$  Alter, die älter als die alpine Hochdruckmetamorphose sind. Die Alter zwischen 280 und 250 Ma repräsentieren die originalen magmatischen Alter des granitischen Protoliths. Innerhalb der Schieferung der beiden Proben existieren Isotopengradienten, welche auf einer Distanz von 50  $\mu\text{m}$  Altersunterschiede von bis zu 50 Ma zwischen zwei Einzelmessungen ausmachen. Die Erhaltung solcher Gradienten kann durch eine verminderte Fluid- und Argonmobilität während der Glimmerrekristallisation unter relativ "trockenen" hochdruckmetamorphen Bedingungen erreicht werden. Die stark variierenden Alter zwischen 250 und 120 Ma sind das Ergebnis von partiellem Verlust von radiogenem Argon während der grünschieferfaziellen Überprägung der Scherzone, welche mit einer limitierten Fluidinfiltration verbunden war und durch das Auftreten von späten Quarz-Adern gekennzeichnet ist. Eine ähnlich komplexe Entwicklung der Scherzone, charakterisiert durch partielle Homogenisierung des Isotopensystems, kann in der Strontium-Isotopie der verschiedenen Scherzonen-Lithologien beobachtet werden. Es zeigt sich, daß mindestens zwei Events notwendig sind, um die beobachtete Strontium-Isotopie in den Weißschiefern zu erklären, wobei die zweite partielle Homogenisierung alpinen Alters ist, und ebenfalls durch Fluidinfiltration während der grünschieferfaziellen Metamorphose erklärt werden kann. Die Ergebnisse dieser isotopischen Studie zeigen daher, daß unter fluid-armen Bedingungen die isotopische Mobilität begrenzt ist. Außerdem scheint es kein allgemein gültiges "Schließverhalten" des Argon Isotopensystems in metamorphen Gesteinen zu geben. Eher ist das Verhalten des Argon-Isotopensystems unter hochdruckmetamorphen Bedingungen auf ein individuell sehr variables Zusammenspiel zwischen verschiedenen Faktoren zurückzuführen, wie z.B. Deformation, Argon-Diffusivität, Fluidinfiltration und dessen Mobilität. Diese Faktoren müssen mit Hilfe von hochauflösenden Analysemethoden für eine korrekte Interpretation von Argon-Daten sorgfältig evaluiert werden.

Weiterhin wurden aus Proben des Monte Rosa Granits sowie aus der Scherzone Monazite chemisch und auch isotopisch datiert. Mit Hilfe mikrostruktureller Beobachtungen können verschiedene Monazitgenerationen unterschieden werden. Große, einzelne Monazite ergaben permische Alter und werden als magmatische Relikte interpretiert. Desweiteren finden sich Matrixmonazite innerhalb der Schieferung der Proben, die meist eozäne Alter zwischen 30 und 40 Ma ergeben und das Alter der Hochdruckmetamorphose in der Monte Rosa Decke repräsentieren.

## Summary

A detailed geochemical and geochronological study has been carried out to contribute to the understanding of the geological evolution of the Monte Rosa nappe, a continental basement massif occurring within the Penninic units of the Western Alps. It is generally assumed to be structurally equivalent to the Gran Paradiso and Dora Maira massifs. The Monte Rosa nappe consists of a high-grade metapelitic basement, which was intruded by the Monte Rosa granite, and partially remnants of a post-Variscan cover still attached to the basement rocks. The Monte Rosa nappe was overprinted by an Alpine eclogite-facies metamorphism and a later, greenschist-facies retrogression.

A unique paleogeographic reconstruction of the pre-Alpine basement units in the Alps is mainly hindered due to the polyphase Alpine metamorphic evolution and abundant lack of protolith dating and geochemistry. To integrate the Monte Rosa nappe into a large-scale, pre-Alpine geological context, a detailed U-Pb geochronological study with high-resolution dating techniques (SHRIMP and conventional isotope dilution method) on zircons and monazites has been carried out. These investigations revealed a Permian intrusion age of the Monte Rosa granite of  $270 \pm 4$  Ma. Interpretation of the ages is supported by cathodoluminescence investigations. The Monte Rosa granite belongs to the post-Variscan magmatic assemblage mainly present in the internal parts of the Alpine basement units. This magmatic activity demonstrates the instability of the continental crust leading to the breakup of the Pangea super-continent during Mesozoic times, and in turns, the opening of the Neo-Tethys. Furthermore, constraints can be placed on the paleogeographic origin of the Monte Rosa nappe either as southern part of the so-called "Briançonnais domain" located south of the European continental margin or even as small continental fragment south of the Briançonnais. Disturbance of the U-Pb isotopic system during the subsequent geological evolution of the Monte Rosa nappe is indicated by uranium-rich zircons.

Discrete shear zones hosting talc-chloritoid-kyanite-bearing rocks occur within the Monte Rosa granite. These "whiteschists" are indicators for an Alpine high-pressure metamorphism within the Monte Rosa nappe. Detailed geochemical and geochronological work on one of those shear zones occurring within an otherwise undeformed part of the Monte Rosa granite was carried out. Weakly deformed granite grades into progressively more deformed gneiss leading to whiteschist. A garnet-talc-chloritoid-calcite-pyrite-quartz boudin marks the center of this shear zone. Mass balance calculations were done in order to assess the nature and amount of mass transfer necessary to produce the whiteschist from a granitic protolith. The results indicate enrichment of Mg and H<sub>2</sub>O with minor Si, Fe and K. Na, Ca, Sr, Ba, Pb and locally U are depleted. Stable isotope signature of carbon and oxygen from the carbonate points towards a magmatic fluid. A model for the evolution of the whiteschist is presented here: A pre-Alpine argillitic alteration leads to a chlorite-rich metasomatic alteration of the granite around a hydrothermal gangue mineralization. During Alpine high-pressure metamorphism, these special rocks with the critical high-pressure metamorphic assemblage kyanite-talc-chloritoid were formed from the altered granitic protolith due to strain localization into these rocks. This formed a deformational weak zone in the otherwise dry Monte Rosa granite. The presence of hydrous phases prior to metamorphism led to abundant recrystallization during high-pressure metamorphism.

Application of *in-situ* <sup>40</sup>Ar/<sup>39</sup>Ar UV-laser ablation analyses yields a heterogenous distribution of white mica ages within two samples from the kyanite-talc-chloritoid-bearing shear zone. Based on microstructural and chemical investigations, the analyzed phengites belong to the Alpine mineral assemblage in both samples. Only <sup>40</sup>Ar/<sup>39</sup>Ar ages in excess of the Alpine high-pressure event have

### *Summary*

been found. Ages as high as 250 to 280 Ma are present giving the original magmatic ages of the granitic protolith of this shear zone. A restricted fluid and argon mobility during the Alpine high-pressure metamorphic overprint is implied since small-scale argon isotopic gradients are maintained within the samples. Ages as young as approximately 120 Ma are the result of partial loss of radiogenic argon from the system during Alpine, eclogite and especially greenschist-facies metamorphism. A similar evolution, characterized by partial homogenization, is observed in the strontium isotopic composition of whole rock samples from different lithologies in the shear zone. It can be shown that at least two events are necessary to explain the strontium isotopic composition observed within the whiteschists today, whereby the second partial homogenization occurred during the Alpine metamorphism. The results of this study show that the evolution and behavior of the argon isotopic system under high-pressure metamorphism is a highly variable process characterized by a complex interaction of several processes. For a correct interpretation of argon geochronological data, several aspects as e.g. deformation, argon diffusivity, and especially fluid infiltration and its mobility, have to be evaluated carefully for a given sample with the help of high-resolution analyses techniques to identify small-scale isotopic and diffusional characteristics within individual samples. Therefore, it is not possible to explain the argon isotopic signatures of a given sample by a generally applied „closure behavior“ for argon in metamorphic rocks which evolved under similar conditions.

Monazites from the Monte Rosa granite and from samples of the shear zone were chemically and isotopically dated. Based on microstructural observations, different monazite generations can be distinguished. Large, single monazites yielded Permian ages and are interpreted as magmatic relics. On the other hand, matrix monazites located within the foliation yielded mostly Eocene ages of 30 to 40 Ma. They are interpreted as representing the age of the high-pressure metamorphism within the Monte Rosa nappe.



# **Chapter 1**

## **General introduction**

The present work is a contribution to the understanding of the evolution of the polymetamorphic Monte Rosa nappe located in the Western Alps.

Chapter 2 provides the geological background of the Monte Rosa nappe within the geological framework of the Western Alps, the previous studies performed in the Monte Rosa area, and states the aims and problems to be clarified during this study.

The paleogeography of the pre-Alpine basement units is still a matter of recent discussions and research (e.g. Von Raumer and Neubauer, 1993; Dal Piaz, 1993; Von Raumer, 1998; Neubauer et al., 1999; Von Raumer et al., 1999; Froitzheim, 2001). Therefore, a precise geochronological study of the Monte Rosa granite by high-resolution dating techniques as SHRIMP and conventional isotope dilution method on single zircons and monazites was carried out. The new geochronological data revealed a Permian ( $270 \pm 4$  Ma) intrusion age of the Monte Rosa granite and place constraints on the pre-Alpine geodynamic evolution of this large basement nappe within its large-scale geologic context. It is concluded that the Monte Rosa granite belongs to the post-Variscan magmatic assemblages, which indicate the instability of the Variscan continental crust leading to the breakup of the Pangea supercontinent during Mesozoic times. Moreover, disturbance of the U-Pb isotopic system in uranium-rich zircons is found and attributed to the re-opening of the U-Pb isotopic system during the subsequent geologic evolution of the Monte Rosa nappe. The results of this geochronological study are presented in chapter 3.

The next two chapters concentrate on the geochemical and geochronological evolution of a shear zone hosting talc-kyanite-chloritoid-bearing rocks occurring within the Monte Rosa granite in the upper Val d' Ayas (Italy), which are referred to as "whiteschists" throughout this thesis. Similar peculiar rocks were reported from several localities in the world, especially from the continental derived high-pressure

units in the Dora Maira and Gran Paradiso massifs of the Western Alps (e.g. Chopin et al., 1991; Dal Piaz and Lombardo, 1986; Sharp et al., 1993). Since there has been lack of knowledge concerning the protolith and the geochemical processes causing their formation, a genetical model for the evolution of whiteschists beyond the Monte Rosa geological context is given here. This model is based on a combined field, geochemical and stable isotope study on two detailed profiles taken across the studied shear zone. Mass transfer calculations were performed to demonstrate the chemical changes necessary to produce the whiteschists from the granitic protolith. The results imply that the special whole rock chemistry evolved during a pre-Alpine argillitic, hydrothermal alteration of the Monte Rosa granite. The later Alpine metamorphic overprint of this hydrothermally altered granitic protolith resulted in the formation of the critical high-pressure metamorphic assemblage talc-kyanite-chloritoid within the whiteschists. In chapter 5 a former suggested but not in detail described whiteschist-forming process and their petrological significance is described. Understanding of their genesis and a time-calibrated metamorphic history of those whiteschists is crucial for unravelling the geological evolution of the Monte Rosa nappe, since those whiteschists with their critical mineral assemblage talc-kyanite-chloritoid provide implications for the existence of an Alpine high-pressure metamorphism in the Monte Rosa nappe.

In Chapter 4 an *in-situ*  $^{40}\text{Ar}/^{39}\text{Ar}$  geochronological study on white micas of two shear zone samples is presented. Based on microstructural and chemical investigations, the analyzed phengites belong to the Alpine high-pressure mineral assemblage present in both samples. Only  $^{40}\text{Ar}/^{39}\text{Ar}$  ages in excess of the Alpine high-pressure event have been found. Ages as high as 250 to 280 Ma are the original magmatic cooling age of the Monte Rosa granite, which was obtained from U-Pb dating of zircon and monazite (Chapter 3). Ages as young as approximately 120 Ma are the result of partial loss of radiogenic argon during the Alpine greenschist-facies retrogression. The obtained argon ages and their distribution across the foliation show the preservation of small-scale argon isotopic gradients during the Alpine high-pressure metamorphism. Thus, a restricted fluid and argon mobility during white mica recrystallization during the Alpine high-pressure overprint is implied. A similar evolution, characterized by partial homogenization, is observed in the strontium isotopic composition of whole rock samples from different lithologies in the shear zone. Strontium evolution diagrams of the shear zone reveal that at least two events are necessary to explain the observed isotopic signatures in the whiteschists. The results demonstrate that the Alpine high-pressure metamorphism in the Monte Rosa

nappe has taken place under relatively dry conditions. Under these conditions, the argon isotopic system is more retentive than the strontium isotopic system. Therefore, this chapter provides suggestions on the behavior of the argon isotopic system during high-pressure metamorphism and deformation.

Chapter 6 gives a short presentation and discussion of unpublished microprobe data and results from chemical and isotopic dating of monazites from several samples of the Monte Rosa granite and whiteschist samples from the shear zone. Furthermore, it presents preliminary results and interpretations of fission track data of apatite from samples of the granite selected from different structural levels of the nappe in attempting to unravel the late-stage exhumation history of the Monte Rosa nappe.

Based on microstructurally observations and geochronological results, different generations of monazites can be distinguished. Large, unzoned single grains reveal Permian ages, which are interpreted as original magmatic ages of the Monte Rosa granite. On the other hand, monazites found either as single grains or aggregates of several small monazites within the foliation show ages between 30 to 40 Ma. Those ages are interpreted as the age of the Alpine high-pressure metamorphism.

Preliminary results of apatite fission track length revealed no obvious trend of varying fission track length in vertical direction between the different samples taken from different structural positions within the nappe. Therefore, a continuous cooling of the Monte Rosa nappe since 9 to 17 Ma is suggested. The results coincide with data for the Monte Rosa granite presented in the literature by Hurford et al. (1989, 1991). In comparison with literature data on zircon and apatite of adjacent tectonic units, a more-or-less simultaneous cooling of all tectonic units is suggested from existing data of zircon, which revealed a temperature of all units of  $<225^{\circ}\text{C}$  at ca. 33 Ma (Hurford et al., 1989; Hurford et al., 1991). However, differences between apatite data between the different tectonic units imply a tectonically based episodic uplift, probably related to the exhumation of those different units along major structural elements, e.g. the Insubric Line and the Aosta-Ranzola Fault (Hurford et al., 1989; Hurford et al., 1991).

## **1.1 Published parts**

Parts of this thesis have been submitted for publication. The following chapters were written as independent scientific papers and have been modified to fit the layout of this thesis.

Chapter 3 is identical to a manuscript submitted to the European Journal of Mineralogy in August 2001. Co-authors are U. Poller, L.P. Baumgartner and W. Todt.

Chapter 4 will be submitted to Earth and Planetary Science Letters in September 2001. Co-authors are L.P. Baumgartner and M.A. Cosca.

Chapter 5 is accepted for publication in the Schweizerische Mineralogische und Petrographische Mitteilungen. It will be published in Volume 81/3 in December 2001. Co-author is L.P. Baumgartner.

In addition, the results of this work were presented at several national and international conferences:

*Lange, S.*, Nasdala, L., Poller, U., Baumgartner, L.P. and Todt, W. (2000): Crystallization age and metamorphism of the Monte Rosa granite, Western Alps.- 17<sup>th</sup> Swiss Tectonic Studies Group Meeting, Zürich, p. 51; poster presentation.

*Lange, S.* and Baumgartner, L.P. (2000): Pre-metamorphic mass transfer in a high-pressure shearzone within the Monte Rosa granite, Western Alps.- Eur. J. Min., Vol. 12, Beih. 1, p. 109; oral presentation. DMG 2000 in Heidelberg.

*Lange, S.* and Baumgartner, L.P. (2000): Pre-metamorphic mass transfer in a high-pressure shearzone within the Monte Rosa granite, Western Alps.- Swiss Society for Mineralogy and Petrology annual meeting, Winterthur; poster presentation.

*Pawlig, S.* and Baumgartner, L.P. (2000): Development of a High-Pressure Shearzone in the Monte Rosa Nappe, Western Alps.- EOS Transactions, American Geophysical Union, Vol. 81, No. 48, F1365; poster presentation. AGU Fall Meeting in San Francisco.

***Pawlig, S.***, Baumgartner, L.P., Poller, U. and Todt, W. (2001): Rare Earth Element Mobility and Rb-Sr Open System Behaviour in a High-Pressure Shear Zone of the Monte Rosa Nappe (Western Alps).- J. Conf. Abs., 6, 613; oral presentation. EUG XI in Straßburg.

***Pawlig, S.***, Cosca, M.A. and Baumgartner, L.P. (2001): Retention of pre-Alpine  $^{40}\text{Ar}/^{39}\text{Ar}$  white mica ages through Alpine high-pressure metamorphism in a talc-kyanite-chloritoid shear zone in the Monte Rosa (Western Alps).- Eur. J. Min., Vol. 13, Beih.1, 138; oral presentation. DMG 2001 in Potsdam.

## Chapter 2

### Geological overview

#### ***2.1 The Monte Rosa nappe within the framework of the Western Alps***

Over the last two centuries, a wealth of geological data has been accumulated for the Alps, which are part of the Alpine-Himalayan orogenic system and represent the collision zone of the European and African continental plates.

During Mesozoic times, breakup of the Pangea supercontinent led to the formation of the Tethyan ocean, a large elongate pull-apart basin related to the opening of the Atlantic ocean. The Tethys separated the European continental plate to the north and the African continental plate to the south (Trümpy, 1980; Coward and Dietrich, 1989; Hsü, 1989). The Alpine orogen results from the consumption of the Tethyan ocean and the following collision of the European and African continental plates due to the southward subduction of the European continental margin beneath the African plate (e.g. Laubscher, 1983). The Alpine nappe pile was assembled by southeast over northwest thrusting (Argand, 1911; Trümpy, 1980; Froitzheim et al., 1996; Froitzheim, 2001). The boundary between the European and African plate is considered to be located at the base of the Austroalpine nappes (e.g. Coward and Dietrich, 1989). Three major tectonic nappe complexes, the Helvetic, the Penninic and the Austroalpine/South Alpine units (Fig. 2.1) characterize the geometry of the Alps. The Helvetic and Penninic units represent the shelf, slope and adjacent ribbon continents related to the European continental margin, whereas the Austroalpine nappes and South Alpine units are related to the overriding African plate (e.g. Hsü, 1989). Remnants of the Tethyan ocean are represented by ophiolitic rocks occurring in different structural units of the Alpine nappe pile, e.g. the Zermatt-Saas and Antrona ophiolites (Bearth, 1953, 1962, 1967, 1973; Gosso et al., 1979; Milnes et al., 1981; Beccaluva et al., 1984; Platt, 1986; Pfeifer et al., 1989; Polino et al., 1990). The restoration of the paleogeography of the Alpine units is a longstanding problem due to polyphase deformation and metamorphism during the complex Alpine history, and is object of recent debates. Several attempts are published for the

Western Alps concerning the position of the basement forming nappes as well as the number of oceanic basins ranging from one single to at least three oceanic basins (e.g. Platt, 1986; Polino et al., 1990; Froitzheim et al., 1996; Escher and Beaumont, 1997; Stampfli et al., 1998; Froitzheim, 2001). It is generally accepted that at least two basins existed during Jurassic to Cretaceous time, a northern one, the so-called *Penninic* or *Valaisan basin* and a southern one, the *South Penninic* or *Ligurian basin*. They were separated by the Briançonnais microcontinent (Platt, 1986; Froitzheim et al., 1996; Froitzheim, 2001). The northern, Valaisan basin consisted of thinned continental and possibly oceanic crust (e.g. Trümpy, 1980; Polino et al., 1990; Stampfli, 1993; Florineth and Froitzheim, 1994; Schmid et al., 1996; Stampfli and Marchant, 1997). On the other hand, the Ligurian basin separated the Briançonnais and the African continent to the south and was clearly characterized by large amounts of oceanic crust (e.g. Bearth, 1967, 1973; Dal Piaz, 1974; Platt, 1986; Polino et al., 1990). Different schematic paleogeographic reconstructions of the Alpine Tethys are given in figure 2.2.

In the following part, a brief description of each major tectonic unit of the Western Alps from bottom to top is given based on Escher and Beaumont (1997). The Western Alps are mainly made up by Helvetic and Penninic units, apart from few klippen and slices of the Austroalpine units which are included in the most internal part, i.e. the Mt. Emilius and Dent Blanche klippen and the Sesia-Lanzo Zone. The large-scale tectonic relationship of those units seems rather simple at first glance: The Helvetic and Penninic units, representing the paleo-European margin and adjacent ribbon continents (i.e. the Briançonnais high), are tectonically overlain by the ophiolitic rocks of the former Tethyan ocean floor. The Austroalpine units derived from the paleo-African (Adriatic) margin overlie the ophiolites in turn (Fig. 2.3).

### **2.1.1 The European continental basement**

The European continental crust and cover is mainly represented by the external (Helvetic) part of the arcuate belt (Fig. 2.2, 2.3). Those updomed basement nappes (i.e. Mont Blanc massif, Aiguilles Rouges massif, Belledonne massif, Pelvoux and Argentera massifs) consist of a polymetamorphic basement intruded by Variscan granitoids. They are separated by their Mesozoic cover and form initially N- to W-vergent structures (von Raumer et al., 1999). Later, S-vergent backfolding related structures are only observed southeast of the Aiguilles Rouges. The early Alpine deformation took place under greenschist-facies conditions in the external parts, whereas in the more internal parts amphibolite-facies is recorded. The later

backfolding was characterized by retrograde greenschist-facies metamorphism (Escher and Beaumont, 1997). During formation of the basement nappes, the cover was detached, displaced towards the northwest and is now forming the Helvetic cover nappes. Triassic evaporites served as detachment horizons.

### ***2.1.2 The Valais basin***

A discontinuous zone of remnants of the Valais basin, i.e. the Sion-Courmayeur Zone, the Rosswald Series or the Infra Moncucco Ophiolites, is found in between nappes derived from the European continental crust and those originating from the Briançonnais microcontinent (Trümpy, 1980; Platt, 1986; Polino et al., 1990; Escher and Beaumont, 1997; Fig. 2.2). Those remnants are mainly made up by calcschists, schists, limestones, quartzites and conglomeres („schistes lustrés“) with locally occurring mafic to ultramafic rocks. Those locally mafic rocks may indicate the presence of either an oceanic or a thinned continental crust. Alpine metamorphism of the schistes lustrés mainly took place under greenschist-facies conditions (Polino et al., 1990; Florineth and Froitzheim, 1994; Froitzheim et al., 1996).

### ***2.1.3 The Briançonnais continental lithosphere***

A large system of continental nappes are assumed to form a central zone between the Valaisan and the Ligurian oceanic basins off the paleo-European margin, the so-called Briançonnais or Grand St. Bernard nappe system (Fig. 2.2; e.g. Escher et al., 1988; Sartori, 1990; Stampfli, 1994; Escher and Beaumont, 1997; Stampfli et al., 1998). The Grand St. Bernard nappe system is separated into several independent nappes (Fig. 2.3), the „Zone houillère“, the Pontis and the Siviez-Mischabel nappes, and the Mont Fort nappe (Ballèvre and Merle, 1993). The „Zone houillère“ is made up by Carboniferous and Permo-Triassic siliceous detrital sequences and partially associated Triassic platform carbonates. Alpine deformation and greenschist-facies metamorphic overprint is recorded. The Pontis and the Siviez-Mischabel nappes comprise pre-Alpine basement with abundant relics of amphibolite-facies, and rare relics of eclogite-facies metamorphism as well as a greenschist-facies retrogression and deformation (e.g. Ballèvre and Merle, 1993). The Mont Fort nappe consists of an Upper Paleozoic basement and its Mesozoic sedimentary cover. Blueschist-facies assemblages developed during the Alpine metamorphic history as well as greenschist-facies assemblages during retrogression (Ballèvre and Merle, 1993).



The more internal part of the nappe pile observed in the Western Alps is characterized by the three large basement nappes, the Dora Maira massif, the Gran Paradiso massif and the Monte Rosa nappe (Fig. 2.3). They are also assumed to originate from the Briançonnais high but a more internal position with respect to the Grand St. Bernard nappe system is assumed (Bearth, 1939; Platt, 1986; Escher et al., 1988; Escher and Beaumont, 1997). In particular, Platt (1986) suggested that the Monte Rosa nappe represents an isolated continental fragment separated from the Briançonnais by a narrow oceanic basin, now represented by the Antrona ophiolite (Fig. 2.2). The Monte Rosa, Gran Paradiso and Dora Maira massifs commonly consist of voluminous, pre-Alpine granites intruded into an a pre-Variscan basement (Bearth, 1952; Compagnoni et al., 1974; Dal Piaz and Lombardo, 1986; Chopin et al., 1991; Paquette et al., 1999; Brouwer, 2000; Bertrand et al., 2001). Partially, remnants of a post-Variscan cover are still attached to the basement rocks of all three massifs (Bearth, 1952; Vialon, 1966; Compagnoni et al., 1974; Bearth and Schwander, 1981; Dal Piaz and Lombardo, 1986; Borghi et al., 1996; Froitzheim, 2001). All three continental basement units were deformed and metamorphosed under high- to partially ultrahigh-pressure metamorphic conditions during the Alpine orogeny implied by occurrences of eclogites and partially coesite relics (Dal Piaz, 1966; Wetzel, 1972; Klein, 1978; Chopin, 1984; Dal Piaz and Lombardo, 1986; Massonne and Chopin, 1989; Chopin, 1991; Schertl et al., 1991; Henry et al., 1993; Gebauer et al., 1997; Brouwer, 2000). An Alpine greenschist-facies overprint followed the Alpine eclogite-facies metamorphism (e.g. Frey et al., 1976; Dal Piaz and Lombardo, 1986; Chopin et al., 1991; Borghi et al., 1996; Brouwer, 2000). Since recent geochronological studies yielded Eocene ages (35 Ma) for the Alpine high- to ultrahigh-pressure metamorphism of the Monte Rosa and Dora Maira basement massifs (Gebauer et al., 1997; Rubatto and Gebauer, 1999), a fast exhumation is indicated when combining the peak metamorphic ages with published fission track data of zircon and apatite of 30 Ma and 10 to 20 Ma as obtained for the Gran Paradiso and Monte Rosa nappes, respectively (Hurford et al., 1989; Hurford et al., 1991).

#### *2.1.4 The Tethyan oceanic unit*

This study focus on the northern part of the Western Alps, and thus, the description of the oceanic derived units will be restricted to the eclogite- and partially coesite-bearing Zermatt-Saas Zone (Reinecke, 1998) and the Combin Zone, a mélange which partially bears ophiolitic relics (Ballèvre and Merle, 1993).

The Zermatt-Saas Zone is a large slice of oceanic lithosphere and associated oceanic sediments (Bearth, 1967; Reinecke, 1991; Bowtell et al., 1994; Reinecke, 1998). It underwent high- to ultrahigh-pressure metamorphic conditions during Alpine subduction (Bearth, 1967; Meyer, 1983; Ernst and Dal Piaz, 1978; Barnicoat and Fry, 1986; Martin and Tartarotti, 1989; Reinecke, 1991; van der Klauw et al., 1997; Reinecke, 1998). Those ultrahigh-pressure conditions were constrained from the discovery of coesite relics in MORB-type metabasalts and in the overlying metasediments at Lago di Cignana (Val Tournanche, Italy). Maximum PT-conditions during ultrahigh-pressure metamorphism were about 600 to 630°C and 27 to 29 kbar. Later retrogression followed under greenschist-facies conditions (Reinecke, 1998). Jurassic formation of the oceanic crust was given by U-Pb SHRIMP zircon ages of  $164 \pm 3$  and  $163.5 \pm 1.8$  Ma for the Mellichen and Allalin metagabbros, respectively (Rubatto et al., 1998). Those ages are supported by the maximum deposition ages of  $161 \pm 11$  Ma for Mn-rich metasediments which are found on top of the oceanic crust at Lago di Cignana (Rubatto et al., 1998). Age constraints for the Alpine subduction of the Tethyan oceanic crust have been presented by Bowtell et al. (1994), Rubatto et al. (1998), Reddy et al. (1999) and Amato et al. (1999), which report  $52 \pm 18$  Ma,  $44 \pm 1$  Ma,  $46.4 \pm 0.6$  Ma and  $41 \pm 3$  Ma for the eclogite-facies metamorphism, respectively. The Zermatt-Saas ophiolite reached greenschist-facies conditions around  $38 \pm 2$  Ma as deduced from Rb-Sr whole rock–phengite isochrons (Amato et al., 1999).

The Combin Zone situated structurally above the Zermatt-Saas Zone only underwent blueschist-facies metamorphism since only relics of blue amphiboles are found in metabasites (Dal Piaz, 1976; Dal Piaz and Ernst, 1978; Sperlich, 1988; Ballèvre and Merle, 1993). Additionally, some carpholite pseudomorphs have been reported by Pfeifer et al. (1991), and thus PT-conditions of 6 to 8 kbar at about 400°C are suggested. Two main units characterize the Combin Zone. The first one is made up by marly metasediments, mainly calcschists, and greenschists, which were derived from basaltic volcanics and partially gabbros as well as some serpentinites and Mn-quartzites indicating the origin from an oceanic unit. According to Sartori (1990), this unit is referred to as the Tsaté nappe and is probably the remnant of an accretionary prism that was formed during the subduction and closure of the oceanic domain. The other one is a sedimentary sequence ranging from Permian siliceous conglomerates to Triassic quartzites and dolomitic marbles deposited on top of a continental crust. Also some calcareous sequences of presumed Jurassic age are present (Ballèvre and Merle, 1993).

The Combin and the Zermatt-Saas Zones are separated by a large-scale, extensional detachment fault, named „Combin fault“ by Ballèvre and Merle (1993) and „Gressoney Shear Zone“ by Reddy et al. (1999). Both are used for the contact that separates the greenschist-facies rocks of the Combin Zone at structurally higher levels from the immediately underlying eclogite-facies rocks of the Zermatt-Saas Zone (Reddy et al., 1999). Reddy et al. (1999) presented Rb-Sr whole rock-phengite isochron data for the timing of orogenic extension along the Gressoney Shear Zone which took place between 36 and 45 Ma. In combination of those data with published geochronological data of the Zermatt-Saas Zone, they suggested that this extensional deformation immediately after peak eclogite metamorphic conditions was therefore responsible for the initial exhumation of the Zermatt-Saas ophiolite.

### ***2.1.5 The Austroalpine and South Alpine continental lithospheres***

Classically, three main Austroalpine units are distinguished (e.g. Dal Piaz et al., 1972; Compagnoni et al., 1977). The *seconda zona dioritico-kinzigitica (IIDK)* is the upper element, and the *Eclogitic micaschist complex* and the *Gneiss Minuti complex* form the lower units.

The *IIDK* is found in the Sesia-Lanzo Zone and its equivalent is the *Valpelline Series* of the Dent Blanche klippe. The main rock types of the IIDK belong to a pre-Variscan basement recording a pervasive high-temperature metamorphism. These are kinzigites, amphibolites, marbles and ultramafites which show granulite-facies assemblages that are similar to those of the Diorito-Kinzigitic Zone of the Ivrea Zone (Dal Piaz et al., 1971; Pognante et al., 1988; Zingg et al., 1990). The *IIDK* was only slightly affected by Alpine polyphase deformation and greenschist-facies reequilibration (e.g. Pennacchioni and Cesare, 1997; Dal Piaz et al., 2001).

The *Eclogitic micaschist complex* occurs in the southeastern part of the Sesia-Lanzo Zone and some tectonic klippen, referred to as „lower Austroalpine eclogitic outliers“ (i.e. Mt. Emilius, Glacier-Rafray, Etirol-Levaz) by Dal Piaz et al. (2001). It consists of a pre-Alpine basement that is made up by ortho- and paragneisses (Compagnoni et al., 1977). Post-Variscan granitoids intruded the basement, i.e. the Monte Mucrone metagranite (Oberhänsli et al., 1985; Paquette et al., 1989). Early Alpine eclogite-facies metamorphism is recorded in all rocks, with large portions of eclogites preserved in the Mt. Emilius klippe (Biino and Compagnoni, 1988; Dal Piaz et al., 2001).

The *Gneiss Minuti Complex* forms the northern part of the Sesia-Lanzo Zone, and its equivalent in the Dent Blanche and Pillonet klippen is referred to as the

*Arolla Series* (Dal Piaz, 1976; Ballèvre and Merle, 1993). An extensive Alpine greenschist-facies metamorphism is recorded that hinders the recognition of relics of an earlier eclogite-facies metamorphism (Ballèvre and Merle, 1993). The age of the high-pressure metamorphism in the Sesia-Lanzo Zone was dated to 65 Ma by U-Pb SHRIMP on metamorphic zircon-rims from eclogite-facies rocks (Rubatto et al., 1999). Recently presented geochronological data by Dal Piaz et al. (2001) shows that the different tectonic klippen of the Sesia-Lanzo Zone have been subducted concurrently with the Zermatt-Saas ophiolite. They derived 49 to 40 Ma for lower Austroalpine eclogitic outliers, e.g. the Mt. Emilius. Therefore, subduction of those klippen occurred around 25 Ma later than in the Sesia-Lanzo Zone. These data imply a paleogeographic position of e.g. the Mt. Emilius klippe as separated block within the Tethyan ocean (Cortiana et al., 1998; Dal Piaz, 1999; Dal Piaz et al., 2001)

The South Alpine continental lithosphere of the Western Alps is mainly represented by the Ivrea and Strona-Ceneri Zones, which are separated from the Sesia-Lanzo Zone to the north by the Canavese Line. It is the westernmost portion of the Insubric Line. In contrast to the other units described above, the Alpine subduction processes did not affect the Ivrea as well as the Strona-Ceneri Zone. The Ivrea Zone is a subvertical cross-section from the MOHO to the continental crust (Mehnert, 1975; Henk et al., 1997). Gneisses that contain partially mafic and ultramafic rocks displaying granulite facies metamorphism can be found (Zingg et al., 1990). The mid-crustal upper part, the Strona-Ceneri Zone, is formed by a monotonous series of paragneisses, schists and minor amphibolites. An early, eclogite-facies metamorphism took place before Ordovician and was followed by two medium-grade metamorphic overprints in early Ordovician and in Variscan time. Near the contact to the Ivrea Zone, the Strona-Ceneri Zone also experienced an Early Permian heating event which is represented by several granite intrusions.

## **2.2 Previous studies in the Monte Rosa area**

Petrographical work on the Monte Rosa nappe was pioneered by Bearth (1939, 1952) and based on his study, numerous work was carried out (e.g. Dal Piaz, 1966; Hunziker, 1969; Hunziker, 1970; Dal Piaz, 1971; Wetzel, 1972; Frey et al., 1976; Chopin and Monié, 1984; Monié, 1985; Dal Piaz and Lombardo, 1986). Nevertheless, the geological history of the Monte Rosa nappe and its tectonic relationship to the adjacent units remains a matter of ongoing research (e.g. Kramer et al., 2000; Le Bayon et al., 2000; Le Bayon et al., 2001; Scherrer, 2001; Froitzheim, 2001).

This large basement nappe consists of a pre-Alpine high-grade gneissic basement that was intruded by a voluminous granite body, and probably remnants of a post-Variscan basement. Therefore, a polyphase evolution history of the Monte Rosa nappe is postulated, including a pre-Alpine high-temperature metamorphism followed by the intrusion of the granite which partially caused contact metamorphism in the gneissic basement and, finally, the deformation and metamorphism due to Alpine orogeny (e.g. Bearth, 1952; Frey et al., 1976; Chopin and Monié, 1984; Monié, 1985; Dal Piaz and Lombardo, 1986; Borghi et al., 1996).

Granitoid rocks are predominant in the Monte Rosa nappe and were investigated in detail by a combined petrological, stable isotope and a Rb-Sr geochronological study by Frey et al. (1976). The Monte Rosa granite displays a magmatic relic assemblage of quartz-K-feldspar-biotite-muscovite with the common accessory phases zircon, monazite, apatite and xenotime. The magmatic plagioclase was replaced by a fine-grained assemblage of clinozoisite, phengite with up to 3.5 Si per formula unit (p.f.u.) in an albite matrix during Alpine high-pressure metamorphism. Notably, no evidence of the high-pressure reaction of the plagioclase to Na-pyroxene has been found, which is a common feature in the Monte Mucrone metagranite of the Sesia-Lanzo Zone and the Brossasco metagranite of the Dora Maira massif (e.g. Oberhänsli et al., 1985; Biino and Compagnoni, 1992). PT-estimates for the high-pressure metamorphic overprint were therefore constrained to be in the range of 440 to 490°C based on oxygen temperatures of quartz-mica pairs from the Monte Rosa granite (Frey et al., 1976) and pressures of 9 to 10 kbar from the Si-content of 3.3 to 3.4 p.f.u. of phengites analyzed by Frey et al. (1976) using the calibration of Massonne and Schreyer (1987). Borghi et al. (1996) reported thermobarometric results from garnet-biotite geothermometry and mineral assemblages of micaschists of 500 to 550°C at 11 to 13 kbar for the Alpine eclogite-facies metamorphism and a similar temperature at a lower pressure of approximately 5 kbar for the Alpine greenschist-facies retrogression. However, those PT-estimates are by far not as high as those reported for the structural similar Dora Maira massif and the overlying ophiolitic Zermatt-Saas Zone. They partially record ultrahigh-pressure metamorphic conditions, e.g. 28 to 35 kbar and 700 to 750°C for the coesite-bearing pyrope-quartzites of the Dora Maira massif, and 27 to 29 kbar and 600 to 630°C for the coesite-eclogites of Lago di Cignana (Chopin, 1984; Chopin et al., 1991; Reinecke, 1998). Dal Piaz and Lombardo (1986) presented 440 to 530°C at a pressure <14 kbar for eclogites in the Monte Rosa nappe. Those eclogites occur as lenses and boudins mostly along the contact of the Monte Rosa to the Zermatt-Saas Zone. Their tectonic position is somewhat unclear. They could represent tectonic

slivers of the ophiolitic unit rather than *in-situ* eclogitic bodies of the Monte Rosa nappe. Another evidence for an Alpine high-pressure overprint of the continental basement rocks is given by the so-called „silvery micaschists“ or „whiteschists“, which occur in the Monte Rosa nappe, as well as in the structural equivalent Gran Paradiso and Dora Maira massifs (Fig. 2.3; Bearth, 1952; Dal Piaz, 1971; Compagnoni and Lombardo, 1974; Chopin, 1981; Chopin and Monié, 1984; Dal Piaz and Lombardo, 1986; Chopin et al., 1991). The characteristic assemblage of those peculiar rocks is kyanite-chloritoid-talc-phengite. In the Monte Rosa nappe, they occur along shear zones within the granite. Their geochemical characteristics and a model for their evolution is presented in chapter 5. Recent petrological investigations on whiteschists from a shear zone in the Monte Rosa nappe yielded up to 25 kbar at 580°C for the Alpine high-pressure metamorphism (Le Bayon et al., 2000; Le Bayon et al., 2001). Since these PT-conditions are similar to those of the Zermatt-Saas Zone, it seems evident that strain localization within those shear zones led to the formation of high-pressure mineral assemblages whereas the otherwise „dry“ Monte Rosa granite lacks any high-pressure indicators. The PT-estimations of Le Bayon et al. (2000) were based on an assumed water activity of 0.6 for a whiteschist assemblage from the upper Val d' Ayas. In contrast, Chopin and Monié (1984) reported 500°C and 16 kbar at a similar water activity for the same whiteschist assemblage collected from the upper Val d' Ayas leading to a great discrepancy between those two PT-estimations from the same mineral assemblage.

The pre-Alpine high-grade metapelitic basement complex records the typical relic assemblage of biotite-sillimanite-garnet-quartz-K-feldspar-plagioclase and garnet-biotite-muscovite-sillimanite-plagioclase (Bearth, 1952; Dal Piaz, 1971; Dal Piaz and Lombardo, 1986). Petrological investigations by Scherrer (2001) on the gneissic basement in the central and southeastern part of the nappe were recently carried out. The metapelites revealed a polyphase metamorphic evolution characterized by the above mentioned pre-Alpine high-temperature event at sillimanite-K-feldspar grade (approximately 700°C/3-6 kbar) and an Alpine eclogite-facies overprint (approximately 550-600°C/9-10 kbar) which is partially obliterated by a meso-Alpine lower-pressure overprint in the western portion of the nappe. The well-defined albite-oligoclase isograd (Bearth, 1958) shows the same pattern as the regional isotherm in the adjacent units of the Central Alps (Todd and Engi, 1997). Therefore, the last, mostly temperature-dominated overprint in the Monte Rosa nappe is similar to that in adjacent units (Lepontine metamorphism of the Central Alps). The obtained PT-conditions for the eclogite-facies overprint are seemingly not representing the peak conditions, but rather a stage along the decompression path,

since the whiteschists apparently record much higher PT-conditions (Le Bayon et al., 2000). However, it seems a common feature of the different lithologies of the Monte Rosa nappe, that the high-pressure reequilibration was not homogenous but rather localized along high-strain areas (i.e. shear zones), whereas other parts are seemingly unaffected by any high-pressure metamorphic overprint.

The cover series of the Monte Rosa nappe includes a sedimentary-volcanic sequence, the Gornergrat Zone. It mainly occurs at the northern border of the Monte Rosa nappe. Bearth (1964) as well as Bearth and Schwander (1981) assumed a Permo-Triassic age for the albite-muscovite gneisses with partially intercalated rhyolites. Those Permo-Triassic sedimentary-volcanic rocks are covered by Triassic limestones, dolomites, and sedimentary breccias that contain components of Triassic carbonates and of dark limestones. On the basis of the described sedimentary characteristics, Bearth and Schwander (1981) suggested that this sequence represents the detached post-Variscan cover of the Monte Rosa basement.

The so-called „Furgg-Zone“ is a complex zone of strongly deformed gneisses and quartzites with minor marbles and incorporated metabasite boudins (Bearth, 1952; Wetzel, 1972; Dal Piaz, 2001). It separates the Monte Rosa nappe from surrounding units and was formerly interpreted as part of the sedimentary cover of the Monte Rosa nappe, e.g. by Jaboyedoff et al. (1996). Its age was either assumed as Late Carboniferous-Permian to Middle Jurassic (Jaboyedoff et al., 1996) or Cretaceous (Steck et al., 1999). However, during recent structural studies it was suggested that the Furgg Zone is more likely a thick *mélange* zone, formed during subduction of the Monte Rosa nappe, which marks the tectonic contact to the adjacent units (Milnes et al., 1981; Kramer et al., 2000, Froitzheim, 2001).

Reliable age constraints are necessary for a detailed reconstruction of the polyphase evolution of the Monte Rosa nappe. Previous investigations on its temporal evolution revealed Variscan to post-Variscan and „Alpine“ ages (e.g. Bearth, 1952; Hunziker, 1970; Wetzel, 1972; Hunziker, 1974; Frey et al., 1976; Köppel and Grünenfelder, 1975; Chopin and Monié, 1984; Monié, 1985; Paquette et al., 1989; Hunziker et al., 1989; Hunziker et al., 1992, Rubatto and Gebauer, 1999; Scherrer, 2001). Some discrepancies exist, however, whether the Monte Rosa granite intruded during several pulses from Variscan to Late Permian times (Hunziker, 1969; Hunziker, 1970). However, the late- to post-Variscan magmatic phase in the Alps is commonly attributed to continental thinning and rifting accompanied by high heat flow and hydrothermal activity (Hunziker et al., 1992). Still more controversial are interpretations of geochronological data for the Alpine high-pressure event. Based on Ar-Ar dating, a Cretaceous age for the high-pressure metamorphism has been

proposed (Hunziker, 1970; Chopin and Monié, 1984; Monié, 1985), whereas Rubatto and Gebauer (1999) presented an Eo/Oligocene age for the Alpine subduction obtained by SHRIMP on the outermost rims of zircons recovered from a phengite-rich metaquartzite of the Gornergrat Zone. Those young ages for the Alpine metamorphism coincide with geochronological investigations on the Dora Maira massif ( $\approx 32$  to  $35$  Ma, U-Pb SHRIMP on zircons and Lu-Hf on garnet; Duchêne et al., 1997; Gebauer et al., 1997) and on the Zermatt-Saas Zone ( $\approx 40$  to  $44$  Ma, Sm-Nd garnet, U-Pb SHRIMP zircon; e.g. Rubatto et al., 1998; Amato et al., 1999). The previously determined Cretaceous age obtained from  $^{40}\text{Ar}/^{39}\text{Ar}$  dating was therefore interpreted to result from the incorporation of excess argon during the high-pressure stage. Chemical and isotopic age dating on monazites from the metapelitic basement of the internal part of the Monte Rosa nappe resulted in different ages due to the polyphase evolution (Scherrer, 2001). Permian ages are preserved by monazites included in garnets or in the matrix of samples that are devoid of reequilibration during Alpine metamorphism. Sometimes, the Permian monazites are surrounded by an Alpine rim, and ages in the range of  $140$  Ma are clearly attributable to mixing of those age zones (Scherrer, 2001). Monazite ages in the range of  $35$  to  $40$  Ma are interpreted as the age of the Alpine high-pressure metamorphism, which is remarkably similar to the ages of the adjacent tectonic units (i.e. Dora Maira massif and Zermatt-Saas Zone; Gebauer et al., 1997; Amato et al., 1999; Scherrer, 2001). On the other hand, Rb-Sr ages of  $38 \pm 2$  Ma obtained from phengites of the Monte Rosa granite were formerly interpreted as cooling below  $500^\circ\text{C}$  and to represent the late Alpine greenschist-facies under lower pressure conditions rather than the eclogite-facies metamorphism (Hunziker, 1970; Frey et al., 1976; Borghi et al., 1996). In the light of the Rb-Sr data representing a temporal constraint on the greenschist-facies metamorphism, the dated metaquartzite from the Gornergrat Zone yielding an Eo/Oligocene age may date the post-eclogitic rather than the peak eclogitic evolution because the sample is characterized by a typical greenschist-facies mineral assemblage of phengite (3.25 Si p.f.u.), albite, epidote and titanite (Rubatto and Gebauer, 1999).

Since in the Monte Rosa area rocks recording large differences in metamorphic grade are juxtaposed, questions on the tectonic evolution arise. A recent geochronological-structural study on the timing of orogenic extension in the Western Alps reports  $36$  to  $45$  Ma for a major extensional event along the greenschist-facies „Gressoney Shear Zone“ which represents the tectonic contact of the Zermatt-Saas Zone with the structurally higher Combin Zone (Reddy et al., 1999). Thus, it was concluded that the mafic eclogites of the Zermatt-Saas Zone were



emplaced on top of the Monte Rosa continental rocks during a dominated top-SE movement along the Gressoney Shear Zone ( $T \approx 400^{\circ}\text{C}$ ;  $P \approx 9$  kbar) due to crustal extension immediately after the eclogite-facies metamorphism. Those kind of large-scale shear zones seem a major component of eclogite exhumation. However, some discrepancies still remain for the reconstruction of the subduction, nappe emplacement and exhumation history. Evidences for the cooling history of the Monte Rosa nappe and the Gran Paradiso massif are given by fission track dating of zircon and apatite. Those data indicate a cooling to  $200\text{-}250^{\circ}\text{C}$  by 33-34 Ma and to  $100^{\circ}\text{C}$  by 9-14 Ma, respectively (Hurford et al., 1989; Hurford et al., 1991; this study, chapter 6). This implies a fast exhumation of the Monte Rosa nappe from considerable depth to nearly surface conditions.

### **2.3 Aims and problems**

Despite the wealth of data available for the Monte Rosa nappe and the Western Alps as a whole, a clear structural, petrological, geochemical and geochronological reconstruction of the mechanisms of subduction and exhumation of the continental Monte Rosa nappe and the emplacement of the ophiolitic Zermatt-Saas Zone on top of the Monte Rosa nappe remains elusive. Since the whiteschists in the Monte Rosa nappe seem to be reliable indicators for an Alpine high-pressure event, their geochemical and geochronological evolution has to be constrained. They may help to answer the critical questions of the PT-conditions during Alpine high-pressure metamorphism, the tectonic mechanism of nappe emplacement and the timing of this event in the Monte Rosa nappe. On the other hand, the occurrence of the whiteschists along shear zones within the Monte Rosa granite gives the unique possibility to directly observe the geochemical changes responsible for the formation of whiteschists from a granitic protolith. Furthermore, the influence of deformation and fluids on the behavior of different isotopic systems can be studied within this shear zone. Those investigations improve the understanding of the closure behavior of different minerals, which are routinely applied to geochronological questions. The application of high-resolution, *in-situ* analyses techniques (e.g. UV-laser ablation Ar-dating of micas, SHRIMP analyses of zircons and monazites, and U-Pb isotope dilution analyses of zircons) improves the interpretation of obtained geochronological data due to correlation with microstructural information obtained from thin sections.

**2.4 Figures**

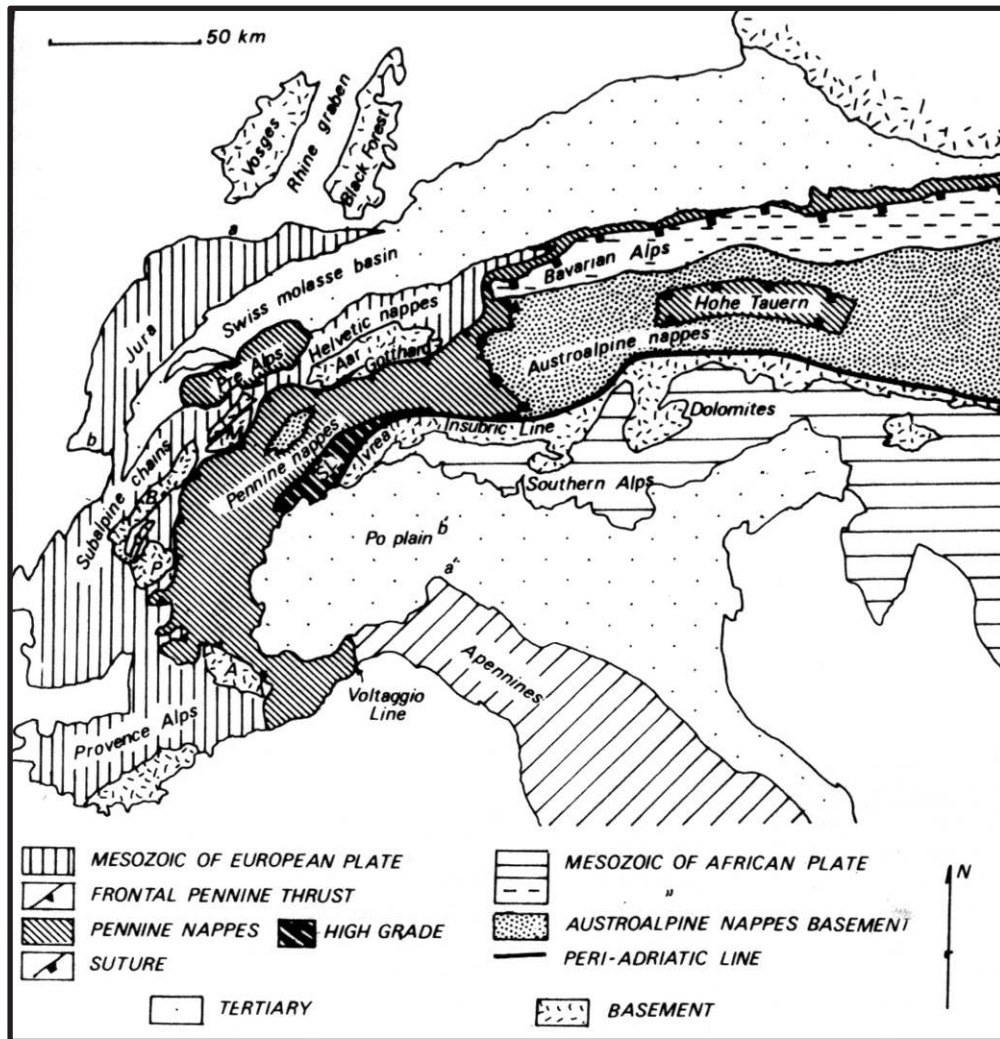


**Fig. 2.1** □ The structural zones of the Alps (from Coward and Dietrich, 1989).  
 □ □ SL = Sesia-Lanzo Zone; M = Mont Blanc massif; B = Belledonne  
 □ □ massif; P = Pelvoux massif; A = Argentera massif.

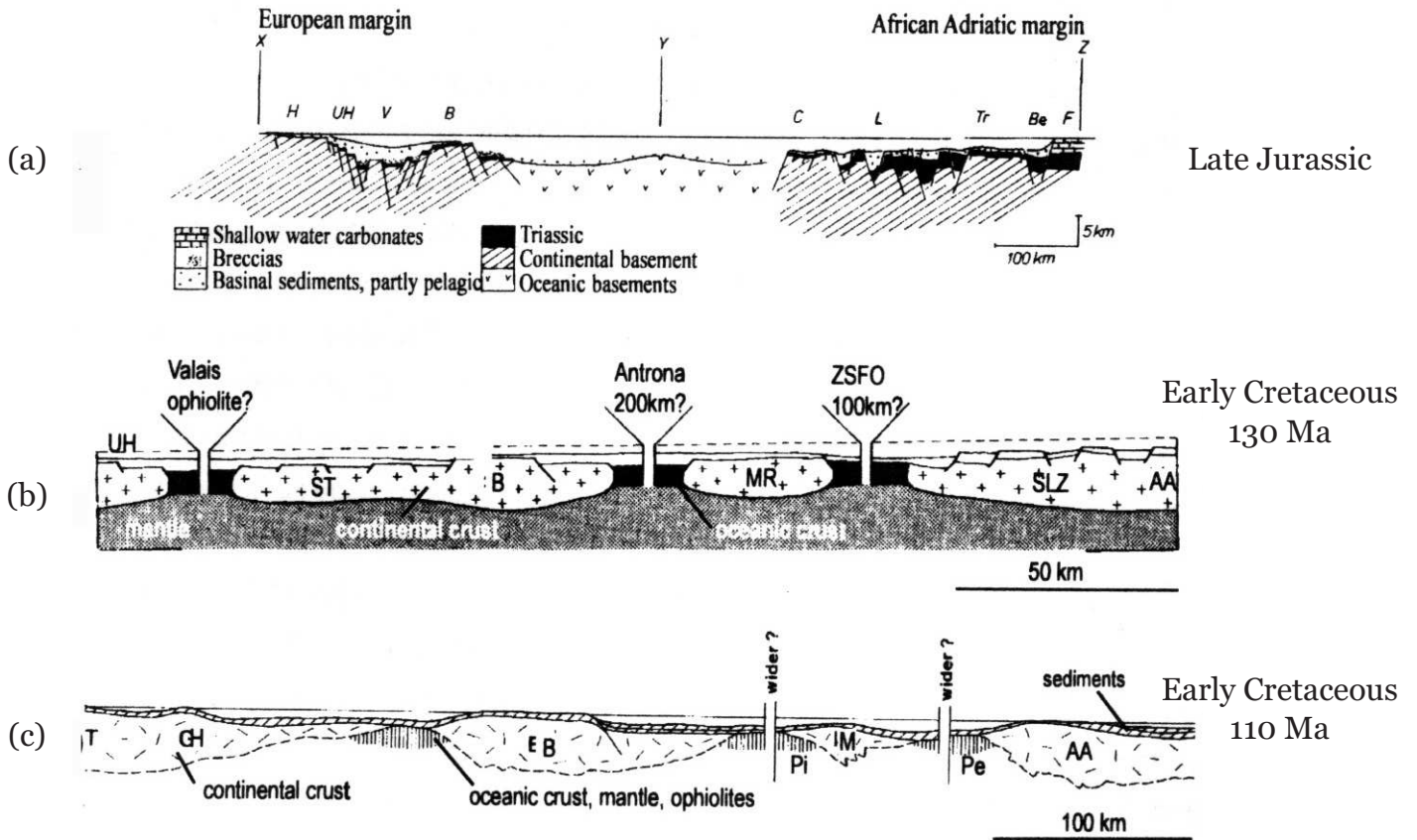


**Figure 2.2** □ Schematic paleogeographic reconstructions of the Alpine Tethys after (a) Laubscher and Bernoulli (1977); (b) Platt (1986); and (c) Trümpy, (1980).  
 □ □ □ AA: Austroalpine; B: Briançonnais; Be: Belluno Zone; C: Canavese; F: Friuli  
 □ □ □ Zone; H: Helvetic; L: Lombardia Zone; M: Margna; MR: Monte Rosa; Pi/Pe:  
 □ □ □ internal and external Piemontese; SLZ: Sesia-Lanzo Zone; ST: Simplon-  
 □ □ □ Tessin gneiss complex; Tr: Trento Zone; UH: Ultrahelvetic; V: Valais; ZSFO:  
 □ □ □ Zermatt-Saas Fee ophiolites.

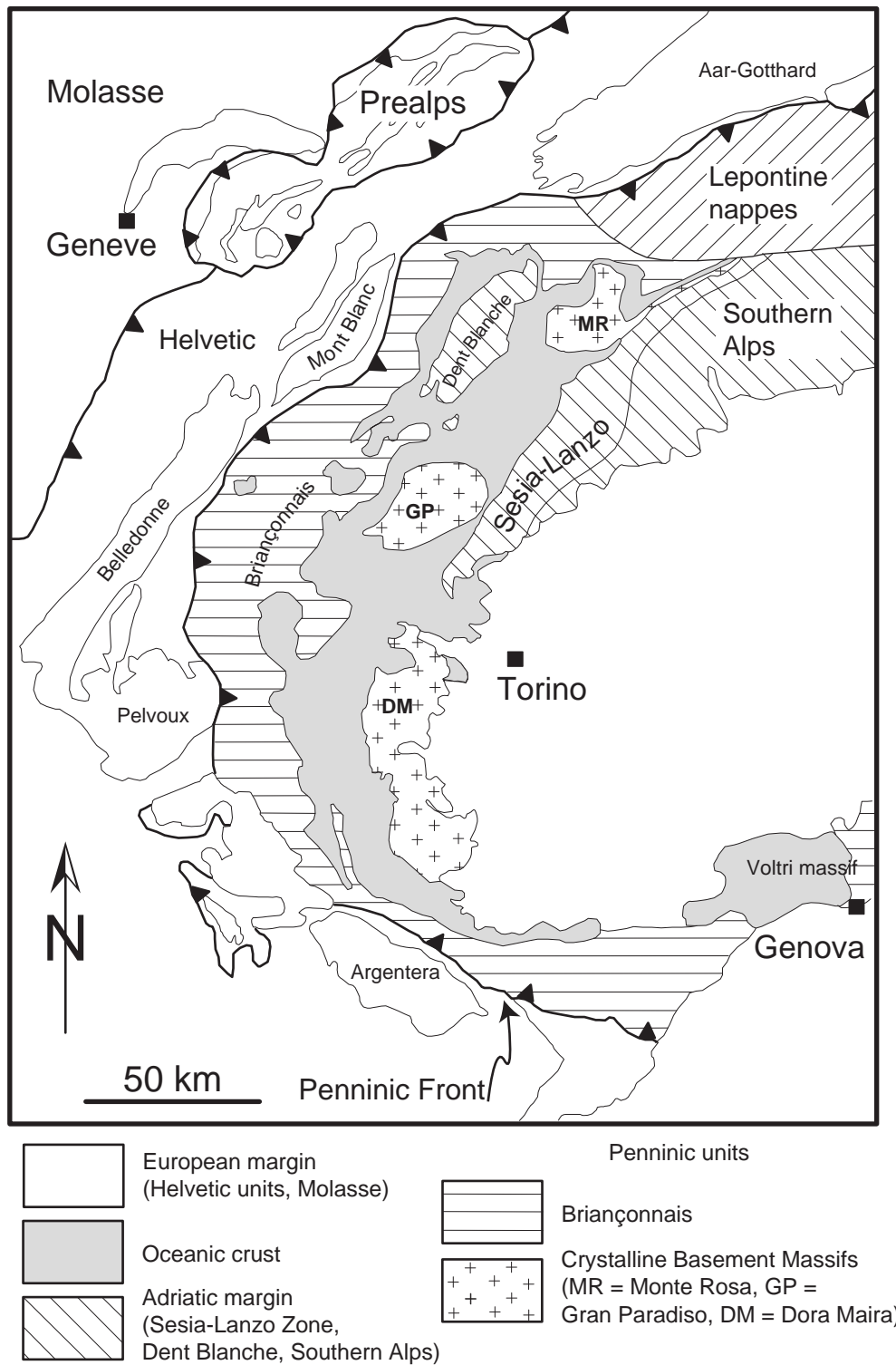


**Fig. 2.3** Major tectonic units of the Western Alps (redrawn after Rubatto, 1998).

## Chapter 3

### New U-Pb data on the crystallization age of the Monte Rosa granite, Western Alps – a combined SHRIMP, TIMS and cathodoluminescence study –

#### **3.1 Abstract**

Zircons and monazites from five Monte Rosa granite samples (Western Alps, upper Val d' Ayas, Italy) have been dated by SHRIMP and conventional thermal ionization mass spectrometry (TIMS) techniques. Interpretation of the ages is aided by cathodoluminescence investigations. A Late Permian intrusion age of  $270 \pm 4$  Ma was obtained for the Monte Rosa granite. It belongs to the post-Variscan magmatic assemblage mainly present in the internal parts of the Alpine basement units. This magmatic activity demonstrates the instability of the continental crust leading to the breakup of the Pangea super-continent during Mesozoic times, and in turns, the opening of the Neo-Tethys. Furthermore, constraints can be placed on the paleogeographic origin of the Monte Rosa nappe either as southern part of the so-called "Briançonnais domain" located south of the European continental margin or even as small continental fragment south of the Briançonnais. Disturbance of the U-Pb isotopic system of uranium-rich zircons indicates re-opening during the subsequent geological evolution of the Monte Rosa nappe.

*Keywords: Monte Rosa, Western Alps, granite, U-Pb geochronology, zircon*

### 3.2 Introduction

The paleogeography of the pre-Alpine basement units is still a matter of debate. A unique reconstruction is mainly hindered by the lack of abundant protolith dating and geochemistry. A tentative reconstruction of these basement areas places them at the northern margin of Gondwana during Late Precambrian to Ordovician times, perhaps partially as independent Gondwana-derived blocks (von Raumer, 1998). The Variscan collision of Gondwana and Laurasia was followed by widespread magmatic activity with intrusive and volcanic rocks. Signs of this magmatic activity are found in all basement units of the Alpine realm, including the External basement units, the Internal Penninic basement units of the Western and Central Alps, the Sesia Lanzo-Zone, the Ivrea Zone, the Southern Alps as well as different units of the Eastern Alps (e.g. Hunziker and Zingg, 1980; Oberhänsli et al., 1985; Bussy and Cadoppi, 1996; Bussy et al., 1996; Bussy et al., 1998; Cortesogno et al., 1998; Thöni, 1999 and references therein; Mayer et al., 2000). Magmatic activity is attributed to post-orogenic instability of the Variscan continental crust. It was followed by post-Variscan orogenic collapse which finally led to the opening of the Neo-Tethys. Differences in geochemical signatures and age relationships of the magmatic rock suites occurring in all units of the Alpine realm suggest variation in geodynamic environment during magma emplacement from a clearly collision to a post-collisional environment (e.g. Finger et al., 1997).

U-Pb dating of zircon can provide reliable magmatic crystallization ages (Bussy et al., 1996). Conventional multigrain or even single-grain zircon dating are known to give geologically meaningless ages for multistage grown zircon populations or zircon domains. Dating of small zones of individual grains with the SHRIMP – in combination with cathodoluminescence (CL) investigations of zonation patterns – is one of the most powerful tools to unravel a complex geologic history recorded in individual zircon grains. It is possible to obtain geological relevant ages with conventional isotope dilution U-Pb single zircon thermal ionization mass spectrometry (TIMS) dating by careful selection of individual grains based on CL investigations (e.g. Poller et al., 1997; Olsen et al., 2000).

This paper reports the first U-Pb SHRIMP and U-Pb TIMS ages of zircons from five samples of the Monte Rosa granite. In addition, monazites from one granite sample were dated by SHRIMP in a preliminary study. The new ages contribute to the reconstruction of the pre-Alpine history of the Monte Rosa nappe. Moreover, disturbance of the U-Pb isotopic system in uranium-rich zircons probably due to re-

opening of the U-Pb isotopic system during the subsequent geological evolution is deduced from SHRIMP measurements.

### **3.3 Geology and sample selection**

The Monte Rosa nappe is located in the Internal Penninic domain of the Western Alps (Fig. 3.1). The paleogeographic position of the Monte Rosa basement area has been assumed to be a) part of the European continental margin (Froitzheim, 2001), b) the southernmost part of the Briançonnais microcontinent (Escher and Beaumont, 1997), c) an isolated continental fragment south of the Briançonnais (Platt, 1986), and d) part of the African continental margin (Stampfli et al., 1998). However, most reconstructions assume a more internal position of the Monte Rosa nappe with respect to the Bernhard nappe. The latter represents the basement of the Briançonnais *sensu stricto* (Platt, 1986; Escher and Beaumont, 1997; Stampfli et al., 1998).

The Monte Rosa nappe is a tectonic window within the overlying eclogite-bearing Mesozoic Piemonte ophiolite nappe, which is part of the former Tethyan oceanic crust and tectonically separates the Monte Rosa nappe from the overlying Sesia-Lanzo Zone, Dent Blanche nappe and the Austroalpine domain (Bearth, 1952; Dal Piaz and Lombardo, 1986; Fig. 3.1).

The Monte Rosa nappe consists of a basement complex with a few intercalated metabasites. The complex was intruded by the Monte Rosa granite (Bearth, 1952; Dal Piaz and Lombardo, 1986). The Monte Rosa basement complex mainly consists of metapelites with relic assemblages of biotite-sillimanite-garnet-quartz-K-feldspar-plagioclase and garnet-biotite-muscovite-sillimanite-plagioclase (Dal Piaz and Lombardo, 1986). These assemblages are interpreted to represent a high-grade metamorphic overprint of the basement complex prior to the intrusion of the Monte Rosa granite (Bearth, 1964; Dal Piaz, 1971; Dal Piaz and Lombardo, 1986). The age of the last isotopic homogenization of the lead isotopic system of the metamorphic basement complex was constrained to be  $415 \pm 10$  Ma from a Pb-Pb feldspar isochron (Curti, 1987). It was interpreted as the age of the high-grade metamorphic overprint of the pre-Alpine basement of the Monte Rosa nappe. The cover series of the Monte Rosa nappe includes sedimentary-volcanic sequences of assumed Permo-Triassic age, the Gornergrat Zone and the Furgg-Zone (Fig. 3.1b). The Gornergrat Zone is characterized by albite-muscovite gneisses with some rhyolitic intercalations (Bearth, 1964). Its age was assumed to be Permo-Triassic



(Bearth, 1964, Bearth and Schwander, 1981). The Furgg-Zone is a complex zone of strongly deformed micaschists, gneisses and quartzites with incorporation of metabasite boudins (Bearth, 1952; Wetzel, 1972). It is a thick *mélange* zone, which was formed during subduction of the Valaisan oceanic basin and separates the Monte Rosa nappe from the adjacent units (Kramer et al., 2000; Froitzheim, 2001). The Monte Rosa nappe was overprinted by Alpine high-pressure metamorphism and a subsequent greenschist-facies retrogression (Bearth, 1964; Frey et al., 1976; Dal Piaz and Lombardo, 1986; Borghi et al., 1996; Frey et al., 1999; Pawlig and Baumgartner, 2000).

A simplified geological map of the upper Val d' Ayas (Italy) as well as the locations of the samples of Monte Rosa granites investigated during this study are given in Figure 3.2. Three samples (98SL133, 99SL125, 99SL159) were collected on the western side of the Verra glacier, east of the Mezzalama refuge (2795 m a.s.l., 625.140/084.130, Swiss Reference Grid) in a relatively undeformed part of the Monte Rosa granite. They show a well preserved granitic texture. The other samples (98SL29, 99SL1A) were taken near the tectonic contact of the Monte Rosa nappe with the overlying Zermatt-Saas ophiolite at the Mezzalama refuge, approximately 3040 m a.s.l. (625.882/084.168, Swiss Reference Grid). All samples contain relics of igneous quartz, K-feldspar, biotite, muscovite as well as the accessories zircon, apatite and xenotime. Magmatic plagioclase was replaced by a fine-grained assemblage of clinozoisite and Si-rich phengite (up to 3.5 Si p.f.u.) and small garnet ( $\text{Alm}_{50}\text{Grs}_{50}$ ) in an albite matrix. A pressure of approximately 13 kbar at 550°C and of approximately 10 kbar at 450°C is obtained from the phengite barometer after Massonne and Schreyer (1987). The K-feldspar is slightly sericitized. The more deformed samples taken from the contact of the Monte Rosa nappe with the overlying Zermatt-Saas ophiolite (98SL29, 99SL1A) are characterized by a well-developed schistosity which is defined by the preferred orientation of the phengites. The samples investigated during this study show no evidence of a high-pressure transformation of the magmatic plagioclase into jadeite+quartz+zoisite as has been described from other high-pressure areas in the Alps (e.g. Paquette et al., 1999; Oberhänsli et al., 1985). Therefore, the high-pressure metamorphic conditions of the Monte Rosa granite were typically constrained to lie below the jadeite stability field suggesting pressures around 10 to 16 kbar at temperatures of 500 to 550°C (Chopin and Monié, 1984; Dal Piaz and Lombardo, 1986; Rubatto and Gebauer, 1999). Recent petrological investigations on chloritoid-talc-kyanite-bearing rocks from discrete shear zones within the Monte Rosa granite indicate a higher pressure for the Alpine metamorphism of up to 25 kbar at a temperature around 580°C (Le Bayon et al.,

2000). These PT-conditions are comparable to that of the Zermatt-Saas ophiolite (Reinecke, 1998). A later, greenschist-facies retrogression is indicated by a temperature of ca. 450°C at a pressure of 6 kbar (Frey et al., 1976; Borghi et al., 1996).

### 3.4 Analytical techniques

Two samples (98SL29, 98SL133) were selected for U-Pb dating of zircons by SHRIMP. Monazites from sample 98SL133 were dated by SHRIMP in a preliminary study. The other samples (99SL1A, 99SL125, 99SL159) were dated by conventional single zircon U-Pb isotope dilution method. Additionally, two multigrain fractions from the samples 99SL1A and 99SL125 were dated by conventional U-Pb isotope dilution method.

The rock samples were crushed, and zircons and monazites were separated according to their magnetic susceptibility and density. Individual grains were finally selected by handpicking under the binocular. The zircon and monazite grains for the analysis with the SHRIMP and single grain dating technique were mounted in epoxy and prepared as 1-inch-diameter mounts with a polished surface. The same mount was used for CL investigation and SHRIMP analyses. The zircons used for U-Pb single grain isotope dilution analysis were prepared in separate mounts and were investigated with CL as well.

The panchromatic CL pictures of all zircon samples were obtained on a Hitachi S450 scanning electron microscope at the Department of Cosmochemistry of the Max-Planck-Institute for Chemistry (Mainz, Germany). U-Th-Pb microanalyses were conducted by means of the SHRIMP II at the Department of Physics, Curtin University of Technology, Perth/Western Australia. The general SHRIMP technique is described in detail elsewhere (Compston et al., 1984; Nelson, 1997). The primary beam of oxygen ions used to sputter the sample surface had a focal diameter of 15 to 20  $\mu\text{m}$ . The Curtin CZ3 standard (Pidgeon et al., 1994) was used for the calibration of the unknown samples. The  $f_{206}$  value, given in table 3.1, represents the ratio of the common  $^{206}\text{Pb}$  over the total  $^{206}\text{Pb}$ , calculated from the  $^{204}\text{Pb}$  count rate. Since the low  $^{204}\text{Pb}$  count rates observed for the unknowns are similar to the low  $^{204}\text{Pb}$  count rates of the standard, a Broken Hill lead composition ( $^{204}\text{Pb}/^{206}\text{Pb} = 0.0625$ ,  $^{207}\text{Pb}/^{206}\text{Pb} = 0.9618$ ,  $^{208}\text{Pb}/^{206}\text{Pb} = 2.2285$ ) was used for the common lead correction. Only two zircons show higher  $f_{206}$  values of 0.038 and 0.068 (Tab. 3.1), respectively, and thus,

were corrected with a lead composition of Cummings and Richards (1975) for 270 Ma ( $^{204}\text{Pb}/^{206}\text{Pb} = 0.0544$ ,  $^{207}\text{Pb}/^{206}\text{Pb} = 0.8519$ ,  $^{208}\text{Pb}/^{206}\text{Pb} = 2.0875$ ).

Eight zircons from a relatively undeformed sample (98SL133) and five zircons from a deformed sample (98SL29) were analyzed with a total of 19 point analyses (Table 3.1). Seven point analyses of two monazites from sample 98SL133 are given (Table 3.2). The monazite data represent preliminary results since the analytical conditions of the SHRIMP were optimized for zircon analysis, not monazite. Errors cited for individual analyses include errors from counting statistics, the common lead correction and the U/Pb calibration based on reproducibility of U/Pb measurements of the standard. All errors given for the isotopic ratios and the single ages obtained from the SHRIMP are quoted at the  $2\sigma$  level (Table 3.1 and 3.2).

Zircons for TIMS analyses were selected based on grain size and CL structures. They were recovered from the SEM mounts for isotope dilution analyses. Two multi-grain fractions containing clear, long-prismatic zircons from the samples 99SL1A and 99SL125 were dated by isotope dilution U-Pb method. They were spiked with a mixed  $^{205}\text{Pb}$ - $^{233}\text{U}$  spike prior to dissolution in teflon bombs. After dissolution, lead and uranium of the single zircons were loaded together on Re-filaments with silica-gel without performing any chemical separation. Lead and uranium were measured from the same filament at temperatures of 1250 and 1350°C, respectively. For the two multigrain fractions, uranium and lead were separated using column chemistry after Krogh (1973) and loaded on separate Re-filaments with silica-gel. The zircon uranium-lead measurements were performed on a Finnigan MAT261 mass spectrometer at the Geochemistry Department at the Max-Planck-Institute for Chemistry (Mainz, Germany) operating in multiplier mode. The total lead blank was about 5 pg. The following ratios were used for blank corrections:  $^{206}\text{Pb}/^{204}\text{Pb} = 17.3355$ ,  $^{207}\text{Pb}/^{204}\text{Pb} = 15.0393$  and  $^{208}\text{Pb}/^{204}\text{Pb} = 36.1760$ . K-feldspars from sample 98SL133 ( $^{206}\text{Pb}/^{204}\text{Pb} = 18.4779$ ,  $^{207}\text{Pb}/^{204}\text{Pb} = 15.6852$  and  $^{208}\text{Pb}/^{204}\text{Pb} = 38.6924$ ) were used for common lead corrections. All ratios were corrected for fractionation using a NBS 981-Umix standard as reference (Todt et al., 1996). The resulting isotopic ratios and the errors of the TIMS measurements as well as the resulting errors of the ages are quoted at the  $2\sigma$  level in table 3.3.

### **3.5 Morphology and CL-investigations**

The zircons recovered from all samples are clear, colorless to slightly colored, and have varying morphologies ranging from acicular, slender and euhedral to short

prismatic. All zircons appeared to be unzoned and did not show noticeable features of internal structures under the binocular. CL images, however, revealed heterogeneities on the micron-scale. The zircons from the relatively undeformed rock samples (98SL133, 99SL125 and 99SL159) are characterized by distinct oscillatory zoning (Fig. 3.3, 3.5, 3.6), typical for primary magmatic zircons (Hanchar and Miller, 1993). The most common morphology of zircons in those samples are needle-shaped grains, around 250  $\mu\text{m}$  long, slightly colored, and characterized by homogenous oscillatory zoning (Fig. 3.3a, 3.5c, 3.6a, 3.6d). Some contain inclusions of apatite (Fig. 3.3a, 3.5b, 3.5c). Other zircons are larger and short prismatic (Fig. 3.3b and c), but they also show oscillatory zoning. Some short prismatic zircons are characterized by a core which is overgrown by an oscillatory zoned rim (Fig. 3.5a).

CL zoning from the stronger deformed rock sample (98SL29) is rather diffuse. Figure 3.4 shows typical zircons from the deformed Monte Rosa granite, which are prismatic to rounded, and partially asymmetric. The internal structures of these zircons vary from diffuse, oscillatory zoned (Fig. 3.4b and c) to cloudy and unzoned (Fig. 3.4a).

### **3.6 Geochronological results**

#### **3.6.1 SHRIMP ion probe measurements**

Results of SHRIMP ion probe measurements of zircons and monazites are presented with  $2\sigma$  errors in table 3.1 and 3.2. The concordia diagrams are given in figure 3.7a to c.

The zircons from the weakly deformed sample (98SL133) yielded concordant ages. A weighted mean  $^{206}\text{Pb}/^{238}\text{U}$  age of  $270 \pm 4$  Ma was calculated from nine measurements (Fig. 3.7a, Tab. 3.1). The zircons from the deformed Monte Rosa granite (98SL29) yielded a weighted mean  $^{206}\text{Pb}/^{238}\text{U}$  age of  $268 \pm 4$  Ma calculated from eight measurements (Fig. 3.7b, Tab. 3.1).

Two zircons with very low luminescent zones have been found in sample 98SL133. Figure 3.3b shows one of those zircons, characterized by oscillatory zoning in the core. A diffuse zone with very low luminescence is found towards the rim. Inclusions, which are too small to be identified with the electron microprobe, can be observed in the secondary electron (SE) image. The orientation of these inclusions follows the growth zoning visible in CL (Fig. 3.3b, right). This grain yields a

$^{206}\text{Pb}/^{238}\text{U}$  core age of  $277 \pm 3$  Ma. In contrast, the apparent  $^{206}\text{Pb}/^{238}\text{U}$  rim age of  $185 \pm 2$  Ma is significantly younger. The analysis point was placed on both, the low luminescent zone as well as the regular zoned rim of the zircon, and therefore, the resulting age of  $185 \pm 2$  Ma is interpreted to represent a mixing age of both zones. Another short prismatic zircon grain with comparable features is shown in Figure 3.3c. It is characterized by a big, unzoned core with low cathodoluminescence intensity. A small rim with an oscillatory zoning pattern surrounds the core. One SHRIMP analysis covering the transitional area of core and rim yields an apparent  $^{206}\text{Pb}/^{238}\text{U}$  age of  $143 \pm 2$  Ma. This analysis also represents a mixture of core and rim component. These younger ages correlate with the highest uranium contents of 4121 ppm and 4939 ppm as well as with very low Th/U ratios of 0.11 and 0.01, respectively. The observations made in CL together with the porous surface due to very small inclusions in these zircons and the high uranium contents suggest that the low luminescent zones may represent metamict areas in these zircon grains.

The preliminary results of seven SHRIMP analysis on monazites from sample 98SL133 are compatible with the zircon data. A weighted mean  $^{206}\text{Pb}/^{238}\text{U}$  age of  $263 \pm 2$  Ma was obtained from five measurements (Fig. 3.7c, Tab. 3.2). Two analyses points of the monazites are characterized by higher apparent ages of  $287 \pm 2$  and  $276 \pm 2$  Ma, respectively. They either represent inherited components or analytical artefacts.

### *3.6.2 TIMS multigrain and single zircon dating*

Results of the two multigrain fractions as well as the single zircons dated by the conventional U-Pb isotope dilution method with  $2\sigma$  errors are given in table 3.3 and in the concordia diagram in figure 3.7d. The corresponding CL pictures for the single zircons are shown in figures 3.5 and 3.6. Two zircons out of eight single zircons are reverse discordant, which is interpreted to result from incomplete dissolution of the zircons or, alternatively, incomplete homogenization of the spike.

The analyzed multigrain fractions, each containing thirty long-prismatic, slightly colored zircons from the samples 99SL1A (0.061 mg) and 99SL125 (0.087 mg) yielded  $^{206}\text{Pb}/^{238}\text{U}$  ages of  $199.9 \pm 1.5$  Ma and  $202.8 \pm 0.7$  Ma, respectively. The zircon 98SL133-87 (Fig. 3.5a), a fragment of a short-prismatic zircon, is characterized by a core, which does not display a distinct zonation pattern, and an oscillatory zoned rim. This grain yields a discordant  $^{206}\text{Pb}/^{238}\text{U}$  age of  $360.1 \pm 3.3$  Ma. Zircon 99SL125-10 (Fig. 3.5b) is a short prismatic zircon with dominant prisms. It shows distinct

oscillatory zoning with a low luminescent middle zone. In the SE image (Fig. 3.5b, right), small inclusions can be observed in this zone. This grain yields a concordant  $^{206}\text{Pb}/^{238}\text{U}$  age of  $197.9 \pm 1.0$  Ma. A concordant  $^{206}\text{Pb}/^{238}\text{U}$  age of  $235.2 \pm 1.5$  Ma is obtained from the oscillatory zoned, long-prismatic zircon 99SL125-17 (Fig. 3.5c). The fragment of a long-prismatic, oscillatory zoned zircon 99SL159-1 (Fig. 3.6a) gives a discordant  $^{206}\text{Pb}/^{238}\text{U}$  age of  $224.3 \pm 1.4$  Ma. A concordant  $^{206}\text{Pb}/^{238}\text{U}$  age of  $278.8 \pm 2.7$  Ma is obtained from the short prismatic zircon 99SL159-16 (Fig. 3.6b) with single phase oscillatory zoning. A slight discordant  $^{206}\text{Pb}/^{238}\text{U}$  age of  $283.7 \pm 1.8$  Ma is given by zircon 99SL125-22 (Fig. 3.6c).

### 3.7 Discussion

The concordant  $^{206}\text{Pb}/^{238}\text{U}$  ages of  $270 \pm 4$  Ma and  $268 \pm 4$  Ma of the zircons from the samples dated by SHRIMP are interpreted to represent the intrusion age of the Monte Rosa granite. The weighted mean  $^{206}\text{Pb}/^{238}\text{U}$  age of  $263 \pm 2$  Ma obtained from the monazite analyses and the concordant age values obtained by the single grain isotope dilution analyses (99SL159-22:  $283.7 \pm 1.8$  Ma, 99SL159-16:  $278.8 \pm 2.7$  Ma, Fig. 3.7d) are compatible with the zircon data.

Köppel and Grünenfelder (1975) presented concordant U-Pb ages of monazites of  $260 \pm 5$  Ma from the Monte Rosa nappe as well as Rb-Sr mineral ages of muscovite of  $248 \pm 10$  and  $255 \pm 22$  Ma. U-Pb SHRIMP data of zircon cores from a metaquartzite of the sedimentary cover in the Gornergrat Zone of the Monte Rosa nappe gave Early Permian ages ( $263 \pm 5$  Ma and  $268 \pm 4$  Ma,  $1\sigma$ ), which are indicative for the maximum depositional age of the sedimentary cover of the Monte Rosa nappe (Rubatto and Gebauer, 1999).

Previous geochronological studies indicated a Late Hercynian ( $310 \pm 50$  Ma) age for the crystallization of the Monte Rosa granite, based on a Rb-Sr whole-rock isochron obtained by Hunziker (1970). Another whole-rock isochron age of  $260 \pm 10$  Ma in gneissic parts of the granite was interpreted to represent a „Permian phase of the Hercynian metamorphism in this area“ (Hunziker, 1970). By the same technique, an age of  $125 \pm 20$  Ma obtained from a strongly deformed gneiss was assumed to date early Alpine tectonic movements (Hunziker, 1970). In the light of the new zircon data obtained during this study, it is more likely that the scattering of the previous Rb-Sr whole rock data reflects partial disequilibrium of the Rb-Sr isotopic system during intrusion.

The discordant zircon yielding  $360.1 \pm 3.3$  Ma (98SL133-87) contains a large inherited component. It provides valuable information on the protolith of the Monte Rosa granite in combination with the SHRIMP analyses of the same sample. The discordia line has an upper intercept of  $2000 \pm 160$  Ma. This age is commonly obtained for inherited components in zircons from the Alps (Schaltegger and Gebauer, 1999). The younger but concordant age of the zircon 99SL125-17 ( $235.2 \pm 1.5$  Ma) may be due to a disturbance of the U-Pb isotopic system. The concordant ages around 200 Ma of the multigrain fractions and the zircon 99SL125-10 can be compared with the uranium-rich parts of the two zircons from sample 98SL133, which gave ages of  $143 \pm 2$  and  $185 \pm 2$  Ma, respectively (Fig. 3.3b, 3.3c). All zircons, which yielded ages of 200 Ma and younger, show similar CL features: low luminescent zones with numerous small inclusions (Figs. 3.3b, 3.3c, 3.5b). The SHRIMP analyses on those low luminescent zones revealed high uranium contents of 4121 ppm and 4939 ppm, respectively (Tab. 3.1). Generally, high-uranium zircon domains become metamict as a result of uranium-decay producing  $\alpha$ -particles and fission products. It has been shown by several authors that the susceptibility of zircon for secondary lead-loss is clearly enhanced by a high degree of radiation damage (e.g. Silver and Deutsch, 1963; Mezger and Krogstad, 1997; Nasdala et al., 1998). Thus, the crystal structure in those zones is more disturbed than in low-uranium zircon domains. A similar interpretation is favored for some of the single zircons dated by isotope dilution. These ages may reflect a re-opening of the U-Pb isotopic system during the subsequent metamorphic history of the Monte Rosa nappe.

### **3.8 Geodynamic implications**

During the Late Devonian to the Early Permian convergence and collision of Gondwana and Laurasia led to the consolidation of the Variscan fold belt forming the core of the super-continent Pangea (Ziegler, 1993). Fundamental plate-reorganization in the Variscan fold belt was related to a change in the convergence direction of Gondwana and Laurasia after their amalgamation phase leading to a new tensional regime affecting the super-continent Pangea during Late Permian to Early Mesozoic times (Ziegler, 1993).

Variscan magmatic activity can be observed in several units of the Alpine realm (Fig. 3.8). The External basement units clearly show Variscan magmatic activity (see review of von Raumer et al., 1999). The Internal Penninic basement units as well as parts of the Eastern Alps are characterized by a widespread chemically

bimodal magmatic activity during Permian to Mesozoic times (see reviews by Schaltegger and Gebauer, 1999 and Thöni, 1999).

It is apparent from the distribution of the magmatism over the Alpine geotectonic units and their age (Fig. 3.8), that the activity migrated towards the more internal parts of the Alpine realm, e.g. the Internal Penninic units, the South Alpine units, the Sesia Lanzo-Zone and Ivrea Zone, and the Eastern Alps (Bussy and Cadoppi, 1996; von Raumer, 1998). The ages suggest that the magmatism in the External basement units was related to the Variscan collision of Gondwana and Laurasia. The younger, bimodal magmatism in the more Internal parts can be attributed to post-Variscan processes as a consequence of post-orogenic uplift and extension (Finger et al., 1997).

The Late Permian Monte Rosa granite belongs to the post-Variscan granitoids of the Internal parts of the Alpine realm. The necessary heat input for plutonism in the upper crust can be provided by mantle-derived mafic magmas. Examples for these mantle magmas are present in the Ivrea Zone and the Southern Alpine basement, where a number of gabbro intrusions can be found (Schaltegger and Gebauer, 1999; Mayer et al., 2000).

The Late Permian to Early Mesozoic bimodal magmatism occurs in the Internal parts of the Alpine area and characterizes a transitional time span from a collision dominated geodynamic environment towards continental rifting. Early Jurassic rifting of the Neo-Tethyan ocean is dated in this area by the formation ages of the Mellichen and Allalin metagabbros of  $164 \pm 2.7$  and  $163.5 \pm 1.8$  Ma, respectively (Rubatto et al., 1998). These ages are supported by a maximum deposition age of around  $161 \pm 11$  Ma for Mn-rich sediments that overlie the oceanic crust at Lago di Cignana (Rubatto et al., 1998). The opening of the Tethyan ocean defines the onset of the Alpine event.

Recent reconstruction of the paleotectonic position of the Monte Rosa nappe was mainly based on its present tectonic position in the Alpine nappe stack (e.g. Platt, 1986; Escher and Beaumont, 1997; Froitzheim, 2001 and references therein). The high-pressure metamorphic overprint in the Monte Rosa was suggested to be younger ( $\approx 35$  Ma; Rubatto and Gebauer, 1999) than in the overlying Zermatt-Saas ophiolite (41 to 44 Ma; Rubatto et al., 1998; Amato et al., 1999). Hence, the paleotectonic position of the Monte Rosa nappe with affinity to the European continental margin was suggested, either as part of the continental margin or as part of the Briançonnais domain (Escher and Beaumont, 1997; Rubatto and Gebauer, 1999; Froitzheim, 2001). However, the paleogeographic location of the Monte Rosa nappe on the basis of pre-Alpine geochronological data supports a relationship to the more internal parts of the



Alpine realm. The basement units derived from the paleo-European continental margin only show Variscan ages, whereas Permian to Mesozoic magmatic ages are mainly found in the Internal basement units and in the South Alpine and Austroalpine domains. Therefore, the paleotectonic position of the Monte Rosa nappe either as the southern part of the Briançonnais domain as proposed by Escher and Beaumont (1997), as continental fragment south of the Briançonnais (Platt, 1986), or even at the paleo-African margin is possible (Stampfli et al., 1998; Fig. 3.8), rather than a position at the paleo-European continental margin as recently proposed by Froitzheim (2001).

### **3.9 Acknowledgements**

U-Th-Pb microanalyses were performed by means of the SHRIMP II in Perth (Western Australia), which is operated by a consortium consisting of Curtin University of Technology, the Geological Survey of Western Australia, and the University of Western Australia. We are most grateful to L. Nasdala for performing analyses and data reduction, and to A.K. Kennedy and A.A. Nemchin for experimental help with ion probe analysis. J. Huth (Max-Planck-Institute for Chemistry, Department of Kosmochemistry) is thanked for his help at the SEM. Polished ion-microprobe mounts were produced by D. Dettmar (Bochum). This research was supported by a Ph.D. fellowship to S.P. from the graduate program „Stoffbestand und Entwicklung von Kruste und Mantel“ of the Johannes Gutenberg-University and the Max-Planck-Institute for Chemistry in Mainz provided by the German Science Foundation (DFG Grant 392/1).

## *Chapter 3*

### **3.10 Tables**

**Table 3.1** SHRIMP data (corrected for common Pb) for zircons from the Monte Rosa granites (samples 98SL29 and 98SL133).  $2\sigma$  errors are given.

Zircon	Spot	Th (ppm)	U (ppm)	Th/U	$f^{206}\text{Pb}$	$^{206}\text{Pb}^*/^{238}\text{U}$	Age $^{206}\text{Pb}^*/^{238}\text{U}$	$^{207}\text{Pb}/^{206}\text{Pb}$
98SL133-A	1	392	868	0.45	0.002	$0.0430 \pm 12$	$272 \pm 4$	$0.0522 \pm 24$
	2	398	1048	0.38	0.003	$0.0431 \pm 12$	$272 \pm 4$	$0.0517 \pm 20$
98SL133-B	1	76	558	0.14	0.019	$0.0425 \pm 12$	$269 \pm 4$	$0.0506 \pm 80$
98SL133-C	1	183	948	0.19	0.002	$0.0427 \pm 14$	$270 \pm 4$	$0.0492 \pm 26$
98SL133-D	1	81	874	0.09	0.004	$0.0419 \pm 12$	$264 \pm 4$	$0.0512 \pm 12$
98SL133-E	1	234	1438	0.16	0.038	$0.0439 \pm 10$	$277 \pm 3$	$0.0507 \pm 26$
	2	38	4121	0.01	0.008	$0.0292 \pm 8$	$185 \pm 2$	$0.0497 \pm 18$
98SL133-F	1	59	1991	0.03	0.002	$0.0430 \pm 12$	$271 \pm 4$	$0.0510 \pm 12$
	2	35	1654	0.02	0.003	$0.0432 \pm 12$	$273 \pm 4$	$0.0508 \pm 18$
98SL133-G	1	537	4939	0.11	0.068	$0.0224 \pm 6$	$143 \pm 2$	$0.0486 \pm 48$
98SL133-H	1	881	1273	0.69	0.008	$0.0414 \pm 12$	$262 \pm 4$	$0.0511 \pm 40$
mean $^{206}\text{Pb}^*/^{238}\text{U}$ age (nine measurements*):							$270 \pm 4$	
98SL29-A	1	92	158	0.58	0.016	$0.0420 \pm 14$	$265 \pm 4$	$0.0497 \pm 114$
98SL29-B	1	96	329	0.29	0.018	$0.0426 \pm 12$	$269 \pm 4$	$0.0506 \pm 82$
98SL29-C	1	70	233	0.3	0.008	$0.0420 \pm 14$	$265 \pm 4$	$0.0507 \pm 62$
	2	66	240	0.28	0.013	$0.0422 \pm 14$	$266 \pm 5$	$0.0512 \pm 88$
98SL29-D	1	95	1145	0.08	0.002	$0.0432 \pm 12$	$272 \pm 4$	$0.0515 \pm 22$
	2	103	489	0.21	0.005	$0.0423 \pm 12$	$267 \pm 4$	$0.0520 \pm 40$
98SL29-E	1	167	460	0.36	0.009	$0.0431 \pm 12$	$272 \pm 4$	$0.0510 \pm 50$
	2	140	395	0.35	0.008	$0.0430 \pm 12$	$271 \pm 4$	$0.0514 \pm 66$
mean $^{206}\text{Pb}^*/^{238}\text{U}$ age (eight measurements):							$268 \pm 4$	

\* = except 98SL133-E spot 2 and 98SL133-G spot 1 (see text for discussion)

**Table 3.2** SHRIMP data (corrected for common Pb) for monazites from the Monte Rosa granite (sample 98SL133).  $2\sigma$  errors are given.

<b>Monazite</b>	<b>Spot</b>	<b>f<sup>206Pb</sup></b>	<b><sup>206Pb</sup>*/<sup>238U</sup></b>	<b>Age</b> <b><sup>206Pb</sup>*/<sup>238U</sup></b>	<b><sup>207Pb</sup>/<sup>206Pb</sup></b>
98SL133-A	1	0.009	0.0437 ± 8	276 ± 2	0.0520 ± 24
	2	0.040	0.0418 ± 8	264 ± 2	0.0514 ± 76
	3	0.003	0.0455 ± 8	287 ± 2	0.0520 ± 10
	4	0.011	0.0421 ± 8	266 ± 2	0.0519 ± 22
	5	0.005	0.0415 ± 6	262 ± 2	0.0519 ± 12
98SL133-B	1	0.003	0.0412 ± 6	260 ± 2	0.0523 ± 10
	2	0.002	0.0415 ± 6	262 ± 2	0.0520 ± 6
mean <sup>206Pb</sup> */ <sup>238U</sup> age (five measurements*):					263 ± 2

\* = except 98SL133-A spot 1 and spot 3 (see text for discussion)

**Table 3.3** TIMS data of the Monte Rosa granite (samples 98SL29, 98SL133, 99SL1A, 99SL125 and 99SL159). 2 $\sigma$  errors are given.

Sample	Zircon #	sample weight mg	U <sub>tot</sub> /Pb*	Measured isotopic composition <sup>a</sup>				Isotopic ratios <sup>b</sup>				
				<sup>206</sup> Pb/ <sup>204</sup> Pb	<sup>207</sup> Pb/ <sup>206</sup> Pb	<sup>208</sup> Pb/ <sup>206</sup> Pb	<sup>206</sup> Pb*/ <sup>238</sup> U	<sup>207</sup> Pb*/ <sup>235</sup> U	<sup>207</sup> Pb/ <sup>206</sup> Pb			
98SL133 (undeformed granite)												
133-87	nd		15.27	690.6 ± 17.7	0.0918 ± 5	0.1261 ± 6	0.0575 ± 6	0.5712 ± 144		0.0721 ± 11		
99SL1A (deformed granite, m = multigrain fraction)												
1A-m	0.0606		28.90	142.1 ± 0.3	0.1539 ± 10	0.3213 ± 2	0.0315 ± 2	0.2180 ± 31		0.0502 ± 7		
99SL125 (undeformed granite, m = multigrain fraction)												
125-10	nd		28.71	390.0 ± 2.6	0.0878 ± 2	0.1697 ± 5	0.0312 ± 2	0.2165 ± 32		0.0504 ± 6		
125-17	nd		24.72	536.1 ± 3.6	0.0781 ± 2	0.1153 ± 6	0.0372 ± 2	0.2605 ± 37		0.0509 ± 5		
125-30	nd		28.70	454.0 ± 17.5	0.0799 ± 2	0.1492 ± 10	0.0315 ± 4	0.2066 ± 92		0.0476 ± 17		
125-m	0.0869		28.69	261.6 ± 0.2	0.10701 ± 3	0.19239 ± 7	0.0320 ± 1	0.2236 ± 12		0.0508 ± 2		
99SL159 (undeformed granite)												
159-1	nd		26.26	873.8 ± 17.3	0.0707 ± 2	0.0677 ± 3	0.0354 ± 2	0.2691 ± 47		0.0551 ± 5		
159-16	nd		20.32	647.1 ± 10.1	0.0733 ± 3	0.1255 ± 7	0.0442 ± 4	0.3131 ± 82		0.0514 ± 9		
159-22	nd		20.14	350.1 ± 2.9	0.0942 ± 1	0.1633 ± 5	0.0450 ± 3	0.3293 ± 60		0.0531 ± 7		
159-25	nd		20.46	692.8 ± 30.5	0.0666 ± 3	0.0758 ± 6	0.0461 ± 10	0.2926 ± 17		0.0461 ± 19		

nd = not determined

<sup>a</sup> Corrected for fractionation<sup>b</sup> Corrected for blank, spike and common Pb

## *Chapter 3*

### **3.11 Figures**

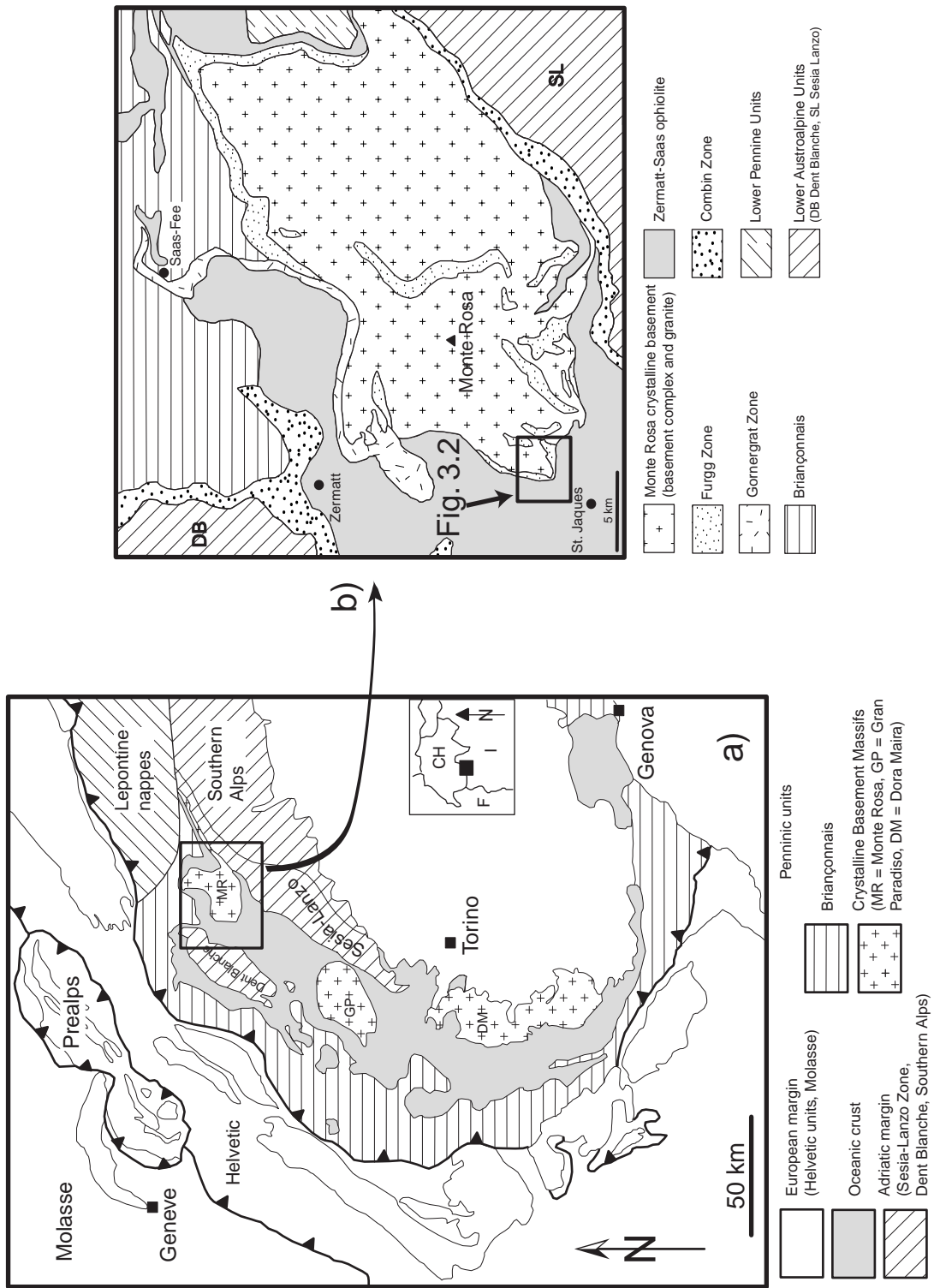


**Figure 3.1** a) Sketch map of the main tectonic units of the Western Alps (after Rubatto et al., 1999). b) Simplified geological map of the Monte Rosa region. After Bearth (1952) and Chopin & Monié (1984). The study area is indicated by the box.

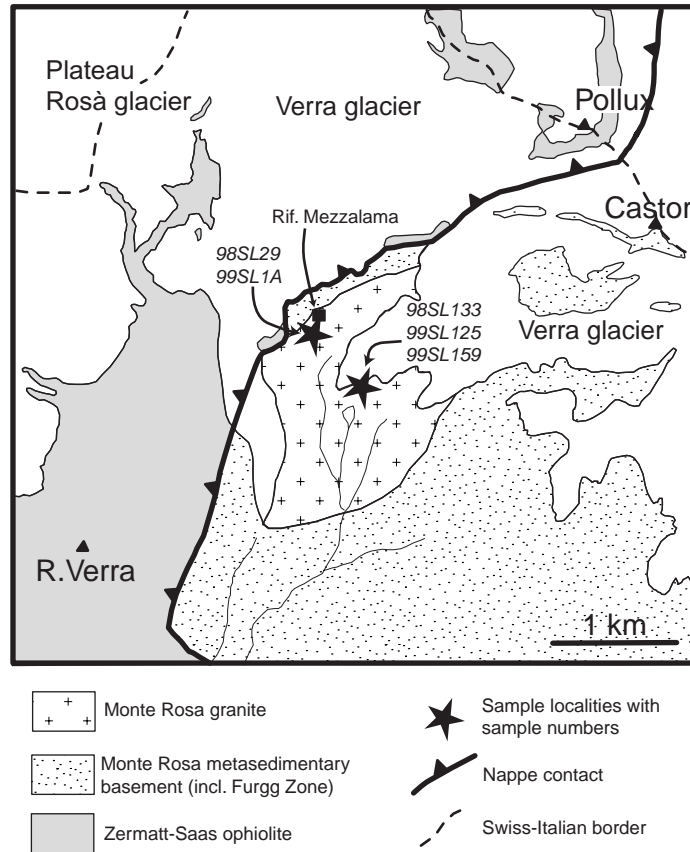


**Figure 3.2** Geological setting of the upper Val d'Ayas after Dal Piaz (1971) and Dal Piaz and Lombardo (1986). The sample locations are indicated.



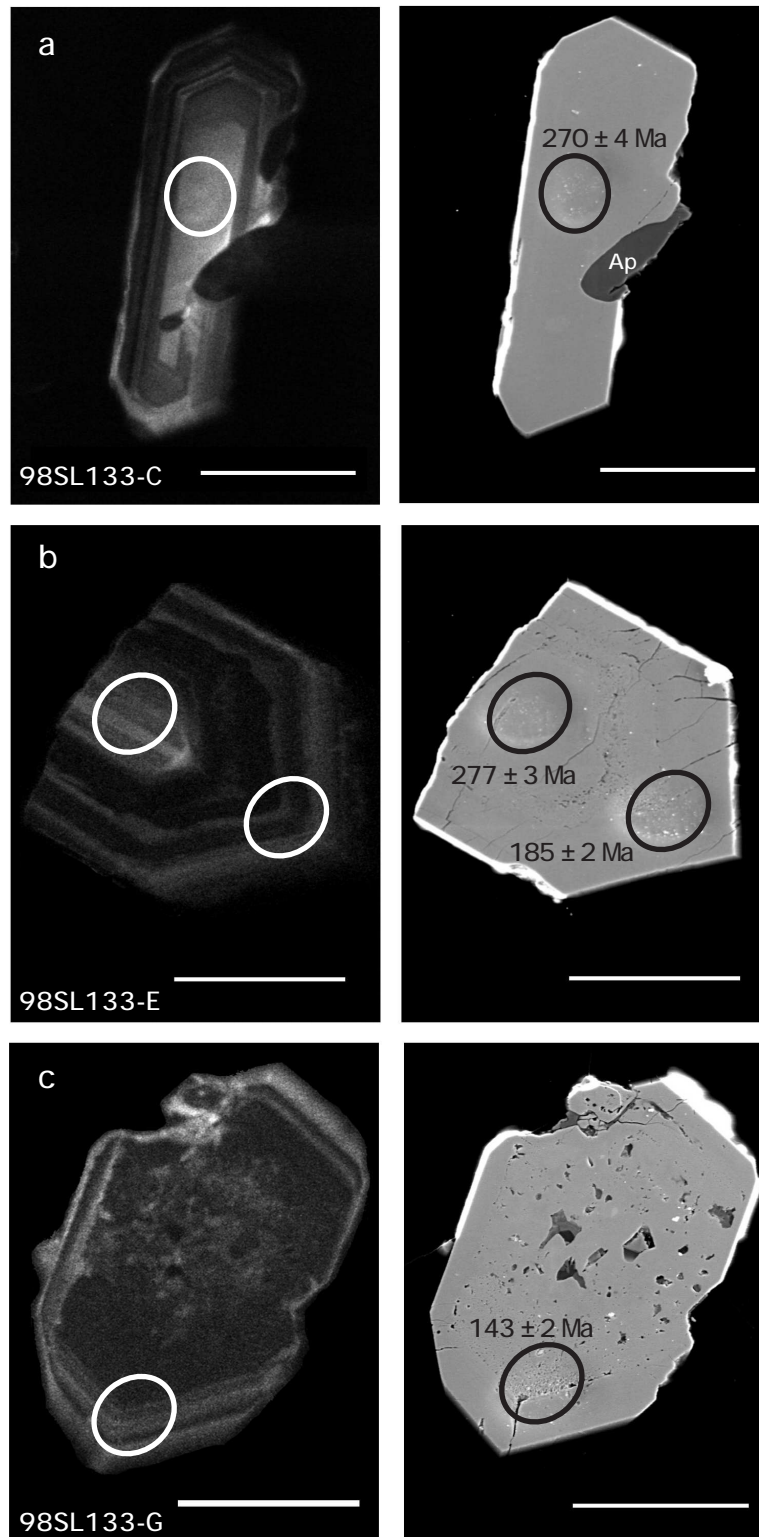


**Figure 3.3** Cathodoluminescence (left) and secondary electron images (right) of zircons from the undeformed sample 98SL133 dated in the current study. The circles indicate the locations of the SHRIMP spots. The apparent age for each spot is quoted with the  $2\sigma$  error. (a) The long, prismatic zircon displays homogenous, magmatic zoning. Note an apatite inclusion. (b) A pyramid fragment from a prismatic zircon shows oscillatory magmatic zoning. A low luminescence zone is visible in the secondary electron image. Several small inclusions are found following the growth zone with the lowest luminescence. (c) A short prismatic zircon shows a low luminescent, unzoned (diffuse) core, and a small rim characterized by regular growth zoning. The core contains a lot of small inclusions. The scale bars are 50  $\mu\text{m}$  in length.

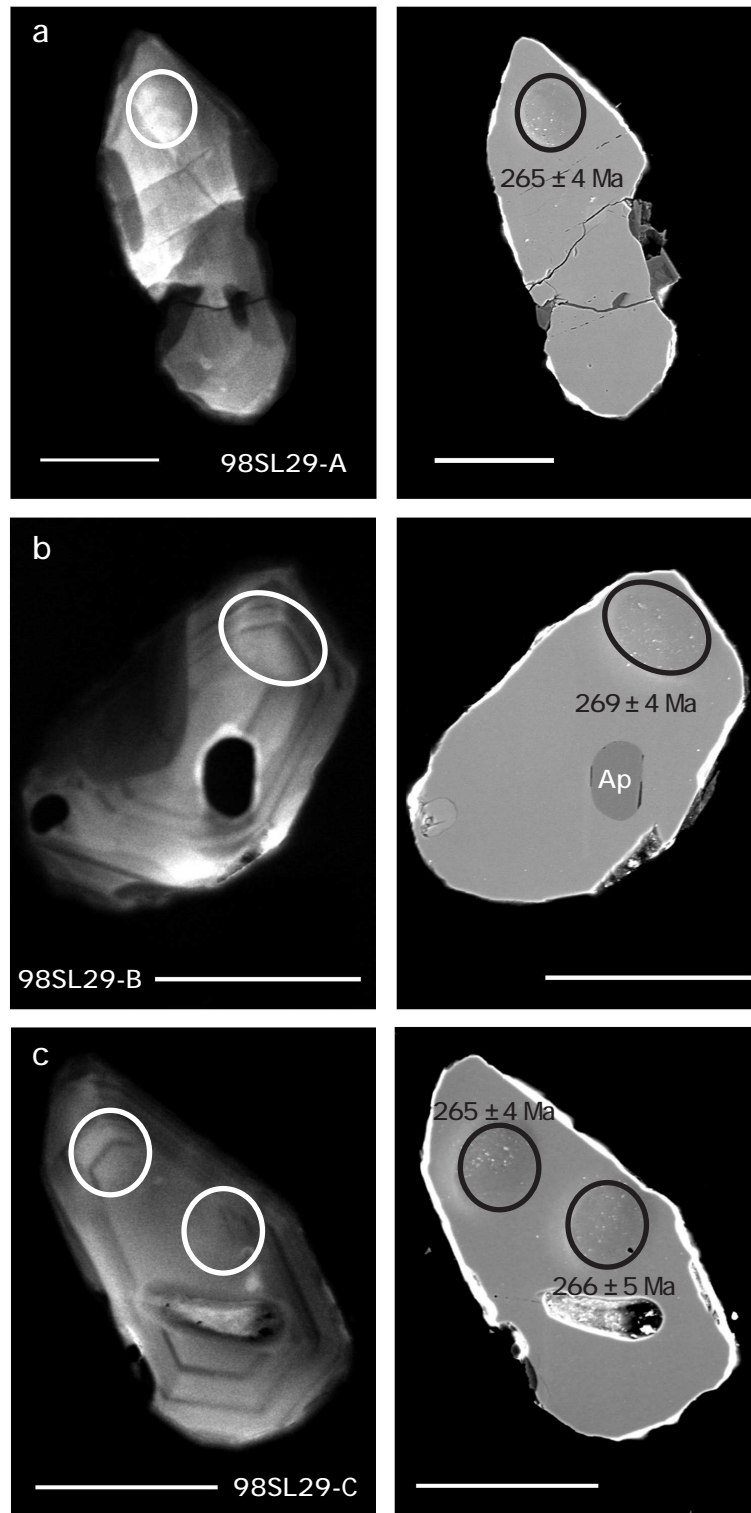


**Figure 3.4** Cathodoluminescence (left) and secondary electron images (right) of zircons dated from the deformed sample 98SL29. The circles are the locations of the SHRIMP analysis. The apparent age for each marked SHRIMP spot is given with the  $2\sigma$  error. (a) A prismatic zircon with one rounded pyramid is characterized by diffuse, patchy zoning. (b) A rounded zircon with two inclusions (the bigger one is apatite) displays diffuse oscillatory zoning. (c) The asymmetric, short prismatic zircon possesses a diffuse magmatic oscillatory zoning. It is comparable to the zircon 98SL29-B. The scale bars are 50  $\mu\text{m}$  in length.

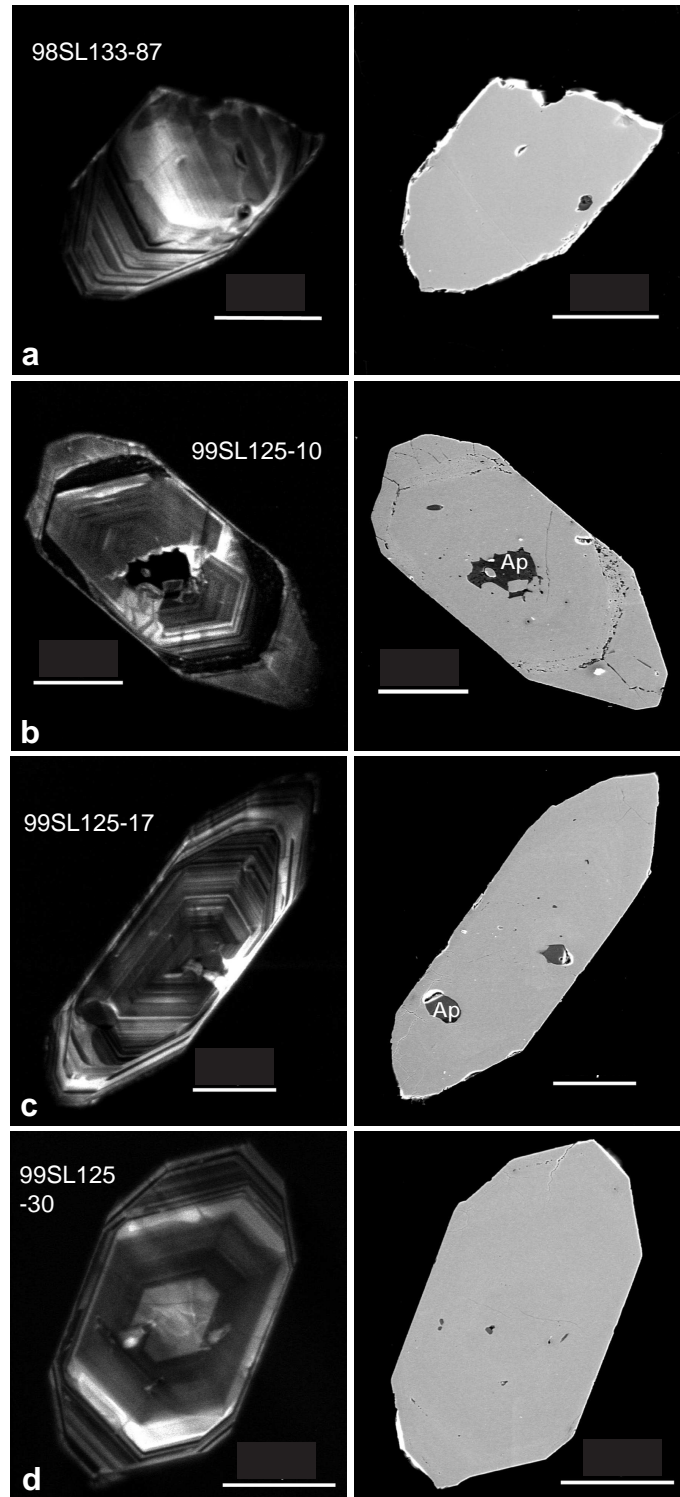


**Figure 3.5** Cathodoluminescence (left) and secondary images (right) of single zircon grains from the samples 98SL133 (a) and 99SL125 (b to d) which are dated by U-Pb isotope dilution analysis. (a) A fragment of a short prismatic zircon with a slightly diffuse core region and an oscillatory zoned rim. (b) A short prismatic zircon displaying a regular zoned core, followed by a low luminescent, unzoned (diffuse) zone and a small rim of regular growth zoning. The dark zone shows a lot of small inclusions. An apatite inclusion can be seen in the core. (c) A long prismatic zircon with regular oscillatory zoning and small apatite inclusions. (d) A short prismatic zircon with regular zoning. The scale bars are 50 μm in length.

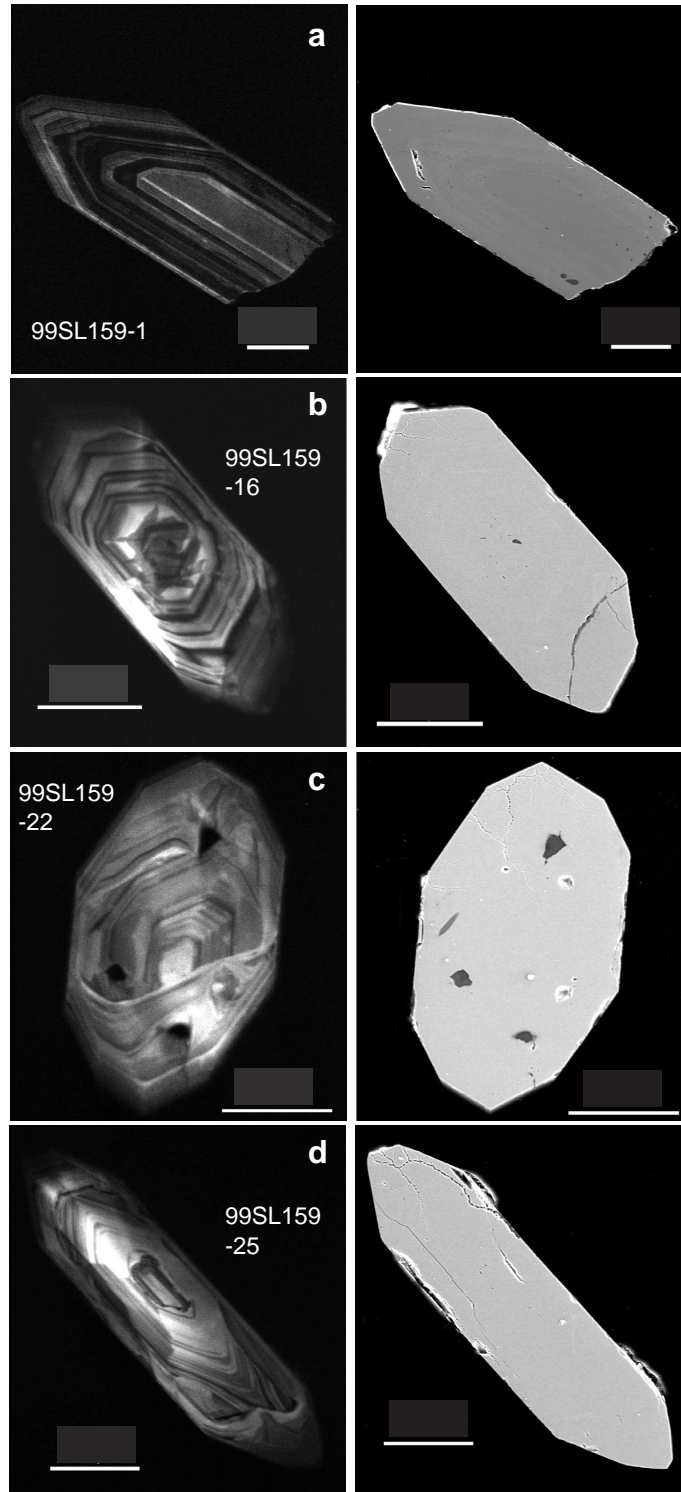


**Figure 3.6** □ Cathodoluminescence (left) and secondary images (right) of single zircon grains from the sample 99SL159 dated by U-Pb isotope dilution analysis. (a) A fragment of a long prismatic zircon with homogenous oscillatory zoning, which developed during a single growth event. (b) A short prismatic, slightly asymmetric zircon shows regular zonation pattern. (c) An asymmetric, rounded zircon displaying a regular zoning pattern. (d) A long prismatic zircon showing regular growth zoning. The scale bars are 50  $\mu\text{m}$  in length.

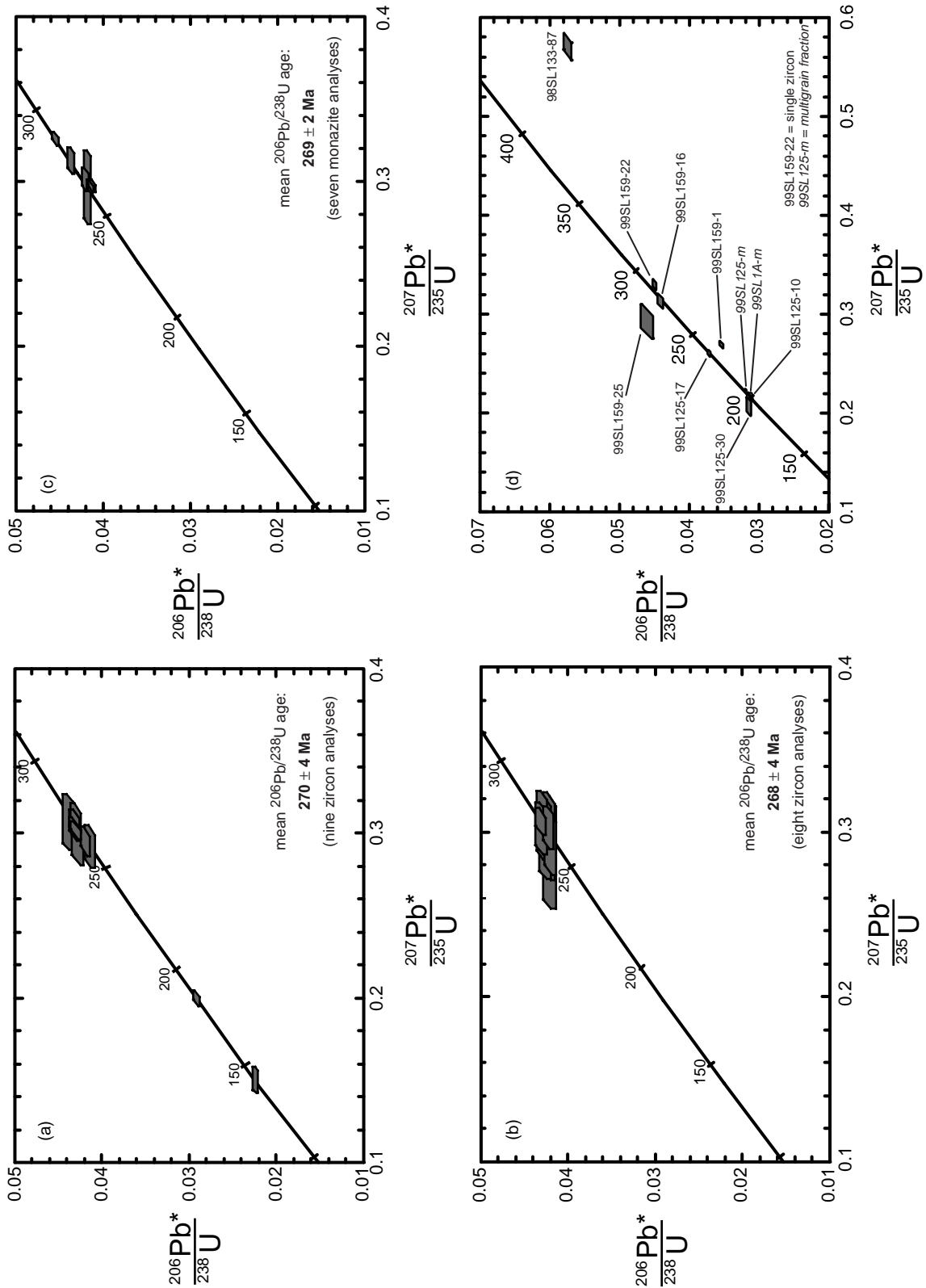


**Figure 3.7** Concordia plots for U-Pb data measured in zircons and monazites from the Monte Rosa granite. (a) Eleven SHRIMP analyses obtained from eight zircon grains from the undeformed granite (98SL133). (b) Eight SHRIMP analyses obtained from five zircon grains from the deformed granite (98SL29). (c) Seven SHRIMP analyses obtained from two monazites from the undeformed granite (98SL133). (d) Data obtained from single zircon and multigrain dating by isotope dilution from samples 98SL133, 99SL1A, 99SL125 and 99SL159. Label explanation: „99SL159-1” denotes a dated single zircon and the respective CL-image can be found either in Figure 3.5 or 3.6 depending on the sample number. „99SL1A-m” marks a dated multigrain fraction. The uncertainties in the  $^{206}\text{Pb}/^{238}\text{U}$  ages are reported at the  $2\sigma$  level.

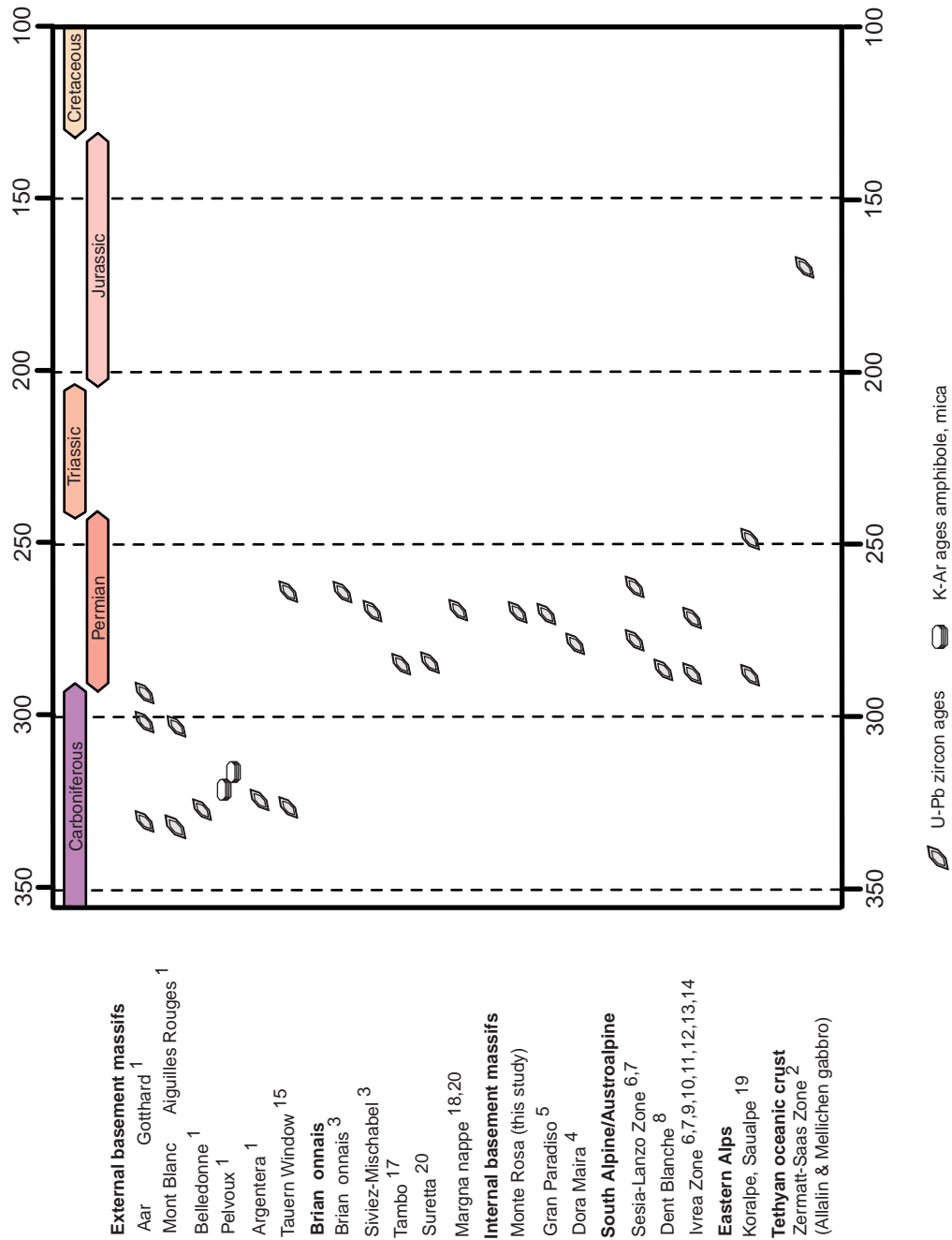


**Figure 3.8** Comparison of pre-Alpine magmatic ages in the Alpine realm. References: <sup>1</sup> von Raumer et al., 1999; <sup>2</sup> Rubatto et al., 1998; <sup>3</sup> Bussy et al., 1996; <sup>4</sup> Bussy & Cadoppi, 1996; <sup>5</sup> Bertrand et al., 2000; <sup>6</sup> Hunziker & Zingg, 1980; <sup>7</sup> Stille & Buletta, 1987; <sup>8</sup> Bussy et al., 1998; <sup>9</sup> Köppl & Grünenfelder, 1978/1979; <sup>10</sup> Rubatto et al., 1999; <sup>11</sup> Mayer et al., 2000; <sup>12</sup> Oberhänsli et al., 1985; <sup>13</sup> Paquette et al., 1989; <sup>14</sup> Paquette et al., 1999; <sup>15</sup> Eichhorn et al., 2000; <sup>16</sup> Marquer et al., 1994; <sup>17</sup> Hansmann et al., 1996; <sup>18</sup> Thöni, 1999; <sup>19</sup> Stampfli et al., 1998; <sup>20</sup> Herrmann et al., 1997.



## Chapter 4

### Retention of pre-Alpine white mica ages through Alpine high-pressure metamorphism in a talc-kyanite-chloritoid shear zone in the Monte Rosa (Western Italian Alps): insights from *in-situ* $^{40}\text{Ar}/^{39}\text{Ar}$ UV-laser ablation analyses combined with a Sr isotopic study

#### 4.1 Abstract

Application of *in-situ*  $^{40}\text{Ar}/^{39}\text{Ar}$  UV-laser ablation analyses yields a heterogeneous distribution of white mica ages within two samples from a kyanite-talc-chloritoid-bearing shear zone occurring in the Monte Rosa nappe (Western Italian Alps). Based on microstructural and chemical investigations, the analyzed phengites belong to the Alpine mineral assemblage in both samples. Only  $^{40}\text{Ar}/^{39}\text{Ar}$  ages in excess of the Alpine high-pressure event have been found. Ages as high as 250 to 280 Ma are present giving the original magmatic cooling ages of the Monte Rosa granite, the protolith of the shear zone. Ages as young as approximately 120 Ma are the result of partial loss of radiogenic argon from the system during late-Alpine, greenschist-facies metamorphism. A restricted fluid and argon mobility during the Alpine high-pressure metamorphic overprint is implied since small-scale argon isotopic gradients are maintained within the samples. A similar evolution, characterized by partial homogenization, is observed in the strontium isotopic composition of whole rock samples from different lithologies in the shear zone. The results demonstrate that the Alpine high-pressure metamorphism of the Monte Rosa nappe has taken place under relatively dry conditions. Therefore, locally closed system conditions were present on the scale of the shear zone, and under these conditions, the argon isotopic system is more retentive than the strontium isotopic system.

**Keywords:** *Geochronology, Monte Rosa, in-situ  $^{40}\text{Ar}/^{39}\text{Ar}$  UV-laser ablation, isotopic redistribution, strontium*

## 4.2 Introduction

The  $^{40}\text{Ar}/^{39}\text{Ar}$  method is a powerful tool to obtain geochronological information from metamorphic rocks (Mc Dougall and Harrison, 1988). In combination with other geochronological systems, structural analysis and petrological investigations, it can be used to gain insight into the understanding and the quantification of large-scale orogenic processes. This approach is generally based on the use of the „blocking temperature“ or „closure temperature“ concept after Jäger (1967) and Dodson (1973), respectively. During recent studies, however, it was realized that the rate of isotopic transport is not just driven by the temperature but also by other processes, i.e. fluid circulation and deformation (Jenkin, 1995; Reddy et al., 1997; Scaillet, 1998; Villa, 1998; Kühn et al., 2000; Di Vincenzo and Palmeri, 2001; Reddy et al., 2001 and references therein). Therefore, the understanding of the processes and mechanisms that influence the behavior of the argon isotopic system during regional metamorphism is of fundamental importance for a correct interpretation of argon geochronological data.

Several attempts have been made to correlate structural and chemical observations with argon geochronological data in order to place constraints on the controlling parameters of the argon isotopic behavior, i.e. mica composition, crystal-chemical characteristics, deformation, fluids, and diffusion processes (e.g. Scaillet et al., 1992; Hames and Bowring, 1994; Dahl, 1996; Reddy et al., 1996; Reddy et al., 1997; Reddy et al., 2001). The development of high-resolution, *in-situ* analyses techniques provides an opportunity to improve the interpretation of ages, especially if used in combination with microstructural and chemical information. In this way, the existence of small-scale, intrasample argon isotopic gradients is revealed. Different mechanisms have been proposed to preserve small-scale gradients within a sample during its metamorphic evolution. Reddy et al. (1997) suggested that localized fluid infiltration produces small-scale argon reservoirs, which escaped subsequent homogenization. On the other hand, nearly fluid-absent, high- to ultrahigh-pressure metamorphic conditions have been interpreted to cause restricted fluid and isotopic mobility (Scaillet, 1996; Scaillet, 1998; Giorgis et al., 2000). Another problem often ascribed to argon geochronology, especially for high-pressure metamorphic rocks, is the incorporation of excess argon leading to high apparent ages which are assumed to be geologically meaningless or to reflect a complex evolution history (e.g. Chopin and Monié, 1984; Li et al., 1994; Arnaud and Kelley, 1995; Giorgis et al., 2000).

Here, we report the results of an *in-situ*  $^{40}\text{Ar}/^{39}\text{Ar}$  ultra-violet (UV) laser ablation geochronological investigation on white micas from two samples which were



collected in a kyanite-talc-chloritoid-bearing shear zone in the Monte Rosa granite (Monte Rosa nappe, Italian Western Alps; Fig. 4.1). These two samples display either a mineral assemblage related to the Alpine high-pressure event or to the later greenschist-facies overprint of the Monte Rosa nappe. Microprobe analyses of the white micas are used to combine microstructural and chemical information with the geochronological data to study the influence of microstructural position, petrological aspects and the chemical composition of the analyzed white micas on the behavior of the argon isotopic system. The combination of argon data with strontium isotopic data of whole rock samples from two profiles across the shear zone are used to demonstrate the complex and polyphase metamorphic evolution of the Monte Rosa nappe. Strontium evolution diagrams within the shear zone reveal that at least two events are needed to explain the observed isotopic signatures in the whiteschist.

### **4.3 Geological background**

The Monte Rosa basement nappe is a tectonic window within the eclogite-bearing Mesozoic Piemonte ophiolite complex of the Western Alps (Fig. 4.1). It is commonly assigned to the southernmost part of the European continental assembly, and correlated with the structurally similar Dora Maira and Gran Paradiso massifs. With respect to the Bernhard nappe system, a more internal paleotectonic position of the Monte Rosa nappe is assumed (Bearth, 1952; Dal Piaz and Lombardo, 1986; Platt, 1986; Pawlig et al., *subm.*; Dal Piaz et al., 2001 and references therein). The Monte Rosa nappe consists of a high-grade metapelitic basement complex that was intruded by the Monte Rosa granite at  $270 \pm 4$  Ma (Pawlig et al., *subm.*). An inferred Permian to Mesozoic cover consists of sedimentary-volcanic sequences, the Gornergrat Zone and the Furgg-Zone (Bearth, 1952; Dal Piaz and Lombardo, 1986). The basement complex is characterized by relic high-grade assemblages of biotite-sillimanite-plagioclase-garnet-quartz-K-feldspar-plagioclase and garnet-biotite-muscovite-sillimanite-plagioclase, which pre-date the intrusion of the Monte Rosa granite (Dal Piaz and Lombardo, 1986). Evidences for an Alpine high-pressure metamorphism of the Monte Rosa nappe are given by eclogites that are partially associated with the metapelitic basement as well as the occurrence of several discrete shear zones hosting talc-kyanite-chloritoid bearing rocks within the Monte Rosa granite (Bearth, 1952; Dal Piaz and Lombardo, 1986). Those special rocks were described as „silvery micaschists“ by Dal Piaz and Lombardo (1986) and are referred to as „whiteschists“ in this study. The metamorphic conditions of the Alpine high-pressure event in the

Monte Rosa nappe still remain a matter of ongoing debates since its present tectonic position below the coesite-bearing, oceanic Zermatt-Saas Zone is critical for unravelling the tectonic evolution of the Western Alps. The Monte Rosa granite lacks any indications of the high-pressure reaction of albite forming Na-pyroxene+quartz. It rather displays a relic magmatic assemblage of K-feldspar + quartz + muscovite + biotite ± zircon ± apatite ± monazite ± xenotime, whereby the magmatic plagioclase is overprinted by phengites with high-Si contents (up to 3.5 Si p.f.u.), small garnet and zoisite in an albite matrix. PT-estimates based on the Si-content of the phengites from the granite at a temperature of 550°C for the Alpine high-pressure event after Dal Piaz and Lombardo (1986), and 450°C as a temperature for the later greenschist-facies retrogression after Borghi et al. (1996) using the calibration of Massonne and Schreyer (1987) leads to pressures of 13 kbar and 10 kbar, respectively. PT-investigations by Frey et al. (1976) and Borghi et al. (1996) resulted in approximately 6 kbar and 450°C for the greenschist-facies metamorphism.

Geochronological implications on the timing of the Alpine high-pressure metamorphic event in the Western Alps have been presented in several recent studies (see Gebauer, 1999 and Dal Piaz et al., 2001 for reviews). Evidence that the subduction of different structural levels propagated from internal, paleo-African derived units to external, paleo-European derived ones is given by an Eoalpine onset of the subduction of the Sesia-Lanzo Zone at around 65 Ma after Rubatto et al. (1999), followed by the Tertiary consumption of the Tethyan oceanic crust at around 44 Ma (Rubatto et al., 1998; Amato et al., 1999), and finally the Eocene-Oligocene subduction of the Briançonnais domain including the Monte Rosa continental basement nappe at approximately 35 Ma (Rubatto and Gebauer, 1999). An Eoalpine subduction was assumed for the Monte Rosa nappe, constrained by  $^{40}\text{Ar}/^{39}\text{Ar}$  step heating investigations on a Mg-chloritoid-bearing high-pressure assemblage (Chopin and Monié, 1984). They reported a  $110 \pm 3$  Ma plateau age, which was interpreted to result from the incorporation of a homogeneously distributed excess argon component. Another plateau age of 70 Ma was assumed to represent the age of the Alpine high-pressure metamorphism. Monié (1985) assigned a first episode around 110 Ma to the subduction of the continental crust. The age of the retrogressive metamorphic overprint was constrained to be 65 Ma under blueschist-facies conditions ( $\approx 8$  kbar at 500°C), followed by an event at 38 Ma under greenschist-facies conditions ( $\approx 5$  kbar at 450°C). The youngest obtained age of 27 Ma was suggested to be related to the Lepontine metamorphism of the Central Alps, reaching greenschist-facies conditions in the Monte Rosa nappe. The variety of the  $^{40}\text{Ar}/^{39}\text{Ar}$  ages was interpreted by Monié (1985) to demonstrate the plurifacial character of the

Alpine metamorphism within the Monte Rosa basement nappe. A 35 Ma U-Pb SHRIMP age obtained from zircon of a quartzite of the Gornergrat Zone was interpreted by Rubatto and Gebauer (1999) to constrain the timing of high-pressure metamorphism in the Monte Rosa nappe. Nevertheless, this assignment is problematic since the quartzite is characterized by a greenschist-facies mineral assemblage of quartz-phengite (3.35 Si p.f.u.)-epidote-titanite-albite  $\pm$  carbonate  $\pm$  apatite  $\pm$  zircon (Rubatto and Gebauer, 1999). Therefore, this age might also represent a maximal time constraint of the greenschist-facies metamorphism.

#### 4.4 Analytical procedures

The two samples, which were selected from the shear zone, were prepared as polished microprobe sections. Mineral chemistry and backscattered electron images (BSE) on those sections were obtained with a JEOL JXA8900RL (Mineralogy, University of Mainz). Operating conditions were 15 kV accelerating voltage and 12 nA sample current. Representative mica compositional data for each sample are listed in table 4.1 and the location of the microprobe analyses points are documented within thin section sketches (Fig. 4.2).

An approximately 8 to 10 mm square with a thickness of ca. 300 to 400  $\mu\text{m}$  was prepared from the remaining thin section chip of each sample and represents the mirror image of the part analyzed with the microprobe. They were polished on one side for the *in-situ* UV-laser ablation analyses. Those samples, bulk mineral separates and standards were irradiated for 40 h in the central thimble position of the USGS TRIGA reactor in Denver (CO), USA (Dalrymple, et al., 1981). The neutron flux was monitored using the MMhb-1 standard with an age of 520.4 Ma (Samson and Alexander, 1987), and the calculated  $J$  value was  $0.00479 \pm 0.00003$ . The *in-situ* UV-laser ablation analyses were performed in the  $^{40}\text{Ar}/^{39}\text{Ar}$  laboratory of the University of Lausanne (Switzerland) with a pulsed excimer (KrF) laser operating at a wavelength of 248 nm. The size and the depth of the laser ablation pits varied in order to obtain  $^{40}\text{Ar}$  signals at least 10 times of the blank value. The sample was observed during the ablation process with a CCD camera co-axial to the laser beam. After ablation of the sample using short (10 ns) laser pulses and purification, the gas was expanded into a MAP 215-50 noble gas mass spectrometer equipped with an electron multiplier for isotopic analyses. System blanks were measured over the time of analysis and were subtracted from the overall signal. The argon data corrected for

blank, radiogenic decay and interfering Ca-, K- and Cl-derived isotopes, and calculated  $^{40}\text{Ar}/^{39}\text{Ar}$  ages with  $1\sigma$  uncertainty are presented in table 4.2.

Whole rock samples from all lithologies of the shear zone were crushed and powdered in a tungsten carbide mill. Rb and Sr concentrations were determined on powder pellets by X-ray fluorescence with a Philips PW 1400 spectrometer with a rhodium X-ray tube (Mineralogy, University of Mainz). Approximately 50 to 200 mg of the whole rock powder depending on the Rb and Sr concentrations were weighted into 5 ml Savillex™ screw-top beakers and dissolved in a mixture of HF-HNO<sub>3</sub> within Parr™ bombs at 200 °C for several days. The samples were evaporated on a hot plate, dissolved with 6N HCl, and once more evaporated. Rb and Sr were separated in columns filled with Dowex AG50WX12 resin. Sr was loaded with TaF<sub>5</sub> on single W filaments. The isotopic ratios were measured on a Finnigan MAT261 mass spectrometer (Max-Planck Institute for Chemistry, Department of Geochemistry, Mainz) operating in static mode. The  $^{87}\text{Rb}/^{86}\text{Sr}$  ratios were calculated according to Faure (1986). The errors for concentrations and calculated  $^{87}\text{Rb}/^{86}\text{Sr}$  ratios are in the range of 2 to 5%. Repeated runs of the SRM NBS987 standard yielded a mean  $^{87}\text{Sr}/^{86}\text{Sr}$  value of  $0.710204 \pm 27$  ( $n = 15$ ). Fractionation was corrected by normalizing the ratios of  $^{86}\text{Sr}/^{88}\text{Sr}$  to 0.1194. All errors for isotope results are given at  $2\sigma$ , and the data are presented in table 4.3.

### 4.5 Sample description

The samples investigated by microprobe and by *in-situ*  $^{40}\text{Ar}/^{39}\text{Ar}$  UV-laser ablation analyses as well as the whole rock samples studied for strontium isotopic composition were selected from two profiles sampled across a talc-kyanite-chloritoid shear zone which occurs within the Monte Rosa granite in the upper Val d' Ayas, Italy (Dal Piaz, 1971; Dal Piaz and Lombardo, 1986; Fig. 4.1a). The shear zone shows progressive deformation, from the undeformed Monte Rosa granite to granitic gneiss, and finally talc-kyanite-chloritoid-bearing whiteschists in the center (Fig. 4.1b). For a detailed description of the shear zone lithology, whole rock chemistry and genesis see (Pawlig and Baumgartner, in press). Petrological investigations on a similar whiteschist-bearing shear zone of the Monte Rosa nappe resulted in PT-conditions of up to 25 kbar at 580 °C for the Alpine high-pressure metamorphism from the stability of the assemblage chloritoid + talc + kyanite + phengite (Le Bayon et al., 2000). Later greenschist-facies retrogression is recorded by the replacement of the high-pressure mineral assemblage by muscovite + Mg-chlorite within the whiteschist.

The two samples investigated by *in-situ* UV-laser ablation and microprobe analyses, 99SL119 and 99SL146, were taken from the granitic gneiss and the whiteschist, respectively (Fig. 4.1b). The whiteschist sample, 99SL146, contains kyanite, chloritoid, phengite, quartz, muscovite, chlorite, minor rutile, monazite and zircon. The foliation consists mainly of phengite and wraps around large composite aggregates of kyanite and chloritoid. Those aggregates are replaced by a rim of chlorite and muscovite during greenschist-facies metamorphism, which shows a preferred orientation at high angle to the first foliation (Fig. 4.2a). The sample of the granitic gneiss (99SL119) is characterized by a strong planar fabric defined by oblate grains of quartz, oriented phengite and minor chlorite (Fig. 4.2b). Epidote, small garnets with atoll structures, minor carbonate, zircon, apatite, rutile, sphene and tourmaline can be present in the granitic gneiss as well, but they were not observed in the part of the sample investigated in detail. Incipient biotite alteration is present along the margins or the cleavage traces of chlorite and phengite in the granitic gneiss. Those biotites were rarely observed in the analyzed area of sample 99SL119.

In the whiteschist sample (99SL146) two different generations of white micas can be distinguished based on textural and compositional observations (Fig. 4.2a and 4.3). The first generation clearly defines the main schistosity of the sample and is of phengitic composition with Si-contents between 3.2 and 3.5 p.f.u. and low molar paragonite components of 3 to 6% (Tab. 4.1, Fig. 4.2a and 4.3). These high-Si phengites belong to the high-pressure metamorphic assemblage of kyanite + chloritoid + quartz  $\pm$  rutile. The chloritoid is characterized by molar contents of the Mg-endmember of 52 to 58%. Chopin and Monié (1984) have reported similar values in a previous study for a similar assemblage from the Monte Rosa nappe. The second generation is muscovitic with Si-contents of 3.0 to 3.1 p.f.u. and slightly higher molar paragonite components of 10 to 14% (Tab. 4.1, Fig. 4.2a and 4.3). The muscovites occur mainly together with Mg-chlorite, which is characterized by  $X_{Mg}$ -values [=Mg/(Mg+Fe+Mn)] of 0.75 to 0.77. Muscovite + Mg-chlorite assemblages form narrow rims around composite aggregates of kyanite + chloritoid or occur in between those aggregates (Fig. 4.2a). However, some phengite relics are preserved within the rims formed by muscovite and Mg-chlorite (Fig. 4.2a, Tab. 4.1, e.g. analyses #16 and #41). Most analyses plot slightly below the line of the ideal Tschermak-substitution (Fig. 4.3) due to partial replacement of the  $Al^{VI}$  by  $Fe^{3+}$  and Ti. The textural and chemical observations suggest that the assemblage muscovite + Mg-chlorite is formed from the high-pressure mineral assemblage during the late-Alpine, greenschist-facies metamorphic overprint.

The analyzed white micas of the granitic gneiss (99SL119) are preferably oriented within the direction of the foliation and show a broad but continuous variation of the Si-content from 3.1 to 3.4 p.f.u. and a molar paragonite component of 5 to 14% (Fig. 4.2b and 4.3, Tab. 4.1). The continuous variation in Si-content of the white micas suggests a continuous decrease of pressure and temperature from eclogite- to greenschist-facies conditions during the Alpine metamorphic evolution. The granitic gneiss shows alternating layers of quartz and phengite  $\pm$  Mg-chlorite. The Mg-chlorite is characterized by  $X_{Mg}$ -values of 0.83 to 0.86. Field observations and whole rock geochemical characteristics obtained in a previous study (Pawlig and Baumgartner, in press) as well as textural and mineral chemical investigations suggest that the mineral assemblage phengite + Mg-chlorite + quartz in the granitic gneiss grew during the Alpine greenschist-facies metamorphic event during deformation.

### 4.6 Results

#### 4.6.1 *In-situ* $^{40}\text{Ar}/^{39}\text{Ar}$ UV-laser ablation analyses of white micas

The *in-situ* UV-laser ablation analyses yield a broad variation of  $^{40}\text{Ar}/^{39}\text{Ar}$  ages in both analyzed samples. Ages in the range of 280 to around 40 Ma are obtained and are presented in a histogram plot (Tab. 4.2, Fig. 4.4). The youngest ages in both samples are characterized by low radiogenic  $^{40}\text{Ar}^*$  contents. They do not represent reliable ages (Tab. 4.2, analyses #1 to #9 of the granitic gneiss (99SL119); analyses #1, #2 and #41 of the whiteschist (99SL146)). Series of CCD camera images of the polished rock slabs show the laser ablation pits in the micas within their microstructural context (Fig. 4.5). All analyses in both samples were made on phengites, which belong to Alpine mineral assemblage and are part of the foliation (Fig. 4.5). Profiles across the foliation yielded large intergrain age variations.

Within the whiteschist from the center of the shear zone (99SL146), 45 analyses on individual micas gave  $^{40}\text{Ar}/^{39}\text{Ar}$  ages in the range of  $119 \pm 8$  to  $287 \pm 10$  Ma which are characterized by high radiogenic  $^{40}\text{Ar}^*$  contents (Tab. 4.2). Profiles across the foliation revealed large age variations from  $171 \pm 4$  to  $243 \pm 3$  Ma, and hence age differences of up to 60 Ma are observed on distances of approximately 50  $\mu\text{m}$  (Fig. 4.5a and 4.5b). Within the granitic gneiss (99SL119), 47 analyses were carried out on individual micas located within the foliation. The resulting  $^{40}\text{Ar}/^{39}\text{Ar}$  ages vary between  $124 \pm 4$  and  $257 \pm 3$  Ma (Tab. 4.2). A profile across the foliation

shows a similar age variation as observed in the whiteschist (Fig. 4.5c).  $^{40}\text{Ar}/^{39}\text{Ar}$  ages of  $158 \pm 4$  to  $203 \pm 3$  Ma are observed, and age differences of up to 30 Ma are found on distances of approximately 50  $\mu\text{m}$  (Fig. 4.5c). One analysis in the same profile yielded a  $^{40}\text{Ar}/^{39}\text{Ar}$  age of  $40 \pm 5$  Ma (Tab. 4.2; #2 in sample 99SL119), but is characterized by a low radiogenic  $^{40}\text{Ar}^*$  content and a low  $^{40}\text{Ar}/^{36}\text{Ar}$  ratio of 402.

Based on these observations, the age distribution in both samples appears quite complex and seems not to be correlated to the geometry and the microstructural position of the analyzed grains. No systematic or clear gradient was observed across the foliation. Hence, age variations in both samples seem to occur at the scale of single micas crystals due to the development of single age domains with variations of up to 60 Ma at a distance of approximately 50  $\mu\text{m}$  (Fig. 4.5).

#### 4.6.2 Rb-Sr geochemistry

Across the shear zone, an enormous variation in the Rb-Sr geochemical characteristics within the different lithologies can be observed (Tab. 4.3). The samples of the Monte Rosa granite show homogenous, crustal  $^{87}\text{Sr}/^{86}\text{Sr}$  ratios of 0.73315 to 0.73605 as well as typical Rb and Sr concentrations of 183 to 248 and 110 to 124 ppm, respectively. The resulting  $^{87}\text{Rb}/^{86}\text{Sr}$  are 4.6 to 6 (Tab. 4.3). Traversing from the granitic gneiss towards the whiteschist in the center of the shear zone, an increase of the  $^{87}\text{Sr}/^{86}\text{Sr}$  ratios can be observed (Fig. 4.7a). The dark variety of the granitic gneiss shows similar values as the granites, and the red, partially mylonitic variety of the granitic gneiss shows slightly increased ratios ranging from 0.75180 to 0.79626. For a petrographic and geochemical description of the different lithologies of the shear zone see Pawlig and Baumgartner (in press). The whiteschists show high  $^{87}\text{Sr}/^{86}\text{Sr}$  ratios of 0.78071 to 0.82301 (Fig. 4.7a). The Rb and Sr concentrations in the gneisses and the whiteschists show a homogenous Rb concentration of 177 to 289 ppm with one exception in a whiteschist, which only contains 92 ppm Rb. The Sr concentration decreases from the granitic gneiss towards the whiteschist from 84 to 20 ppm in the gneiss to 19 to 8 ppm in the whiteschist. These characteristics are reflected in the  $^{87}\text{Rb}/^{86}\text{Sr}$  ratios, which increase towards the whiteschist to values up to 72 (Tab. 4.3).

#### 4.7 Discussion

The observed  $^{40}\text{Ar}/^{39}\text{Ar}$  ages reveal a broad range of ages between 280 and approximately 120 Ma in both samples (Fig. 4.4). Although the temperature of the Alpine high-pressure metamorphism (580°C at 25 kbar, Le Bayon et al., 2000) was higher than the generally accepted closure temperature of approximately 350°C for the argon isotopic system in white mica (Mc Dougall and Harrison, 1988), the original magmatic cooling ages (280 to 250 Ma) of the Monte Rosa granite are retained, which is clearly the protolith of the shear zone (Pawlig and Baumgartner, in press).

The apparent  $^{40}\text{Ar}/^{39}\text{Ar}$  ages characterized by low  $^{40}\text{Ar}/^{36}\text{Ar}$  ratios are excluded for this discussion because of the large amount of atmospheric contamination present (Tab. 4.2, analyses #1 to #9 of the granitic gneiss (99SL119); analyses #1, #2 and #41 of the whiteschist (99SL146)). They are most probably the result of the ablation of intergrown phases with low  $^{40}\text{Ar}/^{36}\text{Ar}$  ratio, i.e. quartz; especially in the case of analysis #2 of the granitic gneiss (99SL119) yielding the youngest age of this sample of  $40 \pm 5$  Ma (Fig. 4.5c; Tab. 4.2, #2 in sample 99SL119). An analysis of quartz grains from the granitic gneiss revealed a  $^{40}\text{Ar}/^{36}\text{Ar}$  ratio of approximately 102, and supports the interpretation of the young ages being contaminated by intergrown quartz with a low  $^{40}\text{Ar}/^{36}\text{Ar}$  ratio. Only one Alpine age of  $42 \pm 3$  Ma was obtained within the granitic gneiss. It is interpreted as a reliable age constraint because it is characterized by a high  $^{40}\text{Ar}/^{36}\text{Ar}$  ratio of 1602 (see Tab. 4.2, analysis #22, sample 99SL119). Information on potential relationships between apparent age, mica composition and/or atmospheric contamination can be gained from correlations between the ratios of  $^{36}\text{Ar}/^{39}\text{Ar}$ ,  $^{37}\text{Ar}/^{39}\text{Ar}$  and the  $^{38}\text{Ar}/^{39}\text{Ar}$  (Roberts et al., 2001). Those ratios are plotted against the  $^{40}\text{Ar}/^{39}\text{Ar}$  age (Fig. 4.6). No correlation between the apparent age and the  $^{36}\text{Ar}/^{39}\text{Ar}$  ratio has been found for both samples. The  $^{36}\text{Ar}/^{39}\text{Ar}$  ratios for the whiteschist (99SL146) have values up to 0.0424, and for the granitic gneiss (99SL119) they are partially higher with values up to 0.0536. Therefore, a systematic contamination of especially the younger ages by a low  $^{40}\text{Ar}/^{36}\text{Ar}$  component, i.e. with atmospheric composition of 295.5 (Mc Dougall and Harrison, 1988), can be excluded. The  $^{37}\text{Ar}/^{39}\text{Ar}$  and  $^{38}\text{Ar}/^{39}\text{Ar}$  ratios also do not exhibit any significant correlation (Fig. 4.6b and 4.6c). In both samples, no ages considerably higher than the Permian age of the granitic protolith are observed, which was obtained from U-Pb dating on zircon and monazites in a previous study (Pawlig et al., *subm.*). Therefore, the argon ages of both samples measured during this study are not contaminated by an excess argon component derived external to



the rocks. In contrast, Arnaud and Kelley (1995) found an excess argon component for the Brossasco metagranite, because obtained argon ages of 565 and 614 Ma clearly exceed the crystallization age of the granite of 303 Ma which was revealed from U-Pb zircon ages (Paquette et al., 1999). Previously, an  $^{40}\text{Ar}/^{39}\text{Ar}$  age of 110 Ma obtained from a step-heating experiment of phengites from a similar phengite-talc-chloritoid-kyanite-assemblage of the Monte Rosa nappe has been interpreted as the result of homogeneously incorporated excess argon, whereas an age of around 70 Ma was considered as the age of the Alpine high-pressure metamorphism (Chopin and Monié, 1984; Monié, 1985). However, despite Alpine regional metamorphism only one Alpine age was found within the sample of the granitic gneiss during this study (99SL119; Tab. 4.2, analysis #22), although the analyzed phengites of both samples clearly belong to the Alpine metamorphic mineral assemblage. No compositional zoning of the phengites can be observed within the foliation and on the scale of single crystals, and no clear gradient of the respective  $^{40}\text{Ar}/^{39}\text{Ar}$  ages can be found as well (Fig. 4.5). Therefore, argon isotopic gradients are present at the grain scale, which are obviously not dependent on the mica composition. Moreover, the  $^{40}\text{Ar}/^{39}\text{Ar}$  ages which are younger than the magmatic cooling ages of the Monte Rosa granite are considered to reflect partial loss of radiogenic argon from the phengites during greenschist-facies Alpine metamorphism. Therefore, small-scale argon domains showing different degrees of argon loss and, thus, different  $^{40}\text{Ar}/^{39}\text{Ar}$  ages are observed within profiles across the schistosity at distances of approximately 50  $\mu\text{m}$  (Fig. 4.5a to c).

The observed argon isotopic characteristics of the talc-chloritoid-kyanite shear zone within the Monte Rosa granite can be explained by a restricted fluid and isotopic mobility during the high-pressure Alpine metamorphic overprint. Restricted fluid mobility during high-pressure metamorphism was already suggested, e.g. by Philippot and Selverstone (1991), Philippot (1993), and Philippot et al. (1995), and based on determined grain-scale heterogeneities in argon isotopic ratios, a limited isotopic mobility under such restricted fluid mobility was proposed by Scaillet et al. (1990). The chlorite-rich assemblages of the late magmatic, hydrothermally altered granitic protolith of the shear zone reacted to form the high-pressure assemblage chloritoid + kyanite + talc + phengite + quartz by prograde reactions. During high-pressure metamorphism, no large-scale circulation of free, chemically uniform fluids took place within the shear zone rocks. The micas recrystallized under those relatively dry metamorphic conditions and preserved their pre-Alpine  $^{40}\text{Ar}/^{39}\text{Ar}$  ages. Field observations and geochemical characteristics of the granitic gneiss (Pawlig and Baumgartner, in press) combined with the geochronological results obtained during

this study argue for a localized and heterogenous fluid infiltration during the late-Alpine, greenschist-facies retrogression due to the occurrences of quartz veins which are at high angle to the shear zone. This fluid infiltration enhanced the localized partial loss of radiogenic argon along the cleavage planes of the phengites and led to the observed highly variable age distribution in both samples investigated during this study (Fig. 4.4). A similar pattern of  $^{40}\text{Ar}/^{39}\text{Ar}$  ages was obtained by Kramar et al. (in press) on large, Variscan micafishes from the Siviez-Mischabel nappe (Bernhard nappe system, Western Alps). They showed that the deformation along micro-shearbands clearly enhanced the diffusional loss of radiogenic argon during Alpine greenschist-facies metamorphism, while less deformed parts of the muscovites retained their Variscan cooling ages. Therefore, potential causes of complex argon isotopic behavior during metamorphic evolution that hinder a simple interpretation of obtained geochronological data are limited fluid circulation and accompanied limited isotopic exchange (Scaillet et al., 1990; Scaillet, 1996; Girogis et al., 2000; this study), and deformation as a direct controlling parameter on argon diffusion length scale (Kramar et al., in press).

A similar evolution, characterized by partial homogenization, is observed in the strontium isotopic system of whole rock samples from different lithologies in the shear zone. A strontium evolution diagram showing the temporal evolution of the  $^{87}\text{Sr}/^{86}\text{Sr}$  isotopic composition of the granite with an intrusion age of 270 Ma (Pawlig et al., *subm.*) and a resulting initial  $^{87}\text{Sr}/^{86}\text{Sr}$  of 0.714107 is given in Fig. 4.7b. If it is assumed that the whiteschists are the result of a metasomatic alteration of the granite, then the whole rock chemistry of the granite must have been changed during its evolution. During this alteration process, around 84% of the Sr were leached from the granite, whereas most of the Rb remained in the system since only 14% were lost (Pawlig and Baumgartner, *in press*; their Fig. 5c). Therefore, the Rb/Sr ratio was changed from around 2 in the granite to ratios of 6 up to 25 in the altered equivalent, coinciding with the high Rb/Sr ratios observed in the whiteschist samples today (Tab. 4.3). In the strontium evolution diagram, the samples with such high Rb/Sr ratios will evolve at steeper lines resulting in higher  $^{87}\text{Sr}/^{86}\text{Sr}$  ratios (Fig. 4.7b). The strontium evolution lines of the Monte Rosa whiteschists roughly intersect at around 40 to 50 Ma, indicating a partial homogenization of the strontium isotopic system during Alpine times probably related to fluid infiltration during the late-Alpine, greenschist-facies metamorphism. This localized fluid infiltration leads to heterogenous, partial homogenization of the strontium isotopic system within the whiteschist. This heterogeneity is given by the highly variable intersections of the whiteschist evolution lines with the evolution lines of the Monte Rosa granite (Fig.

4.7b). Nevertheless, a pre-Alpine age estimation of the hydrothermal alteration is suggested, because calculation of a single, high-pressure related hydrothermally alteration of the granite at approximately 50 Ma did not result in those high strontium isotopic ratios observed in the whiteschist today. Therefore, at least two events are needed to explain the observed strontium isotopic signature in the whiteschists.

#### **4.8 Conclusion**

The results of the *in-situ*  $^{40}\text{Ar}/^{39}\text{Ar}$  UV-laser ablation analyses obtained during this study demonstrate the existence of argon isotopic gradients on the micrometer scale within phengites of two samples from a talc-kyanite-chloritoid-bearing shear zone within the Monte Rosa granite. Those gradients are due to mica recrystallization under relatively dry high-pressure metamorphic conditions during Alpine orogeny. The apparent lack of fluid mobility during high-pressure metamorphism contributes to the evolution of the shear zone as a locally closed system for the argon isotopic system. The observed highly variable pre-Alpine  $^{40}\text{Ar}/^{39}\text{Ar}$  ages observed in both samples are the result of partial loss of radiogenic argon from the system during late-Alpine, greenschist-facies metamorphism. Therefore, our data support the hypothesis that argon isotopic mobility is limited under relatively dry high-pressure metamorphic conditions, which are characterized by the lack of infiltration of external derived fluids. Partial homogenization of the strontium isotopic system of whole rock samples from different lithologies in the shear zone during Alpine metamorphism underscores the argon isotopic systematics as the result of late-Alpine partial loss of radiogenic argon. Therefore, the results of this investigation provide evidence that the argon isotopic system is more retentive than the strontium isotopic system under those conditions.

Our data provide a clear estimate that the evolution and behavior of the argon isotopic system under high-pressure metamorphism is a highly variable process characterized by a complex interaction of several processes. For a correct interpretation of argon geochronological data, several aspects as e.g. deformation, argon diffusivity, and especially fluid infiltration and its mobility, have to be evaluated carefully for a given sample with the help of high-resolution analyses techniques to identify small-scale isotopic and diffusional characteristics within individual samples. Therefore, it is not possible to explain the argon isotopic

signatures of a given sample by a generally applied „closure behavior“ for argon in metamorphic rocks which evolved under similar conditions.

#### ***4.9. Acknowledgements***

Fruitful discussions and support with the analytical facilities in Lausanne by N. Kramar and D. Giorgis are gratefully acknowledged. S.P. would like to thank A. Hofmann for access to the analytical facilities at the Max-Planck-Institute for Chemistry, Department of Geochemistry (Mainz). W. Todt and U. Poller are thanked for support with the analytical facilities in Mainz and constructive discussions. This research was supported by the German Science Foundation (Graduiertenkolleg GK392/1).

## *Chapter 4*

### *4.10 Tables*









## Chapter 4

**Table 4.2**  $^{40}\text{Ar}/^{39}\text{Ar}$  analytical data for *in-situ* UV-laser ablation analysis of white micas from two shear zone samples. Data are corrected for blank, radiogenic decay and interfering Ca-, K- and Cl-derived isotopes. Error of age is at  $1\sigma$  level.

RunID#	$^{40}\text{Ar}$ ( $\times 10^{-16}$ mol)	+ $^{40}\text{Ar}$	$^{39}\text{Ar}$ ( $\times 10^{-18}$ mol)	+ $^{39}\text{Ar}$	$^{38}\text{Ar}$ ( $\times 10^{-20}$ mol)	+ $^{38}\text{Ar}$	$^{36}\text{Ar}$ ( $\times 10^{-19}$ mol)	+ $^{36}\text{Ar}$	$^{40}\text{Ar}/^{36}\text{Ar}$	$^{40}\text{Ar}^*/^{39}\text{Ar}$	Age (Ma)	$\pm$ $1\sigma$	
26	20UL-SL25	29.423	0.099	95.985	0.323	1.474	0.005	4.022	0.014	7315.70	29.67	240	12
27	20UL-SL117	45.184	0.287	210.215	1.334	405.226	2.572	5.148	0.033	8777.05	20.74	171	4
28	20UL-SL120	26.702	0.212	114.102	0.905	450.555	3.572	3.063	0.024	8719.00	22.56	185	7
29	20UL-SL35	50.328	0.137	156.744	0.427	59.508	0.162	6.674	0.018	7541.09	31.37	253	7
30	20UL-SL26	74.750	0.247	245.484	0.811	182.496	0.603	2.603	0.009	28718.64	30.06	243	4
31	20UL-SL36	49.573	0.227	208.608	0.955	74.692	0.342	2.220	0.010	22330.92	23.61	193	5
32	20UL-SL17	41.808	0.219	171.970	0.901	117.888	0.618	0.862	0.005	48504.78	24.16	198	5
33	20UL-SL32	47.353	0.214	194.431	0.877	163.054	0.735	0.852	0.004	55562.69	24.26	198	6
34	20UL-SL33	36.088	0.182	152.741	0.772	27.803	0.141	0.497	0.003	72566.38	23.53	193	7
35	20UL-SL116	82.462	0.239	273.010	0.790	737.627	2.135	0.015	0.000	5686156.72	30.13	243	3
36	20UL-SL27	49.091	0.226	164.509	0.759	65.293	0.301	0.452	0.002	108663.00	29.91	242	6
37	20UL-SL104	117.205	0.109	441.143	0.409	29.418	0.027	0.848	0.001	138151.23	26.60	216	3
38	20UL-SL28	41.336	0.255	175.729	1.085	166.939	1.031	0.431	0.003	95820.06	23.69	194	6
39	20UL-SL31	59.617	0.246	182.836	0.755	32.642	0.135	0.042	0.000	1402942.80	32.88	264	7
40	20UL-SL118	50.775	0.266	182.767	0.958	482.286	2.527	0.580	0.003	87531.08	28.33	230	5
41	20UL-SL5	9.778	0.129	38.366	0.505	—	—	21.961	0.289	445.25	14.28	119	8
42	20UL-SL3	22.420	0.190	68.467	0.582	1.481	0.013	20.556	0.175	1090.66	32.60	262	15
43	20UL-SL4	36.411	0.321	102.860	0.907	26.463	0.233	22.775	0.201	1598.73	35.04	280	10
44	20UL-SL2	34.060	0.288	109.491	0.925	6.023	0.051	15.220	0.129	2237.83	30.19	244	4
45	20UL-SL1	83.737	0.452	270.681	1.462	291.868	1.577	1.625	0.009	51522.72	31.63	254	4

Dashes indicate values at or below the blank values.

**Table 4.3** Rb-Sr data of whole rock samples from the shear zone

Sample	Rb (ppm)*	Sr (ppm)*	$^{87}\text{Rb}/^{86}\text{Sr}$	$\pm ^{87}\text{Rb}/^{86}\text{Sr}$	$^{87}\text{Sr}/^{86}\text{Sr}$	$\pm ^{87}\text{Sr}/^{86}\text{Sr}$
<i>Granite</i>						
98SL133	248	124	5.802402	0.122217	0.735778	0.000016
99SL125	183	116	4.575723	0.096379	0.733153	0.000011
99SL159	225	110	5.934429	0.124998	0.736045	0.000011
<i>Granitic Gneiss</i>						
99SL115	226	15	43.96935	0.926135	0.796260	0.000062
99SL118	200	84	6.911287	0.145574	0.741217	0.000030
99SL119	177	20	25.7923	0.543268	0.782354	0.000030
99SL127	289	20	42.049780	0.885703	0.766935	0.000018
99SL128	174	69	7.327510	0.154341	0.751803	0.000773
99SL153	188	55	9.925469	0.209062	0.744705	0.000014
<i>Whiteschist</i>						
98SL132	200	11	53.15938	1.119706	0.815501	0.000086
99SL110	235	18	38.11048	0.802728	0.799020	0.000013
99SL120	191	19	29.3348	0.617884	0.795559	0.000024
99SL121	205	14	42.80366	0.901582	0.813419	0.000005
99SL140	197	8	72.05005	1.517604	0.823008	0.000101
99SL149	92	16	16.75503	0.352914	0.780706	0.000009
99SL152	183	12	44.54521	0.938264	0.805720	0.000015

\* values derived from XRF measurement

## *Chapter 4*

### *4.11 Figures*

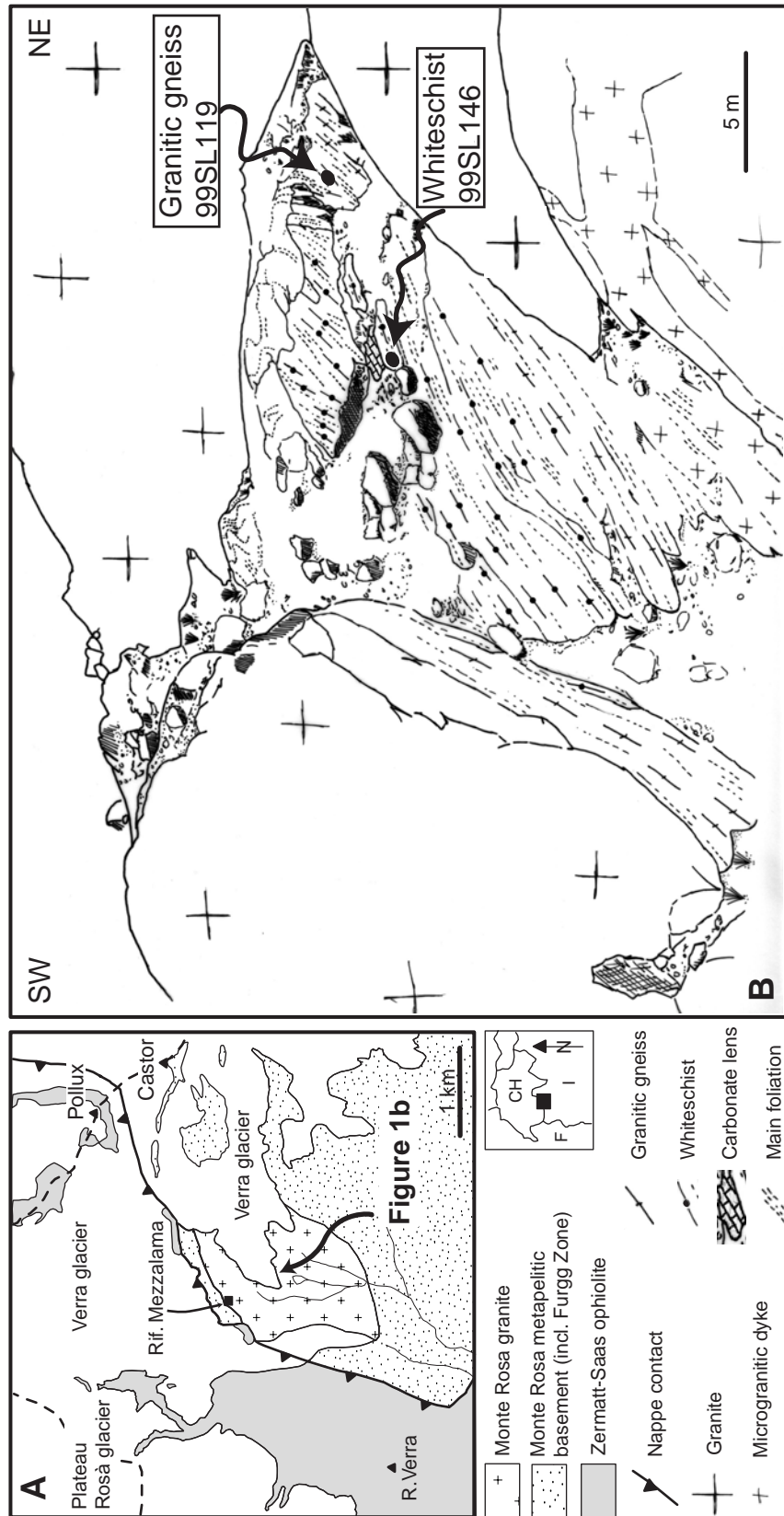


**Figure 4.1** (A) Simplified geological map of the upper Val d' Ayas, Italy (redrawn from Bearth (1952)). (B) Detailed sketch of the investigated shear zone within the Monte Rosa granite. Locations of the two samples analyzed by microprobe and *in-situ*  $^{40}\text{Ar}/^{39}\text{Ar}$  UV-laser ablation during this study are given.



**Figure 4.2** Line drawings of investigated parts of the thin sections to illustrate the microstructural characteristics and the distribution of microprobe analyses points which are given in table 4.1. (A) White-schist (sample 99SL146) from the center of the shear zone. Retrogression of the high-pressure metamorphic assemblage (ky+Mg-cld+phe±qtz±rt) into msc+Mg-chl is developed around large aggregates of ky+Mg-cld. The main foliation is defined by phe. (B) Granitic gneiss (sample 99SL119) shows the assemblage qtz+phe±Mg-chl±carb. The preferred orientation of phe and locally Mg-chl defines the foliation.



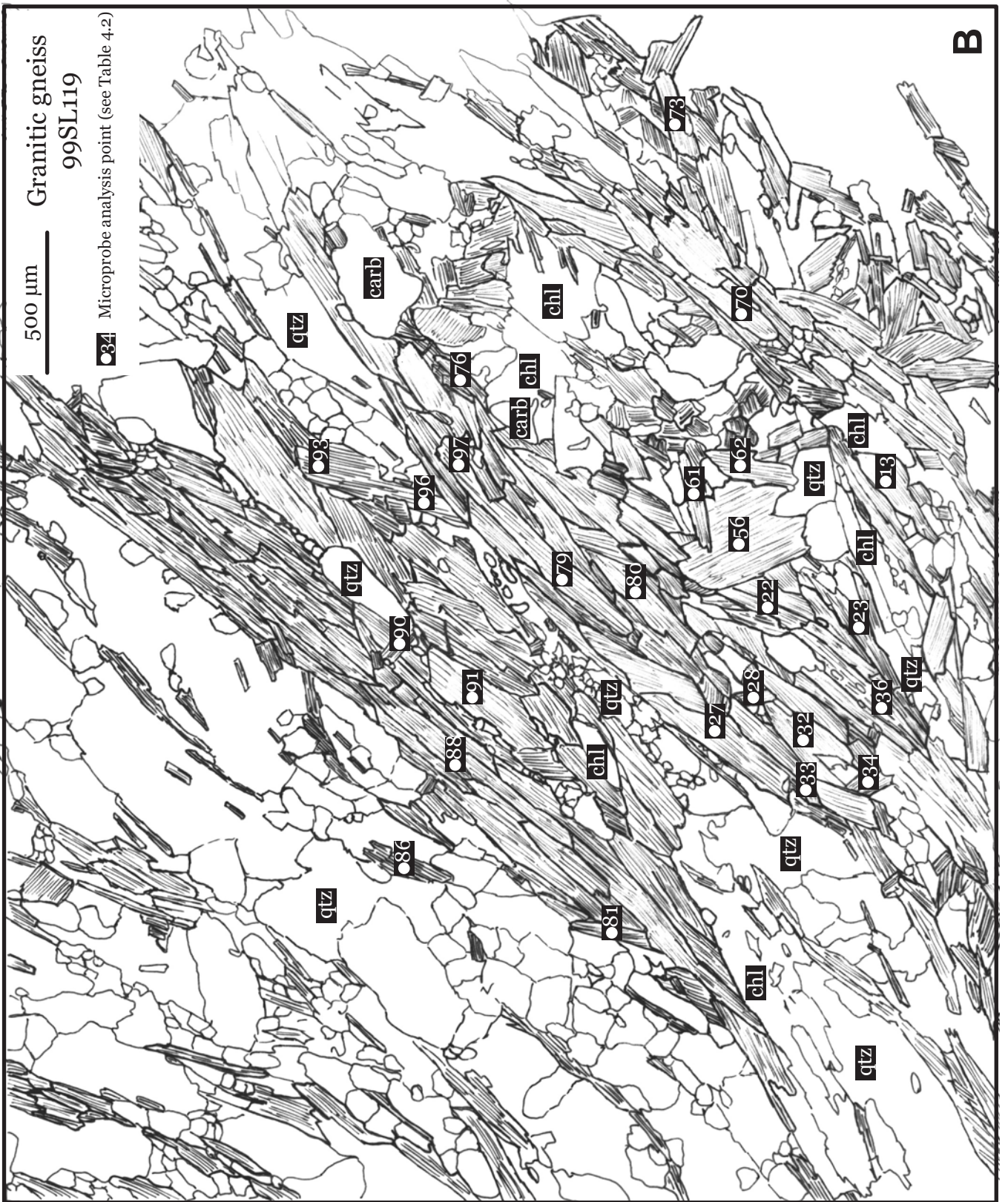
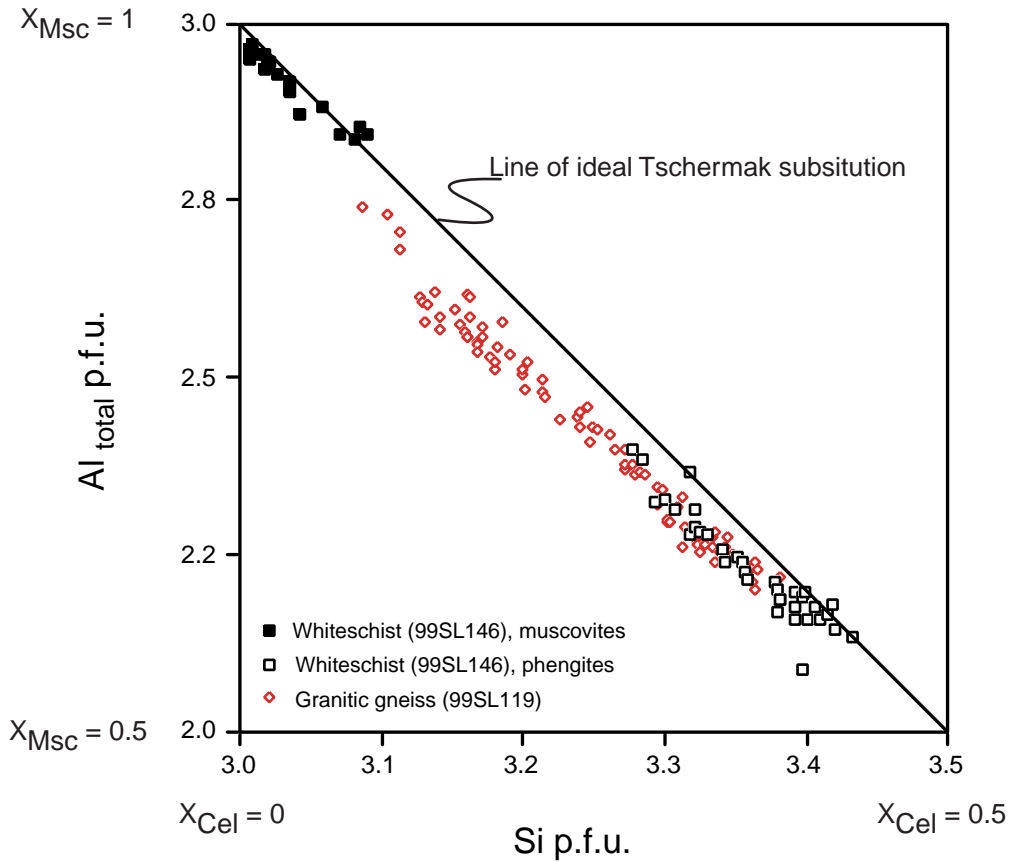
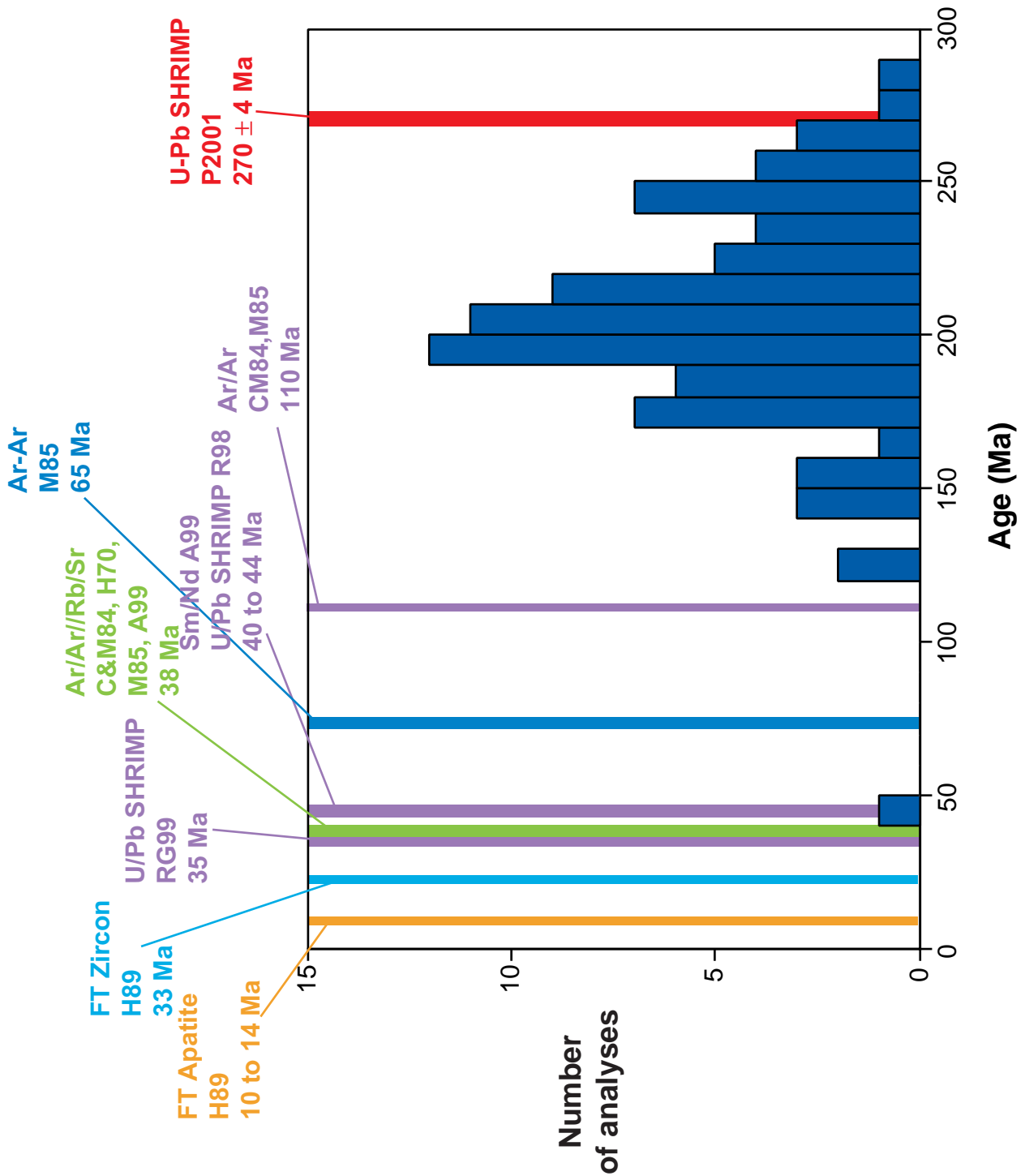


Figure 4.2 Continued.



**Figure 4.3** Compositional variations in the white micas of both investigated samples obtained from microprobe analyses. The plot Si versus  $Al_{total}$  (atoms p.f.u.) shows that nearly all analyses plot slightly below the line of the ideal Tschermak substitution due to small amount of  $Fe^{3+}$  and Ti replacing  $Al^{VI}$  in octahedral position. Two chemically different generations of white micas can be distinguished in the whiteschist (99SL146). The high-pressure phengites are indicated by the open boxes, whereas the retrograde muscovites are given by the filled boxes. In the granitic gneiss (99SL119) only one generation with a continuous variation of Si-content is observed.



**Figure 4.4** Histogram plot of the in-situ  $^{40}\text{Ar}/^{39}\text{Ar}$  UV-laser ablation data revealed from 80 individual analyses on white micas from the two samples of the shear zone (see Tab. 4.2 and Fig. 4.1). Literature data for the timing of intrusion of the Monte Rosa granite and of the Alpine metamorphic history are shown. H70: Hunziker (1970); CM84: Chopin and Monié (1984); M85: Monié (1985); H89: Hurford et al. (1989); R98: Rubatto et al. (1998); RG99: Rubatto and Gebauer (1999); A99: Amato et al. (1999); P2001: Pawlig et al. (subm.).



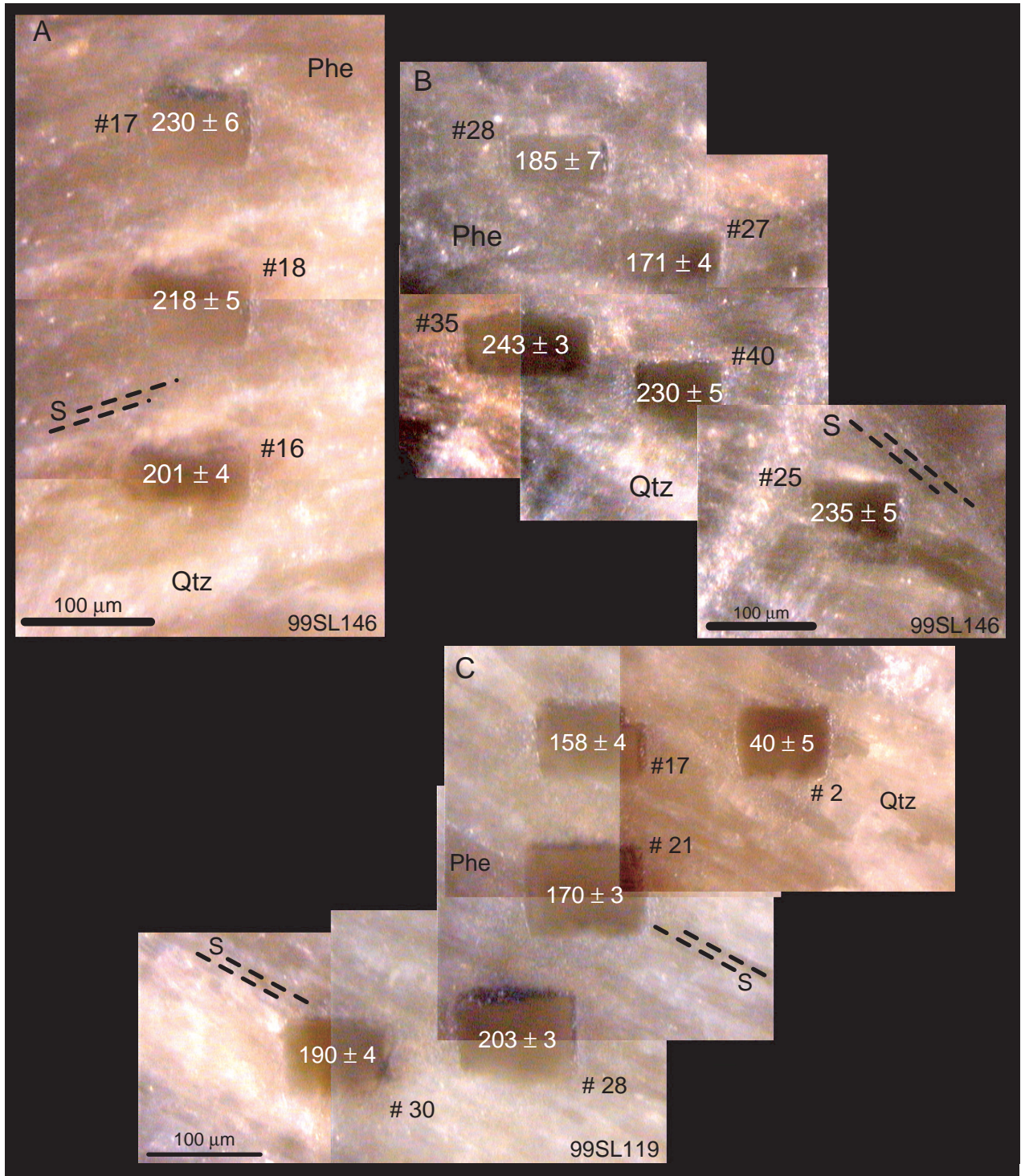


**Figure 4.5** CCD camera image of polished rock slabs showing the UV laser ablation pits in phengite after analyses. The analyzed phengites are located within the foliation. Direction of foliation is indicated. Numbers, e.g. #17, correspond to the analyses numbers given in table 4.2. For each ablation pit the obtained age and the  $1\sigma$  uncertainty is given. (A) Laser ablation pits within the whiteschist yielding pre-Alpine ages. (B) Five laser ablation pits located within the foliation of the whiteschist. Age variations of up to 60 Ma on a distance of 50  $\mu\text{m}$  are observed. (C) Five ablation pits across the foliation of the granitic gneiss. Pre-Alpine ages are obtained with age differences of up to 30 Ma on a distance of 50  $\mu\text{m}$ . Analysis #2 is located next to quartz, and due to low  $^{40}\text{Ar}/^{36}\text{Ar}$  ratio, this age may be contaminated by quartz and does not represent a reliable age. See text for further discussion.

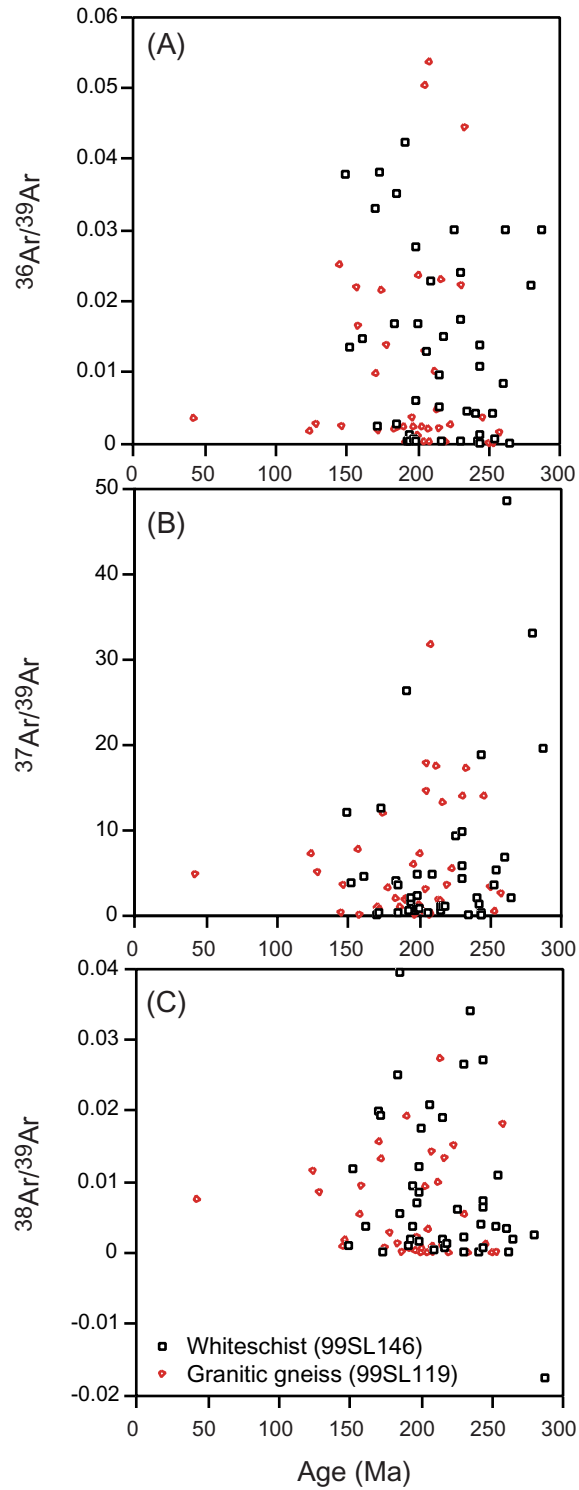


**Figure 4.6** Diagrams showing variations of (A) the  $^{36}\text{Ar}/^{39}\text{Ar}$  ratio versus  $^{40}\text{Ar}/^{39}\text{Ar}$  age; (B) the  $^{37}\text{Ar}/^{39}\text{Ar}$  ratio versus  $^{40}\text{Ar}/^{39}\text{Ar}$  age; (C) the  $^{38}\text{Ar}/^{39}\text{Ar}$  ratio versus  $^{40}\text{Ar}/^{39}\text{Ar}$  age in both samples.

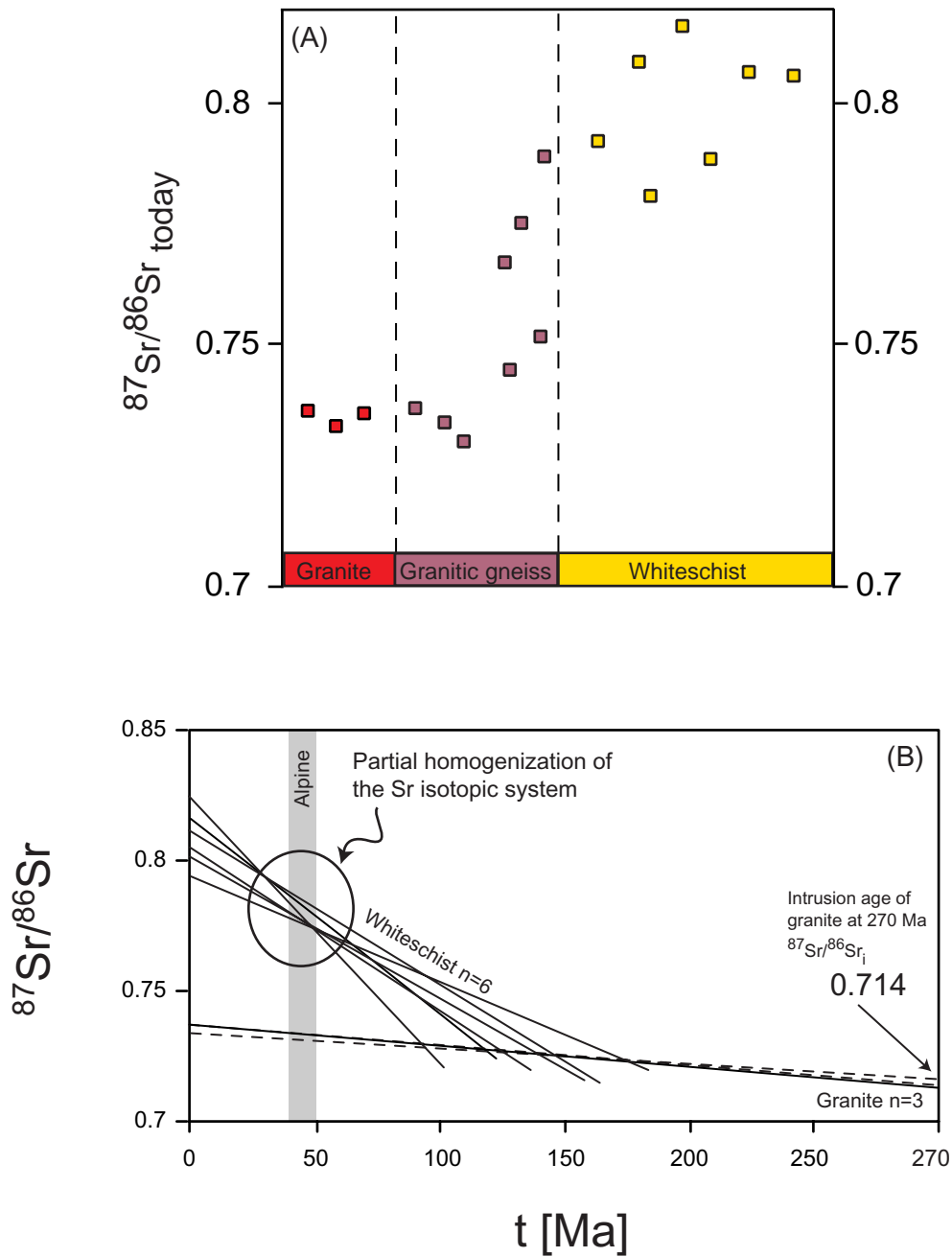


**Figure 4.7** (A) Diagram shows variations of the measured  $^{87}\text{Sr}/^{86}\text{Sr}$  ratios within whole rock samples of the different lithologies of the shear zone. The  $^{87}\text{Sr}/^{86}\text{Sr}$  ratios increase from homogenous crustal values in the granite to more radiogenic values in the granitic gneiss and finally to the most radiogenic values observed within the whiteschists. (B) Strontium evolution diagram showing a homogenous evolution of the Monte Rosa granite. In contrast, the strontium isotopic system is characterized by a partial homogenization during Alpine metamorphism. See text for discussion.

## Chapter 5

### Geochemistry of a talc-kyanite-chloritoid shear zone within the Monte Rosa granite, Val d' Ayas, Italy

*In honor of Prof. Martin Frey*

#### **5.1 Abstract**

Kyanite-talc-chloritoid-bearing rocks are exposed in a shear zone and other places within the Monte Rosa granite in the upper Val d' Ayas (Italy). Weakly deformed granite grades into progressively more deformed gneiss and whiteschist. A garnet-talc-chloritoid-calcite-pyrite-quartz boudin marks the center of this shear zone. The occurrence of weakly deformed whiteschists and discordant whiteschist-granite contacts indicates a pre-deformation origin of the whiteschist chemistry. Mass balance calculations were done in order to assess the nature and amount of mass transfer necessary to produce the whiteschist from a granitic protolith. The results indicate enrichment of Mg and H<sub>2</sub>O, with minor Si, Fe and K. Na, Ca, Sr, Ba, Pb and locally U are depleted. Stable isotope investigations on calcite from the carbonate zone in the center of the shear zone were performed to constrain the fluid source.  $\delta^{13}\text{C}$  values of calcite range from  $-9.60$  to  $-9.81$  ‰ (PDB), while their  $\delta^{18}\text{O}$  values range from  $+9.61$  to  $+10.14$  ‰ (VSMOW). These light isotopic values point towards a magmatic fluid source. We suggest that a pre-Alpine argillitic alteration leads to a chlorite-rich metasomatic alteration of the granite around gangue mineralization. Strain was localized during high-pressure metamorphism and subsequent exhumation into these rocks. This formed a deformational weak zone in the otherwise dry Monte Rosa granite. The presence of hydrous phases prior to metamorphism led to abundant recrystallization during high-pressure metamorphism.

**Keywords:** *Monte Rosa nappe, whiteschist, metasomatism, ISOCON, stable isotope geochemistry*

## 5.2 Introduction

Talc-chloritoid-kyanite-bearing rocks are found in discrete shear zones within the Late Permian Monte Rosa granite, Western Alps (Fig. 5.1a). Occurrences of these rocks in the Monte Rosa nappe were already described by Bearth (1952) and Dal Piaz (1971). Petrological investigations on those phengite-talc-chloritoid-chlorite-kyanite-quartz assemblages from the Monte Rosa nappe in the Val d' Ayas (Italy) were carried out by Chopin and Monié (1984), and Dal Piaz and Lombardo (1986), who reported a pressure of ca. 16 kbar at a temperature of 500°C for their formation at a water activity of approximately 0.6 during the Alpine eclogitic overprint. Recently, Le Bayon et al. (2000) suggested a considerably higher pressure of 25 kbar and a temperature of 580°C for the stability of the assemblage talc-chloritoid within rocks from the Monte Rosa nappe based on an assumed water activity of 0.6 during the Alpine high-pressure metamorphism. A sedimentary origin for those special rocks was suggested by Chopin and Monié (1984) for a piece of the float, whereas several authors proposed that these peculiar rocks resulted from pre- to early Alpine metasomatic transformations of the granitic protolith along high-pressure shear zones in the Monte Rosa granite (Bearth, 1952; Dal Piaz, 1971; Dal Piaz and Lombardo, 1986). Occurrences of similar rock types in the Alps have been reported from the Tauern Window of Austria, the Austroalpine nappes of the Eastern Alps (Hungary), and from the coesite-bearing rocks of the Dora Maira massif in the Western Alps (Abraham et al., 1974; Chopin et al., 1991; Sharp et al., 1993; Demény et al., 1997). Two different mechanisms have been proposed for the formation of Alpine whiteschists: high-pressure metamorphic overprint of Mg-rich evaporitic sedimentary protoliths (Chopin and Monié, 1984), and Mg-metasomatism of gneisses and mica schists along shear zones by metamorphic fluids (Sharp et al., 1993). A stable isotope study was presented by Sharp et al. (1993), in which they proposed that the metasomatic alteration was caused by ascending metamorphic fluids released from the subducted mafic to ultramafic material of the Tethyan oceanic crust of the downgoing slab.

This study focuses on the geochemical evolution of a shear zone containing whiteschists located in an otherwise weakly deformed part of the Monte Rosa granite in the upper Val d' Ayas (Italy). Field and petrographic observations described below provide clear evidence that the whiteschists are the result of a high-pressure metamorphic overprint of a hydrothermally altered granitic protolith and related microgranitic dykes. To constrain the nature and amount of the mass transport necessary to produce these special rocks from a granitic protolith, the approach of

Baumgartner and Olsen (1995) based on the ISOCON method after Grant (1986) and Gresens (1967) was applied. Using carbon and oxygen stable isotope geochemistry of calcite from a garnet-talc-chloritoid-calcite-pyrite-quartz zone located in the center of this shear zone, we address the potential fluid source and the evolution of these magnesian rocks within the shear zone.

### ***5.3 Geology and petrography of the talc-kyanite-chloritoid shear zone in the upper Val d' Ayas***

The shear zone investigated in this study is located in a weakly deformed part of the Monte Rosa granite in the upper part of the Val d' Ayas (Italy). It is located southeast of the Mezzalama refuge, at the southern end of the Verra glacier (Fig. 5.1b; 2796 m a.s.l.; coordinates 625.05/084.143, Swiss Reference Grid). The shear zone is up to 40 m wide, trends NW-SE and dips towards WSW (250/40). The weakly deformed granite grades into more deformed granitic gneiss and finally into a chloritoid-kyanite-talc-bearing whiteschist (Fig. 5.2; Fig. 5.3). Microgranitic dykes were rotated into the shear zone (Fig. 5.4a), indicating a downward movement of the hangingwall (top towards the SW). A small boudin (2.5 m x 1 m) containing garnet-talc-chloritoid-phengite-calcite-pyrite-quartz forms the center of the shear zone (Fig. 5.2). The orientation of both, the whiteschist and the carbonate boudin in the center, is slightly oblique to the generally NW-SE trending southwestern rim of the shear zone. Additionally, a discordant contact of the whiteschist with the Monte Rosa granite can be observed at the eastern rim of the shear zone, whereby the main foliation of the rocks clearly cuts the contact between the two different lithologies (Fig. 5.2). Two detailed profiles document sample location, lithological units and structural data (Fig. 5.3).

Weakly deformed, nearly massif lenses and boudins of chloritoid-talc-felses occur just below the carbonate boudin, indicating an initial near-static crystallization during high-pressure metamorphism. Shearing continued into the greenschist-facies, which is documented by some C-type shear bands containing chlorite, muscovite, and locally biotite in the whiteschist (Fig. 5.4d). The last structural elements within the shear zone are extensional quartz veins, along which intensive alteration of gneisses and whiteschists by chlorite, muscovite and some biotite are observed (Fig. 5.3, section C-D). These late quartz veins are at high angle to the shear zone. A similar succession of deformation fabrics and metamorphic assemblages is observed for the granitic gneisses. Sigma clasts of feldspar in the granitic gneiss (Fig. 5.4c) define a

downward movement of the hangingwall (top towards the SW), as do the C-type shear bands within the whiteschists (Fig. 5.4d). Elongate feldspar and white mica aggregates, as well as prismatic, broken tourmaline crystals define a SW-trending (220/40) stretching lineation in the gneiss (Fig. 5.3). The tourmaline lineation occurs within whiteschists and microgranitic dykes as well. Chlorite, low-celadonic white mica and minor biotite replace phengite, which defines the earliest foliation together with talc in the whiteschist. All structural elements, except the late quartz veins, document a top-to-SW sense of shear with downward movement of the hangingwall. The characteristics of the deformation fabrics within the different lithologies, i.e. within the granitic gneiss and the whiteschist, demonstrate that deformation in the shear zone prevailed continuously from at least the last stages of high-pressure metamorphism to the greenschist-facies overprint.

The weakly deformed, slightly foliated Monte Rosa granite shows a well preserved igneous texture which is dominated by large K-feldspar blasts, large biotite and muscovite flakes, and quartz. Igneous plagioclase is replaced pseudomorphically by aggregates of fine-grained phengite, garnet, clinozoisite, and fine-grained albite. Relic magmatic biotite locally contains sagenite inclusions. Biotite is either overgrown by fine-grained phengite at its rims or, locally replaced by chlorite. Accessory apatite, ilmenite (partially rimmed by titanite), zircon, monazite, xenotime and tourmaline are common. Weakly deformed dykes occur, characterized by a granoblastic texture, consisting of quartz, plagioclase, muscovite, phengite, clinozoisite, small garnet, as well as minor tourmaline and zircon. Relictic, magmatic muscovite flakes are replaced by fine-grained phengite at the rim, whereas the plagioclase shows replacement by an assemblage of phengite-clinozoisite-garnet-albite, similar to that reported for the metagranite.

Metagranite grades within a few centimeters into the shear zone, which starts with two slightly different varieties of granitic gneiss: a dark gray and a red one. The main constituents of both varieties of granitic gneiss are large augen-like feldspar clasts, quartz, phengite, chlorite, and epidote. Small garnet displays atoll structures. Biotite can form thin rims on chlorite and phengite. Minor constituents and accessory phases include zircon, apatite, rutile and titanite. Small amounts of tourmaline occur locally within the red gneiss. Phengite, biotite and epidote are concentrated in layers, defining the main foliation of this rock type, or they wrap around feldspar clasts and oblate quartz aggregates. The two granitic gneisses form alternating layers in the cross section A-B. The red variety is largely of mylonitic character and mainly observed towards the center of the shear zone and in direct contact with the whiteschist in section C-D (Fig. 5.3).

Whiteschists contain the assemblage kyanite-talc-chloritoid-phengite-quartz, with minor amounts of rutile, tourmaline, pyrite, monazite, and zircon. Phengite and talc define the first foliation. The chloritoid-porphyroblasts are up to one cm in size and chloritoid is sometimes intergrown with kyanite to form large aggregates that are also up to one cm in size. This assemblage is partially replaced by the assemblage of chlorite-muscovite and sometimes biotite. Tourmaline occurs either as small grains, or as prisms defining the lineation. Two different protoliths for the whiteschist can be distinguished in the field. One clearly has a granitic protolith and is characterized by large chloritoid, whereas the other, very light variety, with only minor chloritoid, originates from microgranitic dykes. They are separated by sharp contacts parallel to the direction of the shear zone.

In the center of the shear zone, a sulfide-bearing carbonate boudin has been found (Fig. 5.2, 5.4b). It is only slightly foliated, found in sharp contact to whiteschists and oriented parallel to the foliation of the whiteschists, which is slightly oblique to the shear zone. The sharp contact to the whiteschists suggests that the carbonate boudin represents a vein mineralization. It contains the assemblage chloritoid-talc-garnet-phengite-quartz-calcite-pyrite±chalcopyrite. Pyrite and chalcopyrite occur as stringers within the carbonate boudin. Accessory phases are monazite, allanite (from 100 µm to several cm in size), zircon and rutile. Massive, nearly pure carbonate layers with minor quartz and phengite show a sharp contact to layers rich in quartz, chloritoid, garnet, phengite, talc and pyrite with minor carbonate. Talc and phengite define the slight foliation of the samples. They are bent around large chloritoid and garnet crystals. Signs of greenschist-facies retrogression within the carbonate boudin are given by the presence of chlorite, muscovite, and incipient biotite, which occurs as narrow rims around the phengites. Textural relationships of monazites imply that they formed or recrystallized during Alpine metamorphism. They are mainly found within the foliation and occur either as large, single grains or as a number of small grains pseudomorphically replacing larger ones. Several large, unzoned monazite grains from a sample of the carbonate zone yielded  $^{208}\text{Pb}/^{232}\text{Th}$  ages between  $39 \pm 0.9$  and  $31.6 \pm 0.7$  Ma (Scherrer, 2001), and thus provide clear evidence for monazite recrystallization within the shear zone during Alpine metamorphism and deformation.

Combining the textural and geochronological observations of monazites from the carbonate zone with field and petrographic observations from the whiteschist and granitic gneiss it is therefore clear that the shear zone is of Alpine age and provides essential evidence of a high-pressure metamorphic overprint within the Monte Rosa nappe.



#### **5.4 Analytical methods**

Whole rock chemical compositions were determined by XRF measurements. Samples were crushed and powdered in a tungsten carbide mill. Major element concentrations were measured on glass pellets, while trace elements were determined on powder pellets, using a Philips PW 1400 spectrometer with a rhodium X-ray tube. LOI (loss on ignition) was calculated from weight loss by heating whole rock powders to 1000 °C for at least two hours. LOI is assumed to be H<sub>2</sub>O, since the shear zone rocks, with the exception of the carbonate zone within the center of the shear zone, do not contain any CO<sub>2</sub>-bearing minerals. The mean for each sample population is given in table 5.1 with the 1 $\sigma$  standard deviation, calculated from multiple samples of each rock population. The numbers of samples varies between 3 to 8 for the different lithologies occurring within the shear zone (see Tab. 5.1).

<sup>18</sup>O/<sup>16</sup>O and <sup>13</sup>C/<sup>12</sup>C ratios were determined from CO<sub>2</sub>-gas, liberated from calcite by reaction with 100% phosphoric acid at 25°C. Isotopic ratios were analyzed with a VG ISOTECH-PRISM SERIES II mass spectrometer. All values are given relative to PDB standard for  $\delta^{13}\text{C}$  and VSMOW standard for  $\delta^{18}\text{O}$ , respectively. Uncertainties of the isotopic ratios for carbon and oxygen are 0.05 ‰ and 0.1 ‰ (1 $\sigma$ ), respectively. Stable isotope compositions of the analyzed samples are given in table 5.3.

#### **5.5 Mass balance calculations**

Quantitative mass balance calculations based on chemical data requires an assumption with respect to volume or mass change during the alteration process (Gresens, 1967; Grant, 1986; Baumgartner and Olsen, 1995). Typically it is not possible to obtain this information unequivocally from field observations, hence alternative routes are used. In the literature, the assumptions of constant volume or immobile elements are commonly used (e.g. Ague, 1994, 1997; Baumgartner and Olsen, 1995; Grant 1986; Olsen and Grant, 1991). Once a choice has been made, evaluation of mass transport is calculated with the approach of Gresens (1967), or its graphical simplification of Grant (1986). The graphical approach pioneered by Grant (1986) is referred to as the ISOCON method: The concentrations of the elements in the metasomatized rock are plotted versus the concentrations of the least-altered equivalent. The concentrations of all immobile species must lie on a straight line (Gresens, 1967; Grant, 1986):

$$c_i^A = \frac{M^O}{M^A} [c_i^O + \Delta c_i] \quad (1)$$

where  $M^O$  and  $M^A$  are the masses of the original and the altered rock in an equal-sized volume of rock, respectively;  $c_i^O$  and  $c_i^A$  are the concentrations of element  $i$  in the original and in the altered rock, respectively; and  $\Delta c_i$  is the mass change of element  $i$  during the alteration process. The line connecting all elements with no mass change ( $\Delta c_i = 0$ ) is called an ISOCON. Its slope,  $b = M^O/M^A$ , corresponds to the overall mass ratio, which resulted from the alteration process. A significant deviation of data points from the ISOCON is due to the mass change of the corresponding element during alteration. A mass ratio of one ( $b = 1$ ) demonstrates that no overall mass change has taken place during the alteration process, whereas  $b < 1$  indicates mass gain, and  $b > 1$  indicates mass loss. Baumgartner and Olsen (1995) presented a least-squares approach to the ISOCON method of Grant (1986) which takes into account the heterogeneity of the original (parent) and metasomatized (altered) rock population. The method is statistically rigorous, if the heterogeneities of the altered and the parent rock population are described either by a normal or a log-normal distribution. Also, its current implementation assumes that no correlation between the two populations is observed. In practice, inhomogeneities and analytical errors are evaluated through multiple analyses of different samples from one rock population. It is thus possible to obtain the associated uncertainties of the original and the altered rock population for each element. Since sample populations are typically too small to test for the type of distribution, a normal or log-normal distribution is assumed. Here, the results are presented in log-log diagrams, where the concentration of an element  $i$  in the altered rock  $c_i^A$  is related to the concentration in the original rock  $c_i^O$  by rearranging equation (1) to:

$$\log c_i^A = \log \frac{M^O}{M^A} + \log(c_i^O + \Delta c_i) \quad (2)$$

and hence for the ISOCON defining the immobile elements

$$y = \log \frac{M^O}{M^A} + \log c_i \quad (3).$$

The slope of the ISOCON in a log-log diagram is always one. The amount of overall mass change is given by the deviation of the intercept value of the ISOCON from the origin.

Mass balance calculations were performed for the alteration, using the Monte Rosa granite as the original rock type of the shear zone for calculations concerning the alteration towards the granitic gneiss and the whiteschist with granitic origin. The microgranitic dyke is the original rock type for the calculations of the alteration towards the whiteschist with microgranitic origin. The ISOCON was chosen, so as to have a maximum number of elements assumed to have low-solubility, and hence are most likely relatively immobile (Al, Ti, P, Zr, Sc, Y, V). The calculations were performed with the software package „ISOCON“ written in FORTRAN 77 (Baumgartner and Olsen, 1995). Whole rock chemical data as well as their 1 $\sigma$  uncertainty used for the calculations are given in table 5.1. Note that the data for the REE are especially in the whiteschist and in the microgranitic dykes close to or below the detection limit of the XRF.

An ISOCON plot for the alteration of the Monte Rosa granite to the dark gray variety of the granitic gneiss is shown in figure 5.5a. For this calculation, the element combination with the maximum number of the previously mentioned generally immobile elements (Al, Ti, P, Sc, Y, Zr, Nb, Th) was chosen to define the ISOCON. Some additional elements are compatible with this ISOCON as well (Tab. 5.2). The mass balance calculation results in an ISOCON with a mass ratio  $b = 1.0 \pm 0.1$ , which implies that no overall mass change has taken place during the alteration of the granite to the dark gray granitic gneisses. Most elements scatter around the ISOCON within their uncertainty. Only Mg, H<sub>2</sub>O, Fe and Ti plot slightly above the ISOCON, implying enrichment of these elements during the alteration process.

Figure 5.5b shows an ISOCON plot for the alteration of the granite to the red variety of the granitic gneiss. The red variety of the granitic gneiss is observed towards the center of the shear zone, often in direct contact with the whiteschist (Fig. 5.3). They are largely mylonites. The alteration to the red variety of the granitic gneiss is characterized by a gain in Mg and H<sub>2</sub>O, as well as a decrease in concentration of Na, Ca, Sr, Ba, Mn, Fe, and several other trace elements including U, Pb and Ce. The eighteen elements compatible with the ISOCON for the alteration from the Monte Rosa granite to the red granitic gneiss are given in table 5.2. The overall mass gain of 2% is within the uncertainty of the mass ratio  $b = 0.98 \pm 0.03$ .

Results of the mass balance calculation of the whiteschists with a granitic protolith are given in figure 5.5c, with 21 elements being compatible with the ISOCON (Tab. 5.2). Enrichment in Mg and H<sub>2</sub>O and depletion in e.g. Na, Ca, Sr and

Ba are indicated. An estimated overall mass gain of  $17 \pm 6$  percent is shown graphically by the displacement of the ISOCON along the x-axis. Our analysis shows that 12 elements are mobile, whereby Mg, Na and Ca changed the most during the formation of the whiteschist.

Mass balance calculation of the alteration from the weakly deformed microgranitic dykes to the whiteschists with presumed microgranitic origin is shown in figure 5.5d, together with the ISOCON. The compatible elements are given in table 5.2. Again, a similar alteration pattern can be observed, with an enrichment in Mg, Fe and H<sub>2</sub>O, whereas Na and Ca as well as Sr, Mn and Pb are strongly depleted (Fig. 5.5d). In contrast to the previous example, the displacement of the ISOCON in y-direction corresponds to a mass loss of  $15 \pm 9$  percent during the alteration process, mainly due to the large silica loss.

### **5.6 Stable isotope geochemistry**

The stable isotope compositions of carbon and oxygen of calcite from the carbonate zone located in the center of the shear zone were determined in order to constrain the possible origin of the fluids responsible for the hydrothermal alteration of the Monte Rosa granite. Three small samples (3 mm in diameter and 4 mm in depth) of the carbonate were drilled from sample 99SL124. They gave  $\delta^{13}\text{C}_{\text{PDB}}$  values of -9.60 to -9.87 ‰ and  $\delta^{18}\text{O}_{\text{VSMOW}}$  values of +9.48 to +10.14 ‰. Furthermore, two small samples (3 mm in diameter and 3 mm in depth) were drilled from the carbonate of sample 99SL144, which gave  $\delta^{13}\text{C}_{\text{PDB}}$  values of -9.70 to -9.81 ‰ and  $\delta^{18}\text{O}_{\text{VSMOW}}$  values of +9.61 to +9.82 ‰. In a diagram  $\delta^{18}\text{O}_{\text{VSMOW}}$  versus  $\delta^{13}\text{C}_{\text{PDB}}$ , the values of the two analyzed samples fall into the field typical of magmatic fluids (Fig. 5.7; Ohmoto, 1986; Sheppard, 1986).

### **5.7 Discussion**

From field evidence of the shear zone in the upper Val d' Ayas it is obvious that the protoliths for the whiteschists are the Monte Rosa granite and its microgranitic dykes. General geochemical characteristics of the alteration process from the Monte Rosa granite to the whiteschist are summarized in figure 5.6. The alteration increases towards the center of the shear zone. Mainly Mg, H<sub>2</sub>O and to a lesser degree K, Si and Fe are enriched, while Ca, Na, Ba, Sr, Pb were leached from

the Monte Rosa granite to form whiteschists. Hence, the fluid was characterized by a high activity of Mg, K and Si, but a low activity of Ca and Na. Initial chemical differences especially in the Si-content between the granitic and microgranitic protolith produce the apparent differences in the alteration process. Therefore, the difference between the two alterations is restricted mainly to the silica leaching for the production of whiteschists from their microgranitic dyke protolith resulting from those initially present bulk chemical differences (Fig. 5.6b).

The composition of the Monte Rosa granite and its dykes is fairly homogeneous (Tab. 5.1; Fig. 5.5). Similarly, the compositions of the gneisses are still very homogeneous and only slightly altered, while the composition of the whiteschists varies widely. Hence, the compositional heterogeneity of the whiteschists is due to the alteration process, and alteration was heterogeneous. Thus uncorrelated statistics, as assumed by the calculations, is adequate to compare the granite compositions with those of whiteschists. In contrast, the homogeneity in the composition of the granitic gneiss is probably correlated to that of the unaltered, fairly homogenous granite population. The possible correlation of uncertainties of the gneiss population mainly influences the uncertainty estimate of the fit, not so much the location of the ISOCON. Nevertheless, the calculations show that mass transport is definitely small for the change from granite to granitic gneiss.

Metasomatic alteration leading to the shear zone rocks took place either prior to or during high-pressure metamorphism, since the high-pressure assemblages are restricted to the altered rocks. Chopin et al. (1991) and Sharp et al. (1993) argued for syn-high-pressure metasomatism in the Dora Maira massif. They call on metamorphic fluids escaping from the downgoing slab during metamorphism to produce similar whiteschist. Nevertheless, field and structural evidence for a pre-Alpine metasomatic alteration of the granite chemistry is given from occurrences of undeformed to slightly deformed whiteschists within the Monte Rosa granite near the Mezzalama refuge in the upper Val d' Ayas. In this area, the chloritoid-talc-bearing rocks with minor kyanite occur as patches, irregular zones, and vein like structures within the Monte Rosa granite. Microgranitic dykes can locally be traced into the whiteschists as ghost structures while others are totally obliterated by the whiteschists. All foliation discordantly cuts the contact between the Monte Rosa granite and the whiteschists. Thus, clear evidence is given that the metasomatic alteration took place prior to the Alpine metamorphism and deformation.

Magnesium-rich fluids can easily be produced by metamorphism of ultramafic and mafic rocks of the downgoing slab. These fluids might be potassium-rich, because some of the source rocks contain biotite and phengite. A decrease in

temperature will eventually lead to silica saturation (Eugster and Baumgartner, 1987) and silica precipitation. Such fluids will most likely have a light oxygen isotopic signature, in agreement with those measured also for the Monte Rosa shear zone. From a structural point of view, Keller and Schmid (this volume) argue for a development of shear zones within the Monte Rosa nappe during Alpine eclogite-facies metamorphism. However, we prefer a pre-high-pressure metamorphic origin of the whiteschist chemistry, because of the light carbon isotopic values ( $\delta^{13}\text{C}$  from -9.60 to -9.87 ‰) measured in calcite from the carbonate zone in the center of the shear zone. Those light isotopic values for carbon are difficult to explain by metasomatic alteration due to metamorphic fluids, since possible source rocks for the carbon are sedimentary rocks, either of the Monte Rosa cover sequence or the Zermatt-Saas Zone, and those low  $^{13}\text{C}$  values would require organic carbon rich pelites. No graphite-bearing rocks as potential carbon-source have been reported from the Monte Rosa cover sequence (Dal Piaz, pers. comm.). Parts of the Zermatt-Saas Zone were subducted to greater pressures than the Monte Rosa nappe (Reinecke, 1998; Amato et al., 1999) and are thus potential source rocks for fluids, but oceanic sediments produce much heavier carbon isotope compositions than observed here (Ohmoto, 1986; Sheppard, 1986; Valley, 1986; Hoefs, 1987). Another potential fluid sources are ophiicarbonates from the overlying Zermatt-Saas Zone. Studies on ophiicarbonates from different units in the Penninic realm, on the high-pressure/low-temperature ophiolite of Corsica (France) and of high-pressure metamorphic marbles from Tinos (Cyclades, Greece) show heavy values for the  $\delta^{13}\text{C}$  (-6.3 to +3 ‰). This reflects the marine origin of the carbonate (Weissert and Bernoulli, 1984; Burkhard and O'Neil, 1988; Früh-Green et al., 1990; Driesner, 1993; Ganor et al., 1994; Pozzorini and Früh-Green, 1996; Matthews et al., 1999; Cartwright and Buick, 2000; Miller et al., 2001). The  $\delta^{18}\text{O}$  of calcite from the Corsican ophiolite sequence varies between +11.1 and +22.9 ‰ (Miller et al., 2001). They are similar to  $\delta^{18}\text{O}$  values of Corsican schistes lustrés (Cartwright and Buick, 2000), and imply the derivation of the calcite from sedimentary derived fluids (Miller et al., 2001). In fact, if the carbon of the Monte Rosa shear zone precipitated due to infiltration of a fluid derived from calcareous metasediments (i.e. schistes lustrés) during high-pressure metamorphism, the expected  $\delta^{13}\text{C}$  values of carbonate should be around -0‰, or even a mixture between magmatic and sedimentary  $\delta^{13}\text{C}$ . It is thus very difficult to produce the observed carbon isotope signature in the carbonate zone from fluids evolving from a subducted oceanic slab with accompanied oceanic sediments. Another interesting aspect of the ophiolitic high-pressure rocks of the Zermatt-Saas unit is, that many of the eclogites and blueschists are extremely sodium-rich (Ganguin, 1988)

due to fluid interaction during ocean-floor metamorphism. Fluids evolving from these eclogites and blueschists would most likely be quite sodium-rich, which could lead to sodium enrichment, rather than the observed depletion.

Therefore, the most likely cause of metasomatism leading to the precursors of the whiteschists is that of a late magmatic, hydrothermal alteration, which took place prior to Alpine metamorphism.  $\delta^{13}\text{C}$  values for hydrothermal gangue carbonate in ore deposits ranging from -6 to -9 ‰ are quite common (Ohmoto and Rye, 1979; Ohmoto, 1986). The observed assemblage carbonate-quartz-sulfide (pyrite/chalcopyrite) of the Monte Rosa shear zone is common in such rocks. Hence, the carbonate zone represents a late magmatic vein mineralization within the Monte Rosa granite (Figs. 5.7 and 5.4b). In particular, argillitic and potassic alteration (e.g. Meyer and Hemley, 1967) in a magmatic environment leads to the formation of chlorite-rich, potassium-rich rocks, which chemically are similar to the precursor for the whiteschists. No alteration of the magmatic stable isotopic signature of carbon and oxygen during Alpine metamorphic evolution has taken place. Thus, it is suggested that the shear zone has not been infiltrated by significant amounts of fluids during its Alpine metamorphic history.

Based on the above discussion, we suggest the following model for the formation of the Monte Rosa whiteschists (Fig. 5.8). The Monte Rosa granite intruded the high-grade metapelitic basement during Permian times ( $270 \pm 4$  Ma, Pawlig et al., *subm.*; Engi et al., *this volume*; Fig. 5.8a). The assemblage calcite-quartz-sulfide developed as a vein mineralization during late magmatic hydrothermal fluid activity of the Permian Monte Rosa granite. The hydrothermal fluid activity was probably related to post-Variscan processes as a consequence of post-orogenic uplift and extension (Finger et al., 1997; Pawlig et al., *subm.*). Juvenile fluids escaping in this extensional environment altered the surrounding Monte Rosa granite (Fig. 5.8b). So far, no indication of surface water precipitation in the hydrothermal system has been found. This implies that no surface water was available, either due to a relatively deep emplacement level of the pluton or the absence of significant surface waters. Those fluids caused the formation of chlorite- and sericite-rich assemblages from the granitic protolith, whereas calcium and sodium were leached. The presence of pre-existing hydrous minerals in the metasomatized zone and the mineral chemistry promoted the formation of the assemblage kyanite-talc-Mg-chloritoid within this zone during the Alpine high-pressure metamorphic overprint. The surrounding granite maintained its mostly igneous mineralogy due to dry conditions (Fig. 5.8c). The whiteschists might have helped to localize the shear zone. Protracted deformation during exhumation resulted in a partial greenschist-facies overprint of

the whiteschists. The shear zone probably remained active or was reactivated during the subsequent greenschist-facies Alpine metamorphism (Fig. 5.8d).

### ***5.8 Acknowledgements***

This research was supported by the German Science Foundation (Graduiertenkolleg GK392/1). S.P. would like to thank N. Groschopf for performing the XRF analyses. W. Lackmann kindly helped with the stable isotope measurements. This paper has benefitted from discussions and useful comments on earlier drafts by S. Piazzolo and A. Möller. The constructive discussions during the Monte Rosa field trip of the Swiss Mineralogical Society as well as the thoughtful reviews by A. Matthews and M. Engi are gratefully acknowledged and helped to significantly improve the manuscript.



## *Chapter 5*

### *5.9 Tables*

**Table 5.1** Chemical composition of the shear zone samples used for the mass balance calculations. Average compositions and their 1 $\sigma$  variability is shown for multiple samples of different shear zone lithologies.

Rock type Sample	Monte Rosa Granite				Dark grey variety of the granitic gneiss							
	98SL133	99SL125	99SL159	Mean	1 $\sigma$	98SL126	99SL118	99SL126	99SL129	99SL130	Mean	1 $\sigma$
wt%												
SiO <sub>2</sub>	69.77	70.46	70.5	70.24	0.41	70.37	69.83	70.42	69.8	70.76	70.20	0.47
Al <sub>2</sub> O <sub>3</sub>	15.3	14.93	14.73	14.99	0.29	14.72	14.89	14.64	14.61	14.55	14.67	0.15
Fe <sub>2</sub> O <sub>3</sub> *	2.66	2.88	3.03	2.86	0.19	3.18	3.07	3.06	3.14	3.12	3.10	0.04
MnO	0.05	0.05	0.05	0.05	0.00	0.05	0.05	0.06	0.05	0.05	0.05	0.00
MgO	0.74	0.78	0.82	0.78	0.04	0.86	0.85	0.85	0.87	0.83	0.85	0.02
CaO	1.57	1.79	1.68	1.68	0.11	1.76	1.65	1.79	1.71	1.73	1.72	0.06
Na <sub>2</sub> O	3.11	3.21	3.1	3.14	0.06	2.96	3.11	3.71	2.92	2.93	3.17	0.37
K <sub>2</sub> O	5.25	4.3	4.56	4.70	0.49	4.61	3.99	2.84	4.93	4.77	4.13	0.95
TiO <sub>2</sub>	0.41	0.44	0.47	0.44	0.03	0.5	0.51	0.48	0.49	0.48	0.49	0.01
P <sub>2</sub> O <sub>5</sub>	0.21	0.2	0.19	0.20	0.01	0.18	0.2	0.18	0.18	0.18	0.19	0.01
LOI	1.01	1.18	0.99	1.06	0.10	1.41	1.62	1.63	1.19	1.22	1.42	0.24
Total	100.06	100.23	100.12	100.14	0.09	100.6	99.77	99.66	99.89	100.62	99.99	0.43
ppm												
Sc	5	5	6	5.3	0.6	4	6	5	5	4	5	0.8
V	24	25	30	26.3	3.2	31	34	31	30	30	31.3	1.9
Cr	18	9	12	13.0	4.6	13	8	10	9	10	9.3	1.0
Co	51	41	42	44.7	5.5	26	27	26	38	40	32.8	7.3
Ni	7	5	4	5.3	1.5	9	7	7	7	6	6.8	0.5
Cu	8	10	7	8.3	1.5	6	8	5	11	7	7.8	2.5
Zn	54	48	53	51.7	3.2	59	58	46	59	59	55.5	6.4
Ga	19.3	17.6	19	18.6	0.9	18	19.2	18	18	19	18.6	0.6
Rb	248	183	225	218.7	33.0	209	200	151	214	224	197.3	32.4
Sr	124	116	110	116.7	7.0	103	84	108	109	105	101.5	11.8
Y	20	22	24	22.0	2.0	24	24	25	25	22	24.0	1.4
Zr	153	162	174	163.0	10.5	173	175	166	166	169	169.0	4.2
Nb	16	15	16	15.7	0.6	16	17	15	15	17	16.0	1.2
Ba	594	429	433	485.3	94.1	481	382	407	498	416	425.8	50.3
Pb	34.3	33.6	30.7	32.9	1.9	28.1	32.9	16.2	26.8	37.8	28.4	9.3
Th	14.3	15.9	14.3	14.8	0.9	17.4	16.6	15.3	16.5	16.4	16.2	0.6
U	4.3	4.7	4.7	4.6	0.2	4.2	3.1	4	3.8	4.5	3.9	0.6
La	25	27	32	28.0	3.61	28	31	27	31	28	29.0	1.9
Ce	43	49	59	50.3	8.08	59	61	56	63	60	59.8	2.6
Pr	7	10	8	8.3	1.53	6	9	5	8	9	7.4	1.8
Nd	24	27	27	26.0	1.73	28	32	27	30	28	29.0	2.0
Sm	4	8	5	5.7	2.08	5	6	7	5	5	5.6	0.9

\* Total Fe shown as Fe<sub>2</sub>O<sub>3</sub>; Fe<sup>2+</sup>/Fe<sup>3+</sup> not determined.

Table 5.1 continued

Rock type Sample	Whiteschists with granitic origin										Whiteschists with microgranitic origin									
	98SL130	98SL132	99SL26	99SL28	99SL29	99SL30	99SL31	99SL140	Mean	1 $\sigma$	99SL110	99SL120	99SL121	99SL150	99SL152	Mean	1 $\sigma$			
wt%	71.06	73.62	71.46	69.62	70.4	64.86	70.55	67.48	69.88	2.66	60.9	73.66	71.97	63.68	69.98	68.04	5.50			
SiO <sub>2</sub>	11.25	15.19	14.44	14.81	14.81	15.78	14.99	15.96	14.65	1.47	20.28	14.33	14.94	19.72	15.51	16.96	2.82			
Al <sub>2</sub> O <sub>3</sub>	4.22	0.8	1.29	1.47	1.39	3.5	1.62	3.36	2.21	1.28	1.58	1.46	1.77	1.49	1.08	1.48	0.25			
Fe <sub>2</sub> O <sub>3</sub> *	0.04	0.01	0.01	0.01	0.01	0.04	0.01	0.03	0.02	0.01	0.01	0.01	0.02	0.01	0.01	0.01	0.00			
MnO	8.21	2.38	4.64	5.3	4.96	7.76	5.11	4.39	5.34	1.87	5.23	2.6	2.74	3.81	4.11	3.70	1.08			
MgO	0.09	0.26	0.32	0.28	0.29	0.17	0.22	0.17	0.23	0.08	0.83	0.33	0.38	0.25	0.39	0.44	0.23			
CaO	0.04	0.31	0.77	0.71	0.81	0.17	0.28	0.15	0.41	0.31	0.34	0.32	0.32	0.41	0.24	0.33	0.06			
Na <sub>2</sub> O	1.31	4.51	3.7	3.75	3.73	3.28	3.62	3.77	3.46	0.93	5.45	3.97	3.84	5.91	4.33	4.70	0.93			
K <sub>2</sub> O	0.29	0.06	0.34	0.48	0.42	0.52	0.44	0.43	0.37	0.15	0.05	0.04	0.03	0.52	0.44	0.22	0.24			
TiO <sub>2</sub>	0.07	0.19	0.21	0.19	0.2	0.14	0.18	0.13	0.16	0.05	0.62	0.24	0.28	0.19	0.3	0.33	0.17			
P <sub>2</sub> O <sub>5</sub>	4.03	2.87	3.33	3.6	3.42	4.24	3.48	3.56	3.57	0.42	4.3	2.61	2.73	4.03	3.53	3.44	0.76			
LOI	100.6	100.2	100.51	100.52	100.46	100.47	100.51	99.43	100.34	0.38	99.6	99.58	99.03	100.01	99.92	99.63	0.38			
Total																				
ppm																				
Sc	5	3	6	7	4	8	7	8	6.0	1.9	3	2	1	6	4	3.2	1.9			
V	21	3	22	30	28	36	28	36	25.5	10.6	3	7	2	20	21	10.6	9.2			
Cr	5	0	8	9	7	10	5	16	7.5	4.6	0	0	0	11	11	4.4	6.0			
Co	26	23	17	20	23	19	24	16	21.0	3.5	10	28	35	25	23	24.2	9.1			
Ni	12	6	6	6	6	9	7	10	7.8	2.3	4	3	3	3	4	3.4	0.5			
Cu	4	1005	5	2	4	2	3	7	129.0	354.0	3	4	1	4	4	3.2	1.3			
Zn	23	515	16	17	17	20	14	18	80.0	175.8	14	19	32	9	8	16.4	9.8			
Ga	12	18	18	19	19	18	19	19.9	17.9	2.5	17.1	18.8	19.3	21	15	18.24	2.3			
Rb	63	200	173	168	171	157	160	197	161.1	42.6	235	191	205	270	183	216.8	35.7			
Sr	3	11	28	28	29	8	11	8	15.8	10.7	18	19	14	16	12	15.8	2.9			
Y	13	6	19	21	19	16	20	25	17.4	5.8	9	5	5	7	9	7	2.0			
Zr	109	22	120	171	150	173	148	123	127.0	48.5	26	27	26	195	167	88.2	85.3			
Nb	11	8	15	15	15	16	14	15	13.6	2.7	2	12	12	19	12	11.4	6.1			
Ba	43	117	90	104	92	87	86	97	89.5	21.4	130	115	100	161	105	122.2	24.5			
Pb	3.3	11.4	5.9	5	5.8	3.3	3.8	3.2	5.2	2.7	4.4	4.3	4	4.3	3.6	4.12	0.3			
Th	14	1	8.8	13.2	12.3	14.1	12.3	9.4	10.6	4.4	1.8	0.1	0	15.5	13.4	6.16	7.6			
U	2.7	0.9	1.7	2.7	2.1	2.8	3.8	2.7	2.4	0.9	0	0.7	3.7	0.8	0.2	1.08	1.5			
La	16	0	17	23	25	15	23	4	15.4	9.1	0	0	0	1	2	0.6	0.9			
Ce	34	0	28	45	43	30	38	0	27.3	17.8	0	0	0	0	0	0	0.0			
Pr	5	0	3	5	4	4	5	1	3.4	1.9	1	2	1	0	0	0.80	0.8			
Nd	17	0	15	23	23	14	21	5	14.8	8.4	2	0	0	0	1	0.6	0.9			
Sm	2	0	3	5	6	3	5	3	3.4	1.9	3	1	2	3	1	2	1.0			

\* Total Fe shown as Fe<sub>2</sub>O<sub>3</sub>; Fe<sup>2+</sup>/Fe<sup>3+</sup> not determined.

Table 5.1 continued

Rock type Sample	Red variety of the granitic gneiss										Microgranitic dykes									
	99SL119	98SL127	98SL128	99SL115	99SL127	Mean	1 $\sigma$	98SL134	99SL111	99SL112	99SL113	99SL116	99SL156	99SL157	99SL158	Mean	1 $\sigma$			
wt%	69.71	70.12	69.42	73.08	68.61	70.19	1.71	74.99	74.97	74.97	73.92	75.44	72.64	75.87	74.54	74.67	1.00			
SiO <sub>2</sub>	15.02	15.16	14.85	13.95	15.84	14.96	0.68	14.94	14.48	14.43	14.72	14.71	14.76	14.54	14.49	14.63	0.18			
Al <sub>2</sub> O <sub>3</sub>	1.73	1.69	1.91	1.19	1.79	1.66	0.28	0.86	0.67	0.69	0.58	0.86	1.04	0.64	0.89	0.78	0.16			
Fe <sub>2</sub> O <sub>3</sub> *	0.02	0.02	0.03	0.02	0	0.02	0.01	0.03	0.03	0.03	0.02	0.04	0.01	0.03	0.06	0.03	0.01			
MnO	5.09	3.72	4.38	3.03	4.02	4.05	0.76	0.23	0.09	0.1	0.09	0.13	2.44	0.11	0.09	0.41	0.82			
MgO	0.25	0.33	0.34	0.3	0.33	0.31	0.04	0.86	0.69	0.82	0.62	0.65	0.2	0.68	0.48	0.63	0.21			
CaO	0.22	0.11	0.11	0.81	0.11	0.27	0.30	4.15	3.97	4.13	3.85	6.21	0.48	4.88	4.14	3.98	1.61			
Na <sub>2</sub> O	4.21	5.76	5.78	4.92	6.06	5.35	0.77	2.5	3.97	3.29	5.22	1.75	4.37	2.16	3.85	3.39	1.19			
K <sub>2</sub> O	0.49	0.38	0.41	0.07	0.38	0.35	0.16	0.07	0.05	0.05	0.04	0.08	0.06	0.05	0.06	0.06	0.01			
TiO <sub>2</sub>	0.2	0.19	0.2	0.17	0.2	0.19	0.01	0.16	0.19	0.19	0.2	0.18	0.16	0.17	0.2	0.18	0.02			
P <sub>2</sub> O <sub>5</sub>	3.49	2.83	2.58	2.35	2.61	2.77	0.44	1.51	1.04	1	0.93	0.83	2.8	1.13	1.1	1.29	0.64			
LOI	100.43	100.31	100.00	99.89	99.98	100.12	0.23	100.28	100.14	99.7	100.18	100.85	98.97	100.26	99.9	100.04	0.54			
Total																				
ppm																				
Sc	6	7	4	3	5	5	1.58	3	3	2	2	3	5	3	2	2.9	0.99			
V	32	28	29	8	24	24.2	9.50	4	4	3	4	4	2	2	3	3.3	0.89			
Cr	10	6	7	d.l.	8	7.75	1.71	0	0	0	0	0	1	0	0	0.1	0.35			
Co	22	27	28	20	33	26	5.15	50	53	50	55	46	16	46	36	44.0	12.71			
Ni	6	6	6	4	6	5.6	0.89	3	2	2	3	2	1	2	3	2.3	0.71			
Cu	1	3	3	1	2	2	1.00	5	5	5	3	7	3	5	5	4.8	1.28			
Zn	17	27	33	24	28	25.8	5.89	28	21	9	15	21	11	15	37	19.6	9.30			
Ga	17.6	18	19	17	20	18.32	1.19	13	15	14.7	12	14.4	16	14	18	14.6	1.83			
Rb	177	267	292	226	289	250.2	48.68	88	163	139	195	78	178	88	284	151.6	69.60			
Sr	20	20	18	15	20	18.6	2.19	415	28	28	38	47	9	35	54	81.8	135.33			
Y	16	20	21	5	20	16.4	6.66	25	6	8	6	6	8	8	6	9.1	6.49			
Zr	165	139	159	23	142	125.6	58.40	23	17	17	14	25	23	21	31	21.4	5.40			
Nb	15	14	15	5	14	12.6	4.28	7	8	11	6	9	8	6	21	9.5	4.93			
Ba	128	285	223	193	270	219.8	63.10	116	25	14	31	162	107	48	35	67.3	53.82			
Pb	4.6	5.6	5.3	3.8	6.5	5.16	1.02	246.6	34	43.2	68.4	16.5	4.2	32.6	26.9	59.1	78.10			
Th	14.8	12.1	12.7	0.9	13.2	10.74	5.59	1.3	0	0	0	0.6	0	0.3	0.9	0.4	0.50			
U	1.3	2.1	2.9	0.1	3.4	1.96	1.31	2.9	1.5	3.3	1.9	3.5	0	2.3	9.5	3.1	2.81			
La	3	26	22	4	24	15.8	11.32	8	1	0	0	3	0	2	2	2.0	2.67			
Ce	0	49	49	0	46	28.8	26.32	11	0	0	0	0	0	0	0	1.4	3.89			
Pr	1	4	6	1	5	3.4	2.30	0	1	0	0	1	0	0	1	0.4	0.52			
Nd	4	24	26	0	25	15.8	12.70	5	1	1	0	2	0	0	2	1.4	1.69			
Sm	4	6	7	3	4	4.8	1.64	0	5	3	5	1	2	1	2	2.4	1.85			

\* Total Fe shown as Fe<sub>2</sub>O<sub>3</sub>; Fe<sup>2+</sup>/Fe<sup>3+</sup> not determined.

**Table 5.2** Combinations of immobile elements (x) compatible with the ISOCON. Mass balance calculations were done using the "ISOCON" software package (Baumgartner and Olsen, 1995). For each calculation, the ISOCON was chosen to have a maximum number of elements with generally assumed low-solubility (Al, Ti, P, Sc, Y, Zr, Nb, Th). Order of elements is similar to that in table 5.1. Note that mobile elements are outlined.

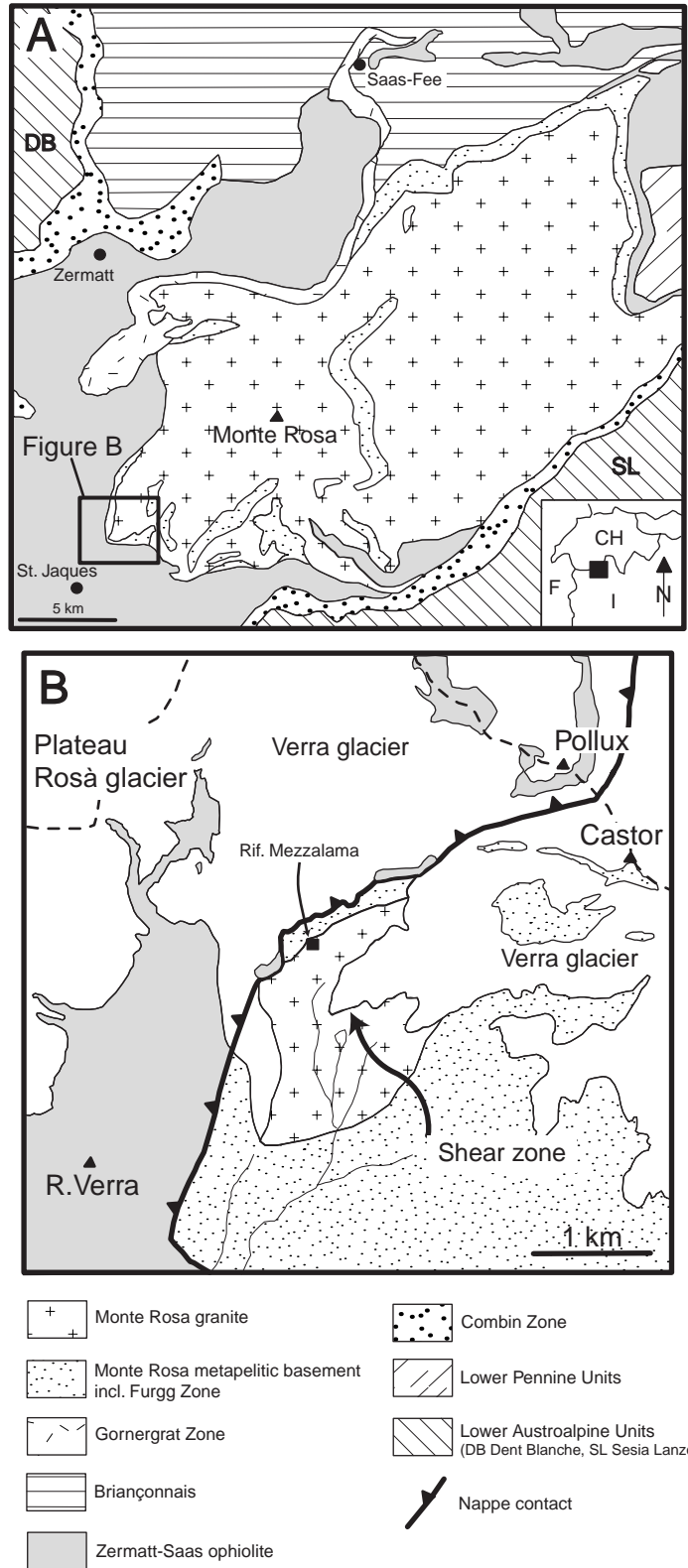
Element	Monte Rosa granite to Dark granitic gneiss	Monte Rosa granite to Red granitic gneiss	Monte Rosa granite to Whiteschist	Microgranitic dyke to Whiteschist
Si	x			
Al	x	x	x	x
Fe			x	
<b>Mn</b>				
<b>Mg</b>				
Ca	x			
Na	x			
K	x	x	x	x
Ti		x	x	x
P	x	x	x	x
<b>H<sub>2</sub>O</b>				
Sc	x	x	x	x
V		x	x	x
Cr	x	x	x	
<b>Co</b>				
Ni	x	x		x
Cu	x			
Zn	x			x
Ga	x	x	x	x
Rb	x	x	x	x
<b>Sr</b>				
Y	x	x	x	x
Zr	x	x	x	x
Nb	x	x	x	x
Ba	x			x
Th		x	x	x
Pb	x			
<b>U</b>				
La	x	x	x	x
Ce			x	
Pr	x	x		x
Nd		x	x	x
Sm	x	x	x	x

**Table 5.3** Stable isotope composition of carbon and oxygen of calcite from two samples of the carbonate lens from the center of the shear zone.

Sample #	$\delta^{13}\text{C}_{\text{PDB}}$ ‰	$\delta^{18}\text{O}_{\text{VSMOW}}$ ‰
99SL124-1	-9.6	10.14
99SL124-2	-9.68	9.48
99SL124-3	-9.68	9.63
99SL144-1	-9.70	9.82
99SL144-2	-9.81	9.61

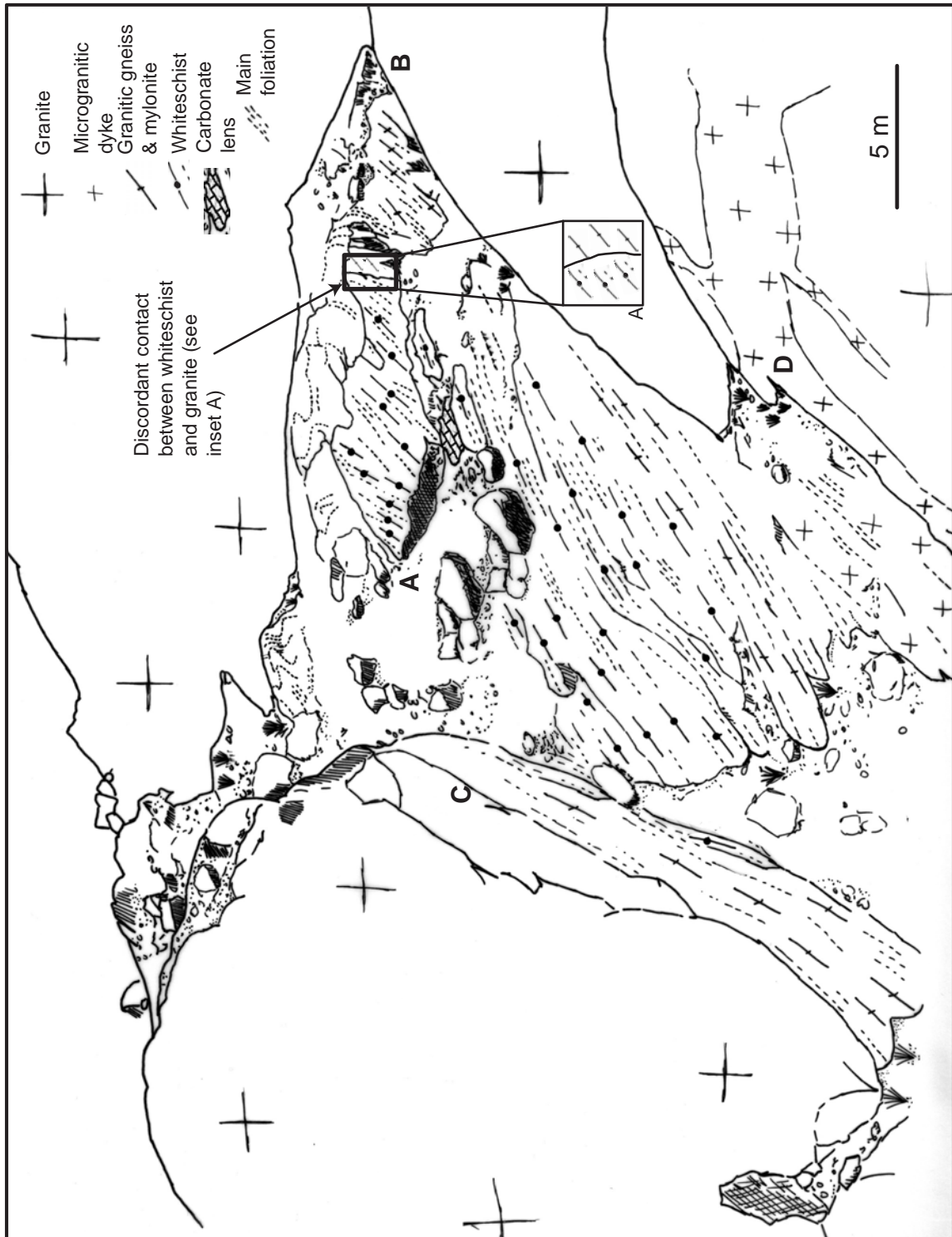
## *Chapter 5*

### *5.10 Figures*



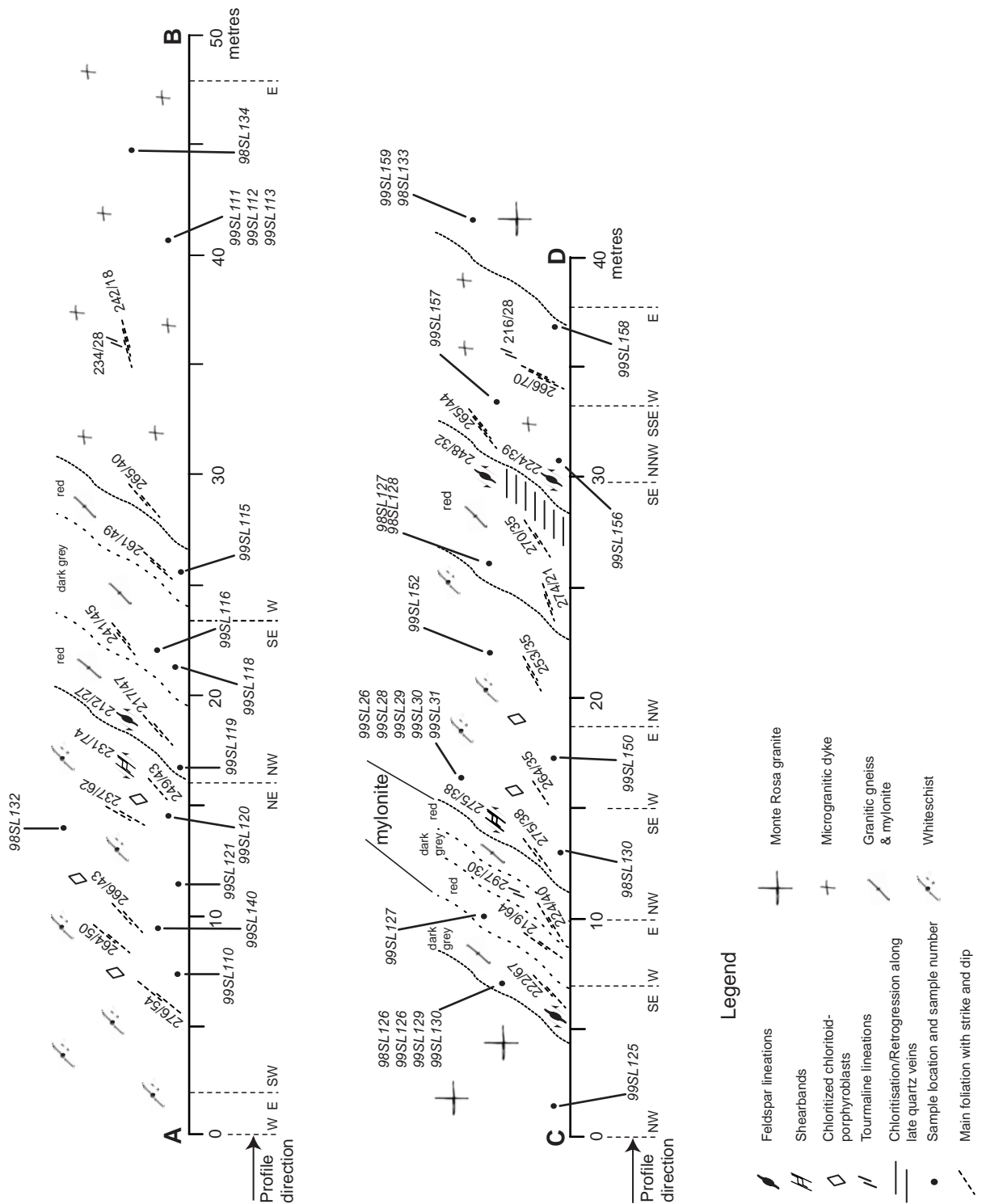
**Figure 5.1** (A) Generalized map of study area showing the Monte Rosa nappe and surrounding tectonic units (modified after Bearth, 1952). (B) Map of the upper Val d' Ayas indicates location of the shear zone (arrow). Modified after Dal Piaz (1971).



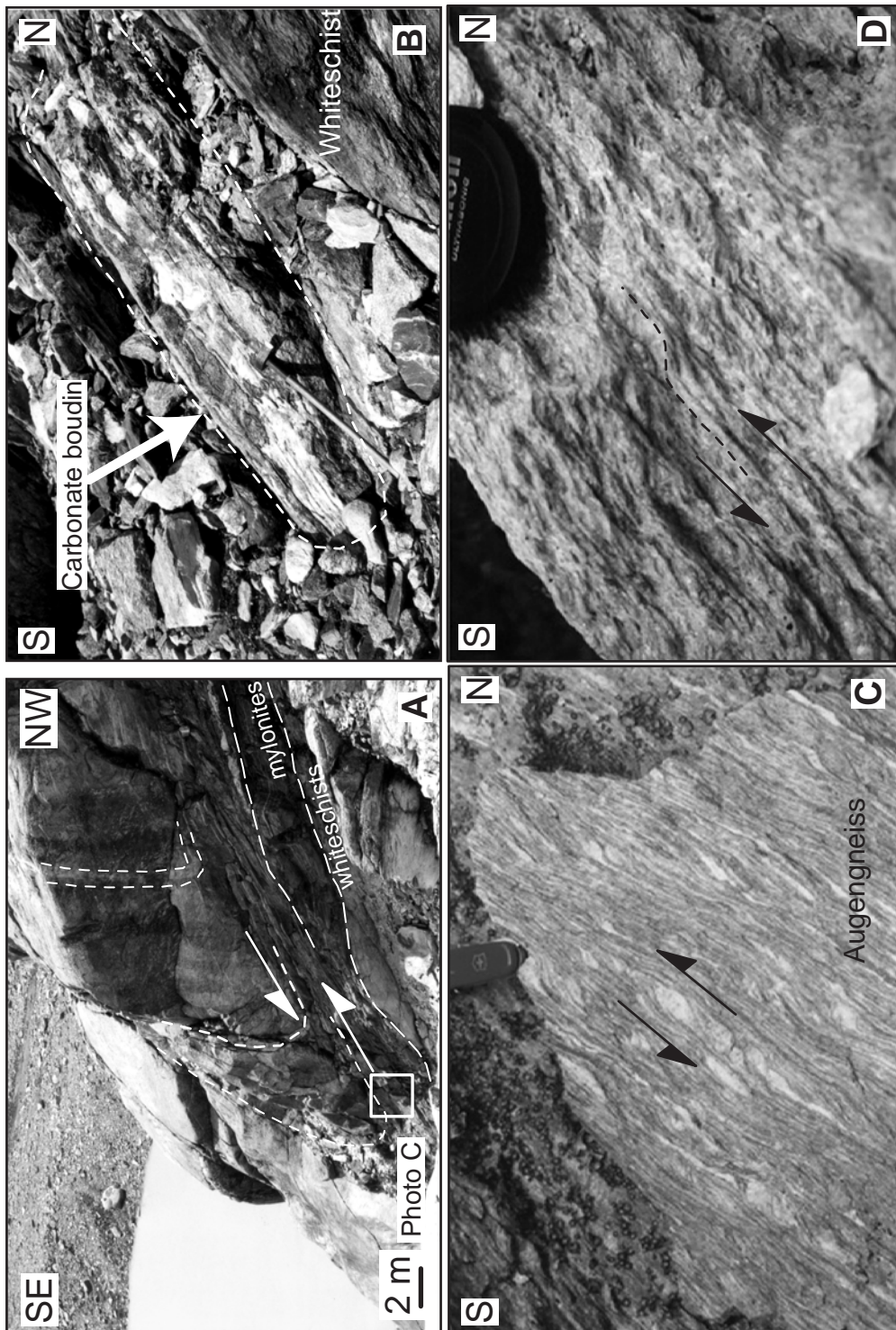


**Figure 5.2**

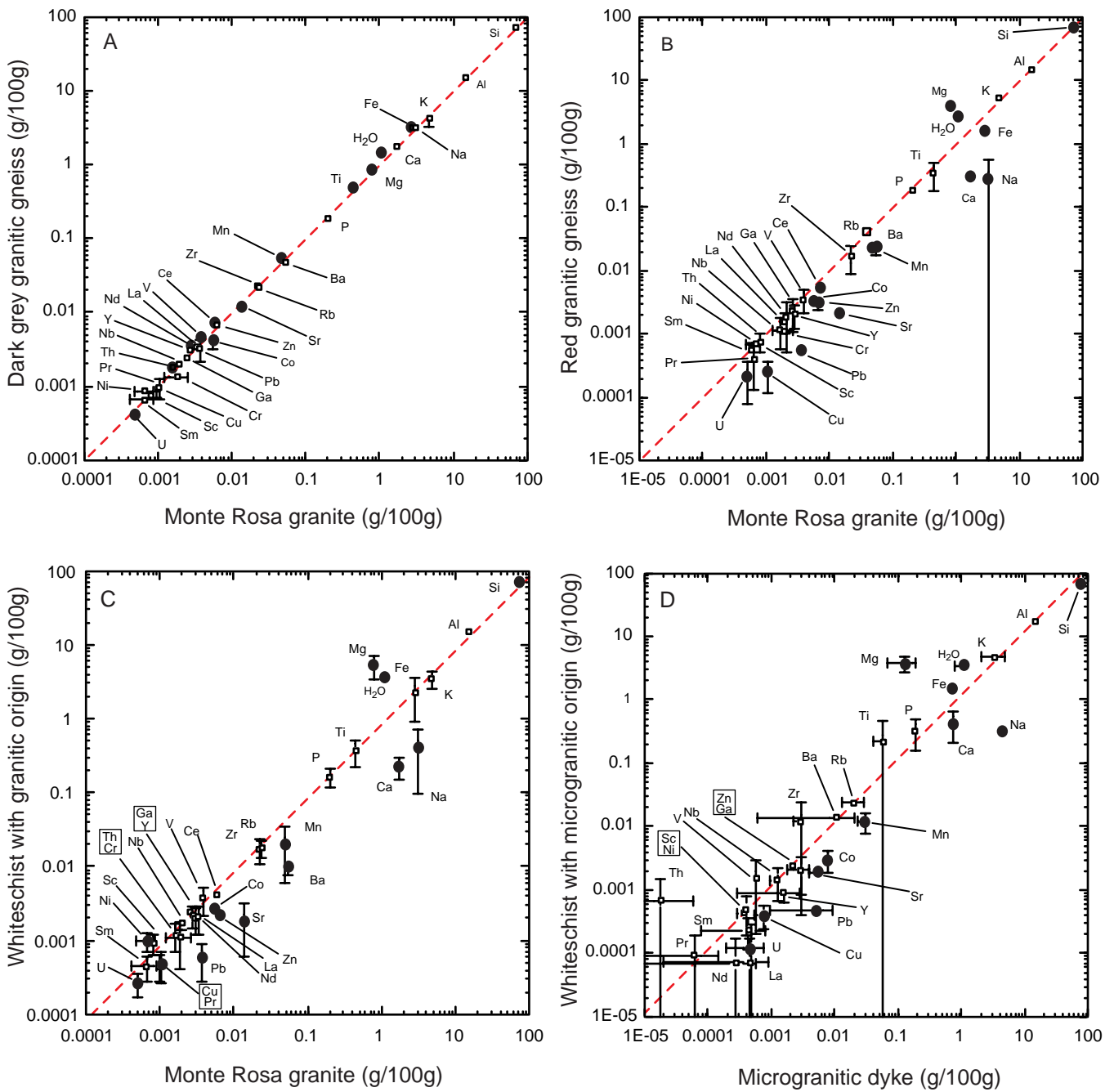
Sketch of the shear zone located at 625.05/084.143 (Ref. Swiss Grid). The view is towards NW. A and B indicate location of section 1; C and D the location of section 2. Note the carbonate boudin located just east of the center and the discordant contact between the whiteschist and the granite as indicated by the arrow. Detail of contact given in inset A.



**Figure 5.3** SW-NE cross sections locations indicated in figure 5.2 across the shear zone drawn with structural information and sample loctions. Section C-D in south-eastern part of the shear zone covers the whole sequence of rocks occurring within the shear zone, with the exception of the carbonate lens.

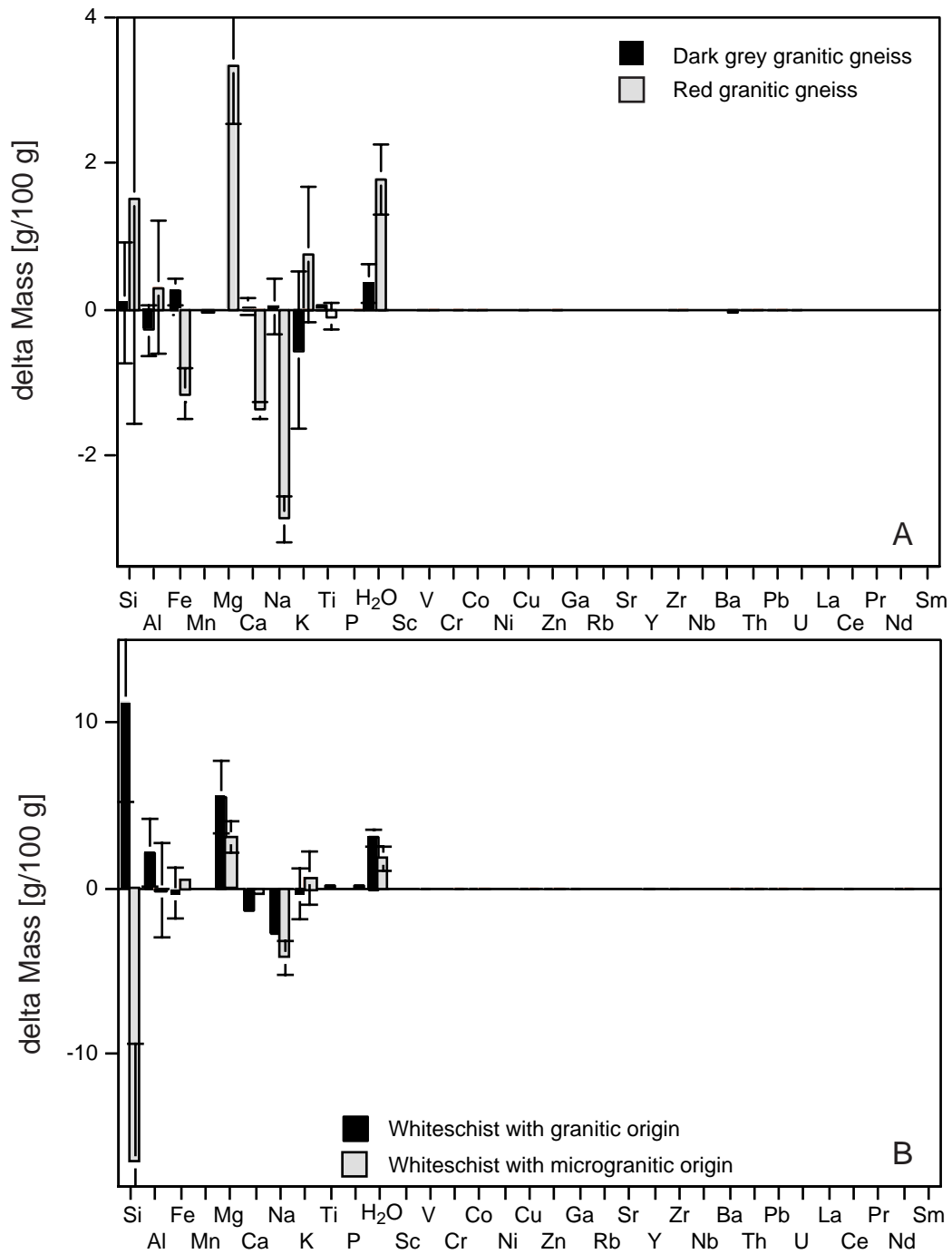


**Figure 5.4** Detailed photographs of the shear zone showing (A) The bottom of this wall shows strongly foliated whiteschists, followed upwards by a layer of mylonite. The microgranitic dykes are sheared into the augengneiss zone of the "grey" granitic gneisses (the locality of photo C is indicated); (B) central carbonate boudin (note hammer of 60 cm length for scale); (C) sigmoidal feldspar porphyroclasts in granitic gneiss in section C-D from western edge of the shear zone; (D) shear bands within whiteschist in section C-D.



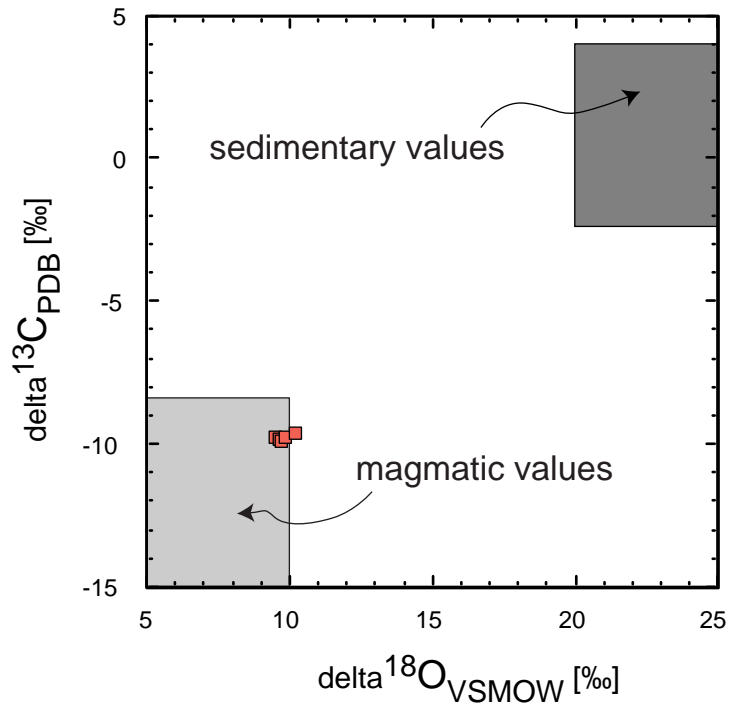
**Figure 5.5**

Isocon diagrams displaying results of mass balance calculations: (A) alteration of granite to dark gray variety of the granitic gneiss; (B) alteration to red variety of granitic gneiss; (C) alteration of granite to whiteschist with granitic; (D) alteration of microgranitic dyke to whiteschist with microgranitic origin. Dashed line in each diagram is best fit ISOCON. Whole rock chemical data are given in table 5.1. Mobile elements in each diagram are indicated by filled circles; immobile elements are shown as open squares. Error bars were calculated from multiple samples, and indicate rock population variability.



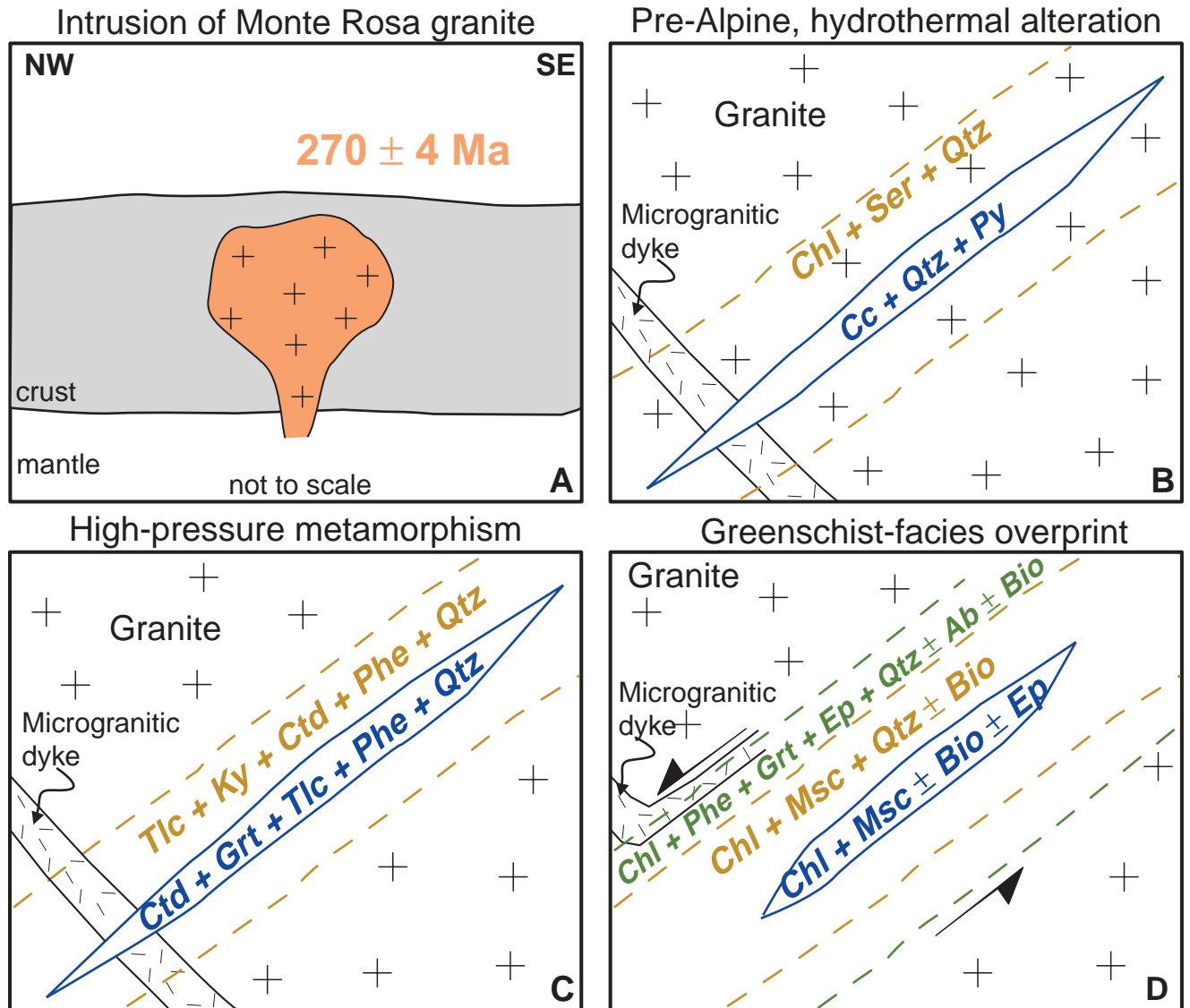
**Figure 5.6.** Calculated mass changes in % for (A) mass gains and losses of elements for both varieties of the granitic gneiss formed from the granite and (B) mass changes for both whiteschist-types formed from the granite and the microgranitic dyke, respectively. The difference between the two alterations is restricted mainly to the silica leaching.





**Figure 5.7**

The  $\delta^{18}\text{O}_{\text{VSMOW}}$  and  $\delta^{13}\text{C}_{\text{PDB}}$  values of calcite-bearing samples from the carbonate zone located within center of shear zone. Unusual, light oxygen and carbon values are most similar to igneous compositions. Values for reference fields of magmatic and sedimentary stable isotope signatures from Valley et al. (1986) and Hoefs (1987).

**Figure 5.8**

Schematic model (not to scale) of geochemical and structural evolution of the shear zone in upper Val d' Ayas, Italy. (A) Permian intrusion of the Monte Rosa granite (Pawlig et al., *subm.*; Engi et al., 2001). (B) Formation of Mg-rich bulk composition within Monte Rosa granite occurred during late-stage, hydrothermal fluid activity along veins. These were filled with gangue assemblage calcite-quartz-pyrite-chalcopyrite. (C) Alpine high-pressure metamorphism causes formation of whiteschists with assemblage talc-kyanite-chloritoid-phengite-quartz from the chlorite-rich, altered granitic protolith. The assemblage chloritoid-garnet-talc-phengite-quartz develops in the vein filling. (D) Strain localization during subsequent exhumation continued well into the greenschist-facies overprint.

## Chapter 6

### Chemical dating of monazite and fission track dating of apatite – Preliminary data

This chapter presents preliminary data on chemical age dating of monazite performed in collaboration with Dr. Nadim C. Scherrer and Prof. Dr. Martin Engi from the Institute of Mineralogy and Petrology, University of Bern, Switzerland, and preliminary results of fission track dating of apatite from granite samples collected at different structural positions within the Monte Rosa nappe. Dr. Meinert Rahn, Institut für Mineralogie, Petrologie und Geochemie, Universität Freiburg, performed the analyses. A short description of the techniques used and the obtained results is given.

#### **6.1 Chemical dating of monazite – an overview**

Monazite, a rare earth element phosphate with the general formula  $(\text{REE})\text{PO}_4$  occurs mainly as accessory phase in magmatic and metamorphic rocks. It is widely used for geochronological purposes either by isotopic dating techniques (e.g. Parrish, 1990; Bingen and van Breemen, 1998) or, recently, by chemical U-Th-Pb dating (Suzuki and Adachi, 1991; Montel et al., 1996; Scherrer et al., 2000). The chemical dating of monazite is based on its generally extremely high  $\text{UO}_2$  (from a few ppm up to 5%) and  $\text{ThO}_2$  (generally between 3 and 15%) contents. It generally does not incorporate appreciable amounts of common lead. Therefore, the measured PbO contents are assumed to represent the amount of radiogenic lead ( $\text{Pb}^*$ ) accumulated during radioactive decay of U and Th.  $\text{Pb}^*$  contents within a level to be measured with the electron microprobe are produced within 100 to 200 Ma (Montel et al., 1996; Scherrer et al., 2000). Apart from low financial effort compared to other micro-scale dating techniques (e.g. SHRIMP), micro-scale dating with the electron



microprobe on thin section scale provides the essential advantage of taking the textural relationship of each monazite into account during interpretation of the obtained age.

The procedure of chemical dating of monazite after Montel et al. (1996) consists of the measurement of the U-Th-Pb contents with the electron microprobe, and the calculation of the apparent age ( $\tau$ ) by iteratively solving the following equation (with the assumption that the common Pb content is negligible and no partial Pb loss has occurred):

$$Pb = \frac{Th}{232} \left[ \exp(\lambda^{232}\tau) - 1 \right] 208 + \frac{U}{238.04} 0.9928 \left[ \exp(\lambda^{238}\tau) - 1 \right] 206 + \frac{U}{238.04} 0.0072 \left[ \exp(\lambda^{235}\tau) - 1 \right] 207$$

where Pb, U and Th are given in ppm, and  $\lambda^{232}$ ,  $\lambda^{235}$  and  $\lambda^{238}$  are the decay constants of  $^{232}\text{Th}$ ,  $^{235}\text{U}$  and  $^{238}\text{U}$ , respectively.

For the microprobe measurements a lead-free polished sample is required to avoid contamination of the sample with common Pb. A recent study on the optimization of microprobe conditions by careful selection of X-ray peaks for the quantitative monazite analysis including the rare earth elements has been carried out by Scherrer et al. (2000).

Additionally, the new *in-situ* and non-destructing XRF-technique can be applied for the chemical dating of monazite (Cheburkin et al., 1997; Scherrer, 2001). For this technique, monazites which were previously quantitatively characterized by electron microprobe are separated from the thin section using micro-drill techniques, and are analyzed by energy-dispersive XRF-microprobe developed at the Institute of Mineralogy and Petrology of the University of Bern, Switzerland. For the description of the XRF-technique refer to Scherrer (2001). A gem quality monazite from Manangotry (Madagascar) served as standard. With this method, chemical ages of monazites can be obtained by determination of ratios between Th-U-Pb. The detection limit for the critical element Pb of the micro-XRF is around 2.5 ppm and therefore more suitable especially for the dating of young monazites (A. Cheburkin, pers. comm., 2000). The ages are calculated by an iteration similar to that used during chemical dating by electron microprobe (Suzuki and Adachi, 1991; Montel et al., 1996). A precision of approximately 5% ( $2\sigma$ ) has been achieved for the monazite standard FC-1 (age  $\approx$  55 Ma) at a spatial resolution of 90  $\mu\text{m}$  and a integration time of 90 minutes at 50kV and 30nA (Scherrer, 2001).

## 6.2 Monazites from the Monte Rosa nappe – Preliminary results

Several samples from the Monte Rosa granite and the kyanite-chloritoid-talc-phengite-bearing shear zone have been selected for chemical dating of monazite. The following samples were investigated during this study: 99SL159, 99SL122-1, 99SL139, 99SL145, 99SL148 and 99SL147. For sample localities and their description see Appendix A.

The Cameca SX50 electron microprobe at the Institute of Mineralogy and Petrology of the University in Bern (Switzerland) was used. Analyses were performed with an accelerating voltage of 25 kV, a sample current of 50 nA and a beam with a diameter of 5  $\mu\text{m}$ . For further information of the standard material used for calibration, counting times for peak and backgrounds see tables B3.1 and B3.2 in Appendix B3 which is attached to this thesis on CD-Rom. Repeated measurements of the monazite standard were done at the beginning and the end of each measurement period in order to check the quality of the calibration and to recognize eventually occurring analytical problems.  $\text{Al}_2\text{O}_3$  and FeO were measured during each analysis to control, if any neighbouring phase contributed to the analysis.

Microprobe analyses revealed rather low contents of  $\text{ThO}_2$ ,  $\text{UO}_2$  and PbO for the monazites of the Monte Rosa nappe. The  $\text{ThO}_2$  content varies between 0.46 and 12.31 wt% (Table B3.3 in Appendix B3). The  $\text{UO}_2$  content was corrected by deriving a correction factor using the following equation based on  $\text{UM}_\beta$  and  $\text{ThM}_\alpha$  lines (Scherrer et al., 2000):

$$\text{U wt\%}_{\text{corr}} = \text{U wt\%}_{\text{measured}} - (0.0052 * \text{Th wt\%}_{\text{measured}})$$

The corrected  $\text{UO}_2$  contents vary between 0.1 and 2.93 wt% (Table B3.3; Appendix B3). With only few exceptions (see Table B3.3), PbO was at or below the detection limit of the microprobe ( $<0.01$  wt.% PbO). The results of the chemical dating of the monazites are given in table B3.4 (Appendix B3). The Th-U-Pb ages for the monazite standard G7 and G1b have been routinely calculated and are included in Table B3.4, too.

After microprobe measurements, suitable monazites were separated from the thin sections for XRF-microprobe by the micro-drill technique as described by Scherrer (2001). Few grains of the Monte Rosa samples yielded mainly ages between  $38.1 \pm 11.5$  and  $88 \pm 16$  Ma when analyzed by micro-XRF (see Tab. 6.1). Eight grains separated from thin sections were also isotopically dated by LA-PIMMS (Laser Ablation Plasma Ionization Multicollector Mass Spectrometry; Parrish et al., 1999;

analyses were done by Dr. N.C. Scherrer at the British Geological Survey, Nottingham) with the isotopic  $^{208}\text{Pb}/^{232}\text{Th}$  dating technique. If single monazites were analyzed with both techniques, data coincide well and for a comparison of the isotopic data with the results obtained by micro-XRF, the isotopic data are given in table 6.1 as well. The structural context of each analyzed grain is documented within table 6.1. A full documentation of all analytical results concerning the monazites can be found in Appendix B3.

Petrographical observations provided the structural contexts of the monazites for a correct interpretation of obtained geochronological data. BSE images document those relationships (Fig. 6.1 and Appendix B3). Figure 6.1 shows typical examples of the monazites from the Monte Rosa nappe. Within the Monte Rosa granite (sample 99SL159, round section), the monazites mostly occur as inclusions in apatite or zircon as well as single matrix monazites (Fig. 6.1a). Two of those single matrix monazites were dated by LA-PIMMS and yielded  $222.9 \pm 5.4$  and  $222.4 \pm 5.3$  Ma (Tab. 6.1), and are therefore representing original magmatic cooling ages. Monazite inclusions and single grains at the boundaries of magmatic micas are also observed within the granite. Some monazites with ages older than 400 Ma have been obtained by microprobe analyses (Tab. B3.4), and they are interpreted as inherited components. Within the samples taken from the shear zone different types of monazites are observed. Single, complexly zoned and rounded monazite grains are partially found within quartz. More common are matrix monazites within the main foliation. However, porphyroblastic relics within the matrix are the most common type of monazites within the shear zone. Those matrix monazites display either fine-grained trails along the schistosity or numbers of small single grains mimicking the grain shape of a former larger single grain (Fig. 6.1b and c). They mainly yielded either ages of 30 to 40 Ma or 60 to 137 Ma, whereby the latter ages are interpreted to result from a mixing of Permian and Alpine components (Tab. 6.1). The Eocene ages are mostly found within the samples displaying the high-pressure mineral assemblage chloritoid–talc–kyanite–phengite–quartz, which were collected in the center of the shear zone. The analyzed monazites are located within the foliation of the samples. Therefore, the Eocene ages are interpreted to indicate the age of the high-pressure metamorphism in the Monte Rosa nappe. Microstructural and geochronological relationships of the youngest monazites indicate therefore a partial recrystallization of the monazites during the Alpine metamorphic history. However, reactions leading to monazite-formation during regional high-pressure metamorphism are so far not completely understood and matter of recent research

(e.g. Akers, 1993; Bingen et al., 1996; Broska and Siman, 1998; Finger, 1998; Scherrer et al., 2001)

### 6.3 Fission track dating of apatite

For constraints on the late-stage exhumation of the Monte Rosa nappe in its geological context, several samples of the Monte Rosa granite from different structural positions within the nappe were selected for fission track dating. The following samples have been selected (the coordinates refer to the Swiss Reference Grid):

**98SL29:** a strongly deformed granite collected at the Mezzalama Refuge near the contact of the Monte Rosa nappe and the overlying Zermatt-Saas Zone (altitude 3040 m a.s.l.; coordinates 624.893/084.711).

**98SL133:** a relatively undeformed granite sample collected at the southwestern rim of the kyanite-talc-chloritoid-phengite bearing shear zone (altitude 2895 m a.s.l.; coordinates 625.121/084.167).

**99SL125:** a sample of the undeformed Monte Rosa granite at the northeastern rim of the shear zone (altitude 2740 m a.s.l.; coordinates 625.129/084.119).

**99SL105:** granite sample taken in a lower part of the Monte Rosa nappe (Zone Arcesaz-Brusson) at the road to Grainees near Brusson at an altitude of 1140 m a.s.l. (coordinates 624.070/065.790).

**99SL159:** undeformed granite at the southwestern rim of the shear zone at an altitude of 2720 m a.s.l. (coordinates 625.105/084.143).

Fission tracks in apatite are used as geochronometers to study the cooling below approximately 110°C (Gleadow et al., 1986; M. Rahn, 2000, pers. comm.). In terms of fission track dating, the term „partial annealing zone“ (PAZ) is used instead of „closure temperature“. Within the PAZ, fission tracks start to accumulate during cooling or are annealed during heating. The fission track length is therefore dependent on the temperature during its formation. If a fission track is formed above the PAZ, it will completely anneal during cooling, whereas a fission track developed within the PAZ will remain as a short fission track after cooling below the PAZ due to partial annealing. A fission track developed below the PAZ will not change its length any more, it thus documents the post-PAZ history of the respective sample. The PAZ for apatite is assigned to cover the temperature range between approximately 120 - 60°C (Rahn, 2000, pers. comm.).

For each sample selected for this study, 100 track length were measured in order to obtain a relevant statistical variation of the data (Rahn and Seward, 2000). The preliminary compilation of apatite fission track (FT) length data and ages from

the southern Monte Rosa are given in figure 6.2. In this diagram, histograms of confined track length for each sample are given with respect to the geographical position of the sample. Additionally, the published confined track length data of the samples KAW411 and KAW412 collected near the Mezzalama Refuge in the Val d'Ayas (Hurford et al., 1989; Hurford et al., 1991) are integrated into the diagram as well as the central apatite FT ages with their  $2\sigma$  uncertainty. Table 6.2 gives a compilation of the apatite FT data. All samples investigated during this study show similar FT lengths of approximately  $13.5 \pm 0.2 \mu\text{m}$ , and the results coincide with those from the samples investigated by Hurford et al. (1989; 1991). For the samples investigated during this study, no trend of varying FT lengths in vertical direction is observed between the different samples. Therefore, a continuous cooling of the Monte Rosa nappe since 10 to 14 Ma is suggested. Those FT lengths of apatite are assumed to demonstrate the cooling of an undisturbed basement, and they demonstrate a slow and continuous cooling from temperatures of approximately  $120^\circ\text{C}$  to surface temperatures (Gleadow et al., 1986). Only one sample, 98SL29, shows a more complex FT length distribution by a stronger tailing towards shorter FT lengths (Fig. 6.2). A dominant group of longer FT lengths is observed, which have formed post-PAZ, and a small group of shorter FT lengths, which has formed within the PAZ and which were partially annealed until cooling below the PAZ.

From the samples KAW411 and KAW412 apatite fission track ages of  $13.8 \pm 1.4$  and  $14 \pm 1.2$  Ma were constrained by Hurford et al. (1991). Additionally, an apatite fission track age of  $10.5 \pm 0.8$  Ma was given for sample KAW416 from Arcesaz-Brusson (Hurford et al., 1989). The results of the dated samples from this study are shown in figure 6.2. Sample 98SL29 taken near the samples dated by Hurford et al. yielded an age of  $13.3 \pm 1.5$  Ma, which is identical to the published ages. Sample 98SL133 was taken from the northeastern rim of the whiteschist-bearing shear zone, which was studied in detail, and yielded an older age of  $17.2 \pm 1.7$  Ma. The same age was obtained from sample 99SL159, which has been sampled at the northeastern rim of the shear zone as well. On the other hand, a sample taken from the southwestern rim of the shear zone (99SL125) gives an age of  $26.8 \pm 2.5$  Ma, which is significantly older than the other two samples. An age difference of 9.5 Ma exists, which might provide the opportunity to calculate the amount of vertical displacement along the shear zone. However, such a suggestion is so far speculative and needs to be confirmed, e.g. if a similar age difference between the same samples exists also for the FT data of zircon. The youngest ages of  $9.5 \pm 0.9$  Ma have been found for the sample of the Brusson tectonic window, and this age coincides with the structural lower position of this sample compared to the others.

The comparison of the obtained results on apatite with published FT data on apatite and zircon from the Monte Rosa nappe and adjacent units revealed a more-or-less simultaneous cooling of all tectonic units until approximately  $<225^{\circ}\text{C}$  at ca. 33 Ma from the zircon data (Hurford et al., 1989; Hurford et al., 1991). The later exhumation however, cannot be explained by simple isostatic uplift due to differences between apatite data of adjacent tectonic units. Those differences between the apatite data of the different tectonic units, e.g. Sesia-Lanzo Zone, Bernhard nappe system, Dent Blanche, Gran Paradiso and Ivrea Zone, may be explained a „differential uplift and cooling histories between 33 Ma and the present“ (tectonically based episodic uplift; Hurford et al., 1991 their Fig. 10). The apatite FT data of the Monte Rosa nappe (approximately 9 to 17 Ma) and the structural equivalent Gran Paradiso massif (20 to 24 Ma) can be explained due to the position of the nappes with respect to the Aosta-Ranzola Fault (Hurford et al., 1991). Additionally, if regarding the present tectonic position of the Monte Rosa nappe with respect to the Southern Steep Belt and the Insubric Line, this tectonic element probably played a major role for the exhumation of the nappe stack. As suggested on the basis of petrological data of metapelites from the Monte Rosa, this nappe could have been tectonically exhumed as a coherent body along this major structural element (Engi et al., 2001). Therefore, the uplift of the Monte Rosa nappe might have taken place due to upward movement along major fault zones, e.g. along the Insubric Line and the Aosta-Ranzola Fault (see Hurford et al., 1991 their Fig. 6).

**6.4 Tables**



n = 15

FindAll Search Fiche Find matrix Copy ages Find grt incl.

Sample	Comment	Position	EMP_Label	Age Ma microXRF	Age Ma LAPIMMS	Age Ma TIMS	context
99SL-139	99SL-139_mo	i3e		61.8 ± 11.1	±	( )	cluster matrix monazite
99SL-139	99SL-139_xe	i3c		n.a. ±	±	( )	xenotime
99SL-139	99SL-139_zi	i3d		n.a. ±	±	( )	zircon
99SL-145	99SL-145_1	i2d		38.1 ± 11.5	39.0 ± 0.9	( 41.9)	cluster matrix monazite
99SL-145	99SL-145_2	i2e		n.a. ±	36.1 ± 0.9	( 43.0)	cluster matrix monazite
99SL-145	99SL-145_3	i2f		n.a. ±	±	( )	cluster matrix monazite
99SL-145	99SL-145_g	i3f		n.a. ±	27.0 ± 2.4	( 67.2)	cluster matrix monazite
99SL-145	99SL-145_h	i3g		88.0 ± 16.0	102.0 ± 3.1	( 110.8)	cluster matrix monazite
99SL-145	99SL-145_i	i3a	sl1	n.a. ±	±	( )	cluster matrix monazite
99SL-145	99SL-145_s	i2g	sl1	n.a. ±	137.1 ± 5.8	( 173.3)	cluster matrix monazite
99SL-145	99SL-145_v	i3b	sl1	n.a. ±	31.6 ± 0.7	( 36.1)	cluster matrix monazite
99SL-145	99SL-145_w	i2h	sl1	n.a. ±	±	( )	cluster matrix monazite
99SL-148	99SL-148_j	i3h		n.a. ±	±	( )	cluster matrix monazite
99SL-159	99SL-159_b	i4a		n.a. ±	222.9 ± 5.4	( 283.0)	single matrix monazite
99SL-159	99SL-159_e	i4b		n.a. ±	222.4 ± 5.3	( 237.0)	single matrix monazite

**Table 6.1** Comparison of monazite geochronological data obtained by micro-XRF and LA-PIMMS. Information of structural context of each grain is given. Errors refer to 2σ level.

**Table 6.2** FT data of apatite from the southern Monte Rosa (Data produced by M. Rahn)

Sample and Locality	Number of apatite crystals	Spontaneous $\rho_s$ ( $N_s$ )	Induced $\rho_i$ ( $N_i$ )	$P\chi^2$	Dosimeter $\rho_d$ ( $N_d$ )	Central FT Age Ma ( $\pm 2\sigma$ )	Mean Track Length SE of Mean	Standard Deviation ( $\pm 1\sigma$ )	Number of Tracks
<b>98SL29</b> Mezzalama	20	0.040 (88)	0.570 (1254)	94%	0.111 (3627)	13.3 (-1.4+1.6)	13.27 $\pm$ 0.23	2.32	100
<b>98SL133</b> shear zone, footwall	20	0.066 (125)	0.707 (1348)	58%	0.108 (4084)	17.2 (-1.6+1.7)	13.60 $\pm$ 0.16	1.56	100
<b>99SL105</b> Brusson window	20	0.043 (149)	0.854 (2959)	62%	0.110 (3780)	9.5 (-0.8+0.9)	13.44 $\pm$ 0.18	1.77	100
<b>99SL125</b> shear zone, footwall	13	0.053 (145)	0.369 (1010)	49%	0.109 (3932)	26.8 (-2.3+2.6)	13.51 $\pm$ 0.15	1.51	100
<b>99SL159</b> shear zone, hangingwall	15	0.065 (128)	0.238 (1359)	2%	0.108 (4236)	17.4 (-1.6+1.7)	13.63 $\pm$ 0.16	1.61	100

**Notes:**

- (i) Track densities are ( $\times 10^7$  tr  $\text{cm}^{-2}$ ), number of tracks counted ( $N$ ) shown in brackets;
- (ii) analyses by external detector method using 0.5 for the  $4\pi/2\pi$  geometry correction factor;
- (iii) ages calculated using dosimeter glasses CN-5 with  $\zeta\text{CN}5 = 343 \pm 5$ ;
- (iv)  $P\chi^2$  is probability for obtaining  $\chi^2$  value for  $v$  degrees of freedom, where  $v =$  number of crystals -1.

**6.5 Figures**

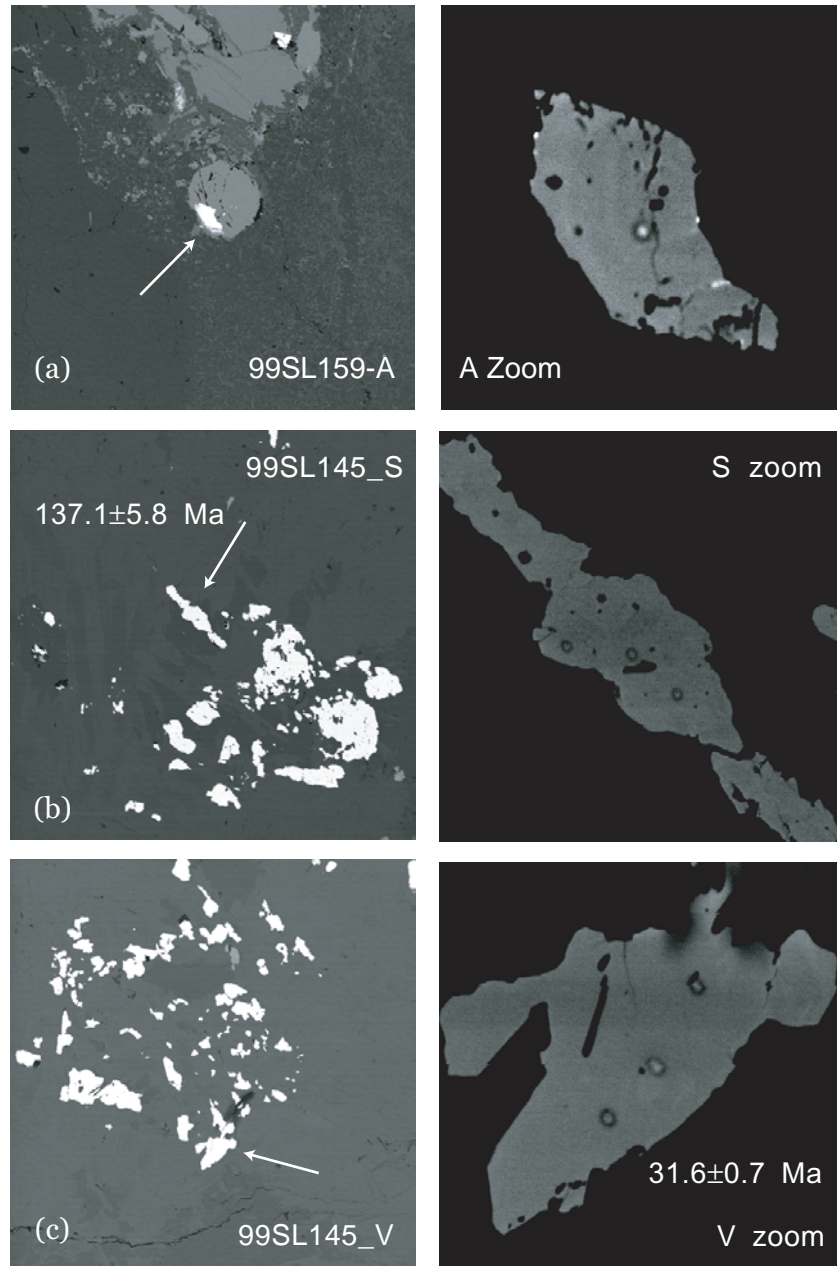


**Figure 6.1** BSE images documenting structural characteristics of the analyzed monazites of the Monte Rosa nappe. Left picture gives a structural overview, and right picture shows a detailed view of the single grain. Arrows indicate location of monazites within overview picture. (a) Large, single monazite grain from granite sample 99SL159 (99SL159-A). Those grains yield Permian magmatic ages. (b) Example of cluster matrix monazites yielding mixing ages of a Permian and an Alpine component (grain 99SL145\_s). (c) Cluster matrix monazites yielding Alpine ages and indicate monazite recrystallization during Alpine metamorphism (grain 99SL145\_v). Length of left picture is 1.34 mm.

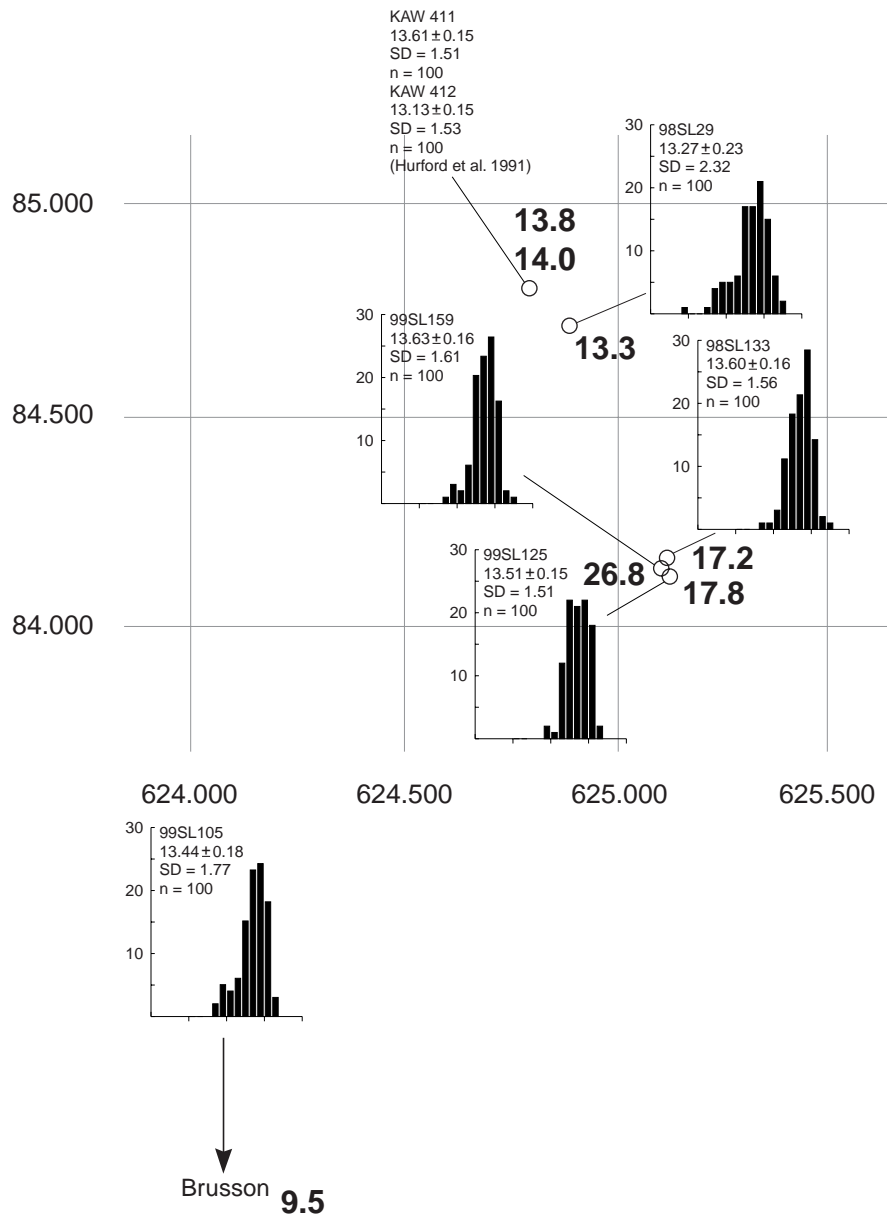


**Figure 6.2** Preliminary apatite FT length data from the southern Monte Rosa.  $\square$  Bold numbers denote central FT ages of apatite in Ma. FT data are  $\square$  given in table 6.2. Results of samples KAW411 and KAW412 of Hur- $\square$ ford et al. (1991) are included in this diagram.

## References

- Abraham, K., Hörmann, P.K. and Raith, M. 1974. Progressive metamorphism of basic rocks from the southern Hohe Tauern area, Tyrol (Austria). *N. Jb. Miner. Abh.* 122, 1-35.
- Ague, J.J. 1994. Mass transfer during Barrovian metamorphism of pelites, south-central Connecticut; I, Evidence for changes in composition and volume. *Amer. J. Sci.* 294, 989-1057.
- Ague, J.J. 1997. Compositional variations in metamorphosed sediments of the Littleton Formation, New Hampshire; discussion. *Amer. J. Sci.* 297, 440-449.
- Akers, W.T., Grove, M., Harrison, T.M. and Ryerson, F.J. 1993. The instability of rhabdophane and its unimportance in monazite paragenesis. In: Watson, E.B., Harrison, T.M. Miller, C.F. and Ryerson, F.J. (eds.). *Cheochemistry of accessory minerals; papers presented at the Third V.M. Goldschmidt Conference. Chem. Geol.*, 169-176.
- Amato, J.M., Johnson, C.M., Baumgartner, L.P. and Beard, B.L. 1999. Rapid exhumation of the Zermatt-Saas ophiolite deduced from high precision Sm-Nd and Rb-Sr geochronology. *Earth Planet. Sci. Lett.* 171, 425-438.
- Argand, E. 1911. Les nappes de recouvrement des Alpes Penniniques et leurs prolongements structuraux. *Mat. Carte géol. Suisse n.s.* 31, 1-26.
- Arnaud, N.O. and Kelley, S.P. 1995. Evidence for excess argon during high pressure metamorphism in the Dora Maira Massif (western Alps, Italy), using an ultra-violet laser ablation microprobe  $^{40}\text{Ar}$ - $^{39}\text{Ar}$  technique. *Contrib. Mineral. Petrol.* 121, 1-11.
- Ballèvre, M. and Merle, O. 1993. The Combin Fault: compressional reactivation of a Late Cretaceous-Early Tertiary detachment fault in the Western Alps. *Schweiz. Mineral. Petrogr. Mitt.* 73, 205-227.
- Barnicoat, A.C. and Fry, N. 1986. High-pressure metamorphism of the Zermatt-Saas ophiolite zone, Switzerland. *J. Geol. Soc. London* 143, 607-618.
- Barnicoat, A.C. and Cartwright, I. 1995. Focused fluid flow during subduction: Oxygen isotope data from high-pressure ophiolites of the western Alps. *Earth. Planet. Sci. Lett.* 132, 53-61.
- Baumgartner, L.P. and Olsen, S.N. 1995. A least-squares approach to mass transport calculations using the isocon method. *Econ. Geol.* 90, 1261-1270.
- Bearth, P. 1939. Über den Zusammenhang von Monte Rosa- und Bernhard-Decke. *Schweiz. Eclogae geol. Helv.* 32, 101-111.
- Bearth, P. 1952. Geologie und Petrographie des Monte Rosa. *Beitr. Geol. Karte Schweiz NF* 96, 94 p.
- Bearth, P. 1953. Geologischer Atlas der Schweiz 1:25000, Blatt Zermatt, mit Erläuterungen. *Schweiz. Geol. Kommission.*
- Bearth, P. 1958. Über einen Wechsel der Mineralfazies in der Wurzelzone des Penninikums. *Schweiz. Mineral. Petrogr. Mitt.* 38, 363-373.
- Bearth, P. 1962. Versuch einer Gliederung alpin-metamorpher Serien der Westalpen. *Schweiz. Mineral. Petrogr. Mitt.* 42, 127-137.
- Bearth, P. 1964. Bericht über die Exkursion der Schweizerischen Mineralogischen und Petrographischen Gesellschaft nach Zermatt. *Schweiz. Mineral. Petrogr. Mitt.* 44, 15-26.
- Bearth, P. 1967. Die Ophiolite der Zone von Zermatt-Saas. *Beitr. Geol. Karte Schweiz NF* 130, 130 p.
- Bearth, P. 1973. Gesteins- und Mineralparagenesen aus den Ophiolithen Zermatt. *Schweiz. Mineral. Petrogr. Mitt.* 44, 299-334.
- Bearth, P. and Schwander, H. 1981. The post-Triassic sediments of the ophiolite zone Zermatt-Saas Fee and the associated manganese mineralizations. *Eclogae geol. Helv.* 74, 189-205.
- Beccaluva, L., Dal Piaz, G.V. and Macciotta, G. 1984. Transitional to normal MORB affinities in ophiolitic metabasites from the Zermatt-Saas, Combin and Antrona units, western Alps. *Geol. Mijnb.* 63, 165-177.
- Bertrand, J., Pidgeon, R., Leterrier, J., Guillot, F., Gasquet, D. and Gattiglio, M. 2000. SHRIMP and IDTIMS U-Pb zircon ages of the pre-Alpine basement in the Internal Western Alps (Savoy and Piemont). *Schweiz. Mineral. Petrogr. Mitt.* 80, 225-248.
- Biino, G.G. and Compagnoni, R. 1988. La scaglia di Grun in Val d'Aosta: un lembo austroalpino composito, incluso nelle metaofioliti della Zona

- Piemontese. *Boll. Soc. Geol. It.* 107, 101-107.
- Biino, G.G. and Compagnoni, R. 1992. Very-high pressure metamorphism of the Brossasco coronite metagranite, southern Dora Maira Massif, Western Alps. *Schweiz. Mineral. Petrogr. Mitt.* 72, 347-363.
- Bingen, B., Demaiffe, D. and Hertogen, J. 1996. Redistribution of rare earth elements, thorium, and uranium over accessory minerals in the course of amphibolite to granulite facies metamorphism: The role of apatite and monazite in orthogneisses from southwestern Norway. *Geochim. Cosmochim. Acta* 60, 1341-1354.
- Bingen, B. and van Bremen, O. 1998. U-Pb monazite ages in amphibolite- to granulite-facies orthogneiss reflect hydrous mineral breakdown reactions: Sveconorwegian Province of SW Norway. *Contrib. Mineral. Petrol.* 132, 336-353.
- Borghi, A., Compagnoni, R. and Sandrone, R. 1996. Composite P-T paths in the Internal Penninic Massifs of the Western Alps: Petrological constraints to their thermo-mechanical evolution. *Eclogae Geol. Helv.* 89, 345-367.
- Bowtell, S.A., Cliff, R.A. and Barnicoat, A.C. 1994. Sm-Nd isotopic evidence on the age of eclogitization in the Zermatt-Saas ophiolite. *J. met. Geol.* 12, 187-196.
- Brodie, K.H., Rex, D. and Rutter, E.H. 1989. On the age of deep crustal extensional faulting in the Ivrea Zone, northern Italy. In: Coward, M.P., Dietrich, D., Park, R.G. (eds). *Alpine Tectonics. Geol. Soc. Spec. Pub.* 45, 203-210.
- Broska, I. and Siman, P. 1998. The breakdown of monazite in the West-Carpathian Veporic orthogneisses and Tatric granites. *Geologica Carpathica* 49, 161-167.
- Brouwer, F.M. 2000. Thermal evolution of high-pressure metamorphic rocks in the Alps. *Mededelingen van de Faculteit Aardwetenschappen, University Utrecht* 199, 221 p.
- Burkhard, D.J.M. and O'Neil, J.R. 1988. Contrasting serpentinization process in the eastern Central Alps. *Contrib. Mineral. Petrol.* 99, 498-506.
- Bussy, F. and Cadoppi, P. 1996. U-Pb zircon dating of gneissoids from the Dora-Maira massif (western Italian Alps). *Schweiz. Mineral. Petrogr. Mitt.* 76, 217-233.
- Bussy, F., Sartori, M. and Th  lin, P. 1996. U-Pb zircon dating in the middle Penninic basement of the Western Alps (Valais, Switzerland). *Schweiz. Mineral. Petrogr. Mitt.* 76, 81-84.
- Bussy, F., Venturini, G., Hunziker, J.C. and Martinotti, G. 1998. U-Pb ages of magmatic rocks of the western Austroalpine Dent-Blanche-Sesia Unit. *Schweiz. Mineral. Petrogr. Mitt.* 78, 163-168.
- Cartwright, I. and Buick, I.S. 2000. Fluid generation, vein formation and the degree of fluid-rock interaction during decompression of high-pressure terranes: the Schistes Lustr  s, Alpine Corsica, France. *J. Met. Geol.* 18, 607-624.
- Cheburkin, A.K., Frei, R. and Shotyk, W. 1997. An energy-dispersive miniprobe multielement analyzer (EMMA) for direct analysis of trace elements and chemical age dating of single mineral grains. *Chem. Geol.* 135, 75-87.
- Chopin, C. 1981. Talc-phengite; a widespread assemblage in high-grade pelitic blueschists of the Western Alps. *J. Petrol.* 22, 628-650.
- Chopin, C. 1984. Coesite and pure pyrope in high-grade blueschists of the Western Alps: a first record and some consequences. *Contrib. Mineral. Petrol.* 86, 107-118.
- Chopin, C. and Moni  , P. 1984. A unique magnesiochloritoid-bearing, high-pressure assemblage from the Monte Rosa, Western Alps; petrologic and <sup>40</sup>Ar-<sup>39</sup>Ar radiometric study. *Contrib. Mineral. Petrol.* 87, 388-398.
- Chopin, C., Henry, C. and Michard, A. 1991. Geology and petrology of the coesite-bearing terrain, Dora Maira massif, Western Alps. *Eur. J. Min.* 3, 263-291.
- Compagnoni, R., Elter, G. and Lombardo, B. 1974. Eterogeneit   stratigrafica del complesso degli "Gneiss Minuti" nel massiccio cristallino del Gran Paradiso. *Mem. Soc. Geol. It.* 13, 227-239.
- Compagnoni, R., Dal Piaz, G.V., Hunziker, J.C., Gosso, G., Lombardo, B. and Williams, P.F. 1977. The Sesia-Lanzo Zone, a slice of continental crust with Alpine high pressure-low temperature assemblages in the Western Italian Alps. *Rend. Soc. It. Mineral. Petrol.* 33, 281-334.
- Compston, W., Williams, I.S. and Meyer, C. 1984. U-Pb geochronology of zircons from Lunar breccia 73217 using a sensitive high mass-resolution ion

- microprobe. *J. Geophys. Res.* 89, 525-534.
- Cortesogno, L., Cassinis, G., Dallagiovanna, G., Gaggero, L., Oggiano, G., Ronchi, A., Seno, S. and Vanossi, M. 1998. The Variscan post-collisional volcanism in Late Carboniferous-Permian sequences of Ligurian Alps, Southern Alps and Sardinia (Italy): a synthesis. *Lithos* 45, 305-328.
- Cortiana, G., Dal Piaz, G.V., Del Moro, A., Hunziker, J.C. and Martin, S. 1998.  $^{40}\text{Ar}$ - $^{39}\text{Ar}$  and Rb-Sr-dating of the Pilonet klippe and Sesia-Lanzo basal slice in the Ayas valley and evolution of the Austroalpine-Piedmont nappe stack. *Mem. Sci. Geol.* 50, 177-194.
- Coward, M. and Dietrich, D. 1989. Alpine tectonics - an overview. In: Coward, M.P., Dietrich, D., Park, R.G. (eds). *Alpine Tectonics*. Geol. Soc. Spec. Pub. 45, 1-29.
- Cummings, G.L. and Richards, J.R. 1975. Ore lead isotope ratios in a continuously changing earth. *Earth Planet. Sci. Lett.* 28, 155-171.
- Curti, E. 1987. Lead and oxygen isotope evidence for the origin of the Monte Rosa gold lode deposits (Western Alps, Italy): A comparison with Archean lode deposits. *Econ. Geol.* 52, 2115-2140.
- Dahl, P.S. 1996. The crystal-chemical basis for Ar retention in micas: inference from interlayer partitioning and implications for geochronology. *Contrib. Mineral. Petrol.* 123, 22-39.
- Dal Piaz, G.V. 1966. Gneiss ghiandoni, marmi ed anfiboliti antiche del ricoprimento Monte Rosa nell'alta Valle d' Ayas. *Boll. Soc. Geol. It.* 85, 103-132.
- Dal Piaz, G.V. 1971. Nuovi ritrovamenti di cianite alpina nel cristallino antico del Monte Rosa. *Rend. Soc. Ital. Mineral. Petrol.* 27, 437-477.
- Dal Piaz, G.V. 1974. Le métamorphisme de haute pression et basse température dans l'évolution structurale du bassin ophiolitique alpino-apenninique. *Schweiz. Mineral. Petrogr. Mitt.* 54, 399-424.
- Dal Piaz, G.V. 1976. Il Lembo Di Ricoprimento Del Pilonet. *Mem. Ist. Geol. Mineral. Padova* 31, 1-61.
- Dal Piaz, G.V. 1993. Evolution of Austro-Alpine and Upper Penninic Basement in the Northwestern Alps from Variscan Convergence to Post-Variscan Extension. In: Von Raumer, J. and Neubauer, J. (eds). *Pre-Mesozoic Geology in the Alps*. Springer, 327-344.
- Dal Piaz, G.V. 1999. The Austroalpine-Piedmont nappe stack and the puzzle of Alpine Tethys. In: Gosso, G., Jadoul, F., Sella, M., Spalla, I.M. (eds) *Third workshop on alpine geological studies, Biella-Oropa 1997*. *Mem. Sci. Geol.* 51, 155-176.
- Dal Piaz, G.V., Gosso, G. and Martinotti, G. 1971. La II Zona diorito kinzigitica tra la Valsesia e la Valle d' Ayas (Alpi Occidentali). *Mem. Soc. Geol. It.* 10, 257-276.
- Dal Piaz, G.V., Hunziker, J.C. and Martinotti, G. 1972. La Zone Sesia-Lanzo e l'evoluzione tettonico-metamorfica delle Alpi Nordoccidentali interne. *Mem. Soc. Geol. It.* 11, 433-460.
- Dal Piaz, G.V. and Ernst, W.G. 1978. Areal geology and petrology of eclogites and associated metabasites of the Piemonte ophiolite nappe, Breuil-St. Jacques area, Italian Western Alps. *Tectonophysics* 51, 99-126.
- Dal Piaz, G.V. and Lombardo, B. 1986. Early Alpine eclogite metamorphism in the Penninic Monte Rosa-Gran Paradiso basement nappes of the northwestern Alps. *Geol. Soc. Am. Mem.* 164, 249-265.
- Dal Piaz, G.V., Cortiana, G., Del Moro, A., Martin, S., Pennacchioni, G. and Trartarotti, P. 2001. Tertiary age and paleostructural inferences of the eclogitic imprint in the Austroalpine outliers and Zermatt-Saas ophiolite, western Alps. *Int. J. Earth Sciences* 90, 668-684.
- Dalrymple, G., Alexander, E., Lanphere, M. and Kraker, G. 1981. Irradiation of samples for  $^{40}\text{Ar}/^{39}\text{Ar}$  dating using the Geological Survey TRIGA reactor. *U.S. Geol. Prof. Pap.* 1176, 55.
- Deer, W.A., Howie, R.A. and Zussman, J. 1992. *An introduction to the rock-forming minerals*. Longman Scientific and Technical, Essex, 696 p.
- Demény, A., Sharp, Z. and Pfeifer, H.R. 1997. Mg-metasomatism and formation conditions of Mg-chlorite-muscovite-quartzphyllites (leucophyllites) of the Eastern Alps (W. Hungary) and their relations to Alpine whiteschists. *Contrib. Mineral. Petrol.* 128, 247-260.
- Di Vincenzo, G. and Palmeri, R. 2001. An  $^{40}\text{Ar}$ - $^{39}\text{Ar}$  investigation of high-pressure metamorphism and the retrogressive history of mafic eclogites from the Lanterman Range (Antarctica):



- evidence against a simple temperature control on argon transport in amphibole. *Contrib. Mineral. Petrol.* 141, 15-35.
- Dodson, M.H. 1973. Closure temperature in cooling geochronological and petrological systems. *Contrib. Mineral. Petrol.* 40, 259-274.
- Driesner, T. 1993. Aspects of petrographical, structural and stable isotope geochemical evolution of ophiocarbonate breccias from ocean floor to subduction and uplift: an example from Chatillon, Middle Aosta Valley, Italian Alps. *Schweiz. Mineral. Petrogr. Mitt.* 73, 69-84.
- Duchêne, S., Blichert-Toft, J., Luais, B., Télouk, P., Lardeaux, J.M. and Albarède, F. 1997. The Lu-Hf dating of garnets and the ages of the Alpine high-pressure metamorphism. *Nature* 387, 586-589.
- Eichhorn, R., Loth, G., Höll, R., Finger, F., Schermaier, A. and Kennedy, A. 2000. Multistage Variscan magmatism in the central Tauern Window (Austria) unveiled by U/Pb SHRIMP zircon data. *Contrib. Mineral. Petrol.* 139, 418-435.
- Engi, M., Scherrer, N.C. and Burri, T. 2001. Metamorphic evolution of pelitic rocks of the Monte Rosa nappe: Constraints from petrology and single grain monazite age data. *Schweiz. Mineral. Petrogr. Mitt.* 81/3, in press.
- Ernst, W.G. and Dal Piaz, G.V. 1978. Mineral parageneses of eclogitic rocks and related mafic schists of the Piemonte ophiolite nappe, Breuil-St. Jacques area, Italian Western Alps. *Amer. Mineral.* 63, 621-640.
- Escher, A., Masson, H. and Steck, A. 1988. Coupes géologiques des Alpes occidentales suisses. *Mém. Géol. Lausanne* 2.
- Escher, A. and Beaumont, C. 1997. Formation, burial and exhumation of basement nappes at crustal scale: a geometric model based on the Western Swiss-Italian Alps. *J. Struct. Geol.* 19, 955-974.
- Eugster, H.P. and Baumgartner, L.P. 1987. Mineral solubilities and speciation in supercritical metamorphic fluids. In: Carmichael, I.S.E. and Eugster, H.P. (eds.). *Mineral solubilities and speciation in supercritical metamorphic fluids. Thermodynamic modeling of geological materials: Minerals, fluids and melts. Reviews in Mineralogy* 17, 367-403.
- Faure, G. 1986. Principles of isotopic geology. 2<sup>nd</sup> edition, John Wiley and Sons, New York, 589 p.
- Finger, F., Roberts, M.P., Haunschmid, B., Schermaier, A. and Steyrer, H.P. 1997. Variscan granitoids of central Europe: their typology, potential sources and tectonothermal relations. *Mineral. Petrol.* 61, 67-96.
- Florineth, D. and Froitzheim, N. 1994. Transition from continental to oceanic basement in the Tasna nappe (Engadine window, Graubünden, Switzerland): evidence for Early Cretaceous opening of the Valais ocean. *Schweiz. Mineral. Petrogr. Mitt.* 74, 437-448.
- Frey, M., Hunziker, J.C., O'Neil, J.R. and Schwander, H.W. 1976. Equilibrium-disequilibrium relations in the Monte Rosa Granite, Western Alps: petrological, Rb-Sr and stable isotope data. *Contrib. Mineral. Petrol.* 55, 147-179.
- Frey, M., Desmons, J. and Neubauer, F. 1999. The new metamorphic map of the Alps: Introduction. *Schweiz. Mineral. Petrogr. Mitt.* 79, 1-4.
- Froitzheim, N., Schmid, S.M. and Frey, M. 1996. Mesozoic paleogeography and the timing of eclogite-facies metamorphism in the Alps: A working hypothesis. *Eclogae geol. Helv.* 89, 81-110.
- Froitzheim, N. 2001. Origin of the Monte Rosa nappe in the Pennine Alps – A new working hypothesis. *Geol. Soc. Amer. Bull.* 113, 604-614.
- Früh-Green, G., Weissert, H. and Bernoulli, D. 1990. A multiple fluid history recorded in Alpine Ophiolites. *J. Geol. Soc. London* 147, 959-970.
- Ganguin, J. 1988. Contribution a la caracterisation du metamorphisme polyphase de la zone de Zermatt-Saas Fee (Alpes Valaisiennes). PhD thesis, ETH Zürich.
- Ganor, J., Matthews, A. and Schliestedt, M. 1994. Post metamorphic low  $\delta^{13}\text{C}$  calcite veins in the Cycladic complex (Greece) and their implications for modeling fluid infiltration processes using carbon isotope composition. *Eur. J. Mineral.* 6, 365-379.
- Gebauer, D. 1996. A P-T-t Path for an (ultra?-)high-pressure ultramafic / mafic rock-association and its felsic country-rocks based on SHRIMP-dating of magmatic and metamorphic zircon domains. Example: Alpe Arami (Central Swiss Alps). *Geophysical*

- Monograph (Earth Processes: Reading the Isotope Code) 95, 307-329.
- Gebauer, D. 1999. Alpine geochronology of the Central and Western Alps: new constraints for a complex geodynamic evolution. *Schweiz. Mineral. Petrogr. Mitt.* 79, 191-208.
- Gebauer, D., Schertl, H.P., Brix, M. and Schreyer, W. 1997. 35 Ma old ultrahigh-pressure metamorphism and evidence for very rapid exhumation in the Dora Maira Massif, Western Alps. *Lithos* 41, 5-24.
- Giorgis, D., Cosca, M. and Li, S. 2000. Distribution and significance of extraneous argon in UHP eclogite (Sulu terrain, China): insight from in situ  $^{40}\text{Ar}/^{39}\text{Ar}$  UV-laser ablation analysis. *Earth Planet. Sci. Lett.* 181, 605-615.
- Gleadow, A.J.W., Duddy, I.R., Green, P.F. and Lovering, J.F. 1986. Confined fission track lengths in apatite: a diagnostic tool for thermal history analysis. *Contrib. Mineral. Petrol.* 94, 405-415.
- Gosso, G., Dal Piaz, G.V., Piovano, V. and Polino, R. 1979. High pressure emplacement of early-Alpine nappes, postnappe deformation and structural levels. *Mem. Sci. Geol. Padova* 32, 15 p.
- Grant, J.A. 1986. The isocon diagram - A simple solution to Gresens' equation for metasomatic alteration. *Econ. Geol.* 81, 1976-1982.
- Gresens, R.L. 1967. Composition -volume relationships of metasomatism. *Chem. Geol.* 2, 47-65.
- Hames, W.E. and Bowring, S.A. 1994. An empirical evaluation of the argon diffusion geometry in muscovite. *Earth. Planet. Sci. Lett.* 124, 161-167.
- Hanchar, J.M. and Miller, C.F. 1993. Zircon zonation patterns as revealed by cathodoluminescence and backscattered electron images of complex crustal histories. *Chem. Geol.* 110, 1-13.
- Hansmann, W., Herrmann, J. and Müntener, O. 1996. U-Pb Datierungen an Zirkonen des Fedozzer Gabbros, einer Intrusion an der Krusten-Mantel Grenze. *Schweiz. Mineral. Petrogr. Mitt.* 76, 116-117.
- Henk, A., Franz, L., Teufel, S. and Oncken, O. 1997. Magmatic under-plating, extension, and crustal reequilibration: insights from a cross-section through the Ivrea Zone and the Strona-Ceneri Zone, Northern Italy. *J. Geol.* 105, 367-377.
- Henry, C., Michard, A. and Chopin, C. 1993. Geometry and structural evolution of ultra-high-pressure and high-pressure rocks from the Dora-Maira massif, Western Alps, Italy. *J. Struct. Geol.* 15, 965-981.
- Herrmann, J., Müntener, O., Trommsdorf, V., Hansmann, W. and Picardo, G.B. 1997. Fossil crust-to-mantle transition, Val Malenco (Italian Alps). *J. Geophys. Res.* B102, 20123-20132.
- Hoefs, J. 1987. Stable isotope geochemistry. 2<sup>nd</sup> ed. Springer, Berlin, 241 p.
- Hsü, K.J. 1989. Time and place in Alpine orogenesis - the Fermor Lecture. In: Coward, M.P., Dietrich, D., Park, R.G. (eds). *Alpine Tectonics*. *Geol. Soc. Spec. Pub.* 45, 421-443.
- Hunziker, J.C. 1969. Rb-Sr-Altersbestimmungen aus den Walliser Alpen - Hellglimmer- und Gesamtgesteinsalterswerte. *Eclogae geol. Helv.* 62, 527-542.
- Hunziker, J.C. 1970. Polymetamorphism in the Monte Rosa, Western Alps. *Eclogae Geol. Helv.* 63, 151-161.
- Hunziker, J.C. 1974. Rb-Sr and K-Ar age determination and the Alpine tectonic history of the Western Alps. *Memorie degli Istituti di Geologia e Mineralogia dell' Università di Padova* 31, 1-54.
- Hunziker, J.C. and Zingg, A. 1980. Lower Paleozoic Amphibolite to Granulite Facies Metamorphism in the Ivrea Zone (Southern Alps, Northern Italy). *Schweiz. Mineral. Petrogr. Mitt.* 60, 181-213.
- Hunziker, J.C., Desmons, J. and Martinotti, G. 1989. Alpine thermal evolution in the central and the western Alps. In: Coward, M.P., Dietrich, D., Park, R.G. (eds). *Alpine Tectonics*. *Geol. Soc. Spec. Pub.* 45, 353-367.
- Hunziker, J.C., Desmons, J. and Hurford, A.J. 1992. Thirty-two years of geochronological work in the Central and Western Alps: a review on seven maps. *Memoires de Geologie (Lausanne)* 13, 59 p.
- Hurford, A.J., Flisch, M. and Jäger, E. 1989. Unravelling the thermo-tectonic evolution of the Alps: a contribution from fission track analysis and mica dating. In: Coward, M.P., Dietrich, D. and Park, R.G. (eds.). *Alpine Teconics*. *Geol. Soc. Spec. Pub.* 45, 369-398.
- Hurford, A., Hunziker, J. and Stöckhert, B. 1991. Constraints on the late thermotectonic evolution of the

- Western Alps: Evidence for episodic rapid uplift. *Tectonics* 10, 758-769.
- Jaboyedoff, M., Béglé, P. and Loblirius, S. 1996. Stratigraphie et évolution structurale de la zone de Furgg, au front de la nappe du Mont-Rose. *Bulletin de Géologie Lausanne* 334, 191-210.
- Jäger, E. 1967. Die Bedeutung der Biotit-Alterswerte. Jäger, E. and Niggli, E. (eds.). Rb/Sr Altersbestimmungen an Glimmern der Zentralalpen. *Beitr. Geol. Karte Schweiz* 66, 28-31.
- Jenkin, G.R.T., Rogers, G., Fallick, A.E. and Farrow, C.M. 1995. Rb/Sr closure temperatures in bi-mineralic rocks: a mode effect and test for different diffusion models. *Chem. Geol.* 122, 227-240.
- Keller, L.M. and Schmid, S.M. 2001. On the kinematics of shearing near the top of the Monte Rosa nappe and the nature of the Furgg Zone in Val Loranco (Antrona Valley, N Italy): tectonometamorphic and paleogeographic consequences. *Schweiz. Mineral. Petrogr. Mitt.* 81/3, in press.
- Klein, J.A. 1978. Post-nappe folding southeast of the Mischabelrückfalte (Pennine Alps) and some aspects of the associated metamorphism. *Leid. Geol. Meded.* 51, 233-312.
- Köppel, V. and Grünenfelder, M. 1975. Concordant U-Pb ages of monazite and xenotime from the Central Alps and the timing of the high temperature Alpine metamorphism, a preliminary report. *Schweiz. Mineral. Petrogr. Mitt.* 55, 129-132.
- Köppel, V. and Grünenfelder, M. (1978/1979). Monazite and zircon U-Pb ages from the Ivrea and Ceneri zones. *Mem. Sci. Geol.* 33, 257.
- Kramar, N., Cosca, M.A. and Hunziker, J.C. 2001. Heterogeneous  $^{40}\text{Ar}^*$  distributions in naturally deformed muscovite: *in situ* UV-laser ablation evidence for microstructurally controlled intragrain diffusion. accepted for *Earth Planet. Sci. Lett.*
- Kramer, J., Schmid, S. and Froitzheim, N. 2000. Superposed thrusting and folding in the Penninic units of the Monte Rosa region, southern Switzerland and northern Italy. Abstract Swiss Society for Mineralogy and Petrology Annual Meeting, Winterthur.
- Kramer, J. and Schmid, S.M. 2001. From ductile mass flow to discrete shear zones: Evolution of the Penninic Units of the Monte Rosa region, Switzerland/Italy. *J. Conf. Abs.* 6, 619.
- Krogh, T.E. 1973. A low-contamination method for hydrothermal decomposition of zircon and extraction of U and Pb for isotopic age determination. *Geochim. Cosmochim. Acta* 37, 485-494.
- Kühn, A., Glodny, J., Iden, K. and Austrheim, H. 2000. Retention of Precambrian Rb/Sr phlogopite ages through Caledonian eclogite facies metamorphism, Bergen arc complex, W-Norway. *Lithos* 51, 305-330.
- Laubscher, H.P. 1983. Detachment, shear and compression in the central Alps. *Geol. Soc. Amer. Mem.* 158, 19-211.
- Laubscher, H.P. and Bernoulli, D. 1977. Mediterranean and Tethys. In: Narin, A.E.M., Kanes, W.K. and Stehli, F.G. (eds). *The ocean basins and margins*. Plenum Press, New York, 1-28.
- Le Bayon, R., de Capitani, C., Chopin, C. and Frey, M. 2000. Modelling of the sequential evolution of whiteschist assemblages: HP in the Monte Rosa (Western Alps). *Beih. Eur. J. Min.* 12, 111.
- Le Bayon, R., de Capitani, C., Chopin, C. and Frey, M. 2001. Modelling equilibrium phase diagrams for white schists: New insights on metamorphic evolution in the Western Penninic Alps. *J. Conf. Abs.* 6, 346.
- Li, S., Wang, S., Chen, Y., Liu, D., Qui, J., Zhou, H. and Zhang, Z. 1994. Excess argon in phengite from eclogite: Evidence from dating eclogite minerals by Sm-Nd, Rb-Sr and  $^{40}\text{Ar}/^{39}\text{Ar}$  methods. *Chem. Geol.* 112, 343-350.
- Marquer, D., Baudin, T., Peucat, J. and Persoz, F. 1994. Rb-Sr mica ages in the Alpine shear zones of the Truzzo granite: Timing of the Tertiary alpine P-T-deformation in the Tambo nappe (Central Alps, Switzerland). *Eclogae Geol. Helv.* 87, 225-239.
- Martin, S. and Tartarotti, P. 1989. Polyphase HP metamorphism in the ophiolitic glaucophanites of the lower St. Marcel valley (Aosta, Italy). *Ophioliti* 15, 135-156.
- Massonne, H.J. and Schreyer, W. 1987. Phengite geobarometry based on the limiting assemblage with K-feldspar, phlogopite, and quartz. *Contrib. Mineral. Petrol.* 96, 212-224.
- Massonne, H.J. and Chopin, C. 1989. P-T history of the Gran Paradiso (Western Alps) metagranites based on phengite

- geobarometry. In: Daly, J.S., Cliff, R.A. and Yardley, B.W.D. (eds). Evolution of metamorphic belts. Geol. Soc. Spec. Pub. 43, 545-549.
- Matthews, A., Lieberman, J., Avigad, D. and Garfunkel, Z. 1999. Fluid-rock interaction and thermal evolution during thrusting of an Alpine metamorphic complex (Tinos Island, Greece). *Contrib. Mineral. Petrol.* 135, 212-224.
- Mayer, A., Mezger, K. and Sinigoi, S. 2000. New Sm-Nd ages for the Ivrea-Verbano Zone, Sesia and Sessera valleys (Northern Italy). *Journal of Geodynamic* 30, 147-166.
- Mc Dougall, I. and Harrison, T.M. 1988. Geochronology and thermochronology by the  $^{40}\text{Ar}/^{39}\text{Ar}$  method. Oxford University Press, 212 p.
- Mehnert, K.R. 1975. The Ivrea Zone - A model of the deep crust. *N. Jb. Mineral. Abh.* 125, 156-199.
- Mercolli, I. and Oberhänsli, R. 1988. Variscan tectonic evolution in the Central Alps: a working hypothesis. *Schweiz. Mineral. Petrogr. Mitt.* 68, 491-500.
- Meyer, J. 1983. Mineralogie und Petrologie des Allalingabbros. PhD thesis., University Basel, 329p.
- Meyer, C. and Hemley, J.J. 1967. Wall rock alteration. In: Barnes, H. L. (ed). *Geochemistry of hydrothermal ore deposits*. Holt, Rinehart and Winston, New York, 166-235.
- Mezger, K. and Krogstad, E.J. 1997. Interpretation of discordant U-Pb zircon ages: An evaluation. *J. met. Geol.* 15, 127-140.
- Miller, J.A., Cartwright, I., Buick, I.S. and Barnicoat, A.C. 2001. An O-isotope profile through the HP-LT Corsican ophiolite, France and its implications for fluid flow during subduction. *Chem. Geol.* 178, 43-69.
- Milnes, A.G., Grellier, M. and Mueller, R. 1981. Sequence and style of major post-nappe structures, Simplon-Pennine Alps. *J. Struct. Geol.* 3, 411-420.
- Monié, P. 1985. La méthode  $^{39}\text{Ar}$ - $^{40}\text{Ar}$  appliqué au métamorphisme alpin dans le massif du Mont-Rose (Alpes Occidentales). *Chronologie détaillé depuis 110 Ma. Eclogae geol. Helv.* 78, 487-516.
- Montel, J.M., Foret, S., Veschambre, M., Nicollet, C. and Provost, A. 1996. Electron microprobe dating of monazite. *Chem. Geol.* 131, 37-53.
- Nasdala, L., Pidgeon, R.T., Wolf, D. and Irmer, G. 1998. Metamictization and U-Pb isotopic discordance in single zircons: a combined Raman microprobe and SHRIMP ion probe study. *Mineral. Petrol.* 62, 1-27.
- Nelson, D.R. 1997. Compilation of SHRIMP U-Pb geochronology data, 1996. *Geol. Surv. West Aust. Rec.* 1997/2.
- Neubauer, F., Hoinkes, G., Sassi, F.P., Handler, R., Höck, V., Koller, F. and Frank, W. 1999. Pre-Alpine metamorphism of the Eastern Alps. *Schweiz. Mineral. Petrogr. Mitt.* 79, 41-62.
- Oberhänsli, R., Hunziker, J., Martinotti, G. and Stern, W. 1985. Geochemistry, geochronology and petrology of Monte Mucrone: an example of eo-alpine eclogitization of permian granitoids in the Sesia-Lanzo zone, Western Alps, Italy. *Chem. Geol.* 52, 165-184.
- Ohmoto, H. 1986. Stable isotope geochemistry of ore deposits. In: Valley, J.W., Taylor, H.P. Jr. and O'Neil, J.R. (eds.). *Stable isotope geochemistry of ore deposits. Stable isotopes in high temperature geological processes. Reviews in Mineralogy* 16, 491-559.
- Ohmoto, H. and Rye, R.O. 1979. Isotopes of sulfur and carbon. In: Barnes, H.L. (ed). *Geochemistry of hydrothermal ore deposits*. 2<sup>nd</sup> ed., John Wiley and Sons, New York, 509-567.
- Olsen, S.N. and Grant, J.A. 1991. Isocon analysis of migmatization in the Front Range, Colorado, USA. *J. met. Geol.* 9, 151-164.
- Olsen, S.N., Johnson, C.M., Beard, B.L. and Baumgartner, L.P. 2000. New U-Pb zircon data and constraints on the age and mode of migmatization in the Aar Massif, Central Alps. *Eur. J. Mineral.* 12, 1245-1260.
- Paquette, J.L., Chopin, C. and Peucat, J.J. 1989. U-Pb zircon, Rb-Sr and Sm-Nd geochronology of high- to very high-pressure meta-acidic rocks from the Western Alps. *Contrib. Mineral. Petrol.* 101, 280-289.
- Paquette, J.L., Montel, J.M. and Chopin, C. 1999. U-Th-Pb dating of the Brossasco ultrahigh-pressure metagranite, Dora-Maira massif, western Alps. *Eur. J. Mineral.* 11, 69-77.
- Parrish, R.R. 1990. U-Pb dating of monazite and its application to geological problems. *Canad. J. Earth Sci.* 27, 1431-1450.

- Parrish, R.R., Nowell, G., Noble, S.R., Horstwood, M., Timmermann, H., Shaw, P. and Bowen, I. 1999. LA-PIMMS: A new method of U-Th-Pb geochronology using micro-sampling techniques. *EUG X, Terra Abstracts*, 11, 799.
- Pawlig, S. and Baumgartner, L.P. 2000. Development of a High-Pressure Shearzone in the Monte Rosa Nappe, Western Alps. *EOS Transactions, American Geophysical Union* 81, F1365.
- Pawlig, S. and Baumgartner, L.P. 2001. Geochemistry of a talc-kyanite-chloritoid shear zone within the Monte Rosa granite, Val d' Ayas, Italy. *Schweiz. Mineral. Petrogr. Mitt.*, Vol. 81/3 in press.
- Pawlig, S., Poller, U., Baumgartner, L.P. and Todt, W. 2001. New U-Pb data on the crystallization age of the Monte Rosa granite, Western Alps – a combined SHRIMP, TIMS and cathodoluminescence study. in review, *Eur. J. Min.*
- Pennacchioni, G. and Cesare, B. 1997. Ductile-brittle transition in pre-Alpine amphibolite facies mylonites during evolution from water-present to water-deficient conditions (Mont Mary nappe, Italian Western Alps). *J. Met. Geol.* 15, 777-791.
- Peters, T. and Stettler, A. 1987. Time, physico-chemical conditions, mode of emplacement and geologic setting of the Totalp peridotite in the eastern Swiss Alps. *Schweiz. Mineral. Petrogr. Mitt.* 76, 285-294.
- Pfeifer, H.R., Colombi, A. and Ganguin, J. 1989. Zermatt-Saas and Antrona Zone: A petrographic and geochemical comparison of polyphase metamorphic ophiolites of the West-Central Alps. *Schweiz. Mineral. Petrogr. Mitt.* 69, 217-236.
- Pfeifer, H.R., Colombi, A., Ganguin, J., Hunziker, J., Oberhänsli, R. and Santini, L. 1991. Relics of high-pressure metamorphism in different lithologies of the Central Alps, an updated inventory. *Schweiz. Mineral. Petrogr. Mitt.* 71, 441-451.
- Pidgeon, R.T., Furfaro, D., Kennedy, A.K., Nemchin, A.A. and Van Bronswijk, W. 1994. Calibration of zircon standards for the Curtin SHRIMP II. In: 8th Int. Conf. Geochronol. Isotope Geol., Berkeley US Geol. Surv. Circular 1107, 251.
- Philippot, P. 1993. Fluid-melt-rock interaction in mafic eclogites and coesite-bearing metasediments: constraints on volatile recycling during subduction. *Chem. Geol.* 108, 93-112.
- Philippot, P. and Selverstone, J. 1991. Trace-element rich brines in eclogitic veins; implications for fluid composition and transport during subduction. *Contrib. Mineral. Petrol.* 106, 417-430.
- Philippot, P., Chevallier, P., Chopin, C. and Dubessy, J. 1995. Fluid composition and evolution in coesite-bearing rocks (Dora-Maira massif, Western Alps): implications for element recycling during subduction. *Contrib. Mineral. Petrol.* 121, 29-44.
- Platt, J P 1986. Dynamics of orogenic wedges and the uplift of high-pressure metamorphic rocks. *Geol. Soc. Amer. Bull.* 97, 1037-1053.
- Pognante, U., Talarico, F. and Benna, P. 1988. Incomplete blueschist recrystallization in high-grade metamorphics from the Sesia-Lanzo unit (Vasario-Sparone subunit, Western Alps): a case history of metastability. *Lithos* 21, 129-142.
- Polino, R., Dal Piaz, G.V. and Gosso, G. 1990. Tectonic erosion at the Adria margin and accretionary processes for the Cretaceous orogeny of the Alps. *Mém. Soc. géol. France, N.S.* 156, 345-367.
- Poller, U., Liebetrau, V. and Todt, W. 1997. U-Pb single-zircon dating under cathodoluminescence control (CLC-method): application to polymetamorphic orthogneisses. *Chem. Geol.* 139, 287-297.
- Pozzorini, D. and Früh-Green, G.L. 1996. Stable isotope systematics of the Ventina Ophicarbonatite Zone, Bergell contact aureole. *Schweiz. Mineral. Petrogr. Mitt.* 76, 549-564.
- Rahn, M. and Seward, D. 2000. How many track length do we need?. *OnTrack, The Newsletter of the International Fission-Track Community*, 10, Issue 20. www-adress: <http://www.erdw.ethz.ch/~spikings/F T/ontrack20.htm#how many>
- Reddy, S.M., Kelley, S.P. and Wheeler, J. 1996. A  $^{40}\text{Ar}/^{39}\text{Ar}$  laser probe study of micas from the Sesia Zone, Italian Alps: implications for metamorphic and deformation histories. *J. met. Geol.* 14, 493-508.
- Reddy, S.M., Kelley, S.P. and Magennis, L. 1997. A microstructural and argon

- laserprobe study of shear zone development at the western margin of the Nanga Parbat-Haramosh Massif, western Himalaya. *Contrib. Mineral. Petrol.* 128, 16-29.
- Reddy, S.M., Wheeler, J. and Cliff, R.A. 1999. The Geometry and Timing of Orogenic Extension: An Example from the Western Italian Alps. *J. met. Geol.* 17, 573-589.
- Reddy, S.M., Potts, G.J. and Kelley, S.P. 2001.  $^{40}\text{Ar}/^{39}\text{Ar}$  ages in deformed potassium feldspar: evidence of microstructural control on Ar isotope systematics. *Contrib. Mineral. Petrol.* 141, 186-200.
- Reinecke, T. 1991. Very-high-pressure metamorphism and uplift of coesite-bearing metasediments from the Zermatt-Saas zone, Western Alps. *Eur. J. Min.* 3, 7-17.
- Reinecke, T. 1998. Prograde high- to ultrahigh-pressure metamorphism and exhumation of oceanic sediments at Lago di Cignana, Zermatt-Saas Zone, western Alps. *Lithos* 42, 147-189.
- Ridley, J. 1989. Structural and metamorphic history of a segment of the Sesia-Lanzo zone, and its bearing on the kinematics of Alpine deformation in the western Alps. In: Coward, M.P., Dietrich, D., Park, R.G. (eds). *Alpine Tectonics*. *Geol. Soc. Spec. Pub.* 45, 189-201.
- Roberts, H.J., Kelley, S.P. and Dahl, P.S. 2001. Obtaining geologically meaningful  $^{40}\text{Ar}-^{39}\text{Ar}$  ages from altered biotite. *Chem. Geol.* 172, 277-290.
- Rubatto, D. 1998. Dating of pre-Alpine magmatism, Jurassic ophiolites and Alpine subductions in the Western Alps. PhD Thesis, ETH Zürich, 173 p.
- Rubatto, D. and Gebauer, D. 1999. Eo/Oligocene (35 Ma) high-pressure metamorphism in the Gornergrat Zone (Monte Rosa, Western Alps): Implications for paleogeography. *Schweiz. Mineral. Petrogr. Mitt.* 79, 353-362.
- Rubatto, D., Gebauer, D. and Fanning, M. 1998. Jurassic formation and Eocene subduction of the Zermatt-Saas-Fee ophiolites: implications for the geodynamic evolution of the Central and Western Alps. *Contrib. Mineral. Petrol.* 132, 269-287.
- Rubatto, D., Gebauer, D. and Compagnoni, R. 1999. Dating of eclogite-facies zircons: the age of Alpine metamorphism in the Sesia-Lanzo Zone (Western Alps). *Earth Planet. Sci. Lett.* 167, 141-158.
- Ruffet, G., Gruau, G., Ballèvre, M., Féraud, G. and Philippot, P. 1997. Rb-Sr and  $^{40}\text{Ar}-^{39}\text{Ar}$  laser probe dating of high-pressure phengites from the Sesia zone (Western Alps): underscoring of excess argon and new age constraints on the high-pressure metamorphism. *Chem. Geol.* 141, 1-18.
- Samson, S. and Alexander, E. 1987. Calibration of the interlaboratory  $^{40}\text{Ar}/^{39}\text{Ar}$  dating standard, MMhb-1. *Chem. Geol.* 66, 27-34.
- Sartori, M. 1990. L'unité du Barrhorn (Zone pennique, Valais, Suisse). *Mém. Géol. Lausanne* 6, 156 p.
- Scaillet, S. 1996. Excess  $^{40}\text{Ar}$  transport scale and mechanism in high-pressure phengites: A case study from an eclogitized metabasite of the Dora-Maira nappe, western Alps. *Geochim. Cosmochim. Acta* 60, 1075-1090.
- Scaillet, S. 1998. K-Ar ( $^{40}\text{Ar}/^{39}\text{Ar}$ ) geochronology of ultrahigh pressure rocks. In: Hacker, B.R. and Liou, J.G. (eds.). *When Continents Collide: Geodynamics and Geochemistry of Ultrahigh-Pressure Rocks*, 161-201.
- Scaillet, S., Féraud, G., Lagabrielle, Y., Ballèvre, M. and Ruffet, G. 1990.  $^{40}\text{Ar}/^{39}\text{Ar}$  laser-probe dating by step heating and spot fusion of phengites from the Dora Maira nappe of the Western Alps, Italy. *Geology* 18, 741-744.
- Scaillet, S., Féraud, G., Ballèvre, M. and Amouric, M. 1992. Mg/Fe and ((Mg, Fe)Si-Al<sub>2</sub>) compositional control on argon behaviour in high-pressure white micas: A  $^{40}\text{Ar}/^{39}\text{Ar}$  continuous laser-probe study from the Dora-Maira nappe of the internal western Alps, Italy. *Geochim. Cosmochim. Acta* 56, 2851-2872.
- Schaltegger, U. and Gebauer, D. 1999. Pre-Alpine geochronology of the Central, Western and Southern Alps. *Schweiz. Mineral. Petrogr. Mitt.* 79, 79-87.
- Scherrer, N.C., Engi, M., Gnos, E., Jakob, V. and Liechti, A. 2000. Monazite analysis; from sample preparation to microprobe age dating and REE quantification. *Schweiz. Mineral. Petrogr. Mitt.* 80, 93-105.
- Scherrer, N.C. 2001. Behaviour of Monazite and Evolution of Polymetamorphic Pelites from the Monte Rosa Nappe, Western Central Alps, Italy. PhD Thesis, University Bern, 65 p.

- Schertl, H.P., Schreyer, W. and Chopin, C. 1991. The pyrope-coesite rocks and their country rocks at Pagiri, Dora Maira Massif, Western Alps: detailed petrography, mineral chemistry and PT-path. *Contrib. Mineral. Petrol.* 108, 1-21.
- Schmid, S.M., Pfiffner, O.A., Froitzheim, N., Schönborn, G. and Kissling, E. 1996. Geophysical-geological transect and tectonic evolution of the Swiss-Italian Alps. *Tectonics* 15, 1036-1064.
- Schreyer, W. 1974. Whiteschist, a new type of metamorphic rock formed at high pressures. *Geol. Rundschau* 63, 597-609.
- Sharp, Z.D., Essene, E.J. and Hunziker, J.C. 1993. Stable isotope geochemistry and phase equilibria of coesite-bearing whiteschist, Dora Maira Massif, western Alps. *Contrib. Mineral. Petrol.* 114, 1-12.
- Sheppard, S.M.F. 1986. Characterization and isotopic variations in natural waters. In: Valley, J.W., Taylor, H.P. Jr. and O'Neil, J.R. (eds.). *Characterization and isotopic variations in natural waters. Stable isotopes in high temperature geological processes. Reviews in Mineralogy* 16, 165-183.
- Silver, L. and Deutsch, S. 1963. Uranium-lead isotopic variations in zircons: a case study. *J. Geol.* 71, 721-758.
- Sperlich, R. 1988. The transition from crossite to actinolite in metabasites of the Combin unit in Vallée St. Barthélemy (Aosta, Italy). *Schweiz. Mineral. Petrogr. Mitt.* 68, 215-224.
- Stampfli, G. 1993. Le Briançonnais, terrain exotique dans les Alpes? *Ecolae geol. Helv.* 86, 1-45.
- Stampfli, G.M. 1994. Exotic terrains in the Alps: a solution for a single Jurassic ocean. *Schweiz. Mineral. Petrogr. Mitt.* 74, 449-452.
- Stampfli, G.M. and Marchant, R. 1997. Geodynamic evolution of the Tethyan margins of the Western Alps. In: Pfiffner, O.A., Lehren, P., Heitzmann, P., Müller, S. and Steck, A. (eds). *Deep structure of the Swiss Alps. Results of NRP20.* Birkhäuser Verlag, 223-239.
- Stampfli, G.M., Mosar, J., Marquer, D., Marchant, R., Baudin, T. and Borel, G. 1998. Subduction and obduction processes in the Swiss Alps. *Tectonophysics* 296, 159-204.
- Steck, A., Bigoggero, B., Dal Piaz, G.V., Escher, A., Martinotti, G. and Masson, H. 1999. Carte tectonique des Alpes de Suisse occidentale et des régions avoisinantes, 1:100.000. *Serv. hydrol. géol. nat., Carte spéc. n. 123, 4 feuilles.*
- Stille, P. and Buletti, M. 1987. Nd-Sr isotopic characteristics of the Lugano volcanic rocks and constraints on the continental crust formation in the South Alpine domain (N-Italy-Switzerland). *Contrib. Mineral. Petrol.* 96, 140-150.
- Suzuki, K. and Adachi, M. 1991. The chemical Th-U-total Pb isochron ages of zircon and monazite from the Gray Granite of the Hida Terrane, Japan. *J. Earth Sci.* 38, 11-37.
- Thöni, M. 1999. A review of geochronological data from the Eastern Alps. *Schweiz. Mineral. Petrogr. Mitt.* 79, 209-230.
- Todd, C.S. and Engi, M. 1997. Metamorphic field gradients in the Central Alps. *J. Met. Geol.* 15, 513-530.
- Todt, W., Cliff, R.A., Hanser, A. and Hofmann, A.W. 1996. Evaluation of a  $^{202}\text{Pb}$ - $^{205}\text{Pb}$  double spike for high precision lead isotope analysis. *Geophysical Monograph (Earth Processes: Reading the Isotope Code)* 95, 429-437.
- Trümpy, R. 1980. *Geology of Switzerland - a guide book. Part A: An outline of the Geology of Switzerland.* Schweiz. Geol. Kommission. Wepf and Co. Publishers Basel, New York, 104 p.
- Valley, J.W. 1986. Stable isotope geochemistry of metamorphic rocks. In: Valley, J.W., Taylor, H.P. Jr. and O'Neil, J.R. (eds.). *Stable isotope geochemistry of metamorphic rocks. Reviews in Mineralogy* 16, 445-489.
- Van der Klauw, S.N.G.C., Reinecke, T. and Stöckhert, B. 1997. Exhumation of ultrahigh-pressure metamorphic oceanic crust from Lago di Cignana, Piemontese zone, western Alps: the structural record in metabasites. *Lithos* 41, 79-102.
- Vialon, P. 1966. *Etude géologique du Massif Cristallin Dora-Maira (Alpes Cottiennes-Italie).* Trav. Lab. Géol. Grenoble mém. 4.
- Villa, I.M. 1998. Isotopic closure. *Terra Nova* 10, 42-47.
- Von Raumer, J.F. 1998. The Paleozoic evolution in the Alps: from Gondwana to Pangea. *Geol. Rundschau* 87, 407-435.
- Von Raumer, J. and Neubauer, J. 1993. Late Precambrian and Palaeozoic evolution of the Alpine basement. In: Von Raumer, J. and Neubauer, J. (eds).

- Pre-Mesozoic Geology in the Alps.  
Springer. 625-639
- Von Raumer, J., Abrecht, J., Bussy, F.,  
Lombardo, B., Ménot, R. and  
Schaltegger, U. 1999. The Paleozoic  
metamorphic evolution of the Alpine  
External Massifs. Schweiz. Mineral.  
Petrogr. Mitt. 79, 5-22.
- Weissert, H. and Bernoulli, D. 1984.  
Oxygen isotope composition of calcite  
in ophicarbonates, a hydrothermal or  
Alpine signal? *Eclogae Geol. Helvet.* 77,  
29-43.
- Wetzel, R. 1972. Zur Petrographie und  
Mineralogie der Furgg-Zone (Monte  
Rosa-Decke). Schweiz. Mineral.  
Petrogr. Mitt. 52, 161-237.
- Ziegler, P.A. 1993. Late Palaeozoic-Early  
Mesozoic plate reorganisation:  
evolution and demise of the Variscan  
fold belt. In: Von Raumer, J.F. and  
Neubauer, F. (eds.). Pre-Mesozoic  
Geology in the Alps. Springer, 203-218.
- Zingg, A., Handy, M.R., Hunziker, J.C. and  
Schmid, S.M. 1990.  
Tectonometamorphic history of the  
Ivrea Zone and its relationship to the  
evolution of the Southern Alps.  
*Tectonophysics* 182, 169-192.



## Appendix A

### Sample Lists and Tectonic Data

#### **A1 Sample Lists**

##### *The complete sample lists (Tab. A1.1 and A1.2)*

The complete sample list contains all samples collected during the field summers in 1998 and 1999 (Tab. A1.1 and A1.2). The layout of this table was setup to document the sample localities which are given in the corresponding maps (Fig. A1.1, A1.2, A1.3 and A1.4). Additionally, information on the state of the sample is shown, e.g. if the sample is oriented or if any thin sections are available. The following abbreviations are used in this table:

VT = Val Tournenche  
VG = Valle di Gressoney  
VA = Val d'Ayas  
ZSZ = Zermatt-Saas Zone  
DB = Dent Blanche  
MR = Monte Rosa  
CZ = Combin Zone  
APVS = Alpe Pian di Verra Superior  
APVI = Alpe Pian di Verra Inferior  
TS = Thin section  
MS = Polished microprobe section  
II L = Section is cut parallel to the lineation

##### *The list with the coordinates of the sample locations (Tab. A1.3)*

This list denotes all coordinates of the sample locations calculated according to the Swiss Reference Grid (for Fig. A1.1 and Fig. A1.2).

##### *The list of studied samples (Tab. A1.4)*

This additional sample list contains each sample which was studied for this PhD thesis. Despite of the sample number and the rock type, the methods used on each sample are given as well (e.g. XRF, microprobe, isotopic investigations).

#### **A2 List of tectonic data**

This list gives all tectonic data for the studied outcrops collected during the two field summers (Tab. A2.1).

The following maps were used:

Val d'Ayas and Val Gressoney: Carta nazionale della Svizzera, 1:50000, sheet # 294 „Gressoney“ and sheet # 293 „Valpelline“, Bundesamt für Landestopographie, 3084 Wabern.

Val Tournenche: Carta dei Sentieri e dei Rifugi, 1:25000, sheet 108, Istituto Geografico Centrale, 10121 Torino.

Valle di St. Marcel: Carta dei Sentieri e dei Rifugi, 1:25000, sheet 109, Istituto Geografico Centrale, 10121 Torino.

Appendix A

**Table A1.1** List of all samples collected during field summer 1998.

Outcrop#	Sample#	Location	Orientation of sample	Rock type	# of thin sections	cut direction of section	TS/MS
SM1	98SL1	St. Marcel, Road to Les Druges, ZSZ		blueschist	3		TS
SM1	98SL2	St. Marcel, Road to Les Druges, ZSZ		talcschist	1		TS
SM2	98SL3	St. Marcel, Mine Servette, ZSZ		metabasite, part. Blueschist	2		TS
SM2	98SL4	St. Marcel, Mine Servette, ZSZ		ctd-tlc-phe-schist	3		TS
SM2	98SL5	St. Marcel, Mine Servette, ZSZ		schist	1	XZ	TS
SM2	98SL6	St. Marcel, Mine Servette, ZSZ		grt-tlc-glc-schist	1		TS
SM2	98SL7	St. Marcel, Mine Servette, ZSZ		grt-tlc-pvrite-schist	2		TS
SM2	98SL8	St. Marcel, Mine Servette, ZSZ		blueschist	1		TS
SM3	98SL9	St. Marcel, ZSZ		eclogite part. Blueschist			
SM3	98SL10	St. Marcel, ZSZ		eclogite in blueschist	3		TS
1	98SL11	VT, ZSZ		epidosite	1		TS
1	98SL12	VT, ZSZ		greenschist	1		TS
2	98SL13	VT, ZSZ	040/60	serpentinite	2		MS
2	98SL14	VT, ZSZ	082/50	serpentinite	1	YZ	MS
4	98SL15	VT, ZSZ		greenschist	1		TS
5	98SL16	VT, CZ		triasquartzite	2	YZ	MS
6	98SL17	VT, ZSZ		prasinite	1		TS
6	98SL18	VT, DB		prasinite	1	XZ	MS
6	98SL19	VT, ZSZ		schiste lustres	1		TS
7	98SL20	VA, MR, float?		metasediment w. and-pseudo.	1		TS
8	98SL21	VA, ZSZ?, float		eclogite	1		
9	98SL22	VA, MR		deformed granite	1		MS
10	98SL23	VG, MR	175/54	metasediment			
11	98SL24	VG, MR	174/84	grt-micaschist			
12	98SL25	VG, MR		metasediment			
12	98SL26	VG, MR	058/34	metasediment			
13	98SL27	VG, ZSZ		serpentinite			
14	98SL28	VG, MR		grt-gneiss			
14	98SL28A	VG, MR		grt-gneiss			
15	98SL29	VA, MR		deformed granite	1		MS
15	98SL30	VA, MR		deformed granite	2		MS
16	98SL31	VA, MR	336/69	metasediment	1	XZ	MS
16	98SL32	VA, MR		deformed granite			
16	98SL33	VA, MR		deformed granite	1		TS
17	98SL34	VA, MR		deformed granite	1		TS
18	98SL35	VA, ZSZ?		eclogite?			
19	98SL36	VA, MR		metasediment	2		TS
20	98SL37	VA, MR		microgranitic part of granite	1		TS
20	98SL38	VA, MR, float		phe-gneiss			
21	98SL39	VA, MR		phe-gneiss	1		TS
21	98SL40	VA, MR		phe-gneiss	1	XZ	TS
21	98SL41	VA, MR		metasediment			
22	98SL42	VA, ZSZ?, float?		eclogite	1		
23	98SL43	VA, ZSZ?, float		eclogite?	1		TS
24	98SL44	VA, ZSZ		serpentinite	1		TS
24	98SL44A	VA, ZSZ		serpentinite	1		TS
17	98SL45	VA, MR		microgranitic part of granite	1		TS
17	98SL45A	VA, MR		microgranitic part of granite			
27	98SL46	VA, MR, float		phengitgneiss	1		MS
28	98SL47	VA, MR, float		metasediment	1		MS
28	98SL48	VA, MR		phe-grt-gneiss			
29	98SL49	VA, MR, float		gneiss	1		MS
30	98SL50	VA, ?		?	1		
31	98SL51	VA, MR, float		gneiss	2		MS
32	98SL52	VA, MR		microgranitic part of granite			
32	98SL53	VA, MR		microgranitic part of granite			
32	98SL54	VA, MR		granite	1		MS
32	98SL55	VA, MR		granite	1		MS
32	98SL56	VA, MR	326/53	granite	1	XZ	MS
33	98SL57	VG, ZSZ		serpentinite			
34	98SL58	VG, ZSZ		serpentinite	1		
34	98SL59	VG, ZSZ	200/40	serpentinite			
34	98SL60	VG, ZSZ		serpentinite			
37	98SL61	VG, ZSZ, float		? Ovardite???			
38	98SL62	VG, ZSZ, float		? Ovardite???			
40	98SL63	VG, ZSZ		serpentinite			
43	98SL64	VA, MR	013/66	phe-gneiss	2	YZ, XZ	MS
44	98SL65	VA, MR	200/18	bio-gneiss	3	YZ, XZ	MS
45	98SL66	VA, MR	140/23	bio-gneiss			
46	98SL67	VA, MR	297/18	?			
46	98SL68	VA, MR	339/26	phe-gneiss			
48	98SL69	VA, MR	350/34	bio-gneiss			
51	98SL70	VA, MR		banded gneiss			

Appendix A

**Table A1.1** List of all samples collected during field summer 1998.

Outcrop#	Sample#	Location	Orientation of sample	Rock type	# of thin sections	cut direction of section	TS/MS
55	98SL71	VA, MR	332/67	banded gneiss			
57A	98SL99	VA, MR	210/76	deformed granite			
57A	98SL100	VA, MR	200/73	granite	1		MS
57A	98SL101	VA, MR		metasediment			
57A	98SL102	VA, MR		phe-gneiss			
65	98SL103	VA, MR	130/50	phe-gneiss			
65	98SL104	VA, ?		mafic greenschist & phe-gneiss			
65	98SL105	VA, MR	228/40	grt-gneiss	2	YZ, XZ	MS
66	98SL106	VA, ?	244/38	boudin, serpentinite			
67	98SL107	VA, MR		chloritised metasediment			
68	98SL108	VA, MR		metasediment			
67	98SL109	VA, ?		mafic with eclogite relicts	1		TS
71	98SL110	VA, ?		mafic			
74	98SL111	VA, MR		late ab/calcite in metasediment			
75	98SL112	VA, MR	268/35	phe-gneiss			
79	98SL113	VA, ZSZ		retrogressed eclogite	1		TS
79	98SL114	VA, ZSZ?		retrogressed eclogite	1		TS
82	98SL115	VA, MR	280/15	phe-gneiss			
83	98SL116	VA, MR		metasediment			
83	98SL117	VA, MR?		retrogressed eclogite	1		TS
84	98SL118	VA, MR	184/84	deformed granite			
86	98SL119	VA, ?		grt-gneiss			
87	98SL120	VA, ?		carbonate, calcsilicate			
87	98SL121	VA, ?		carbonate, calcsilicate			
87	98SL122	VA, MR?		calcsilicate			
88	98SL123	VA, MR	274/22	deformed granite			
90	98SL124	VA, MR, shear zone	228/46	granitic gneiss			
90	98SL125	VA, MR, shear zone		granitic gneiss			
92	98SL126	VA, MR, shear zone	208/52	granitic gneiss	1		TS
92	98SL127	VA, MR, shear zone	165/65	granitic gneiss			
92	98SL128	VA, MR, shear zone		granitic gneiss			
92	98SL129	VA, MR, shear zone	120/55	ctd-schist			
92	98SL130	VA, MR, shear zone	238/47	ctd-schist	4	YZ, XZ	MS
92	98SL131	VA, MR, shear zone	240/52	ctd-schist			
92	98SL132	VA, MR, shear zone	255/37	ctd-schist	1		TS
93	98SL133	VA, MR, shear zone		granite at rim of shear zone	1		
94	98SL134	VA, MR	298/60	gneiss			
94	98SL135	VA, MR	268/70	gneiss			
95	98SL136	VA, MR	158/85	granite			
96	98SL137	VG, ZSZ		gabbro			
97	98SL138	VG, ZSZ		eclogite			
98	98SL139	VG, ?		retrogressed eclogite	1		TS
99	98SL140	VG, MR?		glc-schist			
99	98SL141	VG, MR?		glc-schist w. eclogite relicts			
99	98SL142	VG, MR?		glc-schist			
99	98SL143	VG, MR?		metasediment	2		TS
99	98SL144	VG, MR?	214/45	metasediment			
102	98SL145	VG, MR		metasediment			
102	98SL146	VG, MR	280/68	metasediment			
102	98SL147	VG, ?	328/72	eclogite			
102	98SL148	VG, MR	316/36	bio-gneiss			
102	98SL149	VG, MR	320/38	ctd-bio-gneiss			
102	98SL150	VG, MR, float		bio-gneiss			
102	98SL151	VG, MR, float		gneiss			
104	98SL152	VG, ZSZ?	235/85	quartzite			
109	98SL153	VG, MR		metasediment			
110	98SL154	VG, MR?	208/40	gneiss			
L1	98SZ1	VG, MR		metasediment	1		MS
L2	98SZ2	VG, ZSZ?		eclogite	1		TS
L3	98SZ3	VG, MR		grt-phe-gneiss	1		TS
L4	98SZ4	VG, MR		phe-gneiss	1		TS
L5	98SZ5A	VG, ?		retrogressed eclogite	1		TS
L5	98SZ5B	VG, ?		retrogressed eclogite	1		TS
L5	98SZ5C	VG, ?		eclogitic gabbro	1		TS
L5	98SZ5D	VG, MR		grt-phe-gneiss	1		TS
L6	98SZ6A	VG, ZSZ?		retrogressed eclogite	1		TS
L6	98SZ6B	VG, ZSZ		amp-rich, mafic	1		TS
L6	98SZ6C	VG, ?		gneiss	1		TS
L7	98SZ7	VG, ZSZ		retrogressed eclogite	1		TS
L8	98SZ8	VG, MR?		phe-gneiss			
L9	98SZ9	VG, ?		retrogressed eclogite	1		TS
L10	98SZ10	VG, ?		banded gneiss	1		TS
L11	98SZ11A	VG, ?		gneiss	1		TS

*Appendix A*

**Table A1.1** List of all samples collected during field summer 1998.

Outcrop#	<i>Sample#</i>	Location	Orientation of sample	Rock type	# of thin sections	cut direction of section	TS/MS
L11	<b>98SZ11B</b>	VG, ZSZ		retrogressed eclogite	1		TS
L11	<b>98SZ11C</b>	VG, ZSZ		eclogite	1		TS
L11	<b>98SZ11D</b>	VG, ZSZ		eclogite	1		TS
L11	<b>98SZ11E</b>	VG, ZSZ		retrogressed eclogite	1		TS
L12	<b>98SZ12</b>	VG, ZSZ		ultramafic, mafic	1		TS
L13	<b>98SZ13</b>	VG, ?		gneiss	1		TS

## Appendix A

**Table A1.2** List of all samples collected during field summer 1999.

Outcrop#	Sample#	Location	Orientation of sample	Rock type	# of thin sections	cut direction of section	TS/MS
SM1	99ZS1	Mine Servette, St. Marcel		blueschist			
SM1	99ZS2	Mine Servette, St. Marcel		blueschist			
1	99SL1	VA, Rif. Mezzalama 3090 m	192/74	deformed granite			
1	99SL1A	VA, Rif. Mezzalama 3090 m		deformed granite			
1	99SL2	VA, Rif. Mezzalama 3090 m		deformed granite			
2	99SL3	VA, Rif. Mezzalama 3090 m	314/58	deformed granite			
3	99SL4	VA, APVS, 2340 m	210/25	metasediment			
3	99SL5	VA, APVS, 2340 m		metasediment			
3	99SL6	VA, APVS, 2340 m		metasediment			
3a	99SL7	VA, APVS, 2340 m		metasediment			
3a	99SL8	VA, APVS, 2340 m		metasediment			
3a	99SL9	VA, APVS, 2340 m		metasediment			
3a	99SL10	VA, APVS, 2340 m		metasediment			
4	99SL11	VA, APVS, 2340 m	126/74	granite			
4	99SL12	VA, APVS, 2340 m		granite			
4	99SL13	VA, APVS, 2340 m		granite			
4	99SL14	VA, APVS, 2340 m		granite			
4	99SL15	VA, APVS, 2340 m		granite			
4	99SL16	VA, APVS, 2340 m		granite			
4	99SL17	VA, APVS, 2340 m		granite			
5	99SL18	VA, APVS, 2440 m	322/48	metasediment			
6	99SL19	VA, APVS, 2400 m		metasediment			
6	99SL20	VA, APVS, 2400 m		metasediment			
7	99SL21	VA, APVS, 2430 m	289/54	metasediment			
8	99SL22-A	VA, APVS, 2410 m	312/20	metasediment			
8	99SL22-B	VA, APVS, 2410 m		metasediment			
8	99SL23	VA, APVS, 2410 m		metasediment			
9	99SL24	VA, shear zone, 2796 m	135/37	deformed granite			
9	99SL25	VA, shear zone, 2796 m	102/35	granitic gneiss			
9	99SL26	VA, shear zone, 2796 m	128/65	granitic gneiss			
9	99SL27	VA, shear zone, 2796 m		granitic gneiss			
9	99SL28	VA, shear zone, 2796 m		granitic gneiss			
9	99SL29	VA, shear zone, 2796 m		granitic gneiss			
9	99SL30	VA, shear zone, 2796 m	213/48	whiteschist			
9	99SL31	VA, shear zone, 2796 m		whiteschist			
9	99SL32	VA, shear zone, 2796 m		granitic gneiss			
9	99SL33	VA, shear zone, 2796 m		granitic gneiss red			
10	99SL34	VA, ZSZ, western Vallone di Verra		prasinite			
11	99SL35-A	VA, 1988 m		eclogite?			
11	99SL35-B	VA, 1988 m		eclogite?			
11	99SL35-C	VA, 1988 m		eclogite?			
11	99SL35-D	VA, 1988 m		eclogite?			
12a	99SL36	VA, Mezzalama, 3040 m	020/35	deformed granite			
12a	99SL37	VA, Mezzalama, 3040 m		deformed granite			
12a	99SL38	VA, Mezzalama, 3040 m		deformed granite			
12a	99SL39	VA, Mezzalama, 3040 m		deformed granite			
12a	99SL40	VA, Mezzalama, 3040 m		deformed granite			
12a	99SL41	VA, Mezzalama, 3040 m		deformed granite			
12c	99SL42	VA, Mezzalama, 3040 m	275/29	metasediment			
12c	99SL43	VA, Mezzalama, 3040 m		metasediment			
13	99SL44	VA, Mezzalama, 3040 m	216/31	metasediment			
18	99SL45	VA, Mezzalama, 3036 m	319/05	deformed granite			
18	99SL46	VA, Mezzalama, 3036 m	049/50	deformed granite			
18	99SL47	VA, Mezzalama, 3036 m		deformed granite			
18	99SL48	VA, Mezzalama, 3036 m		deformed granite			
	99SL49	VA, Champoluc		eclogite, sample from float			
	99SL50	VA, Champoluc		eclogite, sample from float			
19	99SL51	VA, APVS, 2410 m	324/70	micaschist, metasediment			
19	99SL52	VA, APVS, 2410 m		micaschist, metasediment			
19	99SL53	VA, APVS, 2410 m	042/35	micaschist, metasediment			
19	99SL54	VA, APVS, 2415 m		metasediment			
	99SL55	outcrop #26 von 1998	234/27	serpentinite			
	99SL56	outcrop #26 von 1998		serpentinite			
20	99SL57	VA, Champoluc		prasinite			
21	99SL58	VA, Champoluc		prasinite			
21	99SL59	VA, Champoluc					
22	99SL60	VA, Colle di Joux, road to FROMY	179/70	prasinite			
23	99SL61	VA, Colle di Joux, church, ca. 1440 m		prasinite			
23	99SL62	VA, Colle di Joux, church, ca. 1440 m		prasinite			
24	99SL63	VA, Colle di Joux		gabbro?			
24	99SL64	VA, Colle di Joux		gabbro?			
24	99SL65	VA, Colle di Joux	172/85	gabbro?			
24	99SL66	VA, Colle di Joux		gabbro?			
	99SL67	VA, Mezzalama, 3036 m	221/53	deformed granite with grt			
	99SL68	VA, Mezzalama, 3036 m		deformed granite with grt			
25	99SL69	VA, Mezzalama, 3095 m		deformed granite			
25	99SL70	VA, Mezzalama, 3095 m		deformed granite			
25	99SL71	VA, Mezzalama, 3095 m		deformed granite			
26	99SL72	VA, Mezzalama, 3105 m		deformed granite			
9	99SL73	VA, shear zone, 2796 m		whiteschist from float			
9	99SL74	VA, shear zone, 2796 m		granite from float			
9	99SL75	VA, shear zone, 2796 m		granite from float			
9	99SL76	VA, shear zone, 2796 m		granite from float			
9	99SL77	VA, shear zone, 2796 m		granite from float			
9	99SL78	VA, shear zone, 2796 m		deformed granite from float			
28	99SL79	VA, APVS, contact granite/sediment, 2575 m	176/70	deformed granite			
28	99SL80	VA, APVS, contact granite/sediment, 2575 m		deformed granite			

Appendix A

**Table A1.2** List of all samples collected during field summer 1999.

Outcrop#	Sample#	Location	Orientation of sample	Rock type	# of thin sections	cut direction of section	TS/MS
28	99SL81	VA, APVS, contact granite/sediment, 2575 m		deformed granite			
28	99SL82	VA, APVS, contact granite/sediment, 2575 m		granite with aplite dyke			
28	99SL83	VA, APVS, contact granite/sediment, 2575 m		granite with aplite dyke			
28	99SL84	VA, APVS, contact granite/sediment, 2575 m	172/75	deformed granite			
29	99SL85	VA, APVS, contact granite/sediment, 2540 m	190/45	metasediment, strongly foliated			
30	99SL86	VA, APVS, contact granite/sediment, 2535 m	275/37	metasediment, strongly foliated			
30	99SL87	VA, APVS, contact granite/sediment, 2535 m		metasediment, strongly foliated			
32	99SL88	VA, APVS, contact granite/sediment, 2525 m	262/50	metasediment, strongly foliated			
33	99SL89	VA, Zone Arcesaz-Brusson, ca. 1705 m	129/22	granite			
33	99SL90	VA, Zone Arcesaz-Brusson, ca. 1705 m		granite			
34	99SL91	VA, Zone Arcesaz-Brusson, ca. 1840 m		serpentinite			
34	99SL92	VA, Zone Arcesaz-Brusson, ca. 1840 m		serpentinite			
34	99SL93	VA, Zone Arcesaz-Brusson, ca. 1840 m		serpentinite			
34	99SL94	VA, Zone Arcesaz-Brusson, ca. 1840 m		serpentinite			
35	99SL95	VA, Zone Arcesaz-Brusson, ca. 1705 m		granite			
35	99SL96	VA, Zone Arcesaz-Brusson, ca. 1705 m		granite			
35	99SL97	VA, Zone Arcesaz-Brusson, ca. 1705 m		granite			
35	99SL98	VA, Zone Arcesaz-Brusson, ca. 1705 m		granite			
35	99SL99	VA, Zone Arcesaz-Brusson, ca. 1705 m		granite			
35	99SL100	VA, Zone Arcesaz-Brusson, ca. 1705 m		granite			
35	99SL101	VA, Zone Arcesaz-Brusson, ca. 1705 m		granite			
35	99SL102	VA, Zone Arcesaz-Brusson, ca. 1705 m		granite			
35	99SL103	VA, Zone Arcesaz-Brusson, ca. 1705 m		granite			
36	99SL104	VA, Zone Arcesaz-Brusson, road to Graines	218/49	granite, strongly deformed			
36	99SL105	VA, Zone Arcesaz-Brusson, road to Graines		granite, strongly deformed			
	99SL106	VA,14.9.99, 2540 m, Eclogite-Boudins, stop 2		eclogite	3		TS
	99SL107	VA,14.9.99, 2540 m, Eclogite-Boudins, stop 2		eclogite	2		TS
	99SL108	VA,14.9.99, 2540 m, Eclogite-Boudins, stop 2		eclogite	1		TS
	99SL109	VA,14.9.99, 2620 m, contact granite/sediments, stop 3		phengite-gneiss			
	99SL110	VA,14.9.99, 2620 m, shear zone, stop 4	265/36	whiteschist	1	XZ	
9	99SL111	VA, shear zone, upper profile	083/72	40.5 m , dyke, massiv	1		MS
9	99SL112	VA, shear zone, upper profile		40.5 m , dyke, massiv	1		MS
9	99SL113	VA, shear zone, upper profile		40.5 m , dyke, massiv	1		MS
9	99SL114	VA, shear zone, upper profile	271/36	31.2 m, dyke, deformed	1	XZ	MS
9	99SL115	VA, shear zone, upper profile	173/45	26 m, red granitic gneiss	1	XZ	MS
9	99SL116	VA, shear zone, upper profile	262/45	22.1 m, dyke, deformed	1		MS
9	99SL117	VA, shear zone, upper profile	247/50	21.8 m	1	XZ	MS
9	99SL118	VA, shear zone, upper profile		21.8 m	1	XZ	MS
9	99SL119	VA, shear zone, upper profile	193/20	15.8 m	3	XZ	MS
9	99SL120	VA, shear zone, upper profile	193/50	ca. 14.5 m	1	XZ	MS
9	99SL121	VA, shear zone, upper profile	114/60	12 m	2	XZ	MS
9	99SL122	VA, shear zone, upper profile	189/63	ca. 20 m	2	XZ	MS
9	99SL123	VA, shear zone, upper profile	196/25	ca. 17.8 m	1	XZ	MS
9	99SL124	VA, shear zone, upper profile		carbonate	1		MS
9	99SL125	VA, shear zone, rim		granite, E side of shear zone	2		MS
9	99SL126	VA, shear zone, rim, SW	224/58	schist	1	XZ	TS
9	99SL127	VA, shear zone, rim, SW	205/45	schist, strong crenulation	1		TS
9	99SL128	VA, shear zone,		dyke massiv	1	XZ	TS
9	99SL129	VA, shear zone, rim, SW	230/48	Schist	1		TS
9	99SL130	VA, shear zone, rim, SW	140/62	deformed granite	1	XZ	TS
9	99SL131	VA, shear zone, lower profile, NE	020/38	late quartz vein	1		TS
9	99SL132	VA, shear zone, lower profile, NE		whiteschist, chloritized	1		TS
9	99SL133	VA, shear zone, lower profile, NE	268/55	whiteschist, chloritized	1		TS
9	99SL134	VA, shear zone, lower profile, NE	255/21	whiteschist, chloritized	1		TS
9	99SL135	VA, shear zone, lower profile, NE	295/57	whiteschist, chloritized	1	XZ	TS
9	99SL136	VA, shear zone, lower profile, NE	256/45	whiteschist, chloritized	1		TS
9	99SL137	VA, shear zone, upper profile	250/42	0 m	1		MS
9	99SL138	VA, shear zone, upper profile	205/57	3 m	1	XZ	MS
9	99SL139	VA, shear zone, upper profile	126/65	7.5 m	2	XZ	MS
9	99SL140	VA, shear zone, upper profile	255/50	10 m, whiteschist	1	XZ	MS
9	99SL141	VA, shear zone, upper profile, carbonate zone		Tlc-Grt-Hgl-Pyrit	3		MS
9	99SL142	VA, shear zone, upper profile, carbonate zone		Ctd-Grt-Karb	1		MS
9	99SL143	VA, shear zone, upper profile, carbonate zone		big allanite	1		MS
9	99SL144	VA, shear zone, upper profile, carbonate zone		carbonate	3		MS
9	99SL145	VA, shear zone, upper profile, carbonate zone		with allanite	1		MS
9	99SL146	VA, shear zone, upper profile, carbonate zone		with allanite	1		MS
9	99SL147	VA, shear zone, upper profile	121/59	whiteschist	3	XZ	MS
9	99SL148	VA, shear zone, upper profile	176/65		1		MS
9	99SL149	VA, shear zone, lower profile	252/34	13.5 m, whiteschist	1		TS
9	99SL150	VA, shear zone, lower profile	240/26	16.5 m, whiteschist	1		TS
9	99SL151	VA, shear zone, lower profile	177/43	20 m, whiteschist with chloritized ctd	2		TS
9	99SL152	VA, shear zone, lower profile	237/25	ca. 22 m, whiteschist	1	XZ	TS
9	99SL153	VA, shear zone, lower profile	105/44	25 m, dark granitic gneiss	1		MS
9	99SL154	VA, shear zone, lower profile	246/30	26.5 m, dark granitic gneiss, chloritized	2	XZ	MS
9	99SL155	VA, shear zone, lower profile	144/78	29 m, dark granitic gneiss, chloritized	1	XZ	TS
9	99SL156	VA, shear zone, lower profile	270/50	ca. 31 m, deformed dyke	1	XZ	TS
9	99SL157	VA, shear zone, lower profile	130/75	ca. 33.5 m, deformed dyke	1		TS
9	99SL158	VA, shear zone, lower profile	272/40	37 m, deformed dyke	1		TS
9	99SL159	VA, shear zone, SW side	082/30	granite	1		TS
40	99SL160	VA, Colle di Joux		granite?			
41	99SL161	VA, Colle di Joux, just after Amay		prasinite			
41	99SL162	VA, Colle di Joux, just after Amay	313/18	prasinite			
41	99SL163	VA, Colle di Joux, just after Amay	290/70	prasinite			
42	99SL164	VA, Colle di Joux		gabbro? with carbonate			
42	99SL165	VA, Colle di Joux		eclogite?			
43	99SL166	VA, Colle di Joux, road to Emarese, Col Tze Core	313/35	eclogite?			
43	99SL167	VA, Colle di Joux, road to Emarese, Col Tze Core		eclogite?			

## Appendix A

**Table A1.2** List of all samples collected during field summer 1999.

Outcrop#	Sample#	Location	Orientation of sample	Rock type	# of thin sections	cut direction of section	TS/MS
43	<b>99SL168</b>	VA, Colle di Joux, road to Emarese, Col Tze Core		eclogite?			
44	<b>99SL169</b>	VA, Arbaz	187/12	eclogite?			
45	<b>99SL170</b>	VA, Castello Graines		serpentinite			
45	<b>99SL171</b>	VA, Castello Graines		serpentinite			
GR1	<b>99GR1</b>	VG, contact at Lago Blu, 2600 m	201/42	metasediment			
GR1	<b>99GR2</b>	VG, contact at Lago Blu, 2600 m	121/89	metasediment			
GR1	<b>99GR3</b>	VG, contact at Lago Blu, 2600 m					
GR1	<b>99GR4</b>	VG, contact at Lago Blu, 2600 m	214/70	gabbro? in metasediment			
GR1	<b>99GR5</b>	VG, contact at Lago Blu, 2600 m	209/65	gabbro? in metasediment			
GR1	<b>99GR6</b>	VG, contact at Lago Blu, 2600 m		metasediment			
GR1	<b>99GR7</b>	VG, contact at Lago Blu, 2600 m		metasediment			
GR3	<b>99GR8</b>	VG, along hiking path 6A		eclogite?			

Appendix A

**Table A1.3** Coordinates of sample locations (Swiss. Ref. Grid.)

Year	Outcrop#	Valley	Coordinates	Year	Outcrop#	Valley	Coordinates
1998	1	VT		1998	97	VG	628.317/080.975
1998	2	VT		1998	98	VG	629.132/080.564
1998	3	VT		1998	99	VG	629.152/080.362
1998	4	VT		1998	102	VG	629.039/081.257
1998	5	VT		1998	104	VG	631.716/079.158
1998	6	VT		1998	109	VG	632.216/079.733
1998	7	VA	625.216/083.990	1998	110	VG	632.335/079.475
1998	8	VA	624.873/083.228	1998	L1	VG	633.814/080.119
1998	9	VA	625.882/084.168	1998	L2	VG	633.784/080.175
1998	10	VG	633.716/080.168	1998	L3	VG	633.676/080.455
1998	14	VG	633.745/080.099	1998	L4	VG	633.814/080.256
1998	15	VA	624.868/084.644	1998	L5	VG	633.718/080.693
1998	16	VA	624.623/082.327	1998	L6	VG	633.578/080.802
1998	17	VA	624.549/082.317	1998	L7	VG	633.191/080.911
1998	18	VA	625.078/082.990	1998	L8	VG	633.147/081.856
1998	19	VA	625.020/083.070	1998	L9	VG	632.912/081.713
1998	20	VA	625.010/083.099	1998	L10	VG	632.913/081.714
1998	21	VA	624.971/083.158	1998	L11	VG	632.637/081.931
1998	22	VA	624.833/083.228	1998	L12	VG	632.637/081.931
1998	23	VA	624.725/083.193	1998	L13	VG	
1998	24	VA	623.382/080.792	1999	1	VA	625.130/085.020
1998	25	VA	623.255/080.752	1999	2	VA	625.070/084.940
1998	26	VA	623.627/081.248	1999	3	VA	624.631/082.688
1998	27	VA	624.402/082.505	1999	4	VA	624.528/082.688
1998	28	VA	624.324/082.347	1999	5	VA	625.133/082.422
1998	29	VA	624.304/082.312	1999	6	VA	624.974/082.375
1998	30	VA	624.020/081.886	1999	7	VA	625.015/082.313
1998	31	VA	625.157/082.777	1999	8	VA	624.979/082.328
1998	32	VA	624.941/083.079	1999	9	VA	625.140/084.130
1998	33	VG	632.056/078.315	1999	10	VA	western V. di Verra
1998	34	VG	632.148/078.241	1999	11	VA	western V. di Verra
1998	37	VG	632.480/078.327	1999	12	VA	624.830/084.870
1998	38	VG	632.431/078.317	1999	13	VA	624.825/084.840
1998	40	VG	631.961/078.144	1999	18	VA	624.898/084.687
1998	43	VA	625.966/081.980	1999	19	VA	624.774/082.276
1998	44	VA	626.020/081.950	1999	20	VA	Champoluc
1998	45	VA	626.015/081.921	1999	21	VA	Champoluc
1998	46	VA	626.025/081.901	1999	22	VA	Colle di Joux
1998	48	VA	625.965/081.881	1999	23	VA	Colle di Joux
1998	51	VA	625.653/081.990	1999	24	VA	Colle di Joux
1998	55	VA	625.361/082.238	1999	25	VA	625.225/085.125
1998	57	VA	625.235/082.970	1999	26	VA	625.310/085.115
1998	57A	VA	625.282/082.960	1999	28	VA	625.604/083.031
1998	65	VA	624.696/084.634	1999	29	VA	625.369/082.982
1998	66	VA	624.598/084.639	1999	30	VA	625.369/082.983
1998	67	VA	624.618/084.718	1999	32	VA	625.371/082.975
1998	71	VA	624.623/084.837	1999	33	VA	Arcesaz-Brusson
1998	74	VA	624.740/084.802	1999	34	VA	Arcesaz-Brusson
1998	75	VA	624.740/084.805	1999	35	VA	Arcesaz-Brusson
1998	79	VA	624.814/084.931	1999	36	VA	Arcesaz-Brusson
1998	82	VA	624.961/085.069	1999	40	VA	Colle di Joux
1998	83	VA	624.980/085.119	1999	41	VA	Colle di Joux
1998	84	VA	625.010/085.163	1999	42	VA	Colle di Joux
1998	86	VA	625.480/085.441	1999	43	VA	Colle di Joux
1998	87	VA	625.422/085.396	1999	44	VA	Colle di Joux
1998	88	VA	625.206/084.302	1999	45	VA	Colle di Joux
1998	90	VA	625.127/084.223	1999	46	VA	625.451/082.089
1998	92	VA	625.118/084.188	1999	47	VA	625.535/083.112
1998	93	VA	625.304/084.356	1999	GR1	VG	632.829/080.200
1998	94	VA	625.980/084.277	1999	GR3	VG	632.800/080.000
1998	95	VA	625.892/084.188				
1998	96	VG	628.208/079.961				



Appendix A

**Table A1.4** List of investigated samples. Used method for each sample is indicated (x).

Sample#	Rock type (Location see Table A1)	Isotopic Investigations							Fission track dating		
		XRF	EMS	U-Pb	Zrc	Ar/Ar	Stable Isotope	Rb/Sr	Sm/Nd	Pb/Pb	apatite, zircon
98SL22	granite		X								
98SL29	deformed granite	X	X	X				X	X	X	X
98SL30	granite		X								
98SL126	dark granitic gneiss	X									
98SL127	red granitic gneiss	X									
98SL128	red granitic gneiss	X									
98SL130	dark granitic gneiss	X	X								
98SL132	whiteschist	X						X	X	X	
98SL133	granite, SW side of shear zone	X	X	X				X	X	X	X
98SL134	granitic gneiss	X									
99SL1A	deformed granite			X							
99SL26	granitic gneiss	X									
99SL28	granitic gneiss	X									
99SL29	granitic gneiss	X									
99SL30	whiteschist	X									
99SL31	whiteschist	X									
99SL73	whiteschist from float	X									
99SL79	deformed granite	X									
99SL80	deformed granite										
99SL105	granite, strongly deformed	X		X							X
99SL110	whiteschist	X						X	X	X	
99SL111	40.5 m , dyke, massiv	X	X								
99SL112	40.5 m , dyke, massiv	X						X	X	X	
99SL113	40.5 m , dyke, massiv	X						X	X	X	
99SL114	31.2 m, dyke, deformed	?									
99SL115	26 m, red granitic gneiss	X						X	X	X	
99SL116	22.1 m, dyke, deformed	X									
99SL117	21.8 m										
99SL118	21.8 m	X						X	X	X	
99SL119	15.8 m	X	X			X					
99SL120	ca. 14.5 m	X						X	X	X	
99SL121	12 m	X						X	X	X	
99SL122	ca. 20 m	X	X								
99SL124	carbonate						X				
99SL125	granite, NE side of shear zone	X	X	X				X		X	X
99SL126	schist	X									
99SL127	schist, strong crenulation	X						X	X	X	
99SL128	dyke massiv	X						X	X	X	
99SL129	Schist	X									
99SL130	deformed granite	X									
99SL131	late quartz vein										
99SL132	whiteschist, chloritised										
99SL133	whiteschist, chloritised										
99SL134	whiteschist, chloritised										
99SL135	whiteschist, chloritised										
99SL136	whiteschist, chloritised										
99SL137	0 m										
99SL138	3 m										
99SL139	7.5 m	X	X								
99SL140	10 m, whiteschist	X						X	X	X	
99SL141	Tlc-Grt-Hgl-Pyrit										
99SL142	Ctd-Grt-Karb										
99SL143	big allanite										
99SL144	carbonate						X				
99SL145	with allanite		X								
99SL146	with allanite		X		X						
99SL147	whiteschist		X								
99SL148			X								
99SL149	13.5 m, whiteschist	X						X	X	X	
99SL150	16.5 m, whiteschist	X						X	X	X	
99SL151	20 m, whiteschist with chloritised ctd										
99SL152	ca. 22 m, whiteschist	X						X	X	X	
99SL153	25 m, dark granitic gneiss	X						X	X	X	
99SL154	26.5 m, dark granitic gneiss, chloritised	X									
99SL155	29 m, dark granitic gneiss, chloritised										
99SL156	ca. 31 m, deformed dyke	X						X	X	X	
99SL157	ca. 33.5 m, deformed dyke	X						X	X	X	
99SL158	37 m, deformed dyke	X						X	X	X	
99SL159	granite, SW side of shear zone	X	X	X				X	X	X	X



Fig. A1\_1

Sample locations in the upper Val d' Ayas (Italy)

Coordinates of the sample locations are given in Tab. A1\_3

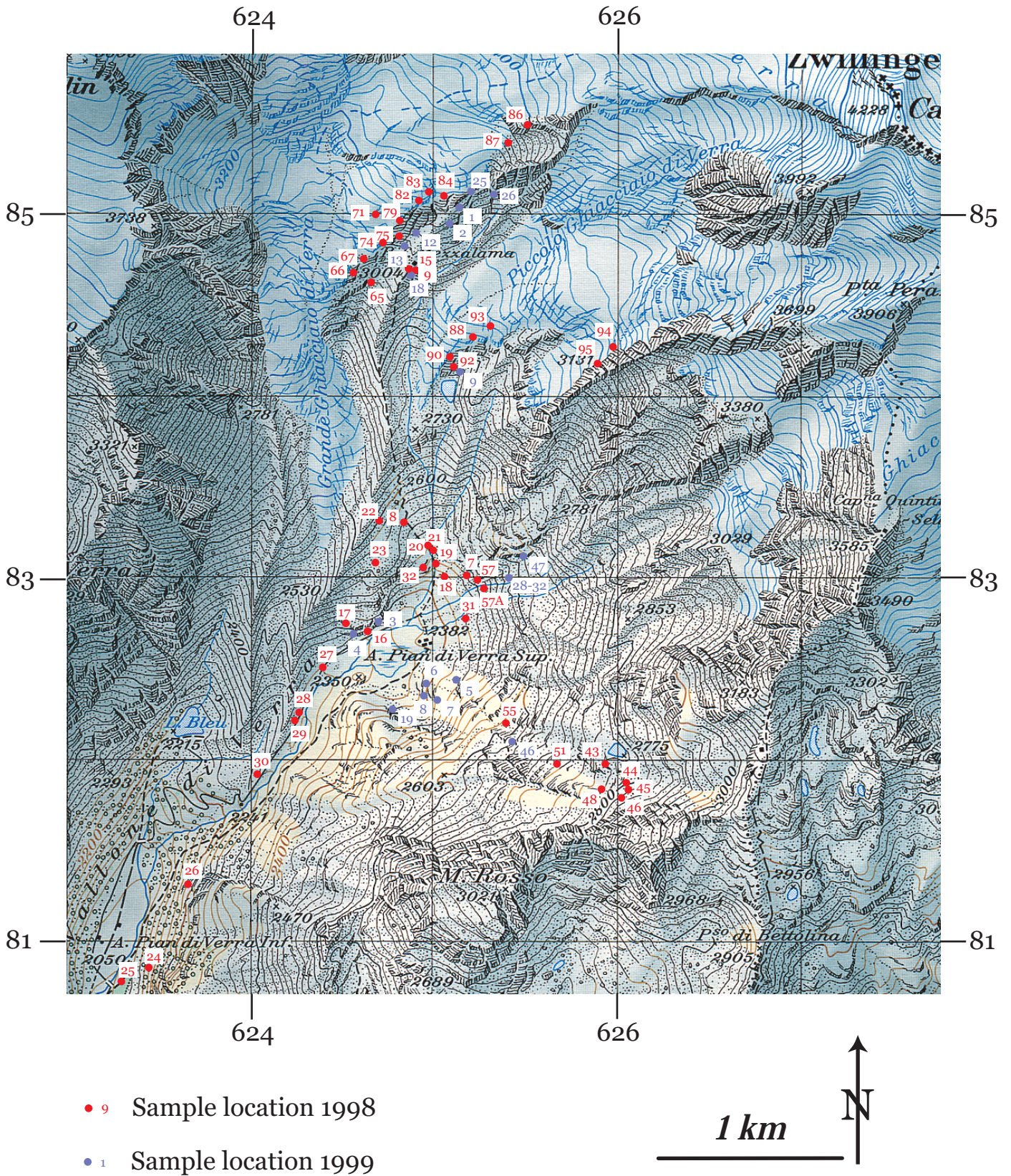




Fig. A1\_2

Sample locations in the Val Gressoney (Italy)

Coordinates of the sample locations are given in Tab. A1.3

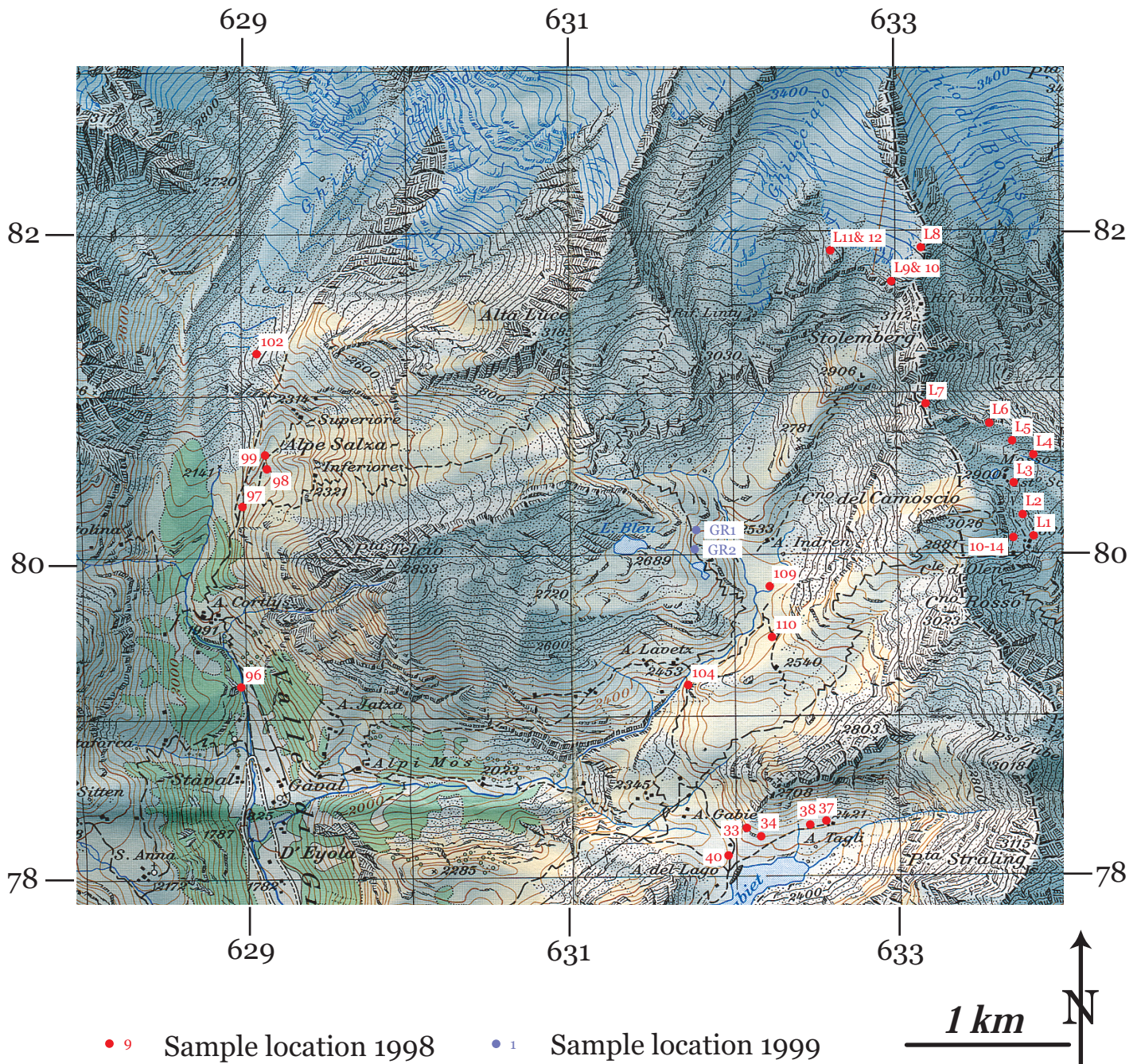




Fig. A1\_3

Sample locations in the Val Tournenche (Italy)

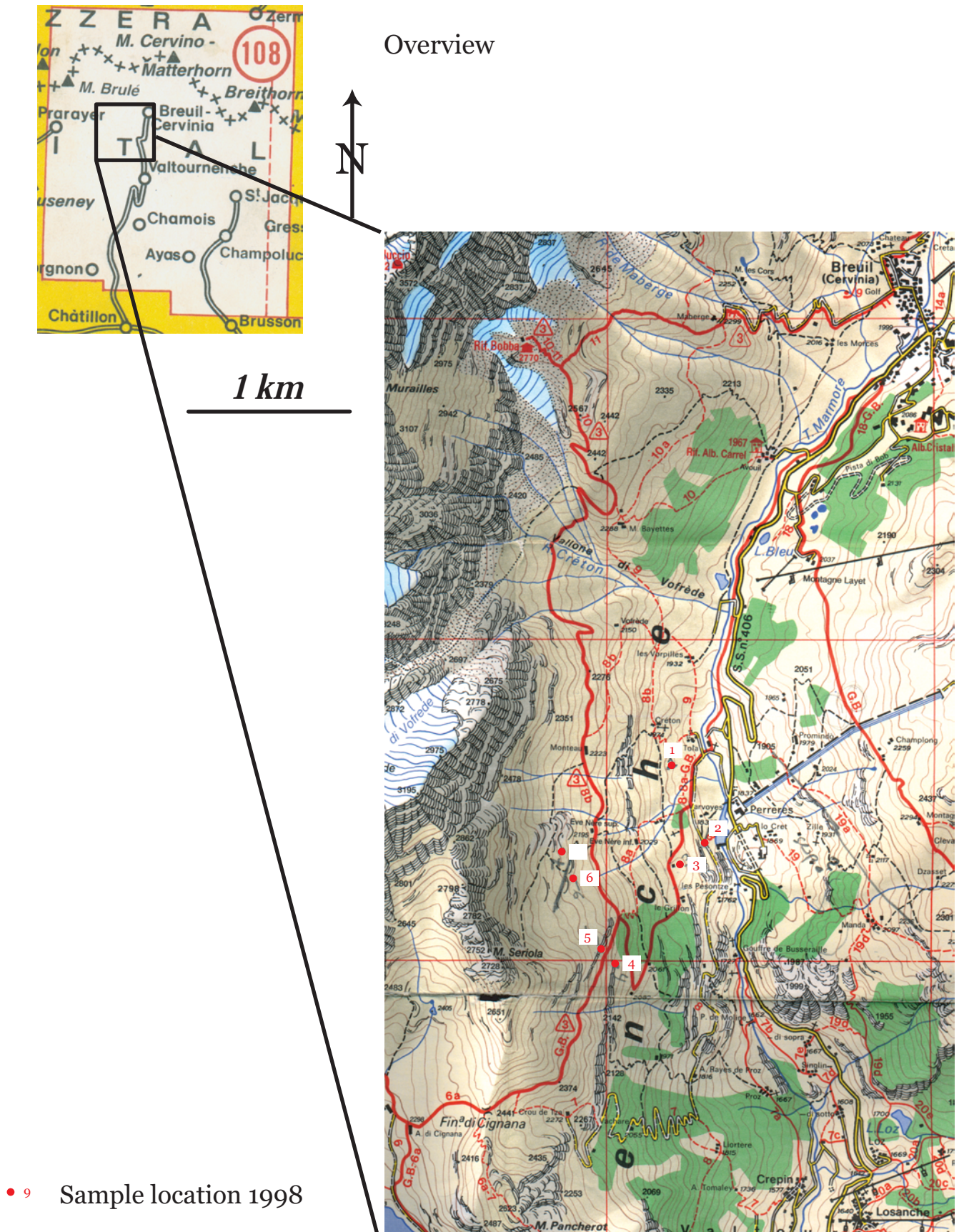
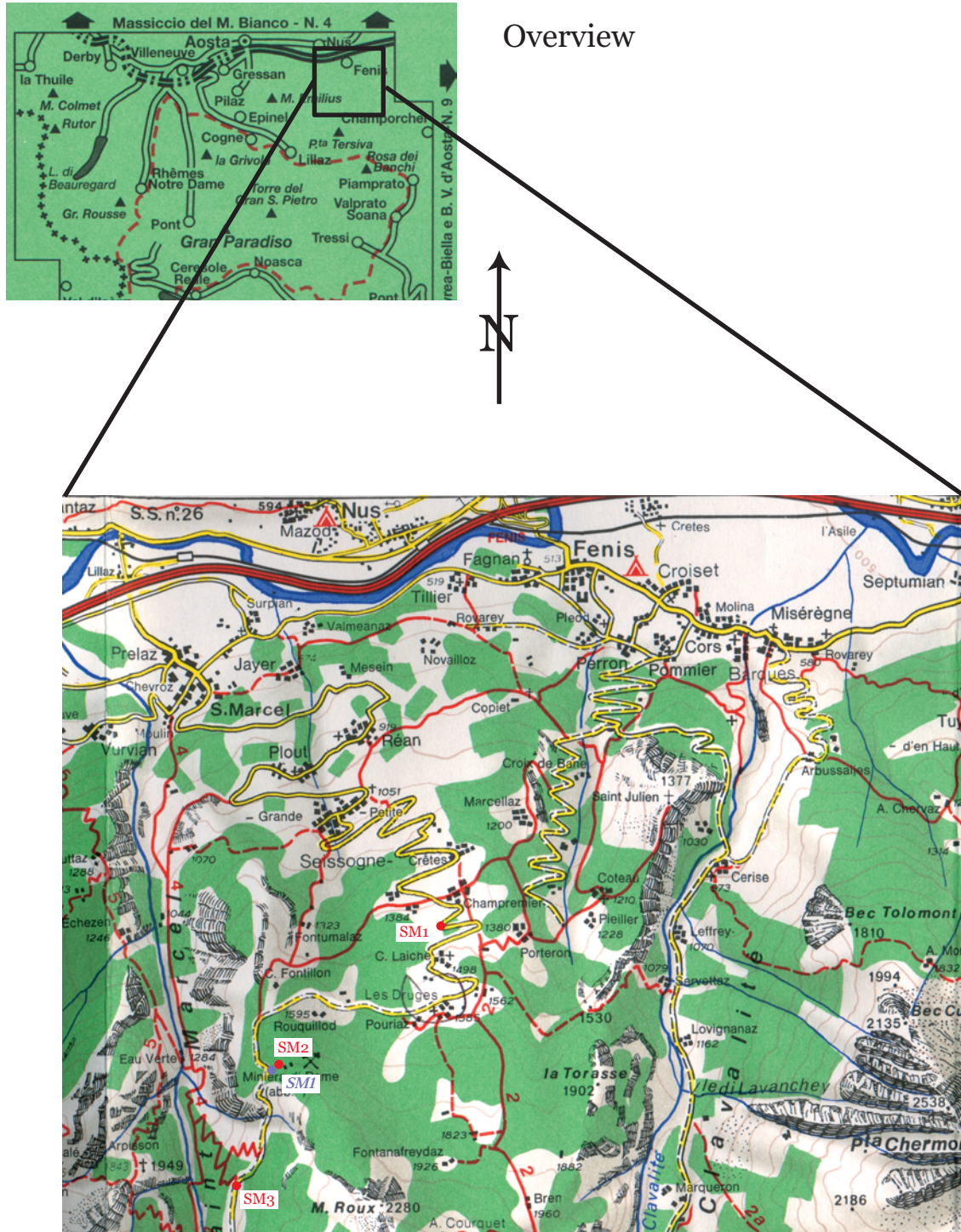




Fig. A1\_4

Sample locations im Valle di St. Marcel (Italy)



- 9 Sample location 1998
- 1 Sample location 1999

2 km

**Table A2.1** Tectonic data

Field season	Outcrop #	Valley	Remarks, description	S1	S2	S3	Lineation	Fold axis undifferentiated	Fold axis of crenulation	Fold axis isoclinal	Fold axis open	Axis plane	Dykes
1998	2	VT	ZSZ							348/27	290/15		
1998	2	VT	ZSZ					000/21	092/35		355/20	288/60	
1998	5	VT	Cz, transquartzite	260/18									
1998	7	VT	DB	018/25									
1998	10	VG	MR	215/20				235/52	156/32				
1998	12	VG	MR	212/18									
1998	13	VG	ZSZ	292/40									
1998	15	VA	MR, Rif, Mezzalama	287/22									
1998	16	VA	APVS, 2430 m	332/83			064/15						0.56/38 quartz
1998	16	VA	APVS, 2430 m	345/86			074/20						
1998	16	VA	APVS, 2430 m	334/75									
1998	16	VA	APVS, 2430 m	332/78									
1998	16	VA	APVS, 2430 m	332/69									
1998	16	VA	APVS, 2430 m	324/80									
1998	16	VA	APVS, 2430 m	329/71									
1998	16	VA	APVS, 2430 m	331/73									
1998	17	VA	APVS, 2430 m	252/13									
1998	17	VA	APVS, 2430 m	243/06									
1998	17	VA	APVS, 2430 m	248/20									
1998	17	VA	APVS, 2430 m	246/15									
1998	17	VA	APVS, 2430 m	251/11									
1998	17	VA	APVS, 2430 m	258/21									
1998	26	VA	APVI, ZSZ	228/32									
1998	26	VA	APVI, ZSZ	258/30									
1998	26	VA	APVI, ZSZ	253/36									
1998	26	VA	APVI, ZSZ	224/34									
1998	26	VA	APVI, ZSZ	224/27									
1998	26	VA	APVI, ZSZ	226/31									
1998	26	VA	APVI, ZSZ	254/32									
1998	26	VA	APVI, ZSZ	234/31									
1998	26	VA	APVI, ZSZ	233/27									
1998	26	VA	APVI, ZSZ	227/35									
1998	33	VG	Rif, Gabbiet, ZSZ	138/24									
1998	33	VG	Rif, Gabbiet, ZSZ	149/08									
1998	34	VG	Lago Gabbiet	170/45									
1998	34	VG	Lago Gabbiet	161/50									
1998	34	VG	Lago Gabbiet	148/35									
1998	34	VG	Lago Gabbiet	164/55									
1998	34	VG	Lago Gabbiet	175/49									
1998	39	VG	Lago Gabbiet	065/50									
1998	42	VG	Lago Gabbiet	167/68									
1998	42	VG	Lago Gabbiet	165/71									
1998	42	VG	Lago Gabbiet	166/65									
1998	42	VG	Lago Gabbiet	165/66									
1998	43	VA	APVS, direction C-Q, Sella, MR	162/34									
1998	43	VA	APVS, direction C-Q, Sella, MR	159/22									
1998	43	VA	APVS, direction C-Q, Sella, MR	160/30									
1998	43	VA	APVS, direction C-Q, Sella, MR	161/28									
1998	43	VA	APVS, direction C-Q, Sella, MR	159/26									
1998	43	VA	APVS, direction C-Q, Sella, MR	174/23									
1998	43	VA	APVS, direction C-Q, Sella, MR	172/34									
1998	43	VA	APVS, direction C-Q, Sella, MR	170/30									
1998	43	VA	APVS, direction C-Q, Sella, MR	192/18									
1998	44	VA	APVS, direction C-Q, Sella, MR	173/18									
1998	44	VA	APVS, direction C-Q, Sella, MR	204/30									

**Table A2.1** Tectonic data

Field season	Outcrop #	Valley	Remarks, description	S1	S2	S3	Lineation	Fold axis undifferentiated	Fold axis of crenulation	Fold axis isoclinal	Fold axis open	Dykes
1998	44	VA	APVS, direction C-Q, Sella, MR	198/26								
1998	44	VA	APVS, direction C-Q, Sella, MR	199/20								
1998	45	VA	APVS, direction C-Q, Sella, MR		284/13							
1998	45	VA	APVS, direction C-Q, Sella, MR		190/28 Lon Si							
1998	45	VA	APVS, direction C-Q, Sella, MR	137/24	191/20 Lon Si							
1998	45	VA	APVS, direction C-Q, Sella, MR	139/24	189/26 Lon Si							
1998	46	VA	APVS, direction C-Q, Sella, MR	228/17								
1998	46	VA	APVS, direction C-Q, Sella, MR	246/15								
1998	47	VA	APVS, direction C-Q, Sella, MR	262/27								
1998	48	VA	APVS, direction C-Q, Sella, MR	124/65				045/10	262/35			
1998	48	VA	APVS, direction C-Q, Sella, MR	118/56								
1998	49	VA	APVS, direction C-Q, Sella, MR	270/21								
1998	49	VA	APVS, direction C-Q, Sella, MR	259/28								
1998	50	VA	APVS, direction C-Q, Sella, MR	290/41								
1998	50	VA	APVS, direction C-Q, Sella, MR	291/46								
1998	51	VA	APVS, direction C-Q, Sella, MR	292/66								
1998	52	VA	APVS, direction C-Q, Sella, MR	244/22								
1998	52	VA	APVS, direction C-Q, Sella, MR	240/25								
1998	53	VA	APVS, direction C-Q, Sella, MR	255/38								
1998	54	VA	APVS, direction C-Q, Sella, MR	243/26								
1998	54	VA	APVS, direction C-Q, Sella, MR	276/30								
1998	55	VA	APVS, direction C-Q, Sella, MR	316/22								
1998	55	VA	APVS, direction C-Q, Sella, MR	357/79							255/68	
1998	57	VA		350/83			250/40					245/62 Pegmatite
1998	57	VA		337/79			52/30					250/65 Pegmatite
1998	58	VA					044/03 Tourmaline					
1998	58	VA					042/03 Tourmaline					
1998	58	VA					242/46					
1998	59	VA	MR, metasediments					263/47				
1998	60	VA	MR, pegmatite in metasediments	352/60								
1998	60	VA	MR, metasediments	280/55								
1998	60	VA	MR, metasediments	339/78								
1998	60A	VA	MR, metasediments	314/57								
1998	60A	VA	MR, metasediments				254/42					
1998	60A	VA	MR, metasediments				230/50 Tourmaline					067/45 Pegmatite
1998	60A	VA	MR, granite	290/55								
1998	60A	VA	MR, metasediments	290/50								
1998	61	VA	MR, contact granite/metasediments	320/85								
1998	63	VA	MR	234/72			278/28 Biotite					
1998	64	VA	MR	263/20			265/38					
1998	65	VA	MR	355/45			260/28					
1998	65	VA	MR				289/50					
1998	65	VA	MR				296/40	324/50				
1998	65	VA	2nd crenulation						000/48			
1998	65	VA	2nd crenulation in open fold				196/20					
1998	65	VA	2nd crenulation in schistosity				280/20					286/27
1998	66	VA	boudin, ultramafite	258/34			262/27					
1998	66	VA	late ab-qtz fillings	269/46	068/13		340/15					
1998	74	VA	MR, 3020 m									
1998	78	VA	MR, 3040 m, shear zone with chl									275/20
1998	79	VA	basite	308/36								
1998	79	VA	MR, metasediments	307/85								
1998	80	VA	MR, 3050 m									
1998	80	VA	MR, 3090 m, metasediments	285/30								318/35
1998	81	VA	MR, 3105 m									
1998	84	VA	MR, 3165 m, granite		268/28	258/60						345/35
1998	84	VA	MR, 3165 m, metasediments									324/20

**Table A2.1** Tectonic data

Field season	Outcrop #	Valley	Remarks, description	S1	S2	S3	Lineation	Fold axis undifferentiated	Axis plane of crenulation	Fold axis isoclinal	Axis plane open	Dykes
1998	85	VA	MR, metasediments					056/28				
1998	88	VA	MR, 2870 m, shear zone	248/65								
1998	89	VA	MR, deformed granite	215/35								
1998	90	VA	MR	194/46			037/59 Tourmaline					
1998	90	VA	MR	230/20			012/34 Feldspar					
1998	90	VA	MR	192/56								
1998	91	VA	MR, whiteschist	248/29					112/15			
1998	92	VA	MR, shear zone, SW part	300/25								
1998	92	VA	MR, shear zone, SW part	266/40								
1998	92	VA	MR, shear zone, SW part	212/50								
1998	98	VG		002/60								
1998	100	VG						335/20			012/12	
1998	101	VG	MR, metasediments							262/33	002/03	262/80
1998	102	VG	MR, metasediments							085/15	250/20	160/45
1998	103	VG	ZSZ, Alpe Gabiet, Weg 6A							138/25	274/20	
1998	104	VG	ZSZ	330/40								
1998	104	VG	ZSZ	205/65								
1998	104	VG	ZSZ	240/50								
1998	104	VG	ZSZ							126/10		
1998	105	VG	ZSZ, 2470 m									
1998	107	VG	ZSZ, 2470 m									
1998	108	VG	ZSZ	227/45								
1998	110	VG	MR? 2525 m	030/45								
1998	110	VG	MR? 2525 m	278/30								
1998	111	VG	prasinite, 2530 m	218/70						310/20	056/65	
1999	1	VA	MR, Rif. Mezzalama, 3090 m	279/25								210/22 Aplite
1999	2	VA	MR, Rif. Mezzalama, 3090 m	308/26								
1999	3	VA	MR, Rif. Mezzalama, 3090 m	301/48								
1999	3	VA	MR, APVS, 2340 m, contact granite/sediments	354/65								
1999	3	VA	MR, APVS, 2340 m, contact granite/sediments	342/59								
1999	3	VA	MR, APVS, 2340 m, contact granite/sediments	356/66								
1999	3	VA	MR, APVS, 2340 m, contact granite/sediments	334/80								
1999	3	VA	MR, APVS, 2340 m, contact granite/sediments	336/85								
1999	3	VA	MR, APVS, 2340 m, contact granite/sediments	339/64								
1999	3	VA	MR, APVS, 2340 m, contact granite/sediments						056/22			
1999	3	VA	MR, APVS, 2340 m, contact granite/sediments						062/23			
1999	3	VA	MR, APVS, 2340 m, contact granite/sediments						058/26			
1999	3	VA	MR, APVS, 2340 m, contact granite/sediments						058/10			
1999	3	VA	MR, APVS, 2340 m, contact granite/sediments	341/70					066/15			
1999	3	VA	MR, APVS, 2340 m, contact granite/sediments						056/25			
1999	4	VA	MR, APVS, 2340 m, contact granite/sediments	340/40								
1999	5	VA	MR, APVS, 2440 m, metasediments	302/45								
1999	5	VA	MR, APVS, 2440 m, metasediments	299/36								
1999	5	VA	MR, APVS, 2440 m, metasediments	296/37								
1999	5	VA	MR, APVS, 2440 m, metasediments	286/41								
1999	6	VA	MR, APVS, 2400 m, metasediments	285/40								
1999	6	VA	MR, APVS, 2400 m, metasediments	295/39								
1999	6	VA	MR, APVS, 2400 m, metasediments	297/34								
1999	7	VA	MR, APVS, 2430 m, metasediments	300/47								
1999	7	VA	MR, APVS, 2430 m, metasediments	306/42								
1999	7	VA	MR, APVS, 2430 m, metasediments	292/46								
1999	7	VA	MR, APVS, 2430 m, metasediments	296/34								
1999	8	VA	MR, APVS, 2410 m, metasediments	302/26								
1999	8	VA	MR, APVS, 2410 m, metasediments	307/28								
1999	8	VA	MR, APVS, 2410 m, metasediments	314/12								338/10
1999	8	VA	MR, APVS, 2410 m, metasediments	300/31								



**Table A2.1** Tectonic data

Field season	Outcrop #	Valley	Remarks, description	S1	S2	S3	Lineation	Fold axis undifferentiated	Fold axis of crenulation	Fold axis isoclinal	Fold axis open	Axis plane	Dykes
1999	8	VA	MR, APVS, 2410 m, metasediments	296/24									
1999	9	VA	MR, shear zone, aplite dykes	228/34									
1999	9	VA	MR, shear zone, granite orientation	177/63									
1999	9	VA	MR, shear zone, granite	271/47									
1999	9	VA	MR, shear zone, granite	240/54									
1999	9	VA	MR, shear zone, granite	250/52									
1999	9	VA	MR, shear zone, granite	245/55									
1999	9	VA	MR, shear zone, granitic gneiss dark	218/46									
1999	9	VA	MR, shear zone, granitic gneiss dark	192/41									
1999	9	VA	MR, shear zone, granitic gneiss dark	218/60									
1999	9	VA	MR, shear zone, granitic gneiss dark	221/50									
1999	9	VA	MR, shear zone, granitic gneiss dark	225/30									
1999	9	VA	MR, shear zone, granitic gneiss red	221/25									
1999	9	VA	MR, shear zone, granitic gneiss red	218/60									
1999	9	VA	MR, shear zone, whiteschist	335/85									
1999	9	VA	MR, shear zone, whiteschist	333/37									
1999	9	VA	MR, shear zone, whiteschist	237/33									
1999	9	VA	MR, shear zone, whiteschist	250/50									
1999	9	VA	MR, shear zone, granitic gneiss	259/85									
1999	9	VA	MR, shear zone, granitic gneiss	257/30									
1999	9	VA	MR, shear zone, granitic gneiss	260/37									
1999	9	VA	MR, shear zone, granitic gneiss red	240/85									
1999	9	VA	MR, shear zone, granitic gneiss red	242/39									
1999	9	VA	MR, shear zone, granitic gneiss red	241/34									
1999	9	VA	MR, shear zone, whiteschist	275/55									
1999	9	VA	MR, shear zone, whiteschist	190/44									
1999	9	VA	2600 m contact MR/ZSZ, Lago Blu	194/48									
1999	9	VA	2600 m contact MR/ZSZ, Lago Blu	196/51									
1999	9	VA	2600 m contact MR/ZSZ, Lago Blu	191/43									
1999	9	VA	2610 m contact MR/ZSZ, Lago Blu	200/17									
1999	9	VA	2610 m contact MR/ZSZ, Lago Blu	213/15									
1999	9	VA	2610 m contact MR/ZSZ, Lago Blu	208/20									
1999	9	VA	2610 m contact MR/ZSZ, Lago Blu	206/16									
1999	9	VA	2610 m contact MR/ZSZ, Lago Blu	205/35									
1999	9	VA	2610 m contact MR/ZSZ, Lago Blu	210/70									
1999	9	VA	2610 m contact MR/ZSZ, Lago Blu	238/24									
1999	9	VA	2610 m contact MR/ZSZ, Lago Blu	233/15									
1999	9	VA	2625 m contact MR/ZSZ, Lago Blu	225/20									
1999	9	VA	2625 m contact MR/ZSZ, Lago Blu	216/25									
1999	9	VA	2625 m contact MR/ZSZ, Lago Blu	226/34									
1999	9	VA	2625 m contact MR/ZSZ, Lago Blu									092/63	
1999	9	VA	2625 m contact MR/ZSZ, Lago Blu									100/10	
1999	9	VA	2625 m contact MR/ZSZ, Lago Blu									121/15	
1999	9	VA	2625 m contact MR/ZSZ, Lago Blu	316/16									
1999	9	VA	2625 m contact MR/ZSZ, Lago Blu	070/07									
1999	9	VA	2625 m contact MR/ZSZ, Lago Blu	323/25									
1999	9	VA	ZSZ, mafic/ultramafic, 2600 m	328/27									
1999	9	VA	ZSZ, mafic/ultramafic, 2600 m										022/20
1999	12a	VA	MR, 3040 m, metasediments	218/52									
1999	12a	VA	MR, 3040 m, metasediments	220/67									
1999	12a	VA	MR, 3040 m, metasediments	220/59									
1999	12a	VA	MR, 3040 m, metasediments	217/57									
1999	12a	VA	MR, 3040 m, metasediments	221/61									
1999	12a	VA	MR, 3040 m, metasediments										282/40
1999	12a	VA	MR, 3040 m, metasediments	192/60									270/55

**Table A2.1** Tectonic data

Field season	Outcrop #	Valley	Remarks, description	S1	S2	S3	Lineation	Fold axis undifferentiated	Axis plane of crenulation	Fold axis isoclinal	Axis plane isoclinal	Fold axis open	Axis plane open	Dykes
1999	12a	VA	MR, 3040 m, metasediments						257/37					
1999	12b	VA	MR, 3040 m, metasediments						308/37					
1999	12b	VA	MR, 3040 m, metasediments	218/73					284/42					
1999	12c	VA	MR, 3040 m, metasediments						270/20			275/43		
1999	12c	VA	MR, 3040 m, metasediments	238/38					258/32					
1999	12c	VA	MR, 3040 m, metasediments						232/35					
1999	13	VA	MR, 3020 m, metasediments	254/32					270/35					
1999	14	VA	MR, 3010 m, metasediments											268/50 Quartz
1999	15	VA	MR, 3020 m, metasediments	249/30										
1999	16	VA	MR, 3025 m, metasediments	265/25					215/43					
1999	16	VA	MR, 3025 m, metasediments	266/32										
1999	16	VA	MR, 3025 m, metasediments	281/35					358/25					
1999	17	VA	MR, 3025 m, metasediments						266/40			251/50		
1999	17	VA	MR, 3025 m, metasediments						278/38					
1999	18	VA	MR, 3036 m, granite	284/25										
1999	18	VA	MR, 3036 m, granite	285/30										
1999	18	VA	MR, 3036 m, granite	298/35						300/45				
1999	18	VA	MR, 3036 m, granite											
1999	18	VA	MR, 3036 m, granite	345/83										
1999	18	VA	MR, 3036 m, granite	343/87										353/89
1999	18	VA	MR, 3036 m, granite	340/85										
1999	18	VA	MR, 3036 m, granite	312/30										
1999	18	VA	MR, 3036 m, granite	315/28										
1999	18	VA	MR, 3036 m, granite	310/29										
1999	19	VA	MR, 2590 m, APVS											
1999	19a	VA	MR, 2410 m, APVS, metasediments	289/26										
1999	19a	VA	MR, 2410 m, APVS, metasediments	269/35										
1999	19a	VA	MR, 2410 m, APVS, metasediments	281/30					094/27					
1999	19a	VA	MR, 2410 m, APVS, metasediments						092/21					
1999	19a	VA	MR, 2410 m, APVS, metasediments						358/10					
1999	19a	VA	MR, 2410 m, APVS, metasediments	285/20										
1999	19a	VA	MR, 2410 m, APVS, metasediments	281/16										
1999	19a	VA	MR, 2410 m, APVS, metasediments	304/18										
1999	19a	VA	MR, 2410 m, APVS, metasediments	297/18					350/06					
1999	19a	VA	MR, 2410 m, APVS, metasediments						322/06					
1999	19a	VA	MR, 2410 m, APVS, metasediments	308/27					006/09					
1999	19a	VA	MR, 2410 m, APVS, metasediments						004/02					
1999	19a	VA	MR, 2410 m, APVS, metasediments	254/28					014/06					
1999	19a	VA	MR, 2410 m, APVS, metasediments						192/30			210/32		
1999	19a	VA	MR, 2410 m, APVS, metasediments	295/34					246/20					
1999	19a	VA	MR, 2410 m, APVS, metasediments	292/20										
1999	19a	VA	MR, 2410 m, APVS, metasediments	293/30										
1999	19b	VA	MR, 2415 m, APVS, metasediments						044/03					
1999	20	VA	ZSZ, Champoluc	160/17										
1999	20	VA	ZSZ, Champoluc	164/20										
1999	20	VA	ZSZ, Champoluc	140/22										
1999	20	VA	ZSZ, Champoluc	155/20										
1999	21	VA	ZSZ, Champoluc	264/11					356/20 Boudin					
1999	21	VA	ZSZ, Champoluc	186/21					163/15					
1999	22	VA	ZSZ, Colle di Joux, road to Fromy	296/25										
1999	23	VA	ZSZ, Colle di Joux	354/16										
1999	24	VA	ZSZ, Colle di Joux, layering	026/10					158/06					
1999	24	VA	ZSZ, Colle di Joux											176/06
1999	25	VA	MR, 3095 m, deformed granite	329/59										

**Table A2.1** Tectonic data

Field season	Outcrop #	Valley	Remarks, description	S1	S2	S3	Lineation	Fold axis undifferentiated	Fold axis of crenulation	Fold axis isoclinal	Fold axis open	Axis plane	Dykes
1999	25	VA	MR, 3095 m, deformed granite	331/54									
1999	25	VA	MR, 3095 m, deformed granite	326/47									
1999	27	VA	MR, 3110 m, deformed granite						254/25				
1999	27	VA	MR, 3110 m, deformed granite				166/34 Tourmaline		250/39			233/47	
1999	9	VA	MR, shear zone, 2810 m, granitic gneiss	193/68					249/36				
1999	9	VA	MR, shear zone, 2810 m, granitic gneiss	199/55					263/30				
1999	9	VA	MR, shear zone, 2810 m, granitic gneiss	204/48									
1999	9	VA	MR, shear zone, 2810 m, granitic gneiss	197/98					258/30				
1999	9	VA	MR, shear zone, 2810 m, granitic gneiss	183/42					256/31				
1999	9	VA	MR, shear zone, 2810 m, granitic gneiss						266/27				
1999	9	VA	MR, shear zone, 2810 m, granitic gneiss	194/36					250/27				
1999	9	VA	MR, shear zone, 2810 m, granitic gneiss	229/31					274/27				
1999	9	VA	MR, shear zone, 2810 m, granitic gneiss	224/55					266/30				
1999	9	VA	MR, shear zone, 2810 m, granitic gneiss	258/20					346/24				
1999	9	VA	MR, shear zone, middle part	215/57					278/19				
1999	9	VA	MR, shear zone, middle part (Umbiegung)	212/53					276/24				
1999	9	VA	MR, shear zone, middle part (Umbiegung)	209/53					277/21				
1999	9	VA	MR, shear zone, SE part of "Umbiegung"	204/31					273/11				
1999	9	VA	MR, shear zone, SE part of "Umbiegung"	208/32					271/20				
1999	9	VA	MR, shear zone, NW part of "Umbiegung"	241/30					260/17				
1999	9	VA	MR, shear zone, NW part of "Umbiegung"	246/20					272/24				
1999	28	VA	MR, APVS, 2575 m, granite	110/62									
1999	28	VA	MR, APVS, 2575 m, granite	114/74									
1999	28	VA	MR, APVS, 2575 m, granite	105/37									
1999	29	VA	MR, APVS, 2540 m, metasediments	110/32					234/44				
1999	30	VA	MR, APVS, 2535 m, metasediments	270/32					320/45				
1999	30	VA	MR, APVS, 2535 m, metasediments	265/47									
1999	30	VA	MR, APVS, 2535 m, metasediments	267/45									
1999	31	VA	MR, APVS, 2530 m, metasediments	246/39									
1999	32	VA	MR, APVS, 2525 m, metasediments	276/46									
1999	34	VA	ZSZ, Zone Arceaz-Brusson, 1840 m, serpentinite	236/35									
1999	36	VA	Zone Arceaz-Brusson, Road to Graines	165/31									
1999	9	VA	MR, shear zone, western end	185/65									
1999	9	VA	MR, shear zone, granitic gneisses	203/48				200/40				234/34	
1999	9	VA	MR, shear zone, granitic gneisses	217/46					210/42			228/34	
1999	9	VA	MR, shear zone, granitic gneisses	235/48					234/46			227/33	
1999	9	VA	MR, shear zone, granitic gneisses	186/60					214/44			210/30	
1999	9	VA	MR, shear zone, granitic gneisses	213/50					215/43			220/44	
1999	9	VA	MR, shear zone, granitic gneisses	175/38					207/38				
1999	9	VA	MR, shear zone, granitic gneisses	196/62					222/40				
1999	9	VA	MR, shear zone, granitic gneisses						227/39				
1999	9	VA	MR, shear zone, granitic gneisses						215/37				
1999	9	VA	MR, shear zone, granitic gneisses						210/39				
1999	9	VA	MR, shear zone, granitic gneisses						222/36				
1999	9	VA	MR, shear zone, granitic gneisses	205/44									
1999	9	VA	MR, shear zone, granitic gneisses	230/48									
1999	9	VA	MR, shear zone, "Umbiegung"	216/40									
1999	9	VA	MR, shear zone, "Umbiegung"	234/44									
1999	9	VA	MR, shear zone, "Umbiegung"	230/40									
1999	9	VA	MR, shear zone, "Umbiegung"	248/30									
1999	9	VA	MR, shear zone, "Umbiegung"	254/28									
1999	9	VA	MR, shear zone, "Umbiegung" NW	266/30									
1999	9	VA	MR, shear zone, upper profile, 4m						260/53			350/54	
1999	9	VA	MR, shear zone, upper profile, 6m	276/54									

**Table A2.1** Tectonic data

Field season	Outcrop #	Valley	Remarks, description	S1	S2	S3	Lineation	Fold axis undifferentiated	Fold axis of crenulation	Axis plane isoclinal	Fold axis open	Axis plane	Dykes
1999	9	VA	MR, shear zone, upper profile, 8m	267/44									
1999	9	VA	MR, shear zone, upper profile, 9m	264/50									
1999	9	VA	MR, shear zone, upper profile, 10m	266/43									
1999	9	VA	MR, shear zone, upper profile, 11m	282/76									
1999	9	VA	MR, shear zone, upper profile, 12m	252/52									
1999	9	VA	MR, shear zone, upper profile, 14m	237/62									
1999	9	VA	MR, shear zone, upper profile, 16m	249/43									
1999	9	VA	MR, shear zone, upper profile, 16m	205/40									
1999	9	VA	MR, shear zone, upper profile, 17m				235/74 crenulation						
1999	9	VA	MR, shear zone, upper profile, 18m	217/47			212/27 Feldspar						
1999	9	VA	MR, shear zone, upper profile, 18m				210/32 White mica						
1999	9	VA	MR, shear zone, upper profile, 22m	241/45									
1999	9	VA	MR, shear zone, upper profile, 22m				210/43 Tourmaline						
1999	9	VA	MR, shear zone, upper profile, 24m	240/40									
1999	9	VA	MR, shear zone, upper profile, 24m	261/49			240/42 Feldspar						
1999	9	VA	MR, shear zone, upper profile, 26m	246/46									
1999	9	VA	MR, shear zone, upper profile, 27m	252/37									
1999	9	VA	MR, shear zone, upper profile, 28m	265/40									
1999	9	VA	MR, shear zone, upper profile, 29m										
1999	9	VA	MR, shear zone, upper profile, 29m	246/35			230/30 Tourmaline						
1999	9	VA	MR, shear zone, upper profile, 34m	254/43			234/28 Tourmaline						
1999	9	VA	MR, shear zone, upper profile, 34m				241/40 Tourmaline						
1999	9	VA	MR, shear zone, upper profile, 36m	242/48			220/34 Tourmaline						
1999	9	VA	MR, shear zone, lower profile, 6m	222/67					310/20				
1999	9	VA	MR, shear zone, lower profile, 8m	219/64					300/37				
1999	9	VA	MR, shear zone, lower profile, 9m	224/40			297/30 Tourmaline						
1999	9	VA	MR, shear zone, lower profile, 10m						282/30				
1999	9	VA	MR, shear zone, lower profile, 16m	264/35									
1999	9	VA	MR, shear zone, lower profile, 16m	267/28		086/39 Cren. plane							
1999	9	VA	MR, shear zone, lower profile, 20m	253/35									
1999	9	VA	MR, shear zone, lower profile, 24m	274/21									
1999	9	VA	MR, shear zone, lower profile, 27m	270/35		016/65 Cren. plane							
1999	9	VA	MR, shear zone, lower profile, 27m				248/32 Feldspar					336/20	
1999	9	VA	MR, shear zone, lower profile, 29m	265/44					282/34				
1999	9	VA	MR, shear zone, lower profile, 30m	265/47			224/39 Feldspar						
1999	9	VA	MR, shear zone, lower profile, 33m	266/70			216/28 Tourmaline						

## **Appendix B**

### CD-Rom

#### Microprobe and isotopic data

A CD-Rom is normally attached to this thesis. It contains tables with microprobe data (folder B1), thin section photographs and backscattered electron images of the analyzed samples with locations of the microprobe analyses points (folder B2). Folder B3 includes the database of microprobe data and respective images on monazites. Tables with Nd and Pb isotopic data can be found in folder B4. For further details, please refer to the README-file on the CD-Rom.

The CD-Rom can be obtained on request from the author.